Studies of Exciton Condensation and Transport in Quantum Hall Bilayers

Thesis by

Aaron David Kiyoshi Finck

In Partial Fulfillment of the Requirements

for the Degree of

Doctor of Philosophy

California Institute of Technology

Pasadena, California

2012

(Defended September 22, 2011)

Acknowledgements

First, I would like to thank Jim Eisenstein for mentoring me during all of the years that I have been at Caltech. I deeply appreciate his patience, wisdom, and great expertise in both scientific and technical areas. I have felt extraordinarily lucky to have an advisor who is so readily available to his students whenever they need him. It has been a great honor to have worked in his group.

Next, I would like to thank Alexandre Champagne, who worked on bilayers with me during my first three years at Caltech. He provided invaluable assistance in the lab, such as teaching me how to operate a dilution refrigerator and helping to work out bugs in my sample processing and measurement circuitry. He also provided moral support when things went wrong.

I would also like to express gratitude to former labmates Bart McGuyer and Ghislain Granger. Bart helped to show me the ropes during my first few months in Jim's lab. Ghislain was always available to bounce ideas off of and to help me out when various pieces of equipment in the cleanroom needed maintenance.

I would like to give a special thanks to Caryn Bullard, Debaleena Nandi, Erik Henriksen, and Jing Xia for all the effort they put into proofreading this thesis.

Finally, I would like to thank my family for all of the love and support that they have given me throughout the years.

Abstract

This thesis is a report of the transport properties of bilayer two-dimensional electron systems found in GaAs/AlGaAs double quantum well semiconductor heterostructures. When a strong perpendicular magnetic field is applied so that the total Landau filling factor is equal to one and if the two layers are close enough together, a novel quantum Hall (QH) state with strong interlayer correlations can form. This QH state is often described as an excitonic condensate, in which electrons in one layer pair with holes in the other. As neutral particles, excitons feel no Lorentz force and are not confined to the edges of the bilayer system like charged quasiparticles are. Instead, excitons are expected to be able to move freely through the bulk and even flow without any dissipation under proper conditions (i.e., excitonic superfluidity). Counterflow studies that directly probe the bulk verify this exciton transport in the electrically insulating interior. We also report on studies of the phase boundary between the correlated and uncorrelated phases at total Landau filling factor one as the effective interlayer separation is tuned. When both phases are fully spin polarized at high Zeeman energy, the phase transition is much broader than when the uncorrelated phase is incompletely polarized at low Zeeman energy. This suggests a possible change in the nature of the phase transition in the regime of complete spin polarization.

Contents

List of Figures

4

Introduction

A two-dimensional system of electrons (2DES) subjected to a large magnetic field displays a rich plethora of unusual phenomena induced by electron–electron interactions. While such interparticle interactions have only a minor effect on most Fermi systems at zero field, the formation of highly degenerate Landau levels in large fields quenches the kinetic energy term in the many-body Hamiltonian by transforming it into a constant. To good approximation, only the Coulomb repulsion term remains to govern the behavior of the electrons. One consequence is the fractional quantum Hall effect (FQHE), which occurs when a fraction of a Landau level is occupied. In a FQHE state, Coulomb interactions cause the electrons to execute an intricate dance in order to avoid each other. The low-energy excitations of fractional quantum Hall states act like particles exhibiting exotic properties such as carrying fractional charges [73] and having fractional exchange-statistics [49, 5].

This thesis focuses on the particular quantum Hall state found in a bilayer system comprised of two 2DESs separated by a small distance d and with a total electron density N_T equal to the degeneracy eB/h of one spin-resolved Landau level. For large values of d, the electrons in one layer are not correlated with the electrons in the other. However, if the ratio of d to the magnetic length $\ell = \sqrt{\frac{\hbar c}{eB}}$ is below a critical value, then interlayer Coulomb interactions are comparable to intralayer interactions, and a unique quantum Hall state can form at total Landau filling factor $\nu_T \equiv N_T/(eB/h) = 1$. In this so-called $\nu_T = 1$ state, the electrons in one layer become bound to the holes in the other to form interlayer excitons. Figure 1 provides a vastly simplified depiction of this electron–hole pairing. As bosons, the excitons can condense into the same state [32] and exhibit superfluid-like properties [125].

Signs of exciton condensation, such as Josephson-like interlayer tunneling [103] and vanishing Hall resistance for currents driven in opposite direction in the two layers [66, 121, 127], have already been observed. However, a number of questions about the $\nu_T = 1$ quantum Hall state remain.
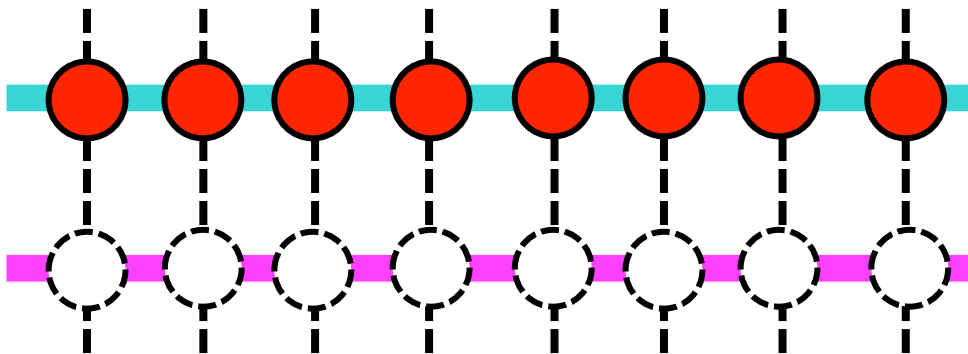
Figure 1: Depiction of exciton condensation at $\nu_T = 1$. The electrons (filled circles) in the upper layer are bound to the holes (empty circles) in the lower layer. A particle-hole transformation has changed the half-filled Landau level in the bottom layer into a combination of a half-filled level of holes and a completely filled level of electrons, which is not shown here.

First, the nature of the phase transition between the correlated and uncorrelated phases of the bilayer system at $\nu_T = 1$ is not well understood. Originally, it was anticipated that the onset of exciton condensation should be characterized by a Kosterlitz-Thouless phase transition at a specific temperature T_{KT}. While there is evidence from tunneling spectroscopy for a finite temperature transition [12], other transport measurements show activated behavior similar to other quantum Hall systems. One important clue is that spin might play a role under most circumstances: recent measurements [106, 71] have revealed that the correlated phase has greater spin polarization than the uncorrelated phase. A discontinuous change in spin polarization across the phase transition would signal a first-order phase transition.

Second, while interlayer tunneling studies show a sharp, Josephson-like peak at zero bias, the width and height of the peak both seem to remain finite even when extrapolated to zero temperature. This is in contrast to a true Josephson effect, where the tunneling conductance should be infinite. Furthermore, the maximum interlayer tunneling current is several orders of magnitude below expected values. These two properties both suggest that disorder might play an important role in tunneling.

Third, evidence for true excitonic superfluidity remains elusive. Wen and Zee [125] predicted that currents driven in opposite directions in the two layers (a flow pattern known as counterflow currents) should correspond to a dissipationless flow of excitons at $\nu_T = 1$. Experiments in Hall bar-shaped samples have revealed counterflow currents possess residual resistance at finite temperature. It is unclear whether the compressible edge channels common to all quantum Hall states might play some role in these counterflow experiments. Thus, up until recently there had been no evidence that counterflow currents could even exist in the bulk of the $\nu_T = 1$ system.

This thesis aims to clarify our understanding of the $\nu_T = 1$ state by seeking answers to these questions. It is organized as follows:

In **chapter 1**, we give an introduction to the physics behind the $\nu_T = 1$ quantum Hall effect. We review Landau quantization as well as the integer and fractional quantum Hall effects in single-layer systems. We will see that similar states can occur within bilayer systems, including the $\nu_T = 1$ state. We will develop the formalism of pseudospin ferromagnetism to describe the $\nu_T = 1$ state and arrive at a model Hamiltonian for the order parameter. We will explain how this state can be equivalently described as an exciton condensate with superfluid-like properties. We will discuss previously reported experimental evidence of superfluid behavior.

Chapter 2 contains a summary of the various materials and methods we use to realize and study bilayer quantum Hall systems. This includes an overview of the GaAs/AlGaAs heterostructures that can house a bilayer system, our sample-processing techniques, cryogenic equipment used to obtain millikelvin temperatures required for the observation of the $\nu_T = 1$ state, and bilayer transport techniques.

Two particular examples of bilayer transport measurements, interlayer tunneling

and interlayer capacitance, are described in greater detail in **chapter 3**. We will review the physics behind single-particle tunneling between two 2DESs at zero magnetic field and show some characteristic tunneling acquired under these conditions. We will then discuss interlayer capacitance and how it is composed of both geometric and quantum mechanical components. Preliminary capacitance measurements at zero and high magnetic field are presented. The analysis of the capacitance data is rudimentary, but this chapter should provide background for more detailed experiments in the future.

In **chapter 4**, we explore how the phase transition between the correlated and uncorrelated phases evolves with Zeeman energy. These results were first reported in reference [38]. We find that while the phase transition is relatively narrow at low Zeeman energy, it is much broader at high Zeeman energy, when both phases are fully spin polarized. We discuss these results in the context of two different models of the phase boundary in which the bilayer system comprises a mixture of correlated and uncorrelated fluids. The increase in width of the phase transition for the two spin regimes could indicate a change in the nature of the phase transition. We then consider the phase transition at finite temperature and analyze the results in terms of a first-order phase transition.

In **chapter 5**, we discuss the area and perimeter dependence of the Josephson-like interlayer tunneling peak at $\nu_T = 1$. We find clear evidence that the tunneling conductance is proportional to the area of the $\nu_T = 1$ system, suggesting that tunneling is a bulk phenomenon. This runs counter to the initial expectation that tunneling current should be confined to within a Josephson length $\lambda_J \approx 1$–10 μm from the perimeter of the exciton condensate. A likely explanation is that disorder permits tunneling in the bulk. Although most of the results we present in this chapter come from a region of phase space near the phase transition, we do find hints that this area dependence persists to relatively low d/ℓ and temperature. These findings were first published in reference [37].

Next, in **chapter 6** we report on transport studies of a bilayer sample with a Corbino geometry, which allows us to directly probe the properties of the bulk. While

charged excitations are gapped out in the interior of the $\nu_T = 1$ state, we find that counterflow currents can propagate through the bulk with relatively little dissipation. We identify these counterflow currents with exciton currents that are generated by an Andreev-like process at the edges of the quantum Hall system. This chapter expands upon our first report of bulk exciton currents in reference [39] and represents the central finding of this thesis.

In the final chapter, we summarize our research on exciton condensation and transport in the $\nu_T = 1$ quantum Hall state. We consider future directions for exploring this unusual correlated system.

Chapter 1

Quantum Hall Effect at $\nu_T = 1$

In this chapter we review the fundamental physics and phenomenology of the $\nu_T = 1$ quantum Hall state. We start by discussing the quantum Hall effect, which is observed in clean two-dimensional electron systems (2DESs) subjected to a strong perpendicular magnetic field. The strong magnetic field causes the formation of highly degenerate Landau levels (LLs) in the energy spectrum of single-particle states. Whenever the chemical potential lies in the gap between two of these levels, the interior of the system becomes incompressible, but current can flow along chiral, dissipationless edge channels. These edge channels dominate the transport properties of the sample, resulting in a quantized plateau in Hall resistance. This phenomenon is known as the integer quantum Hall effect (IQHE) because it is associated with an integral number of filled Landau levels.

A quantizing magnetic field effectively leads to a quenching of the kinetic energy because each of the states within a given Landau level has (in the absence of disorder) the same energy. The kinetic energy consequently can be treated as a constant term in the Hamiltonian and thus the many-body energy spectrum becomes almost completely determined by the interactions between pairs of electrons. Strong Coulomb repulsion leads to the electrons forming a highly correlated state in which they perform an intricate dance around each other. This behavior can lead to incompressible quantum Hall states even when only a fraction of a Landau level is filled; thus, the formation of these correlated states is known as the fractional quantum Hall effect (FQHE). Through the picture proposed by Jain [57], a fractional quantum Hall state

of electrons can be described in terms of an integer quantum Hall state of composite particles known as composite fermions.

The physics of fractional quantum Hall states can be extended to bilayer samples in which one 2DES is situated just above another. When the separation between the two layers is small enough, Coulomb repulsion generates interlayer correlations as electrons in one layer begin to avoid electrons in the other. One of the most famous example of these states (and the focus of this thesis) is the bilayer quantum Hall state occurring when the total Landau filling factor of the bilayer is equal to 1. Generally called the $\nu_T = 1$ state, this system is often described as an exciton condensate. This description is motivated by a wave function in which the electrons in one layer become bound to holes in the other, creating an exciton spread between the two layers. This bilayer system has a number of dramatic transport properties, such as Josephson-like tunneling, vanishing Hall resistance when currents are driven in opposite directions in the two layers, and quantized Hall drag resistance.

1.1 Quantum Hall Effect

A two-dimensional system of electrons cooled to near absolute zero and subjected to a strong perpendicular magnetic field exhibits a rich variety of physics known collectively as the quantum Hall effect. In essence, an energy gap opens up at certain values of the magnetic field due to either Landau quantization (in the case of the integer quantum Hall effect) or Coulomb repulsion (in the case of the fractional quantum Hall effect). Much like a simple band insulator (for example, see chapter 7 in reference [68]), this gap prevents electrical currents from penetrating the interior of the system (that is, the bulk conductivity $\sigma_{xx} = 0$). Unlike a band insulator, a quantum Hall state has one or more edge channels at its boundary that permit the dissipationless transport of charge. Consequently, the Hall conductivity σ_{xy} is nonzero. In this regard, the quantum Hall state is the first known example of a topological insulator [51].

In this section, we will describe how Landau quantization generates a single-

particle energy spectrum that is characterized by a series of highly degenerate peaks known as Landau levels. We will discuss how the combination of a disorder potential and the edge channels lead to the quantized Hall conductivity that lies at the heart of the dramatic transport properties whenever an integer number of Landau levels are populated. We will also show that electron–electron interactions can generate an energy gap and lead to quantized transport even when a Landau level is only partially filled.

1.1.1 Landau Quantization

First, we consider a system of electrons confined to the x-y plane and subjected to a magnetic field $\vec{B} = B\hat{z}$. For now, we will ignore impurities, electron–electron interactions, and spin. We will also treat the electrons as having a parabolic dispersion with isotropic mass m. The Hamiltonian for each electron is then

$$H = \frac{1}{2m}\left(\vec{p} + \frac{e}{c}\vec{A}\right)^2,\tag{1.1}$$

where the vector potential $\vec{A}$ is defined by $\vec{B} = \vec{\nabla} \times \vec{A}$. Here, we are using CGS units; to convert to SI units, one should simply omit the c. To proceed, we choose to fix the gauge of the problem and adopt what is known as the Landau gauge: $\vec{A} = -By\,\hat{x}$. This leads to

$$H = \frac{1}{2m}p_y^2 + \frac{1}{2m}\left(p_x - B\frac{e}{c}y\right)^2.\tag{1.2}$$

We observe that $[H, p_x] = 0$ and thus energy eigenstates can be chosen to be also eigenstates of p_x. By replacing the implicit operator p_x with its eigenvalue $\hbar k_x$, we can write the Hamiltonian as

$$H = \frac{1}{2m}p_y^2 + \frac{1}{2}m\omega_c^2(y - \ell^2 k_x)^2,\tag{1.3}$$

where $\omega_c = \frac{Be}{mc}$ is the classical cyclotron frequency and $\ell = \sqrt{\frac{\hbar c}{eB}}$ is the magnetic length. Now, the system looks identical to a harmonic oscillator with the character-

istic frequency ω_c, but with the potential well centered at $y = \ell^2 k_x$. We can then denote the allowed energy eigenvalues as

$$E_n = \hbar\omega_c(n + \frac{1}{2}), \ n = 0, 1, 2, 3, ..., \tag{1.4}$$

and the eigenstates should be of the form

$$\psi_{n,k_x}(\vec{r}) = \frac{1}{C}e^{ik_xx} \exp\left[-\frac{1}{2\ell^2}(y - \ell^2 k_x)^2\right] H_n(\frac{y}{\ell} - \ell k_x), \tag{1.5}$$

in which $H_n(z)$ are the Hermite polynomials [58] and C is a normalization factor. Note that the energy spectrum does not depend on k_x. Also, the wave functions are localized in the y direction but extend as plane waves in the x direction. This is in contrast to the usual semiclassical picture of electrons executing small, circular orbits.

In the absence of a magnetic field, a two-dimensional electron gas with an isotropic, parabolic dispersion has a constant density of states in terms of energy. Equation (1.4) informs us that a perpendicular magnetic field causes the density of states to collapse into a series of equally spaced and highly degenerate peaks centered on the discrete values of energy E_n. Without any impurities, these peaks are essentially delta functions (see figure 1.3a). Each of these peaks, known as Landau levels (LLs), comprise of a large number of states that are labelled by their momenta k_x. To find the degeneracy of a single Landau level (N_L), we must find the number of allowed k_x values. We consider a rectangular sample with dimensions $L_x \times L_y$. By applying periodic boundary conditions, we find that the allowed values of k_x are

$$k_x = 2\pi\frac{n_x}{L_x}, \ n_x = 0, 1, 2, 3, ..., (N_L - 1). \tag{1.6}$$

With the relation $y = \ell^2 k_x$, the index $n_x = 0$ corresponds to $y = 0$ and $n_x = N_L - 1$ corresponds to $y \approx L_y$. Thus, the number of states in each Landau level is essentially $N_L = \frac{L_y L_x}{2\pi\ell^2}$. For arbitrarily shaped samples, we can replace the product $L_x L_y$ with the sample area S, resulting in

$$N_L = \frac{S}{2\pi\ell^2} \tag{1.7}$$

for the general case. In the limit of zero temperature, N electrons will fill up a number of LLs given by the Landau filling factor $\nu \equiv N/N_L = 2\pi\ell^2 N/S = \frac{hc}{eB}N_S$. Here, N_S is the areal density of electrons.

Real electrons have a spin quantum number, which we have ignored up to this point. Spin provides an additional degree of freedom and adds the Zeeman term $\frac{\mu_B g_s}{\hbar}\vec{S}\cdot\vec{B}$ to the Hamiltonian. Here, $\vec{S}$ is the spin angular momentum of a single electron, $\mu_B = e\hbar/2m_e c$ is the Bohr magneton (in cgs units), and g_s is the material-dependent gyromagnetic ratio. Each spin has its own series of Landau levels, with the spin degeneracy lifted by the Zeeman term. The magnitude of this Zeeman splitting (often referred to as the Zeeman energy) is given by $E_Z = |\mu_B g_s B|$.

1.1.2 Integer Quantum Hall Effect: Edge Channels and Disorder

In this section, we will consider magnetotransport in a system within the quantum Hall regime, where the energy separation between Landau levels is well resolved. Samples under such conditions can show vanishing longitudinal resistance $R_{xx} = 0$ and quantized Hall resistance $R_{xy} = \frac{1}{n}\frac{h}{e^2}$ when the Landau filling factor ν is equal to an integer n. Remarkably, the longitudinal and Hall resistances can remain at these values for a range of ν within the vicinity of $\nu = n$, giving rise to what are known as Hall plateaux. We explain this phenomenon in terms of charge-carrying edge channels, which will dominate transport when the bulk is insulating. We will argue how disorder allows Hall resistance to remain quantized even when ν deviates from an integer value.

Up until now, we have ignored the edges of the system and only considered the bulk. However, real samples are limited in space by a confinement potential $V(x,y)$. While $V(x,y) = 0$ in the interior, the potential rises at the edges of the sample. For a rectangular sample, we redefine these edges to occur at $y = \pm L_y/2$ and $x = \pm L_x/2$. Assuming that the length scale over which $V(x,y)$ varies is large compared to ℓ, we can make the estimation that the Landau levels merely rise in energy at the edges

of the sample and are given by $E_n(x, y) = \hbar\omega_c(n + \frac{1}{2}) + V(x, y)$. This is depicted in figure 1.1a.
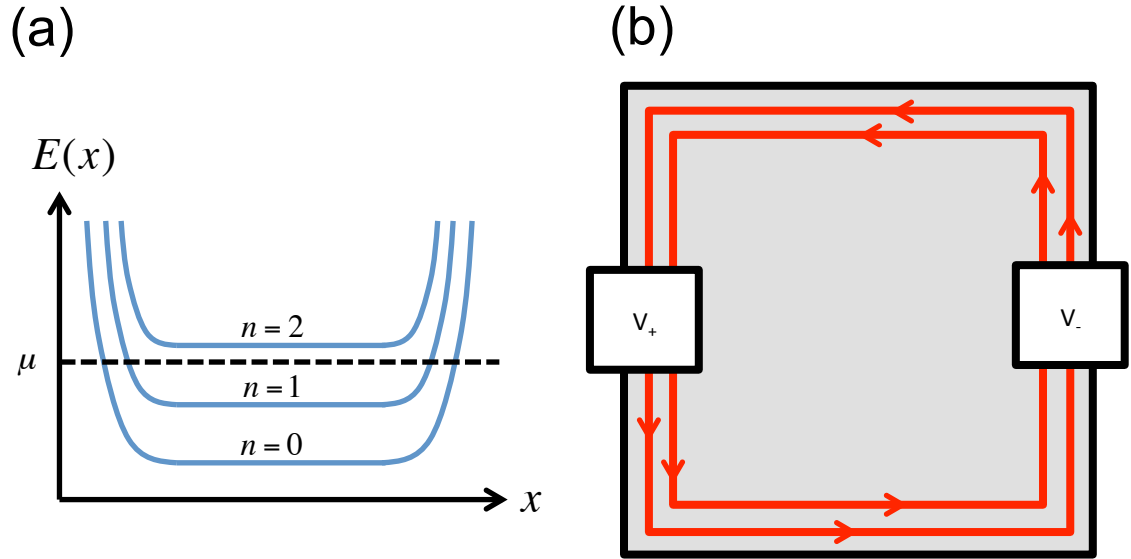
Figure 1.1: (a) Cross section of energy spectrum and its spatial variation due to the confinement potential. Here, the line associated with the chemical potential μ intersects two of the Landau levels at each edge when $\nu = 2$. (b) Cartoon of a square sample at $\nu = 2$, seen from above. Note the two chiral edge channels traveling along the boundary of the sample, with the arrows denoting the direction of the electrons moving through them. The white squares are electrical contacts, held at potentials V_+ and V_-.

We now consider the case where the chemical potential μ lies halfway between two Landau levels while in the bulk. In the interior of the sample, the density of states at $E = \mu$ will be zero. The only way to add another electron in the bulk is to populate a state in the lowest unoccupied LL, which will require an energy of $\frac{1}{2}\hbar\omega_c$. In 2DESs formed in the semiconductor GaAs, the cyclotron energy is $20.1 \times B$ K (for B given in units of teslas). Therefore, excitations into higher LLs are strongly suppressed at typical cryogenic temperatures and large magnetic fields. The interior is said to be *incompressible*.

However, figure 1.1a shows that the chemical potential intersects with each of the LLs at the edges of the sample. This generates a *compressible* edge channel for each LL occupied in the interior. As shown in figure 1.1b, these edge channels circulate around the sample at its boundaries. The electrons within the channels can only propagate in the clockwise or counterclockwise direction, depending on which way the magnetic field is pointing. The chirality of the edge channels implies that electrons cannot backscatter without somehow hopping from one side of the sample to the other. For macroscopic samples, this is highly unlikely because there are no accessible states within the interior so long as μ remains between two LLs. Instead, current flows rigidly around any imperfections at the boundary. We depict this in figure 1.1b for a sample at $\nu = 2$.

In this picture, each edge channel provides a dissipationless and one-dimensional path for current to travel along the boundary. For n edge channels, the two-terminal conductance between two contacts along a particular edge will be $n\frac{e^2}{h}$. In the absence of backscattering or interedge tunneling, one can show that each edge channel provides a conductance of $\frac{e^2}{h}$ by treating them as one-dimensional ballistic conductors with reflection-less contacts [72, 9]. Ignoring spin, the current I in such a conductor connecting two ideal leads with perfect transmission coefficients is given by $I = \frac{L}{2\pi} \int i_k dk = -\frac{L}{2\pi} \int \frac{e}{L} v_k dk$, where L is the length of the conductor and v_k is the velocity of state k. The integral over k is performed over all occupied states and can be converted into a sum over E by noting that $dk = dE/\frac{\partial E}{\partial k}$. But because the velocity of each k state is $\frac{1}{\hbar}\frac{\partial E}{\partial k}$, the current reduces to $I = -\frac{e}{h} \int dE = \frac{e^2}{h}(V_+ - V_-)$, where $V_+ - V_-$ is the voltage difference between the two leads. Thus, we conclude that one-dimensional channel has a conductance of $\frac{e^2}{h}$. Note that this result stems from the fact that in a one-dimensional conductor the k dependence of the velocity is cancelled out by the density of states in k space. The analysis can be generalized for n channels, such that the two-terminal conductance will be $n\frac{e^2}{h}$.

Returning to the case of a 2DES at integer filling factor n, if a potential difference $\Delta V = V_+ - V_-$ is applied to two contacts then a current $I = n\frac{e^2}{h}\Delta V$ will flow between the contacts. The lack of dissipation implies that the chemical potential

of the electrons in the edge channels will not vary as they travel from one contact to another. Due to their low density of states, the edge states emanating from a particular contact will have the same chemical potential as that contact. Thus, in figure 1.1b, the edge channels along the lower edge will have be at potential V_+ while the channels along the upper edge will be at potential V_-. Any ideal voltage probes located along either edge (not shown in the figure) will draw no current from the sample, and thus the edge channels entering such contacts will exit with the same chemical potential. The voltage probe will then equilibrate with those edge channels and measure their chemical potential. We can put this all together to conclude that the longitudinal voltage drop V_{xx} between two voltage probes along a single current-carrying edge will vanish and thus $R_{xx} = 0$. Furthermore, if the Hall voltage were to be measured by using probes located on opposite edges (for example, one situated on the lower edge and one situated on the upper edge in figure 1.1b), one would obtain $V_{xy} = \Delta V$ and find a Hall resistance of $R_{xy} = \frac{h}{ne^2}$.

Analogous to the Shubnikov–de Haas effect in three-dimensional metals [68], one expects there to be transport anomalies whenever the Landau filling factor ν is an integer. The lack of dissipation implies that longitudinal resistance R_{xx} should vanish. One should also observe a Hall resistance given by $R_{xy} = \frac{B}{ecN_S} = \frac{1}{\nu}\frac{h}{e^2}$. Interestingly, it was first discovered by von Klitzing et al. [122] that when ν is tuned (either by varying the electron density at fixed magnetic field or sweeping the field at fixed density), the Hall resistance remains fixed at $R_{xy} = \frac{1}{n}\frac{h}{e^2}$ for a range of ν around the integer value of n. This quantization of Hall resistance (known as the integer quantum Hall effect) is thought to be perfect at $T = 0$ and generally found to be independent of sample geometry.[1] An example of such magnetotransport is shown in figure 1.2.

The appearance of Hall resistance plateaux is unexpected in the clean limit, where the chemical potential should discontinuously jump from one LL to another once ν is swept past an integer value. In that case, the Hall resistance should assume the value of $\frac{1}{n}\frac{h}{e^2}$ only for the *single* value of $\nu = n$. As ν deviates from n, so should the

---

[1]Quantized Hall resistance can be disrupted in mesoscopic samples ($L \leq 1~\mu$m) due to interedge Coulomb scattering or tunneling of electrons between edge channels.
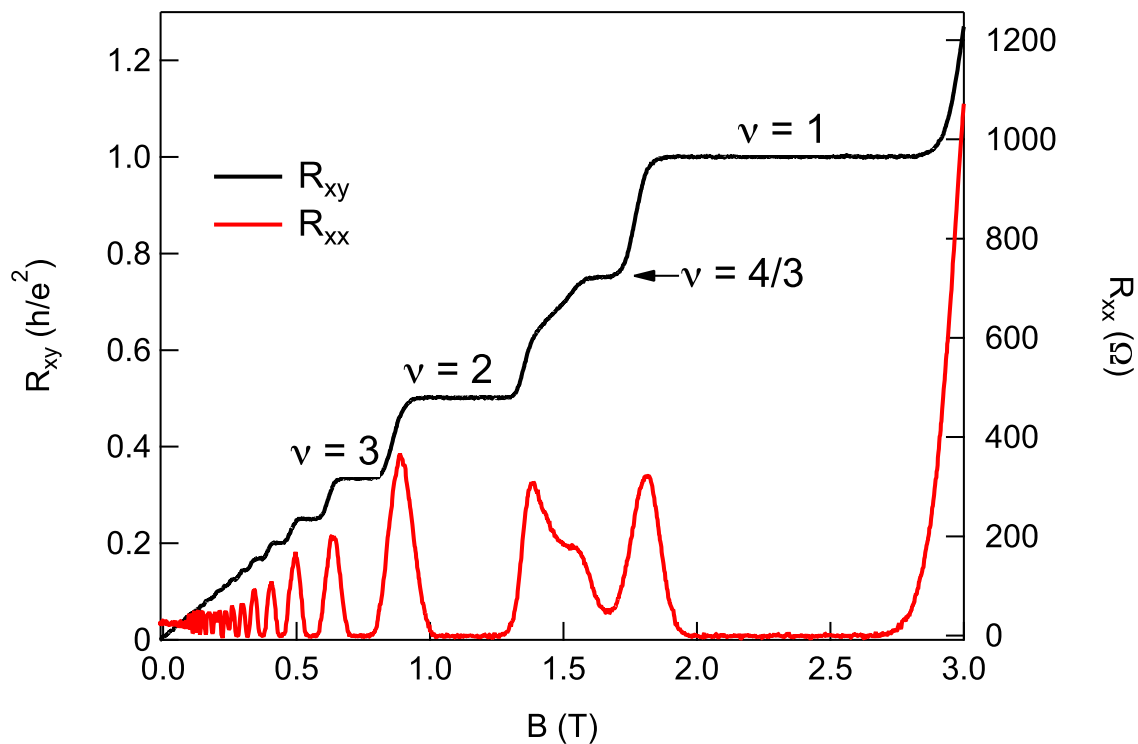
Figure 1.2: Unpublished data for longitudinal resistance R_{xx} and Hall resistance R_{xy} of a 2DES in the quantum Hall regime. Notice that at low magnetic fields R_{xy} is linear but at high fields there are a series of plateaux at $R_{xy} = \frac{1}{n}\frac{h}{e^2}$ for $n = 1, 2, 3, \ldots$ etc. These plateaux correspond to integer Landau filling factor $\nu = \frac{hc}{eB}$. Each plateau in R_{xy} is also coincident with $R_{xx} \approx 0$. Note the appearance of a plateau at $\nu = \frac{4}{3}$.

Hall resistance.
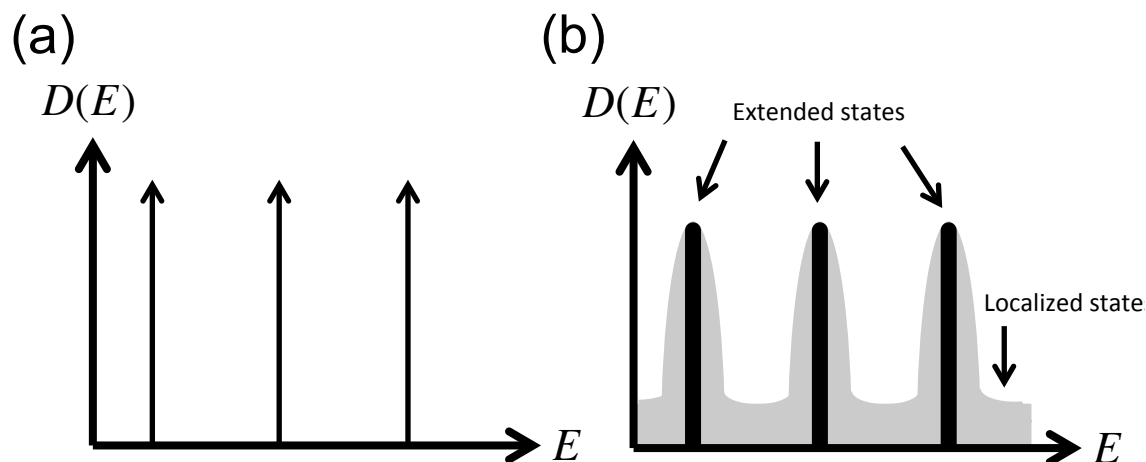
Figure 1.3: (a) Density of states $D(E)$ versus energy E of 2DES in a magnetic field without disorder. The Landau levels are represented by delta functions. (b) Density of states with disorder. Black bands indicate extended states while grey regions are localized states.

The precise quantization of Hall resistance over large ranges of filling factor crucially depends on disorder. Imperfections in real samples will lead to scattering of electrons off of impurities as well as spatial variation of carrier density. Electrons can also be localized by local minima in the disorder potential. These effects will broaden the Landau levels, which we illustrate in figure 1.3b. So long as disorder is not too strong, narrow bands of extended states will exist at the energies E_n given by equation (1.4). These extended states can carry current across the sample and form the edge channels. However, in between the bands of extended states there will in general be a number of localized states. These states represent electrons bound by the disorder potential. One might expect that they do not influence transport measurements because they cannot carry charge from one side of the sample to the other

[47]. Instead, the edge channels alone should determine the transport properties.
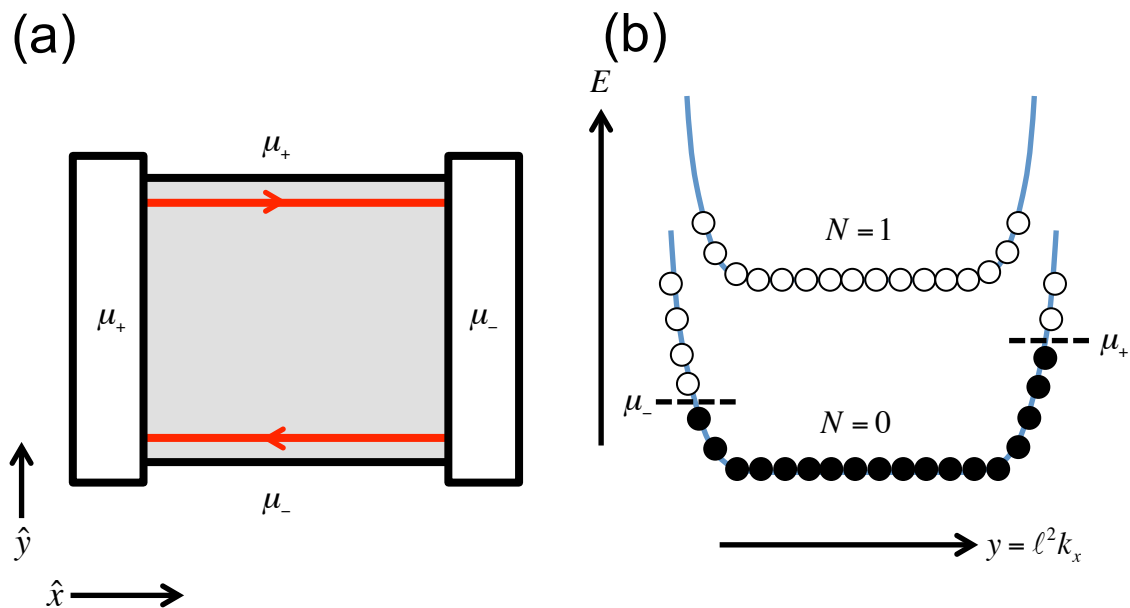
Figure 1.4: (a) Depiction of rectangular sample in the absence of disorder. Electrical contacts are located along the left and right edges of the sample, at chemical potentials μ_+ and μ_- respectively. Each contact sets the chemical potential of the edge channel (red lines with arrows) traveling from it. (b) Energy diagram without disorder. Black dots denote occupied states, white circles denote unoccupied states.

We argue that this is the case by first considering a rectangular sample with dimensions $L_x \times L_y$. We depict this geometry in figure 1.4a. Contacts are located at $x = -L_x/2$ and $x = L_x/2$. The left contact is held at the potential $V = -e\mu_+$ and the right is at $V = -e\mu_-$. For now, we assume that there is no disorder. We once again choose a gauge in which $\vec{A} = -By\,\hat{x}$, such that each eigenstate of energy will also be an eigenstate of momentum in the $\hat{x}$ direction and centered on $y = \ell^2 k_x$. We assume that $\mu_+ - \mu_-$ is small compared to the cyclotron energy and that everywhere the local chemical potential lies between the $N = 0$ and the $N = 1$ Landau levels.[2] The left lead will populate all the states traveling in the $+\hat{x}$ direction up to the energy μ_+, while the right lead will populate all states traveling in the $-\hat{x}$ direction up to

[2]Be aware that we have made a slight change in notation from Section 1.1.1, where N had stood for the total number of electrons and n had indicated the Landau level index.

the energy μ_-.

The energy diagram in the case of no disorder is shown in figure 1.4b. The black dots indicate filled states while the open dots indicate unoccupied states. Because of the relation $y = \ell^2 k_x$, the states on the right half of this diagram ($y > 0$) will travel in the $+\hat{x}$ direction and the states on the left half of this diagram ($y < 0$) will travel in the $-\hat{x}$ direction. As mentioned previously, the confinement potential at the edge causes the energy of the LLs to rise up and intersect with the local chemical potential $\mu_\pm$, thus generating the compressible edge channels. In this sample there are two such edge channels that are traveling in opposite directions and located at $y = \pm L_y/2$. Note that here the Hall voltage is the difference in chemical potential between the two edges and is given by $V_{xy} = -e(\mu_+ - \mu_-)$.

We now calculate the *net* current in the sample. Each energy eigenstate travels in the $\pm\hat{x}$ direction with velocity $v_x = \langle \frac{\partial H}{\partial p_x} \rangle = \frac{1}{\hbar}\frac{\partial E}{\partial k_x} = \frac{\ell^2}{\hbar}\frac{\partial E}{\partial y}$. The net current in the $+\hat{x}$ direction is given by [58]

$$I = \int \vec{J}(\vec{r}) \cdot \hat{x} \; dy \tag{1.8}$$

$$= \frac{1}{L_x} \int \int J_x \; dydx \tag{1.9}$$

$$= -\frac{e}{L_x} \int d^2r \; \rho(\vec{r})v_x(\vec{r}) \tag{1.10}$$

$$= -\frac{e}{L_x} \sum_{occupied} v_x. \tag{1.11}$$

Here, $\vec{J}(\vec{r})$ is the current density and $\rho(\vec{r})$ is the number density of electrons. The first integral is performed along an arbitrary line of constant x across the width of the sample, which can be converted into an integral across the entire sample due to current continuity. The summation in the last line is performed over all occupied states.

We now use the expressions for v_x and k_x to obtain

$$I = -\frac{e}{L_x}\frac{L_x}{2\pi}\int_{occupied} v_x \, dk_x \tag{1.12}$$

$$= -\frac{e}{2\pi}\int_{occupied}\left(\frac{\ell^2}{\hbar}\frac{\partial E}{\partial y}\right)\frac{1}{\ell^2}dy \tag{1.13}$$

$$= -\frac{e}{h}\int_{\mu_-}^{\mu_+} dE \tag{1.14}$$

$$= -\frac{e}{h}(\mu_+ - \mu_-) \tag{1.15}$$

$$= \frac{e^2}{h}V_{xy}. \tag{1.16}$$

Thus the Hall resistance is simply $\frac{h}{e^2}$ for this particular case of a single filled Landau level in the bulk of the sample. This formula can be generalized for n filled Landau levels to arrive at $R_{xy} = \frac{1}{n}\frac{h}{e^2}$.

The key observation one obtains by examining figure 1.4b is that only the states at the edges contribute to the net current flowing through the sample. So long as both μ_+ and μ_- at the edges stay within the local $N = 0$ LL, then the relation $I = -\frac{e}{h}(\mu_+ - \mu_-)$ should hold. But it should also be clear that even though any bulk variations in the energy diagram from a disorder potential might generate local currents in the interior, their net contribution to the observed current is zero. Such variations might even generate hills and valleys in the bulk electron density. These features could have their own edge channels circling them if the local chemical potential intersects a LL in the bulk (see figure 1.5), but so long as such defects do not create a pathway from one edge of the sample to the other they will not disrupt Hall quantization.

However, in order to fully explain the Hall plateaux we must account for why in real samples the chemical potential remains between two different LLs as the filling factor ν is changed, either by sweeping B or altering the electron density. The number of states in the edge regions at $y = \pm L_y/2$ is tiny compared to the Landau degeneracy in the clean limit. Thus, according to our energy diagram in figure 1.4b any change in ν should still cause the chemical potential to quickly jump from one LL to another. The apparent paradox is resolved by recalling that disorder generates a large density
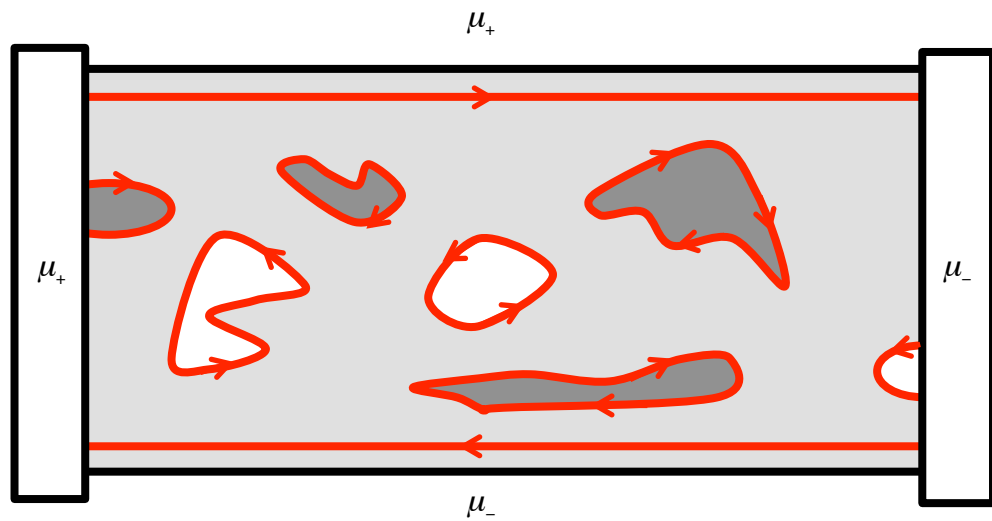
Figure 1.5: Cartoon of disordered sample. Dark grey (white) regions in the bulk indicate puddles of increased (decreased) electron density induced by the disorder potential. Each hill or valley in the disorder potential can be encircled by a separate edge channel. Note that the edge channels surrounding the hills have the opposite chirality as those around the valleys. So long as there are no such puddles connecting the two contacts, Hall resistance will remain quantized at $R_{xy} = \frac{1}{n}\frac{h}{e^2}$.

of *localized* states between the bands of extended states, as depicted in figure 1.3b. As mentioned before, these localized states do not alter the net current traveling through the sample, but they can keep the chemical potential pinned between two adjacent LL for a wide range ν. This is consistent with the observation that the width of Hall plateaux are smaller in cleaner samples.

At finite temperature, one expects perfect quantization to break down. Thermal fluctuations will lead to the population of excited states above the gap within the bulk. Thus, backscattering becomes thermally activated, and in general one observes a longitudinal resistance with the temperature dependence of $R_{xx} \approx R_0 e^{-\Delta/2k_b T}$. Here, Δ is the bulk energy gap. For the integer quantum Hall effect, Δ is typically given by $\Delta \approx \hbar \omega_c - \Gamma$, where Γ reflects the broadening of the Landau levels.

1.1.3 Fractional Quantum Hall Effect

Soon after the integer quantum Hall effect was discovered, Tsui, Stormer, and Gossard [119] found evidence for an incompressible state forming at $\nu = 1/3$ with a Hall resistance plateau of $R_{xy} = 3\frac{h}{e^2}$. Hints of a similar state at $\nu = 2/3$ were also seen. Further studies found quantum Hall states at even more fractional Landau filling factors, such as $\nu = 4/3, 5/3, 2/5, 3/5, 4/5,$ and $2/7$ [110]. These states at fractional Landau filling factors are collectively known as the fractional quantum Hall effect (FQHE). As shown in figure 1.6, modern 2DESs typically show a complicated hierarchy. The appearance of the FQHE seems counterintuitive because it occurs when a Landau level is only partially filled and the chemical potential should lie within the band of extended states. Under these conditions, the system should instead be compressible.

The origin of the FQHE ultimately lies in electron–electron interactions. Although usually treated perturbatively in the case of degenerate Fermi systems, these interactions become vastly more important in the quantum Hall regime. One can understand this by considering the case of an extremely large magnetic field, such that only the lowest Landau level is populated. The Hamiltonian for the many-body system is
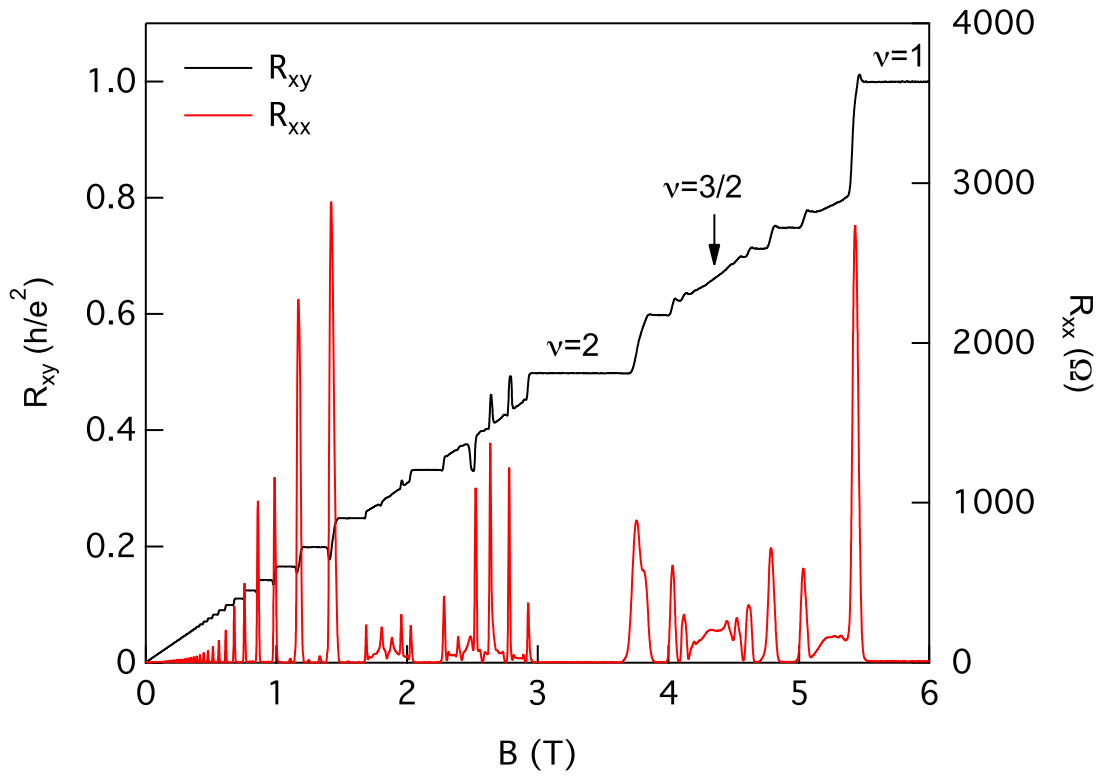
Figure 1.6: Example of magnetotransport from a high quality 2DES at $T = 15$ mK. Unpublished data courtesy of Jing Xia.

given by

$$H = \sum_i \frac{1}{2m}\left(\vec{p_i} + \frac{e}{c}\vec{A}\right)^2 + \sum_{i<j} \frac{e^2}{|\vec{r_i} - \vec{r_j}|}. \tag{1.17}$$

Upon projecting to the lowest Landau level, the kinetic energy term in equation (1.17) becomes a constant equal to $\sum_i \frac{1}{2}\hbar\omega_c$ in the clean limit. Subsequently, it can be ignored and only the Coulomb repulsion term can play a role in electron dynamics. The FQHE is fascinating becomes it involves the *nonperturbative* influence of electron–electron interactions.

For example, Laughlin [73] constructed a trial wave function for the $\nu = 1/m$ states with the following form:

$$\Psi_{1/m} = \prod_{j<k}(z_j - z_k)^m \exp\left[-\frac{1}{4}\sum_i |z_i|^2\right]. \tag{1.18}$$

Here, $z_j = x_j + iy_j$ represents the spatial coordinates of the jth electron expressed in units of the magnetic length ℓ. The critical term in equation (1.18) is the polynomial $(z_j - z_k)^m$, which vanishes as one electron approaches another. Thus, these Laughlin wave functions serve to minimize Coulomb repulsion and provide an excellent ansatz for describing the highly correlated state in which the electrons dance around each other. Fermi-Dirac statistics requires any many-body wave function of fermions to be antisymmetric with respect to particle exchange. This implies that equation (1.18) can only describe systems with odd values of m. Indeed, quantum Hall states are observed at $\nu = 1/3,\ 1/5,\ 1/7, ...$, but not at $\nu = 1/2,\ 1/4,\ 1/8, ...$, for conventional single-layer systems. Through a particle-hole transformation of equation (1.18), one can also describe the states $\nu = 1 - 1/m$ as Laughlin states of holes.

Perhaps one of the most unusual properties of the Laughlin states is that they contain excitations that can be described as quasiparticles with *fractional* charge. Laughlin shows this in reference [73] by considering the insertion of an additional quantum of magnetic flux hc/e into the system. Doing so causes the system to re-arrange itself so as to accumulate an extra amount of charge near the inserted flux equal to $\frac{1}{m}e$. Haldane [46] and Halperin [49] use these fractionally charged quasipar-

ticles to iteratively construct wave functions to describe the various states that do not fall within the Laughlin sequence of $\nu = 1/m$ and $\nu = 1 - 1/m$. In the hierarchy approach, a new quantum Hall state can be formed as a Laughlin state of the fractionally charged quasiparticles of a simpler fractional state.

1.1.4   Composite Fermions

Though mathematically elegant, the hierarchy approach of Haldane and Halperin appears to incorrectly predict the relative strengths of the fractional quantum Hall states [58]. For example, $\nu = 3/7$ and $\nu = 5/13$ are both direct "daughter" states of $\nu = 2/5$, but $3/7$ is far more prevalent than $5/13$ in real samples. As an alternative to the hierarchy approach, Jain reformulated the problem of interacting electrons moving in a magnetic field by describing it as a system of composite particles known as composite fermions [57]. A composite fermion is an electron bound to an even number of quantized vortices in the multiparticle wave function. Each vortex takes the form of $(z_j - z_k)$ and thus the wave function Ψ_ν of the electrons at filling factor ν can be related to the composite fermion wave function Φ_{ν^*} in the following way:

$$\Psi_\nu = \prod_{j<k}(z_j - z_k)^{2p}\Phi_{\nu^*} \tag{1.19}$$

Like in the Laughlin states, the $\prod_{j<k}(z_j - z_k)^{2p}$ will cause the electrons to avoid each other and make the formation of composite fermions energetically favorable. By minimizing the Coulomb repulsion, it is typical to assert that Φ_{ν^*} represents a wave function for a system of *weakly* interacting composite fermions. We will show that because the binding of vortices can be related to the binding of fictitious magnetic flux, the composite fermions subsequently move about in a reduced magnetic field B^* and fill up an integer number of fictitious Landau levels generated by B^*.

We start by considering a system of noninteracting electrons at integer filling factor $\nu^* = n = N_S\phi_0/|B^*|$. Here, N_S is the number density of electrons and $\phi_0 = hc/e$ is the quantum of magnetic flux. Because ν^* is an integer, the system has an energy

gap between the ground state and the first excited state. We convert the electrons into composite fermions by attaching $2p$ magnetic flux quanta to each electrons. This can be accomplished formally through a Chern-Simons gauge transformation, which associates with each electrons the requisite amount of flux [137, 77, 50, 97]. The flux attachment does not change any observables because they make zero net Aharonov-Bohm phase contribution to any Feynman path-integrals. The new system of composite fermions will be incompressible because the original system of noninteracting electrons was also incompressible. We note that these fictitious magnetic flux quanta are identical to the vortices $(z_j - z_k)^{2p}$ because they both cause the phase of the multiparticle wave function to increase by the same amount when one moves one particle in a complete circle around another.

Next, we adiabatically spread each attached flux until it merges with the external magnetic field. This adiabatic evolution is permitted due to the finite energy gap. So long as this gap does not close (which we assume that it does not), we will avoid passing through a phase transition into a completely different state. Thus, we map the problem of noninteracting composite fermions with integer filling factor ν_* into a problem of electrons moving in an external magnetic field $B = B^* + 2pN_S\phi_0$. Using $|B^*| = N_S\phi_0/n$ and taking B to be positive, the electrons will have fractional filling factor,

$$\nu = \frac{n}{2pn \pm 1}. \tag{1.20}$$

Therefore, the fractional quantum Hall effect for electrons can ultimately be explained in terms of an integer quantum Hall effect for composite fermions. A simple example of this is the case of $n = 1$ and $p = 1$. This gives the $\nu = 1/3$ Laughlin state, which can be rewritten as

$$\Psi_{1/3} = \prod_{j<k}(z_j - z_k)^3 \exp\left[-\frac{1}{4}\sum_i |z_i|^2\right] = \prod_{j<k}(z_j - z_k)^2 \Phi_1. \tag{1.21}$$

Here, the term $\prod_{j<k}(z_j - z_k)^2$ represents the binding of two flux quanta to each electron and $\Phi_1 = \prod_{j<k}(z_j - z_k)\exp\left[-\frac{1}{4}\sum_i |z_i|^2\right]$ is the many-body wave function

for a completely filled Landau level, corresponding to a $\nu^* = 1$ state of composite fermions.

The treatment of composite fermions presented here is an oversimplification of the complete theory. It provides an intuitive explanation for an energy gap for a system of interacting electrons at fractional filling factor without accounting for the exact evolution of the energy levels during the attaching and spreading of fictitious magnetic flux. For example, one might incorrectly posit that the energy gap should be given by the cyclotron energy for electrons at filling factor ν^*, which would be dependent on the effective mass of the electrons. This clearly cannot be the case because the projection of the system into the lowest Landau level will quench the kinetic energy of the electrons and cause the spectrum to only depend on the Coulomb repulsion term. Thus, the true energy gap for a system of composite fermions at filling factor ν^* should somehow scale with the Coulomb energy E_C. For a more complete review of composite fermions, see reference [58].

The theory of composite fermions makes a number of testable predictions about the energy spectrum of fractional quantum Hall states. For example, one would expect that the energy gap of a particular FQHE would be grow along with the effective magnetic field B^*, which governs the cyclotron splitting of the fictitious Landau levels of the composite fermions. This is borne out in experiments [15, 74, 16] that observe Shubnikov–de Haas oscillations in the vicinity of $\nu = 1/2$, whose amplitude grows as one moves away from $\nu = 1/2$. Crucially, the theory of composite fermions also suggests that at half-filling factor the composite fermions should feel no effective magnetic field other than a Zeeman field leading to partial spin polarization. Consequently, the composite fermions form a compressible Fermi sea. This is quite remarkable because the system would have an effective mass that is determined by the Coulomb energy rather than the effective mass of the underlying electrons. Experimentally, no quantum Hall plateau is visible at $\nu = 1/2$ in single-layer 2DESs, which is consistent with a compressible system. However, the composite fermion system has no energy gap at $\nu = 1/2$, so it is unclear if it can survive gauge fluctuations during the adiabatic creation of the composite fermions. Nonetheless, Halperin, Lee, and Read [50] have

argued that the features of a Fermi surface likely persists. A variety of experiments (for example, Refs. [128, 63, 43, 69]) have also supported the existence of a composite fermion Fermi sea at $\nu = 1/2$.

1.2 Bilayer Quantum Hall State at $\nu_T = 1$

Up until now, we have considered electrons populating only a single 2DES. We now add a second 2DES parallel to the first and separated from each other by a small distance d. We assert that interlayer tunneling is absent so that no electrical charge can transfer between the two layers. In the quantum Hall regime, these bilayer systems can be characterized by the effective interlayer separation d/ℓ. This particular ratio is important because it measures the importance of the *intralayer* Coulomb energy $E_C = e^2/\epsilon\ell$ relative to the *interlayer* Coulomb energy $E_I = e^2/\epsilon d$. For $d/\ell \gg 1$, the repulsion between electrons is weak and one expects that the two layers will act independently of one another. The situation can be quite different for $d/\ell \approx 1$, in which interlayer interactions are of similar strength as interactions between electrons within the same layer. One anticipates that interlayer correlations can develop at low d/ℓ, leading to bilayer fractional quantum Hall states. This thesis is focused on the particular bilayer state that forms when the total Landau filling factor $\nu_T \equiv \nu_1 + \nu_2$ of the two layers is equal to 1. This $\nu_T = 1$ state is compelling because it can be described as a condensation of interlayer excitons and, unlike most other quantum Hall states, shows signs of a spontaneously broken symmetry.

1.2.1 The 111 State

We first examine the wave functions of generic bilayer quantum Hall states. Analogous to the Laughlin states, Halperin [48] proposed the following set of wave functions to model two-component quantum Hall states:

$$\Psi_{m_1 m_2 n} = \prod_{j<k}^{N_1} (z_j - z_k)^{m_1} \prod_{r<s}^{N_2} (w_r - w_s)^{m_2} \prod_{j,r}^{N_1,N_2} (z_j - w_r)^n. \qquad (1.22)$$

Here, z_j are the coordinates for the N_1 electrons in the first component (e.g., the top layer in a bilayer system) and w_r are the coordinates for the N_2 electrons in the second component (e.g., the bottom layer in a bilayer system). Note that once again we have dropped the exponential terms for the sake of simplicity. If either m_1 or m_2 are even, then a composite fermion Fermi sea term associated with the appropriate component must be added to equation (1.22) to preserve antisymmetry with respect to electron exchange. By considering the number of vortices bound to each electron, the Landau filling factors for the two components are given by

$$\nu_1 = \frac{m_2 - n}{m_1 m_2 - n^2} \tag{1.23}$$

and

$$\nu_2 = \frac{m_1 - n}{m_1 m_2 - n^2}. \tag{1.24}$$

From now on, we specialize to bilayer systems, in which ν_1 and ν_2 represent the filling factors for the two layers. We also assume that the spins of the electrons are frozen out by the large Zeeman field, even though this will ultimately prove to be an over-simplification. In the case of $n = 0$, equation (1.22) would be the product state of two uncorrelated quantum Hall systems (e.g., a bilayer system with $d/\ell = \infty$), with $\nu_1 = 1/m_1$ and $\nu_2 = 1/m_2$. As the strength of interlayer repulsions grow (i.e., d/ℓ is reduced from infinity), one expects that states with $n \neq 0$ would become more favorable energetically, and electrons in one layer will become anticorrelated with electrons in the other layer. As n grows in value while the individual Landau filling factors remain constant, m_1 and m_2 will consequently decrease from their original values when the two layers were uncorrelated with each other. This represents electrons unbinding themselves from vortices associated with electrons in their own layer and becoming attached to the vortices of electrons in the other layer. The exponents m_1 and m_2 will switch back and forth between even and odd values, implying a series of transitions between compressible and incompressible bilayer states as d/ℓ is tuned [134, 94].

If we consider the situation where $m_1 = m_2 = n$, then equations (1.23) and (1.24) seemingly imply that the filling factors for the individual layers are not well defined.

However, we can still write the *total* filling factor as $\nu_T \equiv \nu_1 + \nu_2 = 1/n$. One would then have to invoke layer symmetry to arrive at $\nu_1 = \nu_2 = 1/2n$.

The focus of this thesis is the bilayer system occurring at $\nu_T = 1$. We primarily restrict measurements to the case of equal densities in the two layers, $N_1 = N_2$. Following the previous discussion, in the limit of $d/\ell = \infty$, the system will consist of two independent layers with $m_1 = m_2 = 2$ and $n = 0$. Both layers are compressible Fermi seas of composite fermions, with no Hall plateau. For $d/\ell = 0$, interlayer Coulomb energies are entirely equivalent to intralayer Coulomb energies. One would expect that the system should be described by the wave function in equation (1.22) with $m_1 = m_2 = n = 1$ (i.e., the "111 state"), such that each electron is bound to an equal number of upper and lower layer vortices.

Such a quantum Hall state at $\nu_T = 1$ was first supported by numerical evidence from Chakraborty and Pietiläinen [10]. Experimentally, conventional transport measurements (i.e., driving a total current I_T that is equally split between the two layers) by Suen et al. [113] and Eisenstein et al. [25] found signs of an incompressible state in bilayer systems at $\nu_T = 1$. However, we should note that the splitting Δ_{SAS} of the symmetric and antisymmetric tunneling states can also generate an energy gap, even in the absence of Coulomb interactions. Such a splitting is analogous to the Zeeman splitting between spin-up and spin-down electrons. Murphy et al. [84] explored this possibility by examining a series of weakly tunneling bilayer systems with variable d/ℓ and Δ_{SAS}. Their studies of samples with the smallest tunneling energies revealed that as d/ℓ is reduced below a characteristic value of $d/\ell \approx 2$, an incompressible quantum Hall state develops at $\nu_T = 1$. Samples with larger tunneling energies tended to have larger critical values of d/ℓ, but they found evidence that the $\nu_T = 1$ quantum Hall state remains even in the limit of $\Delta_{SAS} = 0$, leaving Coulomb interactions as the origin of the $\nu_T = 1$ quantum Hall state. In figure 1.7 we show a summary of their results. Note that the critical d/ℓ is finite even at $\Delta_{SAS} = 0$. An example of the evolution of the minimum in R_{xx} with d/ℓ is shown in figure 1.8. Here, the interlayer separation d is kept fixed, but the total density is tuned so as to alter the magnetic length ℓ at $\nu_T = 1$. Thus, one may alter d/ℓ within a single sample *in situ*.
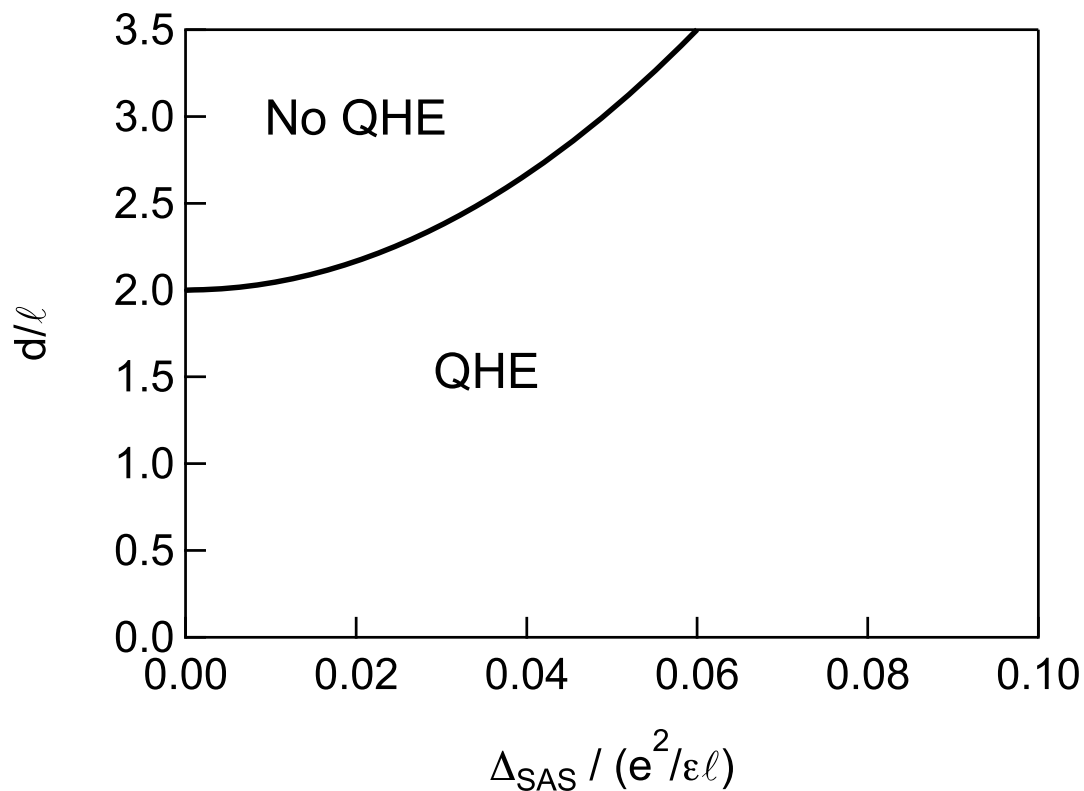
Figure 1.7: Phase diagram of $\nu_T = 1$ QHE with respect to effective interlayer separa-tion d/ℓ and single-particle tunneling energy Δ_{SAS}, obtained by Murphy et al. [84]. Below the black curve, an incompressible QH state is observed at $\nu_T = 1$. Beneath it, the bilayer is compressible. Note that the samples studied in this thesis are very weakly tunneling and would lie along the left boundary of this phase diagram.
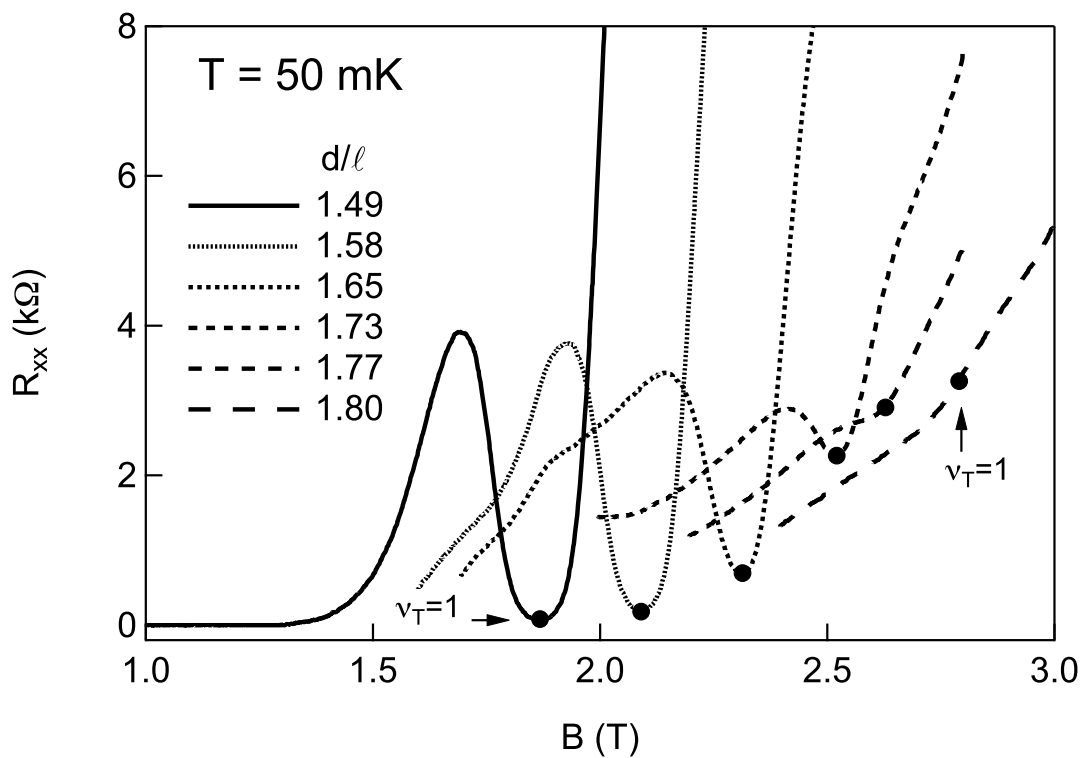
Figure 1.8: R_{xx} in parallel flow versus magnetic field at various values of d/ℓ, which is tuned by changing the electron density and thus modifying the value of ℓ at $\nu_T = 1$). The black dots denote the condition $\nu_T = 1$ for each trace. Data taken using sample 7-12-99.1R at $T = 50$ mK.

Similar to other quantum Hall states, the $\nu_T = 1$ system is characterized by a minimum in R_{xx} and a quantized Hall resistance of $R_{xy} \equiv V_{xy}/I_T = \frac{h}{e^2}$. In this respect, the $\nu_T = 1$ state greatly resembles a single layer of electrons at filling factor 1, with charged excitations confined to the edge. However, the bilayer system has an additional degree of freedom in the form of whether a given electron occupies the upper or lower layer. Wen and Zee [125] argue that because the 111 state does not have a well defined $\Delta N \equiv N_1 - N_2$, states with different ΔN have the same energy in the absence of capacitive coupling or interlayer tunneling. Charged excitations (associated with changes in the total number of electrons, $N_T \equiv N_1 + N_2$) have a finite energy cost and are said to be gapped out. This is connected with the appearance of an incompressible state in conventional transport measurements. But excitations that change ΔN apparently cost little or no energy and thus represent *gapless* excitations. Wen and Zee note that at finite d/ℓ the gapless mode is associated with a spontaneously broken $U(1)$ symmetry and should be accompanied by a superfluid mode. Of course, real samples have a finite tunneling energy that will explicitly break the $U(1)$ symmetry by selecting the symmetric distribution of electrons between the two layers as the ground state. Nonetheless, it is assumed that the essential physics will remain so long as the tunneling energy is much smaller than any other relevant energy such as the Coulomb energy E_C or thermal energy $k_B T$.

1.2.2 Pseudospin Ferromagnetism

The $\nu_T = 1$ quantum Hall state can be described in a number of languages. As is often the case for a physical system, the choice of language depends on which of its features one wishes to explore. For example, the low-energy dynamics and spontaneous $U(1)$ coherence can be made apparent through an analogy to ferromagnetism. To do so, we first adopt the pseudospin formalism [32, 131, 82, 92, 112]. In this language, the "which layer" degree of freedom for each electron is mapped onto a pseudospin vector. An electron occupying the upper layer is considered to have pseudospin-up $|\uparrow\rangle$ and an electron in the lower layer has pseudospin-down $|\downarrow\rangle$. We take these states to be

either parallel or antiparallel to the z-axis of the three-dimensional Hilbert space for each pseudospin vector. The wave function for $\nu_T = 1$ at finite d/ℓ can be written as

$$\Psi_{\nu_T=1} = \prod_{j}^{N_T} \left[\mid j \rangle \otimes \frac{1}{\sqrt{2}}(\mid\uparrow\rangle + e^{i\phi} \mid\downarrow\rangle) \right], \tag{1.25}$$

where $\mid j \rangle$ represents an electron in orbital state j. The pseudospin component of each electron lies within the x-y plane of the pseudospin vector Hilbert space, indicating that the electrons are not localized in one layer or the other. Instead, the electrons are quantum mechanically spread between the two layers with a phase factor $e^{i\phi}$. In the absence of tunneling (i.e., $\Delta_{SAS} = 0$), there is no energy difference between the symmetric and anitsymmetric combinations of $\mid\uparrow\rangle$ and $\mid\downarrow\rangle$. Consequently, there is a $U(1)$ symmetry in which the phase angle ϕ can take any value between 0 and 2π.

Although equation (1.25) specifies a single value of ϕ, one can imagine that the phase angle might fluctuate in space and time, corresponding to excited states. In the low energy regime, the dynamics of ϕ are determined by three key factors. First, strong Coulomb repulsion will generate exchange interactions that will favor all pseudospin vectors pointing in the same direction (hence the term pseudospin ferromagnetism). Second, finite interlayer capacitance will keep the pseudospin vector in the x-y plane by imposing an energy cost proportional to m_z, the pseudospin projection along the z-axis. Finally, real samples have small but nonzero tunneling energy, which will favor pseudospins pointing in the x direction.[3] Thus, the Hamiltonian in the long-wavelength, mean-field theory treatment is [131, 82]

$$H = \int d^2x \left[\rho_s \frac{|\nabla\phi|^2}{2} - \frac{\Delta_{SAS}}{4\pi\ell^2} \cos\phi + \frac{\beta}{2}|m_z|^2 \right]. \tag{1.26}$$

Here, ρ_s is the pseudospin stiffness [130] and β is proportional to the capacitive charging energy. For $\Delta_{SAS} = 0$, equation (1.26) indicates that rotations of the pseudospin vector in the x-y plane will have zero energy in the limit of $\nabla\phi \to 0$. This is identical

---

[3]Thus, a strongly-tunneling bilayer sample is a pseudospin paramagnet. Tuning the tunneling energy should therefore induce a quantum phase transition between paramagnetism and ferromagnetism [131, 95].

to the gapless mode associated with the spontaneous breaking of the $U(1)$ symmetry.

Pseudospin textures carry a fermionic charge density given by the Pontryagin topological density [101, 131, 82, 130]

$$\delta\rho(\vec{r}) = \frac{1}{8\pi}\epsilon^{\mu\nu}\vec{m}\cdot(\nabla_\mu\vec{m})\times(\nabla_\nu\vec{m}). \tag{1.27}$$

At $\nu_T = 1$, the low-lying charged excitations are thought to be topological defects known as "merons." The pseudospin stiffness implies a finite charge gap [131, 82], in contrast to the gapless pseudospin waves.

1.2.3 Exciton Condensate

Alternatively, the $\nu_T = 1$ state can be described as an exciton condensate [32], with superfluid-like properties [125, 30, 82, 80]. This view can be made clear by writing the pseudospin ferromagnet wave function (equation (1.25)) in second-quantized form as

$$\Psi_{\nu_T=1} = \prod_j^{N_T} \frac{1}{\sqrt{2}}\left(c_{1j}^\dagger + e^{i\phi}c_{2j}^\dagger\right)|0\rangle. \tag{1.28}$$

Here, $c_{1j}^\dagger$ is an operator that creates an electron in the top layer in orbital state j while $c_{2j}^\dagger$ creates a corresponding electron in the bottom layer. The symbol $|0\rangle$ denotes a vacuum state devoid of any particles in either layer.

Fertig [32] first noted that one can perform a particle-hole transformation on the top layer by defining a new vacuum:

$$|0'\rangle = \prod_j^{N_T} c_{1j}^\dagger |0\rangle. \tag{1.29}$$

This new vacuum consists of a filled Landau level of electrons in the top layer but no particles in the bottom layer. Equation (1.28) can then be expressed as

$$\Psi_{\nu_T=1} = \prod_j^{N_T} \frac{1}{\sqrt{2}}\left(1 + e^{i\phi}c_{2j}^\dagger c_{1j}\right)|0\rangle. \tag{1.30}$$

This equation resembles the BCS ground state. The product $c_{2j}^\dagger c_{1j}$ now generates an electron in the lower layer and a hole in the upper layer. This is identical to the generation of an exciton spread between the two layers. As bosons, the excitons should condense into the same state at sufficiently low temperatures. Here, this is equivalent to the excitons having uniform phase factor $e^{i\phi}$. We depict this exciton condensation (minus the filled level of electrons) in figure 1.9.
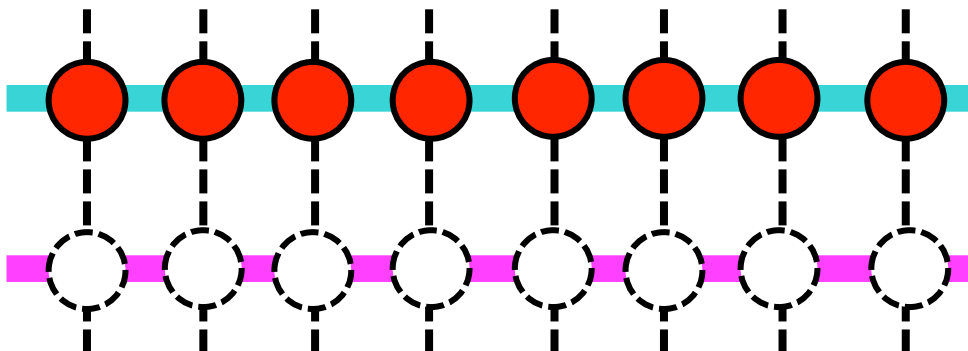
Figure 1.9: Depiction of exciton condensation at $\nu_T = 1$. The electrons in the upper layer are bound to the holes in the lower layer. A particle-hole transformation has changed the half-filled Landau level in the bottom layer into a half-filled level of holes and a completely filled level of electrons, which is not shown here.

The excitonic nature of the $\nu_T = 1$ then implies a host of superfluid-like behavior. As first pointed out by Wen and Zee [125], the gapless and linearly dispersing mode is linked to the flow of excitons. Because the excitons have their "electron component" and "hole component" in different layers, a unidirectional flow of excitons would be equivalent to counterpropagating (or counterflowing) electron currents in the two layers, $J_{CF} = J_1 - J_2$. Analogous to superfluidity, the counterflow current is related to the gradient of the phase angle by $J_{CF} = -\frac{e\rho_s}{\hbar}\nabla\phi$. The excitonic order parameter is a phase angle and falls within the XY universality class. Thus, it was anticipated [125, 131, 82] that the system would exhibit a Kosterlitz-Thouless (KT) transition.

This transition is characterized by mobile vortices and antivortices in the order parameter above a characteristic temperature $T_{KT} \propto \rho_s$. The motion of vortices lead to dissipation and an ohmic response for exciton flow. Below T_{KT}, each vortex becomes bound to an antivortex, leading to a nonlinear $I - V$ for the exciton flow.

Once the exciton condensate is well formed, one also expects that interlayer tunneling should be qualitatively similar to the Josephson effect. Thus, the tunneling current density J_T and the phase angle ϕ should obey the Josephson relations:

$$J_T = \frac{e}{\hbar} \frac{\Delta_{SAS}}{4\pi\ell^2} \sin\phi, \tag{1.31}$$

$$\frac{\partial\phi}{\partial t} = \frac{eV}{\hbar}, \tag{1.32}$$

where V is the interlayer voltage difference. The tunneling current is linear in Δ_{SAS} rather than quadratic, as in the case for weakly coupled bilayers [126]. These Josephson relations and the expected long-range coherence of the condensate together imply that a DC tunneling current $I_T \equiv \int d^2x J_T$ can flow between the two layers at zero interlayer voltage so long at J_T does not exceed $J_{T,max} \equiv \frac{e}{\hbar}\frac{\Delta_{SAS}}{4\pi\ell^2}$. At finite interlayer voltage, ϕ will evolve with time and the time-averaged tunneling current will vanish.

With equations (1.26) and (1.32), we may now derive the complete equation of motion for ϕ. We can write the capacitive charging energy term in the Hamiltonian as $\beta m_z^2 = C_T V^2/2S = (\hbar^2 C_T/2Se^2)(\partial_t\phi)^2$, where C_T is the total interlayer capacitance and S is the system area. If we treat $(\partial_t\phi)^2$ as a kinetic energy and the remaining terms in the Hamiltonian as potential energies [21], then we can construct the following Lagrangian:

$$\mathcal{L} = \int d^2x \left[\frac{\chi}{2}(\partial_t\phi)^2 - \frac{\rho_s}{2}|\nabla\phi|^2 + \frac{\Delta_{SAS}}{4\pi\ell^2}\cos\phi \right], \tag{1.33}$$

where $\chi \equiv \hbar^2 C_T/Se^2$. To find the equation of motion for ϕ, we must minimize $\mathcal{L}$ with respect to variations in ϕ. We can use the standard Euler-Langrange equation (summing over the repeated index μ),

$$\partial_\mu \left(\frac{\partial\mathcal{L}}{\partial(\partial_\mu\phi)} \right) - \frac{\partial\mathcal{L}}{\partial\phi} = 0, \tag{1.34}$$

and finally obtain

$$\chi \frac{\partial^2 \phi}{\partial t^2} - \rho_s \nabla^2 \phi + \frac{\Delta_{SAS}}{4\pi\ell^2} \sin \phi = 0. \qquad (1.35)$$

Thus, ϕ obeys a sine-Gordon equation. When $\partial_t \phi = 0$ and ϕ is small enough that we can use the approximation $\sin \phi \approx \phi$, the Sine-Gordon equation has exponentially decaying or growing solutions. There also exist time-dependent soliton solutions that, depending on the picture one uses, represent either Josephson vortices or pseudospin waves traveling long distances (for example, see Refs. [130, 35, 36]).

Before ending this section, we should note that the exciton condensate wave function in equation (1.30) and the 111 wave function based on equation (1.22) are not entirely equivalent. The exciton condensate wave function has the phase angle ϕ as a good quantum number. On the other hand, the 111 wave function is an eigenstate of total particle number N_T. In condensed matter physics, ϕ and N_T are conjugate variables [3] with the commutation relation $[N_T, \phi] = i$. Thus, the exciton wave function and the 111 wave function are related to each other through a change of basis transformation, using $e^{i\phi N_T}$ as the transformation matrix [3, 102].

1.3 Phenomenology of $\nu_T = 1$

We now give an overview of the bilayer transport properties of the $\nu_T = 1$ quantum Hall state. These measurements rely on making independent electrical contact to the individual layers. We will provide greater detail of the measurement techniques behind these studies in chapter 2 and beyond. For now, we will discuss how these measurements reflect the strong interlayer correlations and superfluid-like properties of the $\nu_T = 1$ state.

1.3.1 Interlayer Tunneling

One of the most distinctive properties of the $\nu_T = 1$ state is the appearance of a zero-bias, Josephson-like peak in interlayer tunneling spectra. At large magnetic fields, the tunneling current flowing between two 2DESs is generally suppressed near zero

interlayer bias due to the Coulomb pseudogap [27]. The origin of this effect is that at high magnetic fields it requires a finite amount of energy to inject an electron into a highly correlated 2DES. The other electrons must rearrange themselves to make room for an injected electron, but the high magnetic field inhibits this motion. Consequently, injected electrons can only access the excited states on the timescale of tunneling [61, 20]. This apparent gap in the tunneling spectrum will occur at $\nu = 1/2$ per layer for high d/ℓ, even though the system is compressible for conventional transport measurements. An example of this tunneling current suppression is shown by the dotted trace in figure 1.10a.

When the $\nu_T = 1$ quantum Hall state forms at low d/ℓ, the story is entirely different. As first discovered by Spielman et al. [103, 104], a tall and narrow peak occurs in the differential tunneling conductance spectrum. An example of this peak can be seen in the solid trace in figure 1.10a. This tunneling peak reflects the ability of charge to transfer between the two layers with little energy cost. Intuitively, each electron has a corresponding hole in the opposite layer (as evident in equations (1.22) and (1.30)), and thus charge can be easily transferred between the two layers by having the electron fall into its matching hole. The tunneling peak has been interpreted in terms of macroscopic phase coherence [6, 34, 40, 55, 56, 60, 90, 107, 123, 124].

The tall and narrow interlayer tunneling peak is highly reminiscent of the Josephson effect, bolstering the view that the $\nu_T = 1$ is an exciton condensate. The appearance of Josephson physics is made more obvious by plotting the DC tunneling current versus interlayer bias, as seen in figure 1.10b. At the lowest temperatures, the tunneling current curve has a nearly discontinuous jump at zero bias. Thermal fluctuations broaden this jump in current and reduce its height. Similar to a Josephson junction, this behavior suggests that current can flow between the two layers with very little dissipation (i.e., zero interlayer voltage difference), with $I = I_{max} \sin \phi$ and $\partial_t \phi = V = 0$. Once the tunneling current exceeds $\pm I_{max}$, the phase angle can no longer be time-independent and a finite interlayer voltage occurs. The rapidly evolving phase angle will subsequently cause the DC tunneling current to decay. However, unlike in a true Josephson junction, the interlayer tunneling peak at $\nu_T = 1$ appears to have a finite
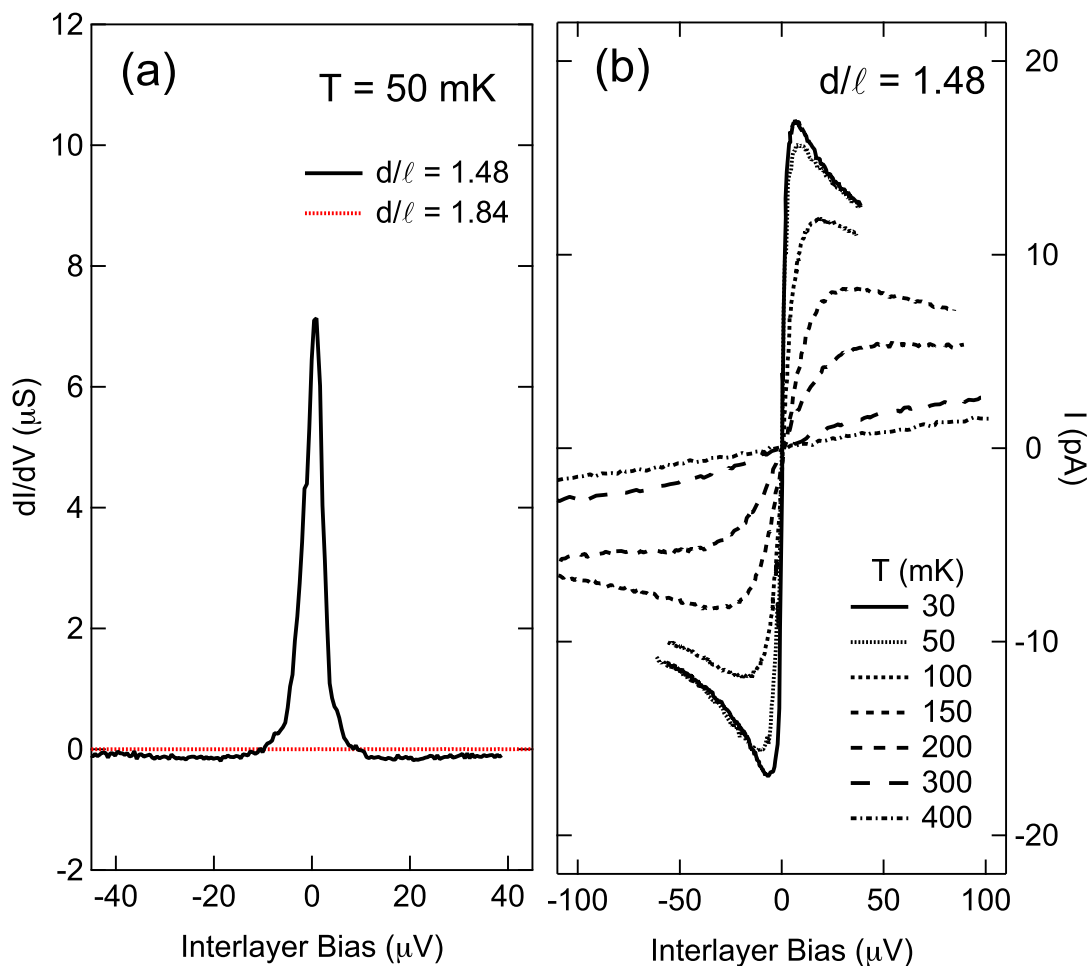
Figure 1.10: Examples of interlayer tunneling measurements at $\nu_T = 1$. All data were taken using sample 7-12-99.1R with a four-terminal method in which the interlayer voltage was measured between two voltage probes on opposite layers. (a) Tunneling conductance spectra for low d/ℓ and high d/ℓ. $T = 50$ mK. (b) Tunneling current versus bias at $d/\ell = 1.48$ taken at numerous temperatures.

width even in the limit of zero temperature [102]. For example, under ideal conditions (low d/ℓ and low temperature) this peak is a few μV wide. It is unclear if this residual width is due to intrinsically disordered superfluidity [6, 107, 98, 34, 123, 33, 54] or finite series resistance [116, 112].

1.3.2 Counterflow Currents

Currents may travel through bilayer systems in two distinct ways. The first, known as parallel flow, is realized by driving currents of the same magnitude and direction through the two layers. Because this represents a net transfer of charge from one part of the bilayer to another, parallel flow is equivalent to a current of charged excitations. Consequently, at $\nu_T = 1$ parallel flow is associated with a Hall voltage in either layer of $V_{xy}^{\parallel} = \frac{h}{e^2} I_T$, where $I_T = I_1 + I_2$ is the total current flowing through the sample.

However, one may also drive currents of equal magnitude but *opposite* direction through the two layers. For example, a current I may flow in the top layer from the left side of the sample to the right side, while an equal current flows from right to left in the bottom layer. This current configuration is known as counterflow. Because no net transfer of charge takes place during counterflow, it has been conjectured [125, 30, 82, 109] that counterflow currents could be carried by excitons with no dissipation. It has been shown [66, 121, 127] that the Hall voltage across either layer will vanish in a counterflow measurement at $\nu_T = 1$. An example of such transport data for both parallel and counterflow currents can be seen in figure 1.11. Hall resistance is clearly nonzero in parallel transport,[4] but vanishes in counterflow.

These results were originally interpreted to be consistent with exciton flow because excitons are charge neutral and thus should feel no Lorentz force. Because both the counterflow Hall resistance R_{xy}^{CF} and longitudinal resistance R_{xx}^{CF} were found to be small, the calculated counterflow conductivity $\sigma_{xx}^{CF} = \rho_{xx}^{CF} / \left[(\rho_{xx}^{CF})^2 + (\rho_{xy}^{CF})^2 \right]$ appeared to be finite but still several orders of magnitude higher than the bulk conductivity of charged excitations, as shown in figure 1.12. This apparently large con-

---

[4]In this figure, the Hall resistance at $\nu_T = 1$ has the value of $2\frac{h}{e^2}$ because here it is defined in terms of the current flowing through a single layer: $R_{xy}^{\parallel} \equiv V_{xy}^{\parallel}/I_1$, where $I_1 = \frac{1}{2} I_T$.
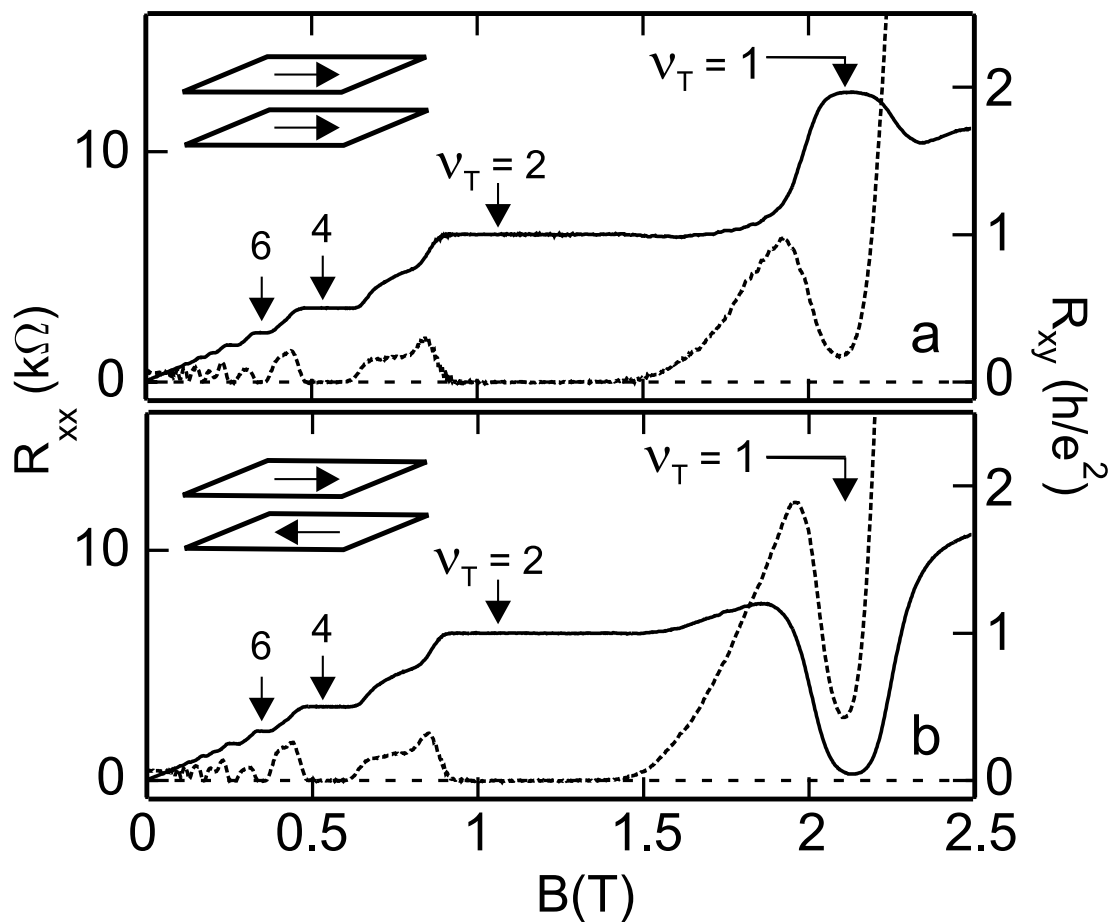
Figure 1.11: Comparison of parallel (top panel) and counterflow (bottom panel) transport in a bilayer system at $d/\ell = 1.58$ and $T = 50$ mK. The solid lines are the Hall resistance R_{xy} and the dotted lines are longitudinal resistance R_{xx}. Reprinted with permission from M. Kellogg, J. P. Eisenstein, L. N. Pfeiffer, and K. W. West, *Phys. Rev. Lett.* **93**, 036801 (2004). Copyright 2004 by the American Physical Society.
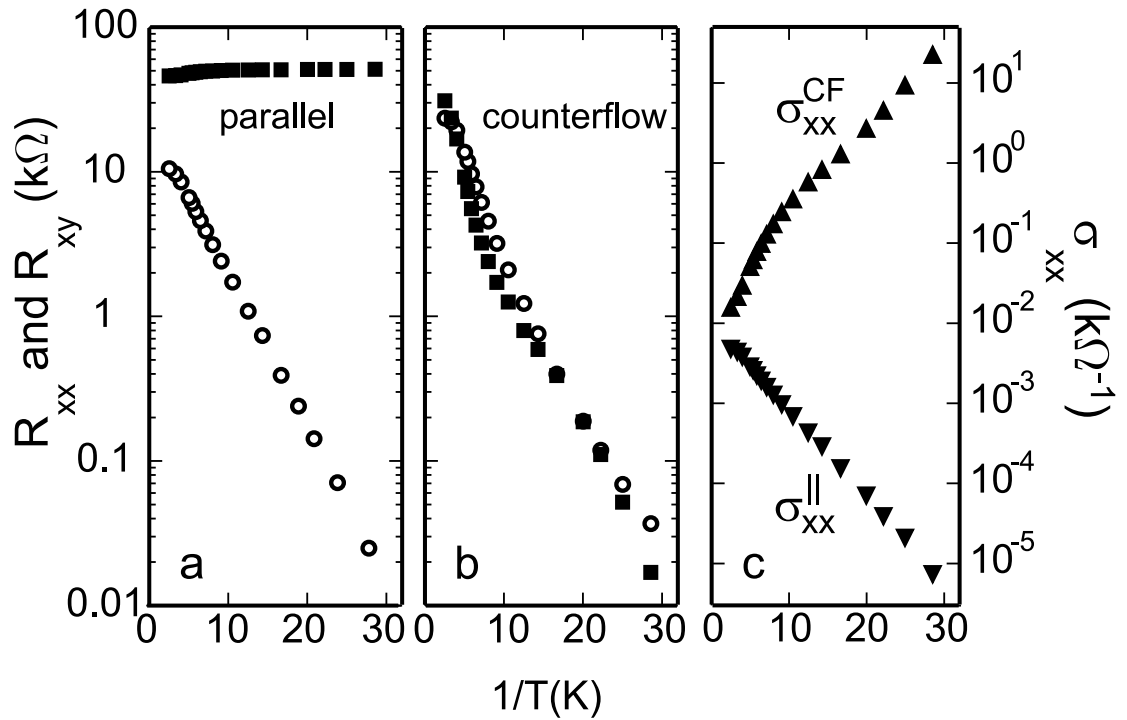
Figure 1.12: Temperature dependence of parallel and counterflow transport at $\nu_T = 1$ and $d/\ell = 1.48$. In the first and second plots, the circles are R_{xx} and the squares are R_{xy}. Reprinted with permission from M. Kellogg, J. P. Eisenstein, L. N. Pfeiffer, and K. W. West, *Phys. Rev. Lett.* **93**, 036801 (2004). Copyright 2004 by the American Physical Society.

ductivity in counterflow was at first thought to be a sign of the anticipated excitonic superfluidity. However, there are no signs of the KT transition between ohmic and nonohmic behavior at a finite temperature. Instead, σ_{xx}^{CF} evolves smoothly with temperature and remains ohmic throughout the explored temperature range. Another complication is that these counterflow studies were performed on Hall bars, in which all of the electrical contacts were connected by charge-carrying edge channels. It is unknown what role they might play in counterflow transport and they prohibit the unambiguous detection of *bulk* exciton currents while using Hall bar samples.

1.3.3 Coulomb Drag

Finally, we comment on a class of transport measurements that is peculiar to bilayer systems: Coulomb drag. A current is driven through only one layer (denoted as the drive layer), while no current is permitted to flow in or out of the passive layer (known as the drag layer). If the two layers are sufficiently close, then electrons in the drive layer can scatter off of the electrons in the drag layer. This interaction can be either due to direct Coulomb repulsion [44, 59] or through phonon-mediated coupling [45]. The interlayer scattering will tend to transfer momentum from the drive layer to the drag layer, whose electrons will want to travel in the same direction as the drive current. However, because the drag layer is constrained to have no net current, instead a voltage drop V_D will develop in the drag layer to prevent any induced current flow there. The ratio of this voltage to the drive current I_{drive} is known as the Coulomb drag resistance. In this thesis, we use the convention $R_{xx,D} = -V_{xx,D}/I_{drive}$ and $R_{xy,D} = V_{xy,D}/I_{drive}$, where $V_{xx,D}$ and $V_{xy,D}$ are the longitudinal and transverse (Hall) drag voltages, respectively. The negative sign in our definition of $R_{xx,D}$ reflects the fact that for bilayer electrons the longitudinal voltage drop in the drag layer is typically in the opposite direction as the one in the drive layer from conventional dissipation.

At either zero magnetic field or large effective layer separation (in the case of $\nu_T = 1$ [76]), interlayer correlations are miniscule and Coulomb drag is only a perturbative

effect. However, as d/ℓ is lowered below the same critical value associated with the $\nu_T = 1$ quantum Hall state, Coulomb drag becomes vastly enhanced [67, 65]. We illustrate typical Coulomb drag data near $\nu_T = 1$ in figure 1.13. We first note that the Hall drag resistance rises up to the quantized value of h/e^2. The robust plateau in Hall drag reflects the nonperturbative interlayer correlations of the $\nu_t = 1$ state; the two layers are clearly not independent of one another. The longitudinal drag resistance has a more complex behavior: as d/ℓ is reduced a peak in $R_{xx,D}$ rises up, achieving a maximum height of ~ 1.5 kΩ at nearly the same d/ℓ at which $R_{xy,D} = \frac{1}{2}h/e^2$. For moderate d/ℓ, the drag resistance peak is centered on the magnetic field corresponding to $\nu_T = 1$. At very low d/ℓ, the peak splits in two and eventually $R_{xx,D} \approx 0$ in the vicinity of $\nu_T = 1$. We emphasize that these results are obtained even when the allowed interlayer tunneling current is much smaller than the drive current [67, 38].

The appearance of a plateau in Hall drag resistance is quite remarkable because naïvely no current appears to be flowing through the drag layer and thus there should be no Lorentz force to create a Hall voltage. The intuitive explanation for quantized Hall drag is as follows: any charge current that is injected into one layer will become quantum mechanically spread between the two layers. This generates an equal Hall voltage across either layer due to the indeterminacy in which layer the charge current is located. Because the $\nu_T = 1$ state consists of a single, completely filled Landau level that is shared between the two layers, the Hall resistance in either layer is h/e^2. Because the measurement circuit provides the constraint that no net current can enter or leave the drag layer, a counterflow current must be simultaneously generated. This counterflow current does not alter the Hall resistance, but ultimately cancels out the charge current induced in the drag layer. One cannot determine the *spatial* distribution of the counterflow current in this picture.

Kun Yang [129] has provided a more rigorous explanation of Hall drag in generic bilayer quantum Hall states. His explanation focuses on the interlayer repulsion between edge states. By driving a current through the drive layer, one populates higher energy states in the edge channels. The chemical potential of the drive layer will consequently rise; this increase is identified with the Hall voltage of the drive
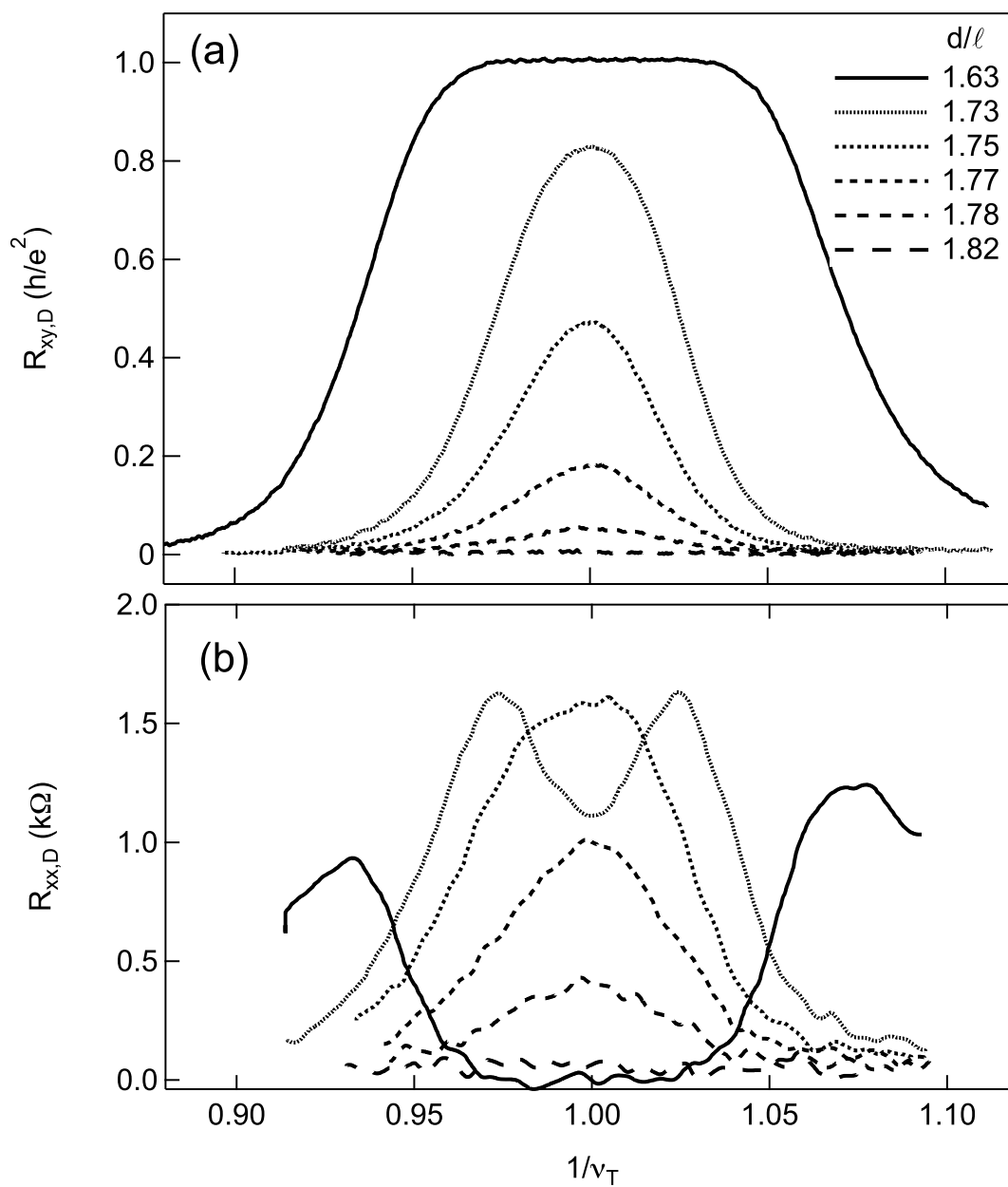
Figure 1.13: (a) Transverse (Hall) and (b) longitudinal Coulomb drag near $\nu_T = 1$ for various d/ℓ taken with sample 7-12-99.1R at $T = 30$ mK. For the sake of clarity, the data in (b) have been binomially smoothed using IGOR Pro's smooth funciton with 1000 operations.

layer. Coulomb repulsion prevents the population of the corresponding states in the drag layer. Hence, the energy cost for adding another electron to the drag layer (i.e., the chemical potential) increases by an amount proportional to the rise in chemical potential of the drive layer. In the case of the 111 state (where the electrons are equally repelled by other electrons in their own layer and the opposite layer), this ultimately leads to $R_{xy,D} = h/e^2$. We should emphasize that Kun Yang's theory can be extended to other bilayer quantum Hall state and does not make explicit reference to any bulk counterflow current.

1.4 Summary and Outlook

In a 2DES, the combination of high magnetic fields and Coulomb repulsion can lead to strongly correlated states that are known as fractional quantum Hall states. A particularly unusual quantum Hall state forms when two 2DESs at total filling factor 1 are placed in close proximity with one another such that interlayer interactions are comparable to intralayer interactions. In this so-called $\nu_T = 1$ state, the electrons in one layer can be described as pairing up with the holes in the other to form excitons. The excitons condense to create a bilayer quantum Hall with superfluid-like properties. However, the analogy to superfluidity does not appear to be exact. The anticipated KT transition at finite temperature has not been definitively observed. The Josephson-like tunneling peak appears to have a residual width even in the limit of zero temperature. Finally, evidence for excitonic superfluidity remains lacking. In the following chapters we seek to address these issues and clarify our understanding of the $\nu_T = 1$ state.

Chapter 2

Materials and Methods

This chapter describes the experimental methods we used to study bilayer samples at low temperature in the quantum Hall regime. First, we describe the semiconductor gallium arsenide (GaAs) and how it can be combined with aluminum gallium arsenide ($Al_xGa_{1-x}As$) to form heterostructures that contain two-dimensional electron systems (2DESs). Next, we summarize the sample-processing techniques that allow us to shape the bilayer system into desired geometries and tune the density in either layer. Finally, we discuss the implementation of the measurements used to probe the transport properties of bilayers.

2.1   Gallium Arsenide

Here we review the basic properties of gallium arsenide (GaAs). GaAs is a semiconductor within the III-V family. It possess a zincblende crystal structure, shown in figure 2.1. This structure is similar to diamond's face-centered cubic structure, but with gallium and arsenic atoms occupying alternating lattice sites [14].

GaAs has a relatively simple band structure near the Fermi energy. Unlike silicon, GaAs possesses a direct band gap. The gap between the electron (conduction) band and the two hole (valence) bands is centered on the Γ high symmetry point. Because we use n-type samples, we will focus on the conduction band. Electrons in the conduction band have an isotropic effective mass of $m^* = 0.067m_e$, where m_e is the mass of the electron in vacuum. Residual spin-orbit coupling modifies the response of
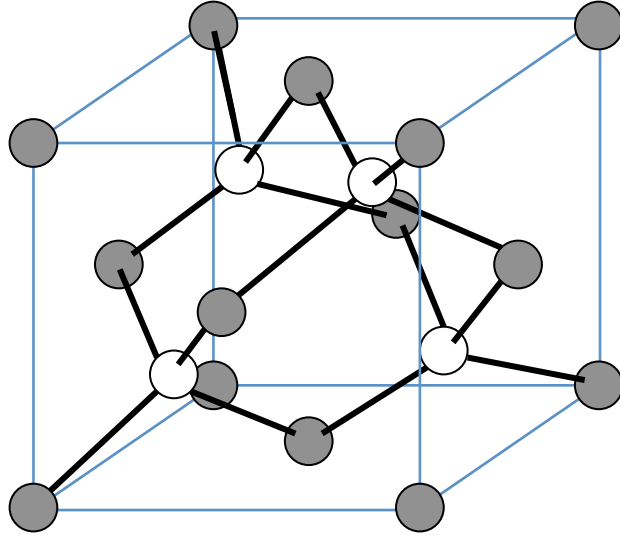
Figure 2.1: Zincblende crystal structure of GaAs.

the electronic energy levels to a Zeeman field, providing an effective g-factor of -0.44 in bulk GaAs [14].

2.2 GaAs/AlGaAs Heterostructures

When two semiconductors with unequal band gaps meet at an interface, charge will transfer from one material to another until the chemical potential is equal in both materials. This excessive charge is known as space charge. The negative and positive space charge will cause the bands to bend within the vicinity of the interface, following Poisson's equation. As seen in figure 2.2, a band offset will form at the interface, in which the energies of the conduction and valence bands will change nearly discontinuously at the heterojunction interface. The offset is generated by the very large electric field between the negative space charge in the GaAs side of the interface and the positive space charge in the AlGaAs side. This offset can act as a potential barrier for electrons in the conduction band [68]. Through proper layering of different semiconductors, one can tune the potential $V(z)$ for electrons in the z direction.

Heterostructures can be grown to high precision and extreme cleanliness using
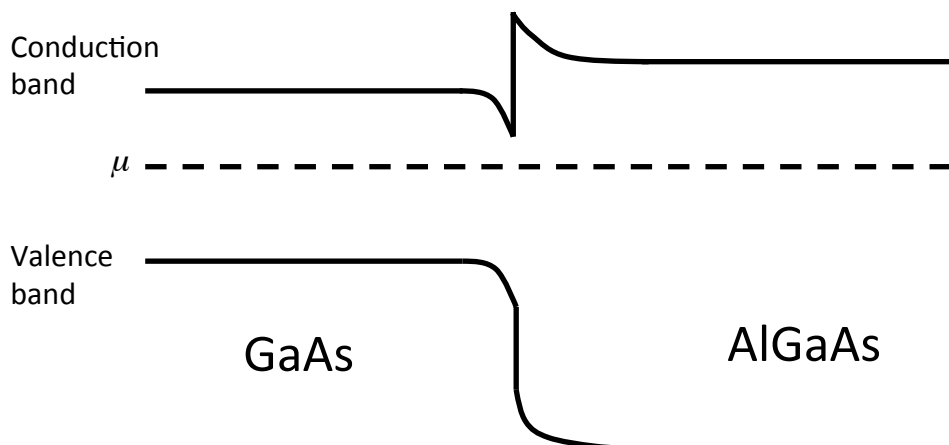
Figure 2.2: Band structure of a GaAs/AlGaAs heterojunction. The dashed line indicates the chemical potential.

molecular beam epitaxy (MBE). In MBE, elemental sources are vaporized within Knudsen cells located in an ultra high vacuum. These Knudsen cells are essentially crucibles with controlled shutters that can release a flux of gaseous atoms for desired intervals. The atoms are directed towards a target wafer, where they combine to form the crystal. The growth rate is slow (roughly one monolayer per second) and can be monitored using reflected high-energy electron diffraction (RHEED). In the RHEED process, a beam of electrons is reflected off of the wafer as the crystal is being grown and forms a diffraction pattern whose intensity varies periodically with each layer grown. Thus, MBE allows atomically precise creation of heterostructures. This in turn permits sophisticated engineering of the band structure in the z direction [14].

For example, a simple heterostructure consisting of a GaAs slab adjacent to a slab of AlGaAs can generate a triangular potential well that can confine the electrons in the z direction. We depict this in figure 2.3. Electrons are free to move in the x and y directions, however. In the absence of disorder, the energy eigenstates can be labeled by their in-plane momentum $k = \sqrt{k_x^2 + k_y^2}$. We can then write the wave function of each electron as $\psi(x, y, z) = \frac{1}{\sqrt{S}}\phi(z)e^{i(k_x x + k_y y)}$. Here, $\frac{1}{\sqrt{S}}$ de-
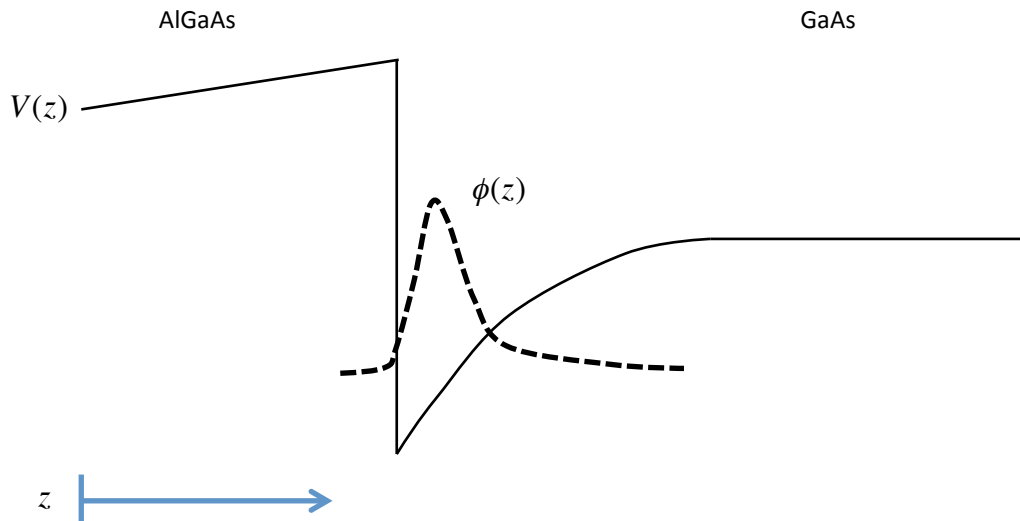
Figure 2.3: Diagram of subband potential $V(z)$ (solid line) and subband wave function $\phi(z)$ (dashed line) for a quantum well formed from a heterojunction.

notes a normalization constant and $\phi(z)$ is the subband wave function. The subband wave function can be found by solving the time-independent Schrödinger equation $\left[-\frac{\hbar^2}{2m^*}\frac{d^2}{dz^2} + V(z)\right]\phi(z) = E\phi(z)$. In practice, the subband potential $V(z)$ must be determined self-consistently from the charge density $\rho \propto |\phi(z)|^2$. If the Fermi level is tuned to be above the lowest subband energy level (i.e., the lowest bound state for electrons in the triangular potential), then the potential well will be populated with a two-dimensional electron system (2DES). The energy of an electron in the triangular well with momentum k can be written as $E(k) = E_0 + \frac{\hbar^2 k^2}{2m^*}$, where E_0 is the energy of the lowest subband [14].

A roughly square potential well can be generated by sandwiching a thin (typically 100–500 Å) layer of GaAs between two thicker layers of $Al_xGa_{1-x}As$. Thin layers of silicon one atom thick can then be positioned a couple thousand angstroms above and beneath the quantum well. Also known as δ-doping layers for the delta function potential wells that they create, these Si layers act as electron donors in the $Al_xGa_{1-x}As$ and populate the quantum well with electrons. By spatially separating the charged donor atoms from the 2DES, the scattering between the electrons and the donor sites
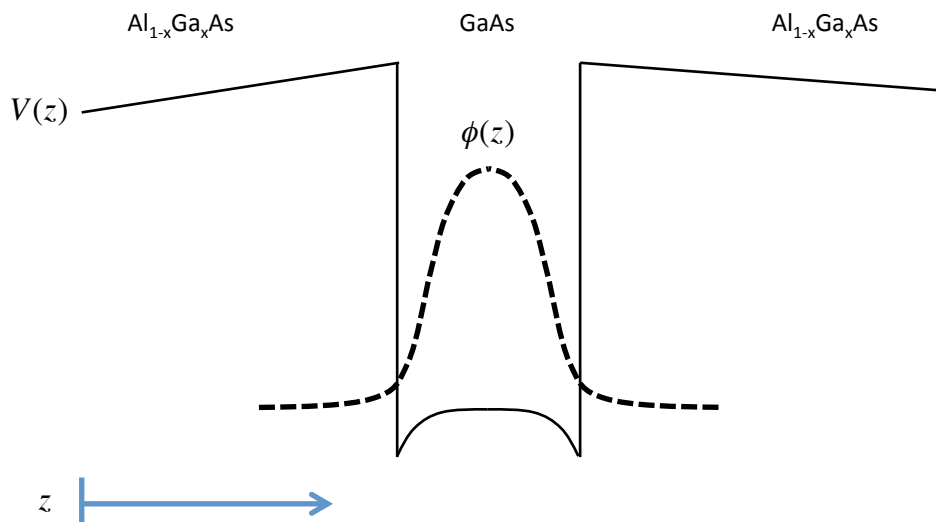
Figure 2.4: Square quantum well and 2DES realized in a $Al_xGa_{1-x}As/$ $GaAs/Al_xGa_{1-x}As$ heterostructure.

is greatly reduced. By combining this with other advances in MBE technology, mobilities of up to 30×10^6 cm^2/ V s can be obtained in these type of GaAs quantum wells. These exceptionally clean samples allow us to see subtle electron–electron interaction effects in the quantum Hall regime that would otherwise be destroyed [7, 99].

MBE also permits the creation of double quantum well (DQW) structures, illustrated in figure 2.5. These are formed by separating two GaAs quantum wells by a layer of $Al_xGa_{1-x}As$. This layer acts as a tunneling barrier. With finite tunneling energy, the subband wave functions for the two individual layers will then hybridize into symmetric and antisymmetric combinations of the wave functions $\phi_{L,U}(z)$ that are localized in either the lower or upper layer. The energy difference between these two eigenstates is generally denoted as $\Delta_{SAS} = t/2$, where t is the associated tunneling energy for an electron hopping from one layer to another. For a tall enough barrier, tunneling can be exponentially suppressed and to good approximation the two layers can be considered as separate 2DESs. As explained in chapter 1, if the barrier is also sufficiently narrow then strong interlayer interactions in the quantum Hall regime can induce interlayer correlations and destroy the notion of separate layers.
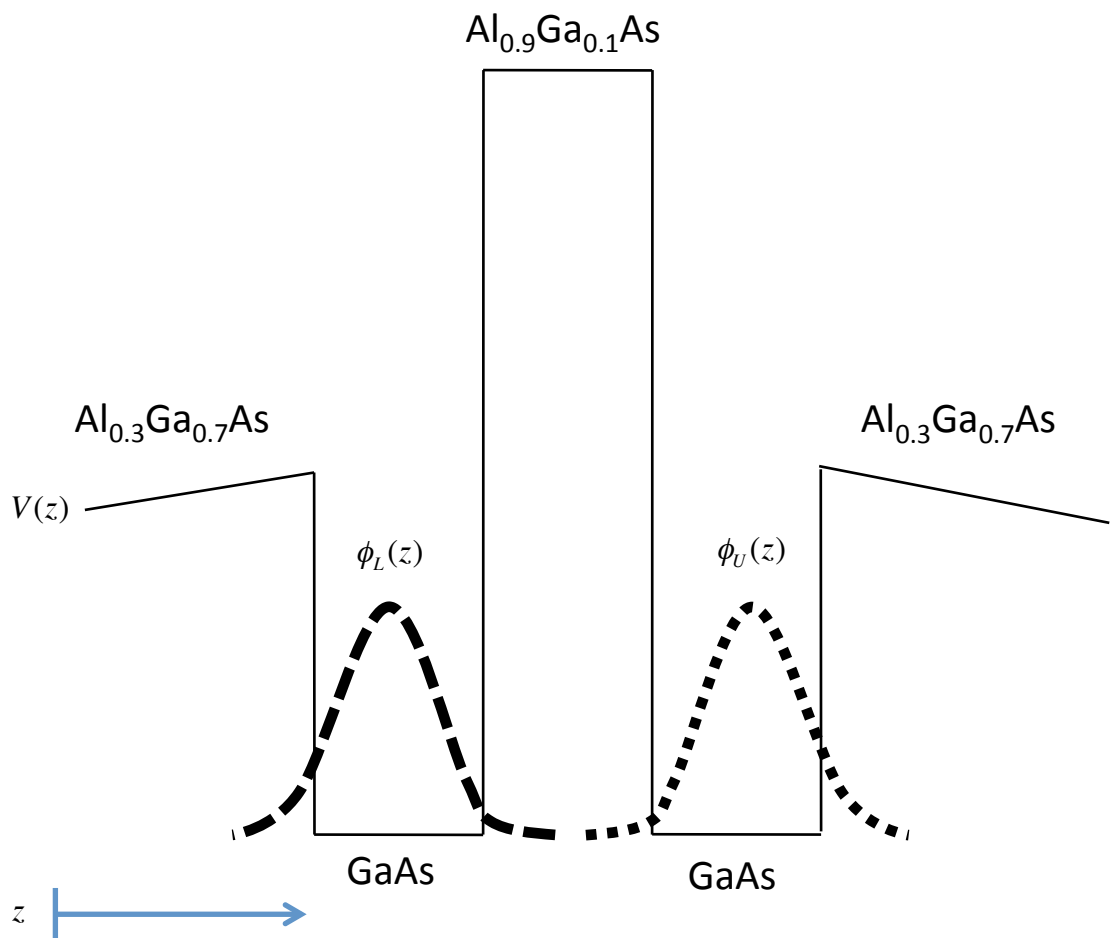
Figure 2.5: Double quantum well heterostructure. Here, we show the lowest subband wave functions for both the upper and lower layers.

In figure 2.6, we show a diagram of the various layers in a typical DQW wafer. In MBE, the layers are grown from bottom to top. We start with a $\sim$500 μm thick GaAs substrate. A series of alternating GaAs and AlGaAs layers are grown to create what is known as a superlattice. The superlattice stage serves to prepare the substrate surface [102]. A 5000 Å layer of $Al_{0.3}Ga_{0.7}As$ is deposited, followed by the lower Si doping layer. The lower setback layer is then grown, consisting of a 2300 Å thick layer of $Al_{0.3}Ga_{0.7}As$. The farther away the doping layer is from the actual 2DESs, the lower their density will be. When the DQW wafers used in this thesis were grown, MBE technology was such that the Si doping layer tended to migrate upwards during this step and thus the actual distance between the δ-doping layer and the 2DESs was less than 2300 Å. More recent advances have eliminated this behavior [21], but no such wafers were used in this thesis.

Once the lower setback layer is completed, the critical DQW layers are grown. The bilayer 2DES resides within these layers. They comprise of a 180 Å GaAs layer (the lower 2DES), a 99 Å $Al_{0.9}Ga_{0.1}As$ layer (tunneling barrier), and another 180 Å GaAs layer (the upper 2DES). A high concentration of aluminum is used in the tunneling barrier to minimize tunneling conductance while keeping the barrier width sufficiently small to observe interlayer interaction effects. A small amount of gallium is included in the tunneling barrier in order to minimize oxidation of the aluminum in the tunneling barrier, which can hamper electrical contact to the lower 2DES [64]. This DQW structure has a computed Δ_{SAS} of 0.4 neV, which is only a factor of 2 or 3 smaller than the values determined from experimentally observed tunneling currents [102]. Slight variations in the tunneling barrier thickness (even on the order of one or two atomic layers) can lead to sizable changes in the tunneling conductance due to the exponential decay of the subband wave function in the barrier. It has been empirically found that the tunneling conductance tends to increase as one moves away from the center of a wafer, where the tunneling barrier is thickest.

Another setback layer (2050 Å of $Al_{0.3}Ga_{0.7}As$) is grown on top of the DQW section, followed by the upper Si doping layer. Once again, this Si layer will migrate upward and increase the ultimate setback distance beyond 2050 Å, resulting in a
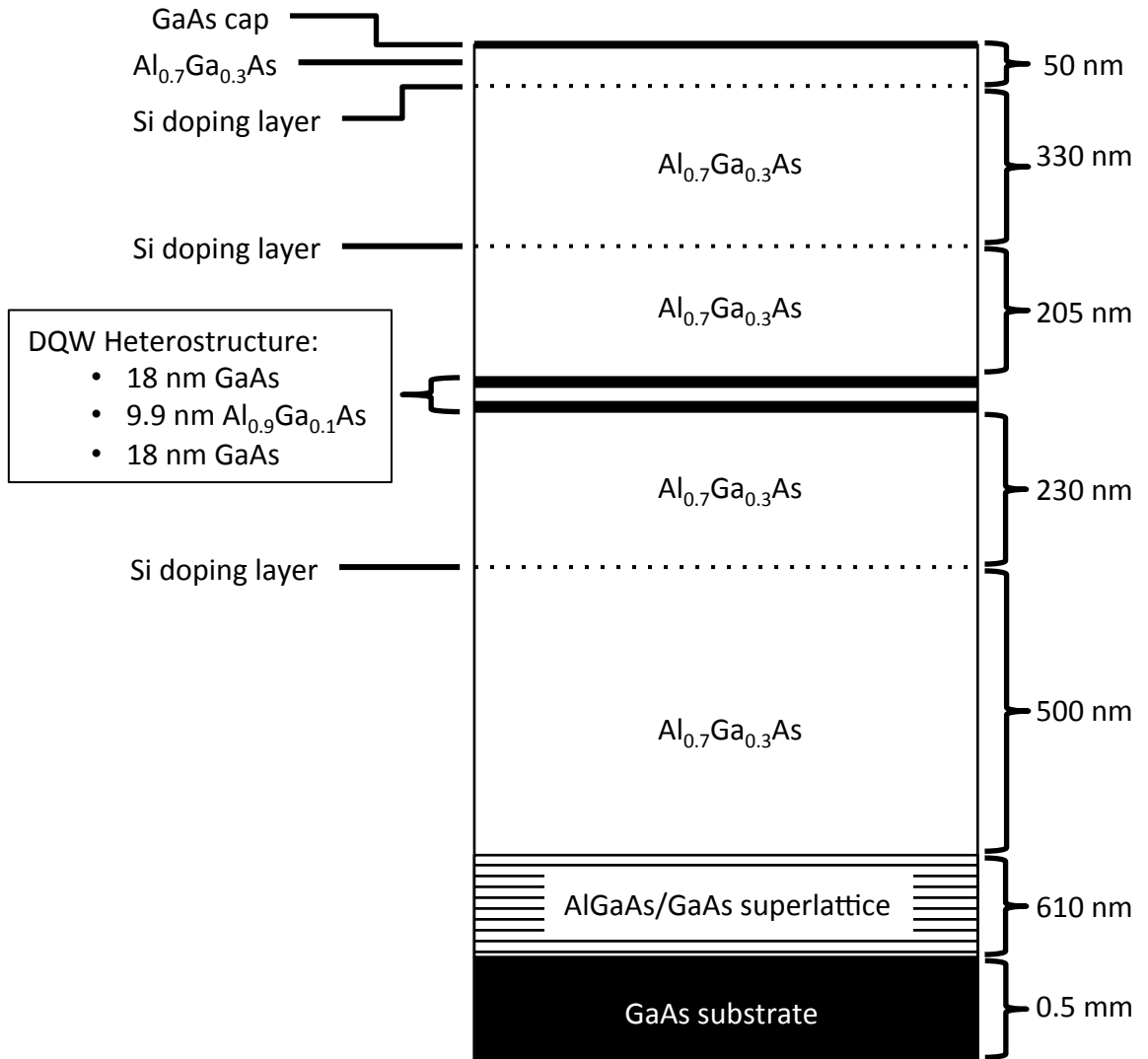
Figure 2.6: Diagram of MBE-grown layers for a typical DQW wafer. The two bottom-most layers are not drawn to scale.

symmetrically doped DQW with nearly equal nominal densities in the two 2DESs. Another 3300 Å of $Al_{0.3}Ga_{0.7}As$ is grown on top of the upper Si doping layer, followed by a final Si doping layer. To complete the DQW wafer, a cap structure is then grown by depositing 400 Å of $Al_{0.3}Ga_{0.7}As$ and then 100 Å of GaAs. Gallium arsenide has a high density of surface states in a narrow band near the middle of its band gap. These surface states pin the Fermi level at the surface within the gap and help to prevent parallel conduction layers beyond the DQW [14].

2.3 Sample Processing

Heterostructures grown by MBE allow for precise engineering of the confinement potential in the z direction. Further processing allows the confinement of electrons in the x and y directions to produce a desired sample geometry for specific experiments. Metallic electrodes deposited on top of and beneath the DQW allow us to capacitively tune the electron density in either 2DES. Here we will describe the basic steps of sample processing used to form such structures.

The general strategy for the creation of micron- and nanometer-sized features is to cover a wafer with a thin layer of organic polymer known as a resist. Some resists (called photoresists) are photosensitive and their chemical properties will change upon exposure to certain wavelengths of electromagnetic waves. For example, by exposing the resist AZ5214E (a photoresist commonly used in our lab) to UV light, it becomes soluble in developer solutions (e.g., AZ400K). To create features no smaller than 5 μm, we can expose a pattern onto a photoresist-coated wafer by shining UV light through an iron oxide mask, allowing certain portions of the photoresist to be subjected to the radiation. Upon rinsing in developer, photoresist will be removed in those regions, exposing the wafer there. Elsewhere, the wafer will still have a protective coating of photoresist. This remaining photoresist thus acts as a stencil with the same pattern as on the mask. A variety of other treatments can be selectively applied to the uncovered regions of the wafer. The process described above is known as photolithography and is limited by the wavelength of UV photons to features larger than 5–10 μm. To go

beyond this limit requires the use of electron beam lithography, in which high energy electrons are used to expose sections of resist as small as 10–30 nm.

We now outline the steps used to fully process DQW wafers. These sample-processing steps are described in further detail in Appendix C. First, we cleave off a 5×5 mm^2 piece of DQW wafer. Pieces from the center of the wafer generally have higher mobility and lower tunneling conductance. Then we use photolithography to define an etch mask made of photoresist in a particular shape near the center of the wafer piece. By dunking the sample in an acid solution for a few minutes, we can etch away the uncovered GaAs. The bilayer 2DESs are then confined to the resulting mesa underneath the remaining photoresist. Once the acid etch is done, the photoresist is removed in warm n-butyl acetate.

A fresh coat of photoresist is applied and exposed in a pattern to create small uncovered squares overlapping with certain regions of the mesa. By thermally evaporating Ni/AuGe onto those exposed squares and then removing the unexposed photoresist (along with the metal on top of it), we can deposit squares of Ni/AuGe in desired locations. Heating the sample at 440° within a flow of H$_2$ and N$_2$ gas will cause the AuGe to anneal down through the heterostructure and produce an electrical contact with both 2DESs directly underneath it. Because these electrical contacts are generally ohmic in behavior, they are known as ohmic contacts. Once the rest of the fabrication steps are done, we can solder wires directly to the ohmic contacts in order to permit electrical transport measurements of the 2DESs.

To tune the density of the 2DESs in the bilayer, we can deposit thin films of aluminum in various shapes on the upper or lower surface of the DQW wafer. These films of aluminum are known as top and bottom gates. Metals such as aluminum will form a Schottky barrier with the semiconducting GaAs [14] that prevents direct conduction between the metal and the 2DES. The aluminum and 2DES together act like a parallel plate capacitor. By applying a negative voltage bias to the aluminum while keeping the 2DESs grounded, one can reduce the electron density of the 2DES within a region that overlaps with the gate.

Annealed Ni/AuGe ohmic contacts will diffuse down to both 2DESs in the bilayer
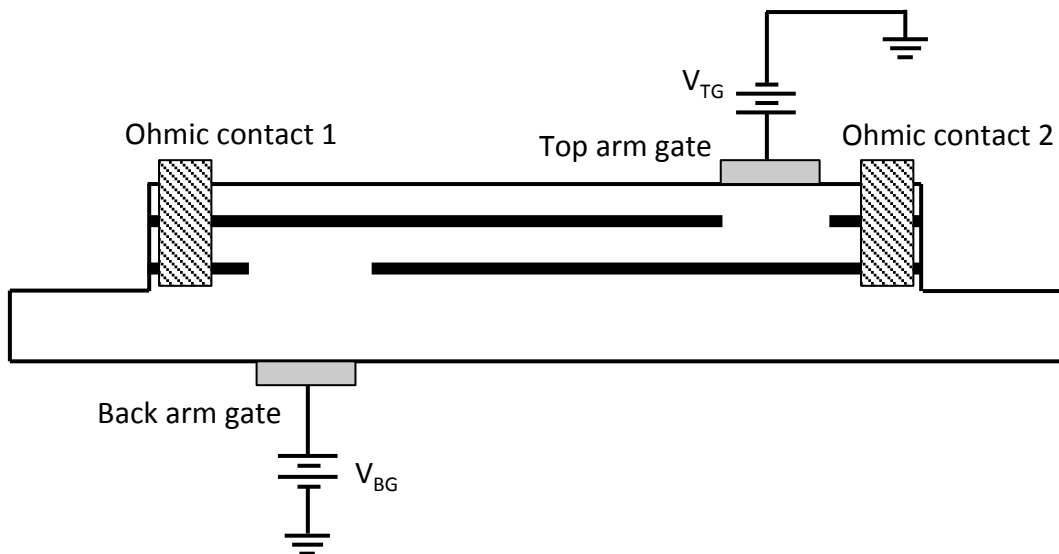
Figure 2.7: Selective depletion technique. Voltage biases V_{TG} and V_{BG} are applied to the top and bottom arm gates, respectively. These biases are set in order to deplete the appropriate region of the 2DES that is closest to the corresponding gate. Thus, ohmic contact 1 becomes effectively connected only to the top layer while ohmic contact 2 is connected only to the bottom layer.

system, shorting them together. Thus, any wire soldered to a given ohmic contact will be electrically connected to both layers simultaneously. The most spectacular transport properties of the $\nu_T = 1$ QH system require current leads and voltage probes that are connected to only one layer at a time, however. To achieve this, we uses the selective depletion technique [26], which we illustrate in figure 2.7. We first note that the upper 2DES will almost totally screen the lower 2DES from the electric field from a top gate, leaving the lower 2DES essentially unaffected by the top gate until the upper layer is completely depleted of electrons. Similarly, the lower 2DES will screen the upper 2DES from the electric field of a bottom gate. We can take advantage of this by creating a mesa where a number of "arms" extend from the central region, which is the region of interest. At the end of each arm, a Ni/AuGe ohmic contact is formed. Each arm is usually also overlapped with both a top gate and a bottom gate; these specialized gates are generally referred to as arm gates. By applying the proper bias to a top arm gate (generally −0.5 V in the traditional

DQW wafers), we can fully deplete the upper 2DES directly underneath that gate. Thus, the ohmic contact in that arm will only be connected to the central region via the *bottom* layer. By applying a large bias to the bottom arm gate for another arm, we will similarly deplete the bottom layer within a localized region in that arm. The ohmic contact associated with that arm will then be connected to the central region only through the *top* layer. An ohmic contact can be fully disconnected from the central region by applying a large bias to its matching top arm gate (generally -1.2 V) to deplete both layers.

The central region itself is covered by one or more top and bottom gates to independently control the electron density in either layer within this central region. Through proper application of biases to the arm gates, we can for example measure interlayer tunneling within the central region using one contact to the upper layer and another contact to the bottom layer. In order to reduce fringe fields to a tolerable level, we must bring our bottom gates to within 50 μm of the bilayer system. To do this, we thin the wafer piece to a thickness of 50 μm using a bromine-methanol etch. Once the sample is thin, the bottom gates can be deposited. We must then carefully solder and epoxy wires to the contact pads for each gate and ohmic contact. The wires are then soldered to an 18-pin header, which can be plugged into the sample holder of a dipping stick or dilution refrigerator.

2.4 Cryogenics

The physics of $\nu_T = 1$ is best observed at low temperatures (T = 15 to 50 mK), which requires the use of dilution refrigerators. However, samples may be tested and characterized at higher temperatures (300 mK to 4.2 K) through quicker means before beginning the relatively time-consuming process of cooling them down in a dilution refrigerator for detailed study.

2.4.1   Liquid Helium Dip: T = 4.2 K

One of the simplest ways of cooling down a device is to immerse it in liquid helium. This allows us to test the ohmic contacts and gates at 4.2 K. Our lab has a number of dipping sticks that can be used to lower a sample into a standard liquid helium storage dewar. Each of these dipping sticks is essentially an enclosed tube with a series of wires connecting the sample holder with a breakout box attached to the upper part of the stick. The end of the tube holding the sample is dipped into the dewar while the breakout box remains at room temperature. The breakout box consists of a number of BNC connectors and switches that permit electrical connection to the sample while it sits in the liquid helium.

The dipping stick should be lowered slowly into the liquid helium dewar in order to minimize any thermal shocks to the sample as well as to avoid violent boil-offs that ultimately waste liquid helium. To warm up the sample, the stick should be raised slowly: about six inches per minute. Once the stick has been fully raised, the sample space is likely to be below 0° C and there is the danger that ice can form on it if it is exposed to air. Such ice can be harmful to sensitive samples. Generally it is sufficient to remove the dipping stick once it is fully raised and then quickly insert its bottom tip into a can through which dry nitrogen flows. To completely avoid exposure to water vapor while the sample is still cold, we can instead install an isolation chamber on top of the liquid helium dewar and clamp the dipping stick onto the top of the chamber. The isolation chamber has a gate valve that can be closed once the sample has been fully raised and spigots to permit the flow of nitrogen gas through the chamber. In either case, the nitrogen should flow for at least 15 minutes to fully warm up the sample before its removal from the dipping stick.

2.4.2 ^{3}He Cryostat: T = 300 mK

Colder temperatures can be reached using a helium-3 cryostat. Although limited to 300 mK, the helium-3 cryostat in our lab is top loading and allows us to quickly cool, test, and warm fup a sample. Often this entire process can be completed in a single

day. Equipped with a superconducting magnet capable of reaching 14 T, the helium-3 cryostat permits magnetotransport studies and more careful characterization of samples than is possible in liquid helium-4 dips.

The principle behind the helium-3 cryostat is conceptually straightforward. The sample is immersed in liquid helium-3. By then pumping on the helium-3 and reducing its vapor pressure, the liquid is evaporatively cooled to $T \approx 0.3$ K. This is a lower temperature than can be obtained with helium-4 for two reasons. First, the helium-3 atom is lighter than the helium-4 atom. Consequently, the vapor pressure of helium-3 will be higher than that of helium-4 at any temperature [78]. Second, helium-3 is a fermion while helium-4 is a boson. Thus, helium-4 can form a superfluid film that acts as a heat link and can limit the ultimate temperature for evaporative cooling [78]. Helium-3, however, does not form a superfluid until its temperature has fallen below 3 mK [87, 86].

Helium-3 is a rare and expensive isotope of liquid helium. To conserve helium-3, we use a sorb pump to perform the evaporative cooling. The sorb pump is a chunk of activated charcoal with enormous effective surface area. By flowing liquid helium-4 around it, the charcoal adsorbs the helium-3 atoms and allows for evaporative cooling. Applying heat to the sorb releases the helium-3 so that it can be liquified once more.

2.4.3   Dilution Refrigerator: T = 15 mK

While rudimentary signs of $\nu_T = 1$ physics are observable at 300 mK, we must go to even lower temperatures to clearly observe the effects of excitonic condensation. The dilution refrigerator is the standard instrument for reaching $T \leq 100$ mK. Our lab has two dilution fridges in operation, with base temperatures of 15 mK and 50 mK. A third is being developed with a demagnetization stage, with projected base temperatures of $T \leq 1$ mK.

The heart of the dilution refrigerator is the mixing chamber, which contains liquified helium-3 and helium-4 during operation. Below $T = 0.86$ K, this mixture will physically separate into two distinct phases: a phase rich in helium-3 (the concen-

trated phase) and a phase consisting of minute amounts of helium-3 dissolved in helium-4 (the dilute phase). Below 0.5 K, helium-4 is essentially in its quantum mechanical ground phase and inert. Only the helium-3 phase is thermodynamically and hydrostatically relevant. The removal of helium-3 from the dilute phase will encourage the passage of helium-3 atoms from the concentrated phase into the dilute phase. This provides cooling power analogous to evaporative cooling. However, the concentration of helium-3 in the dilute phase remains finite even at absolute zero, saturating at the value of $\frac{n_3}{n_3+n_4} = 0.064$ [78]. Thus, while the vanishing vapor pressure $P_{vapor} \approx e^{-\Delta/k_b T}$ of most liquids will cause evaporative cooling to become exponentially suppressed, the raw cooling power of a dilution refrigerator is proportional to T^2 [78]. To allow for continuous operation, the pumped-away helium-3 is recooled and returned to the mixing chamber. A more detailed explanation of the physics and mechanics of dilution refrigeration is given in chapter 3 in reference [78].

2.5 Bilayer Transport Techniques

In this thesis we employ low-frequency transport measurements to probe the properties of bilayers. We make extensive use of lock-in detection [96] in combination with low-noise preamplifiers. Here, we describe the various types of transport measurements used throughout this thesis. This includes both conventional magnetotransport as well as measurements that are unique to bilayer systems, such as interlayer tunneling and Coulomb drag.

2.5.1 Magnetotransport in Bilayers

Longitudinal and Hall resistance measurements at low frequency are among the most common and straightforward ways to probe 2DESs. For these measurements, a small AC current of fixed magnitude is driven through the sample and the voltage difference between two contacts is measured. Depending on the location of the voltage probes relative to the current flow, the ratio of the voltage drop to the drive current gives either longitudinal (R_{xx}) or Hall (R_{xy}) resistance. A typical realization

of this measurement is shown in figure 2.8. Here, the AC drive current is generated by connecting a 10 MΩ resistor in series with a single-layer 2DES sample (denoted by the grey square) and applying an oscillating voltage V_{AC} to the resistor. This voltage originates from a lock-in detector. A current $I = V_{AC}/10$ MΩ is injected into one edge of the square-shaped sample at a single contact and exits to ground from a contact on the opposite edge. R_{xx} is detected by measuring the voltage between two contacts along the same edge. The voltage difference is fed to the inputs of the lock-in detector, which amplifies it to a detectable level. The Hall resistance R_{xy} is found by measuring the voltage drop between two contacts on two opposite sides of the square.
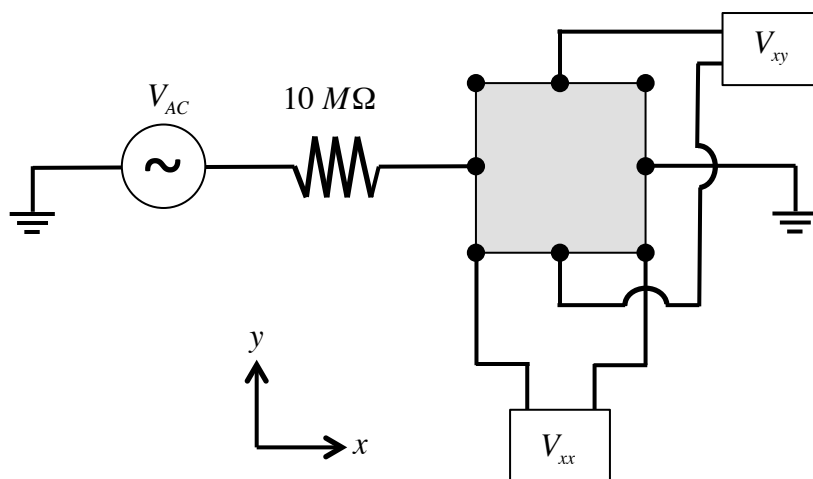
Figure 2.8: Diagram for conventional magnetotransport of a square-shaped single 2DES sample (grey square). Black dots denote ohmic contacts.

In DQW samples, the second layer provides an additional degree of freedom that enables a series of additional transport measurements. For example, in a bilayer sample currents may be driven in the same direction in the two layers (denoted as parallel flow, shown in figure 2.9) or in opposite directions within the two layers (denoted as counterflow, shown in figure 2.10). R_{xx} and R_{xy} are then measured using contacts connected only to one layer; shorting the two layers using a voltage

probe contact can cause current to flow between the two layers at that contact and complicate the measurement. Due to the strong interlayer correlations in the $\nu_T = 1$ QH state, the transport properties for the two current modes can be quite different. For example, parallel flow represents a net transfer of charge from one part of the sample to another. Consequently, parallel flow experiments at $\nu_T = 1$ probe the transport properties of charged excitations. Often, parallel flow is achieved by using current leads that are connected to both the upper and lower layers simultaneously. In a well formed QH state, longitudinal resistance in parallel flow $(R_{xx}^{||})$ vanishes and the Hall resistance is quantized at $R_{xy}^{||} = \frac{h}{e^2} I_T$, where $I_T = I_U + I_L$ is the total current flowing through the system.[1]
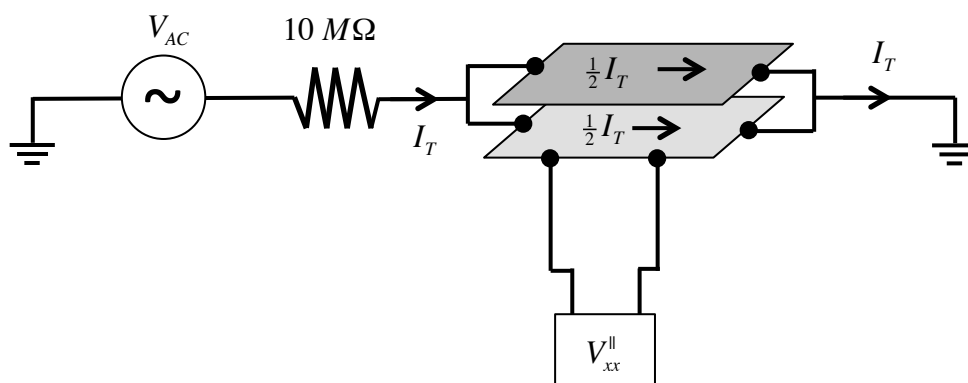
Figure 2.9: Diagram of parallel transport measurement in a bilayer system. For simplicity, only the voltage probes for longitudinal resistance $R_{xx}^{||}$ are shown here.

Counterflow currents, however, are thought to represent unidirectional exciton transport. One possible counterflow measurement in a Hall bar is shown in figure 2.10. A current is driven through one layer at a particular edge, shunted between the

[1]Interestingly, the quantization of the Hall resistance across a single layer does not appear to be disrupted if there is a slight mismatch of the two currents driven through the two individual layers. Any deviation from parallel current is equivalent to a pseudospin current, which generates no Hall resistance. Meanwhile, the total charge current I_T induces the same Hall resistance in both layers. This mechanism is related to the quantization of Hall drag at $\nu_T = 1$.

two layers at the other edge, and collected from the other layer at the first edge. It has been shown in Hall bar samples [66, 121, 127] that R_{xy}^{CF} will vanish at $\nu_T = 1$. As mentioned before, this class of measurements only probes the edge channels and cannot directly detect bulk exciton currents. Outside of $\nu_T = 1$, the two layers act independently of each other and the counterflow Hall resistance is equal to the value obtained for a single layer with current flowing through it.
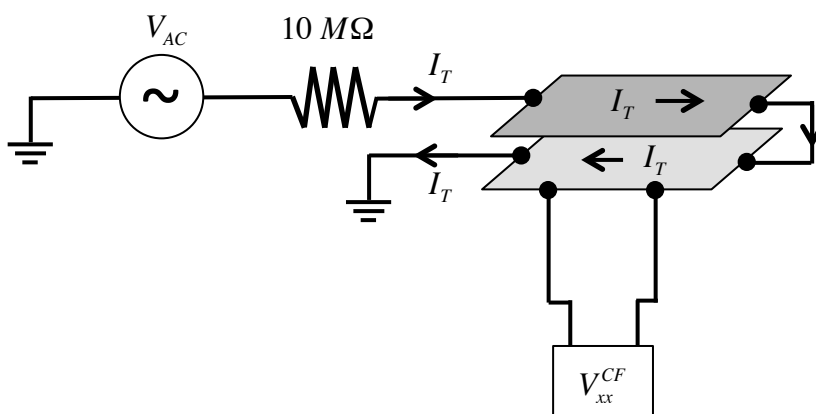
Figure 2.10: Diagram of counterflow transport measurement in a bilayer system. For simplicity, only the voltage probes for longitudinal resistance R_{xx}^{CF} are shown here.

2.5.2 Coulomb Drag

Coulomb drag is a slight variation on the conventional resistance measurement. In a Coulomb drag setup (shown in figure 2.11), a current I_{drive} is driven through one layer (known as the drive layer) and the voltage drops $V_{xx,D}$ or $V_{xy,D}$ across the other layer (known as the drag layer) is measured. The Coulomb drag resistances $R_{xx,D}$ and $R_{xy,D}$ are defined as the ratio between these voltage drops and the drive current: $R_{xx,D} = V_{xx,D}/I_{drive}$ and $R_{xy,D} = V_{xy,D}/I_{drive}$. These drag resistances reflect the transfer of momentum from the drive layer to the drag layer, such as through direct electron–electron scattering [44]. Because no current is allowed to flow in the drag

layer, an electric field must develop to counteract the interlayer momentum transfer.
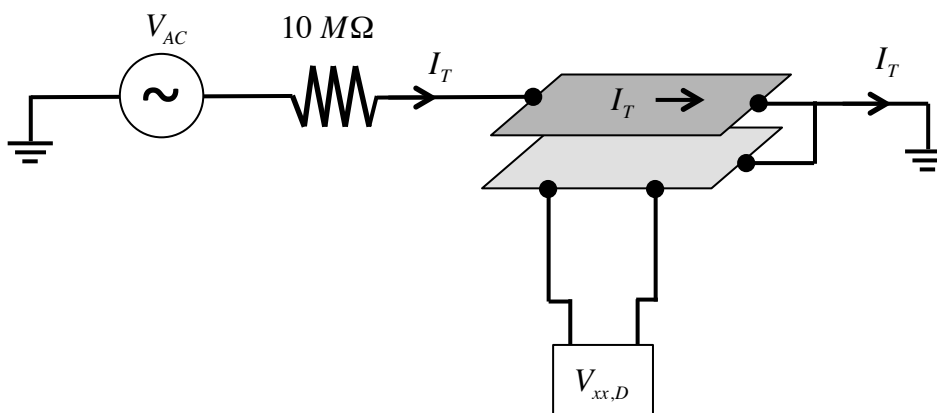
Figure 2.11: Diagram of Coulomb drag measurement. For simplicity, only the voltage probes for longitudinal drag $R_{xx,D}$ are shown here.

Ideally, Coulomb drag measurements should be restricted to samples with small interlayer tunneling conductances. Any current leaking between the layers will give anomalous signals. As an additional precaution, we usually ground the drag layer using the same contact acting as the current drain in the drive layer. By grounding this current drain contact while it is connected to both layers, we will ensure that both layers are kept close to both AC and DC ground and thus suppress spurious signals from interlayer capacitive coupling or tunneling [64].

2.5.3 Interlayer Tunneling

To measure interlayer tunneling, a voltage is applied to one layer while the other layer is grounded through a single contact. The voltage bias drives current between the two layers, which flows to ground and is subsequently detected.

An example of a tunneling measurement circuit is shown in figure 2.12. The voltage bias consists of a DC component (generated by a Kepco 488-122 programmer) and an AC modulation (generated by the oscillator of a PAR 124A lock-in detector).
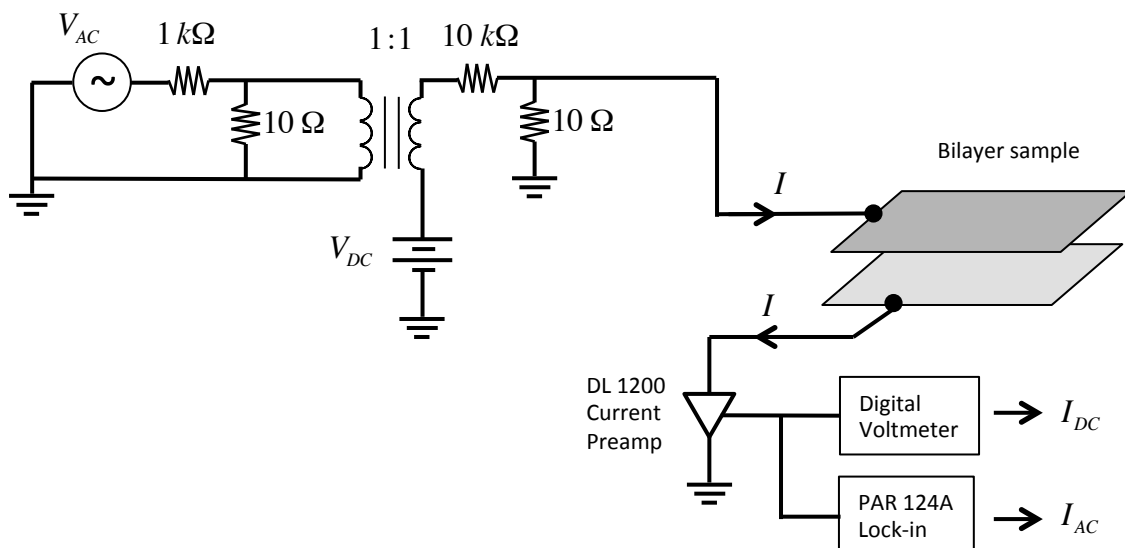
Figure 2.12: Diagram of interlayer tunneling circuit.

The DC bias serves to offset the two layers in terms of energy. The AC excitation enables the measurement of differential tunneling conductance through lock-in detection. Both the DC and AC components are reduced from their raw values using resistor-based voltage dividers. The AC component is added to the DC component via a 1:1 transformer. The voltage bias is applied to a single ohmic contact connected only to one layer (here, the top layer). This bias drives tunneling current between the two layers, which exits the sample via an ohmic contact connected to the other layer (here, the bottom layer).

The tunneling current passes to ground via the input of a DL Model 1211 current preamplifier. The current preamplifier provides a virtual path to ground with relatively low impedance. Its output is a voltage signal proportional to the tunneling current. The DC component can be read directly by a digital voltmeter. The AC component is measured by the lock-in detector.

The circuit shown in figure 2.12 is a two-terminal measurement. Although tunneling resistance is generally much larger than any series resistance, this is not always the case at $\nu_T = 1$. One might implement a four-terminal tunneling circuit by measuring the interlayer voltage difference with probes connected to different layers. However,

the interpretation of the resulting interlayer voltage is complicated by the possibility that tunneling might be unevenly distributed across the sample. The placement of the interlayer voltage probes just outside of the strongly tunneling $\nu_T = 1$ region might avoid this problem, but we will then likely encounter the $\sim h/e^2$ resistance associated with charge entering and exiting a quantum Hall state.

2.5.4 Conclusion

In this chapter, we have discussed the materials, equipment, and measurement techniques employed throughout this thesis. At present, GaAs heterostructures grown through MBE provide a gold standard for 2DESs. The precise subband engineering provided by MBE enables the production of a unique system: two closely spaced 2DESs with vanishing interlayer tunneling. By cooling these high quality bilayer systems down to millikelvin temperatures in a dilution refrigerator, we can realize the $\nu_T = 1$ QH state. In the remainder of this thesis, we will use the various bilayer transport measurements described in this chapter to probe exciton condensation and transport properties of this exotic electronic system.

Chapter 3

Interlayer Transport at Zero Magnetic Field

In this chapter, we describe some of the physics and measurement techniques for interlayer transport in the absence of a magnetic field. In the bilayer samples studied in this thesis, conduction between the two layers is highly suppressed by a 10 nm $\text{Al}_{0.9}\text{Ga}_{0.1}\text{As}$ barrier. Consequently, at $B = 0$ the two 2DESs act as two separate and degenerate Fermi seas of noninteracting electrons. Only weak interlayer transport is permitted, primarily reflecting single-particle physics. Here, interlayer transport includes tunneling and the capacitive coupling between the two layers. Tunneling is a fundamentally quantum mechanical process and is dependent on the overlap of the wave functions of electrons confined to either of the two individual layers. For $T \ll T_F$, 2D to 2D tunneling can reveal the electronic spectral function $A(E, k)$ and the lifetime of the electron states [85]. Meanwhile, interlayer capacitance originates from classical electrostatics, but also includes information about the compressibility of the 2DESs [79].

3.1   Interlayer Tunneling

3.1.1   Tunneling with No Disorder

Due to the tall tunneling barrier between the two 2DESs, the subband wave functions for electrons localized in either quantum well are exponentially suppressed in the

barrier. Thus, there is little overlap between an electronic state in one layer and a state in the other layer. This allows us to treat tunneling as a perturbation and employ Fermi's golden rule. We will see that tunneling reflects the conservation of in-plane momentum and will contain information about the lifetime broadening of the electron states. This section is derived from [24] and the associated lecture notes.

We first consider the form of the energy eigenstates for electrons in either the upper (U) or lower (L) layer. For decoupled layers, such wave functions will be localized in one quantum well or the other. We will first consider the case of no disorder and no electron–electron interactions. In the low temperature and degenerate limits, each quantum well contains a 2DES best described as a Fermi sea. The absence of impurities (magnetic or nonmagnetic) allows us to treat both the in-plane momentum $\mathbf{k}$ and spin σ of each electron as good quantum numbers. Consequently, we can write the energy eigenstates of electrons in the lowest subband of a given quantum well as $|\mathbf{k}, \sigma, J\rangle$. Here, J is the quantum well label ($J = U$ or L).

To calculate the tunneling current, we will use Fermi's golden rule and first write the transition rate for electrons going from, say, the upper layer to the lower layer as

$$R_{U \to L} = \frac{2\pi}{\hbar} \sum_{\mathbf{k}\sigma} \sum_{\mathbf{k}',\sigma'} |\langle \mathbf{k}, \sigma, U | V_L | \mathbf{k}', \sigma', L \rangle|^2 \delta(E_{\mathbf{k},U} - E_{\mathbf{k}',L}). \tag{3.1}$$

Here, V_L describes the quantum well for the lower layer, which acts as a perturbation from the point of view of the electrons in the upper layer. Because V_L is only a function of z and is independent of spin, the matrix element in equation (3.1) is equal to $\delta_{\mathbf{k}\mathbf{k}'}\delta_{\sigma\sigma'}|t|^2$. The interlayer tunneling matrix element t is given by

$$t = \int dz \phi_{0,U}(z)^* V_L(z) \phi_{0,L}(z), \tag{3.2}$$

where $\phi_{0,U}(z)$ and $\phi_{0,L}(z)$ are the subband wave functions of either layer. Finally, the delta function in equation (3.1) enforces energy conservation by insuring that the initial and final energies, $E_{\mathbf{k},U}$ and $E_{\mathbf{k}',L}$ respective, are the same.

We next use the transition rate given in equation (3.1) to determine the net

tunneling current going from the upper layer to the lower layer. First, we must consider not only the electrons tunneling from the upper layer but also the electrons tunneling in the opposite direction from the lower layer. We can accomplish this by subtracting a term given by the transition rate $R_{L \to U}$, which can be found by simply transposing U and L in the equation for $R_{U \to L}$. Second, we must respect the Pauli exclusion principle and only consider the electrons tunneling from filled states in one layer to unfilled states in the other. We can do this by using the Fermi distribution function f, which states the probability that a given state is filled. The result for the net tunneling current is

$$I = \frac{2e\pi}{\hbar} \sum_{\mathbf{k}\sigma} \sum_{\mathbf{k}',\sigma'} |t|^2 \delta_{\mathbf{k}\mathbf{k}'} \delta_{\sigma\sigma'} \delta(E_{\mathbf{k},U} - E_{\mathbf{k}',L})(f_{\mathbf{k},U} - f_{\mathbf{k}',L}). \tag{3.3}$$

In tunneling measurements, a voltage bias V is applied between the two layers and the resulting tunneling current is detected. This voltage bias causes a displacement in the electrochemical potentials of the two layers. We can then modify equation (3.3) by writing the energy difference $(E_{\mathbf{k},U} - E_{\mathbf{k}',L})$ of the states in the two different layers as $\left(\frac{\hbar^2 k^2}{2m} - \frac{\hbar^2 k'^2}{2m} + E_{F,L} - E_{F,U} + eV \right)$, where $E_{F,U}$ and $E_{F,L}$ are the Fermi energies for the upper and lower layers respectively. The expression for the tunneling current can be simplified by performing the sums over $\mathbf{k}'$ and σ' to obtain

$$I = \frac{2e\pi}{\hbar} \sum_{\mathbf{k}\sigma} |t|^2 \delta(E_{F,L} - E_{F,U} + eV)(f_{\mathbf{k},U} - f_{\mathbf{k},L}). \tag{3.4}$$

The sum over spin index produces an overall factor of 2. The sum over $\mathbf{k}$ can be replaced with the integral $\frac{S}{(2\pi)^2} \int d^2\mathbf{k} = \frac{S}{2\pi} \int k \, dk$, where S is the system area and we have invoked cylindrical symmetry to perform the angular integral. The k integral can be converted into an integral over kinetic energy $\epsilon = \frac{\hbar^2 k^2}{2m}$ by noting that $k \, dk = \frac{m}{\hbar^2} d\epsilon$. This results in the integral

$$I = 2\pi |t|^2 \frac{e}{\hbar} S \left(\frac{m}{\pi\hbar^2} \right) \delta(E_{F,L} - E_{F,U} + eV) \int d\epsilon (f_{\mathbf{k},U} - f_{\mathbf{k},L}). \tag{3.5}$$

By taking the limit $T \ll T_F$, the integral over the Fermi functions $\int d\epsilon (f_{\mathbf{k},U} - f_{\mathbf{k},L})$ reduces to the difference in the Fermi energies $E_{F,U} - E_{F,L}$, which is simply eV. We then arrive at

$$I = 2\pi |t|^2 \frac{e^2}{\hbar} S \rho V \delta (E_{F,L} - E_{F,U} + eV). \tag{3.6}$$

Here, $\rho = \frac{m}{\pi \hbar^2}$ is the density of states for a spin degenerate 2DES. As expected, tunneling is proportional to the square of the tunneling matrix, the system area, and the density of states. The delta function implies that tunneling can only take place at a particular voltage bias, given by $eV = (E_{F,U} - E_{F,L})$. By referencing energies with respect to the minimum subband levels $E_{0,U}$ and $E_{0,L}$, we can express the electrochemical different between the two layers as $eV = (E_{F,U} + E_{0,U}) - (E_{F,L} + E_{0,L})$. Thus, in the clean limit tunneling only occurs when $E_{0,U} = E_{0,L}$. This is equivalent to the statement that the bottoms of the two Fermi seas must coincide. One can arrive at this same conclusion by noting that tunneling must conserve both energy and in-plane momentum. If the dispersion curve $E(k) = \frac{\hbar k^2}{2m} + E_0$ of one layer does not have the same subband energy E_0 as the other, the dispersion curves will not intersect and one will not be able to identify any pairs of states in the two layers with both the same energy and momentum.

3.1.2 Tunneling in the Presence of Weak Disorder

In real systems with disorder, electrons can scatter off of impurities. Through Coulomb interactions, they can also scatter off of other electrons. Consequently, an electron in a particular state with a given energy and momentum will scatter to another state over a characteristic lifetime τ. We can model these scattering processes and finite lifetime through the spectral function $A(E, \mathbf{k})$, which gives the probability that an electron with momentum $\mathbf{k}$ will have energy E. The bilayer systems studied in this thesis have relatively little disorder and thus $A(E, \mathbf{k})$ takes the form of a narrow Lorentzian centered on the single particle energy [138]. The width of the Lorentzian is inversely proportional to the lifetime of the momentum states. We ignore interactions and collective motions so that we can describe the eigenstates of each 2DES as

single electron states. We will also assume that the spectral functions A_U and A_L for each layer only depend on E and $\mathbf{k}$ through the combination $\xi \equiv E - \frac{\hbar k^2}{2m} + E_F$. We will also measure energy with respect to the Fermi energy of either layer.

To account for lifetime broadening in our formula for tunneling, we can rewrite equation (3.3) to include the term $\int \int A_U(E, \mathbf{k}) A_R(E', \mathbf{k}') dE dE'$, where E and E' are the energies for states in layers U and L respectively. By still assuming momentum and spin conservation, we can easily perform the summation over $\mathbf{k}'$, σ, and σ'. After using the energy delta function to perform the integral over E', we get

$$I = \frac{4e\pi}{\hbar} \sum_{\mathbf{k}} |t|^2 \int_{-\infty}^{\infty} A_U(E, \mathbf{k}) A_L(E + eV, \mathbf{k}) \left(f_U(E) - f_L(E + eV) \right) dE. \quad (3.7)$$

When the spectral functions are much narrower than the Fermi energy of either 2DES, we can perform a change in variable to finally arrive at

$$I = 2\pi |t|^2 \frac{e^2}{\hbar} S\rho V \int_{-\infty}^{\infty} A_U(\xi) A_L(\xi + E_{F,L} - E_{F,U} + eV) d\xi. \quad (3.8)$$

Once again, the tunneling current is proportional to $|t|^2$ and ρ. But now the delta function previously seen in equation (3.6) is gone and is replaced by a convolution between the spectral functions of the two 2DESs. Interestingly, there is no dependence on the Fermi distribution functions in equation (3.8); this should hold true for as long as $T \ll T_F$. In that case, temperature can only play a significant role in the spectral functions A_U and A_L. This equation ignores the slight change in $E_{0,L}$ and $E_{0,U}$ due to the capacitive shift in charge when an interlayer bias is applied.

The convolution of two Lorentzians is also a Lorentzian. This allows us to write the tunneling current as

$$I = 2\pi |t|^2 \frac{e}{\hbar} S\rho V \frac{\Gamma/2\pi}{(V - V_0)^2 + \Gamma^2/4}, \quad (3.9)$$

where $eV_0 = E_{F,U} - E_{F,L}$ and Γ is the average of the widths of the spectral functions for the two individual layers. The lifetime of momentum states in either layer is then given by $\tau = 2\hbar/\Gamma$.

The broadening of the electron spectral functions as determined from tunneling has a number of contributions. At zero temperature, it should contain information only about quenched disorder, such as localized scatterers. At elevated temperatures, electron–phonon scattering will come into play. At moderate temperatures ($T \approx 1-10$ K), electron–electron scattering is dominant. Considerations of available phase space leads to the prediction that such electron–electron scattering would have a rate that is proportional to $T^2 \ln T$. Indeed, it has been found by Murphy et al. [85] that the width of the tunneling resonance has roughly parabolic behavior, $\alpha_0 + \alpha_1 T^2$ in the range of $T = 2 - 10$ K. Such electron–electron scattering conserved total momentum and thus is not easily detected by standard resistance measurements. Interlayer tunneling, however, allows one to determine the scattering time τ_{ee} associated with electron–electron scattering at zero magnetic field. The measurements by Murphy *et al.* produced values for τ_{ee} that were found to be in good agreement with calculations based on the random-phase approximation with vertex corrections [62].

3.1.3   Examples of Tunneling Spectra

Here, we present some examples of tunneling traces taken with sample 7-12-99.1JJ at zero magnetic field and $T = 15$ mK. This temperature is so low that the width of the tunneling resonances should reflect only static disorder. The tunneling traces are taken in the usual fashion. A voltage with both an AC (20 μV at 13 Hz) and DC component is applied to an ohmic contact connected to the top layer. The resulting AC tunneling current flowing from a bottom layer contact is measured by a current preamp and a lock-in amplifier. The DC current was not directly measured but can be obtained by numerically integrating the differential conductance dI/dV. This method helps to avoid the noise and signal drifts present in the DC output of the current preamp.

Figure 3.1 demonstrates how the relative densities in the two layers can alter the tunneling spectra. The solid traces show the tunneling conductance dI/dV and DC tunneling current I when the two layers have the same density of $N_L = N_U = 0.558 \times$

10^{11} cm^{-2}. The tunneling conductance trace forms a symmetrical peak centered at zero interlayer bias. Under these conditions, the lowest subband energies of the two layers will line up at zero bias and tunneling is allowed, in accordance with equation (3.6). As suggested by equation (3.9), disorder and sample inhomogeneities has broadened the tunneling resonance from a delta function to a peak with finite width.

The dashed traces in figure 3.1 were taken under the same conditions as the black traces, but the bottom layer was depleted slightly to create a small density imbalance. Based on magnetotransport calibration, this density imbalance is estimated to be $\Delta N \equiv N_U - N_L = 9 \times 10^8$ cm^{-2}. Despite this small difference in the densities of the two layers, the tunneling spectrum has clearly changed. The tunneling conductance resonance has become asymmetric and its peak has shifted to negative bias. This reflects the fact that the subband in the upper layer must be raised in energy in order for it to coincide with the subband in the lower layer and achieve tunneling resonance. The sensitivity of the tunneling spectra to imbalance shows that interlayer tunneling is an excellent tool for balancing the density in the two layers at zero magnetic field. After learning what set of top gate and back gate biases can achieve equal densities in the two layers, one can then use magnetotransport (e.g., Shubnikov–de Haas oscillations in tunneling) to determine the *total* density.

We now turn to zero field tunneling data taken at a range of electron densities, as shown in figure 3.2a. For each trace, the upper and lower layers have the same density. As the total density is reduced, the tunneling peak becomes shorter and broader. This is consistent with a decrease in electron lifetimes due to a greater rate of impurity scattering. At higher densities, these charged impurities (generally thought to exist primarily within the delta doping layer) can be screened by 2DESs. As the 2DESs become depleted, the impurities remain and the disorder that they induce becomes relatively more important to electrons at the Fermi level. This is visible in conventional transport measurements, which in general show that mobility is more or less linearly proportional to density.

To determine the lifetime τ of the electrons, one can fit the tunneling current to
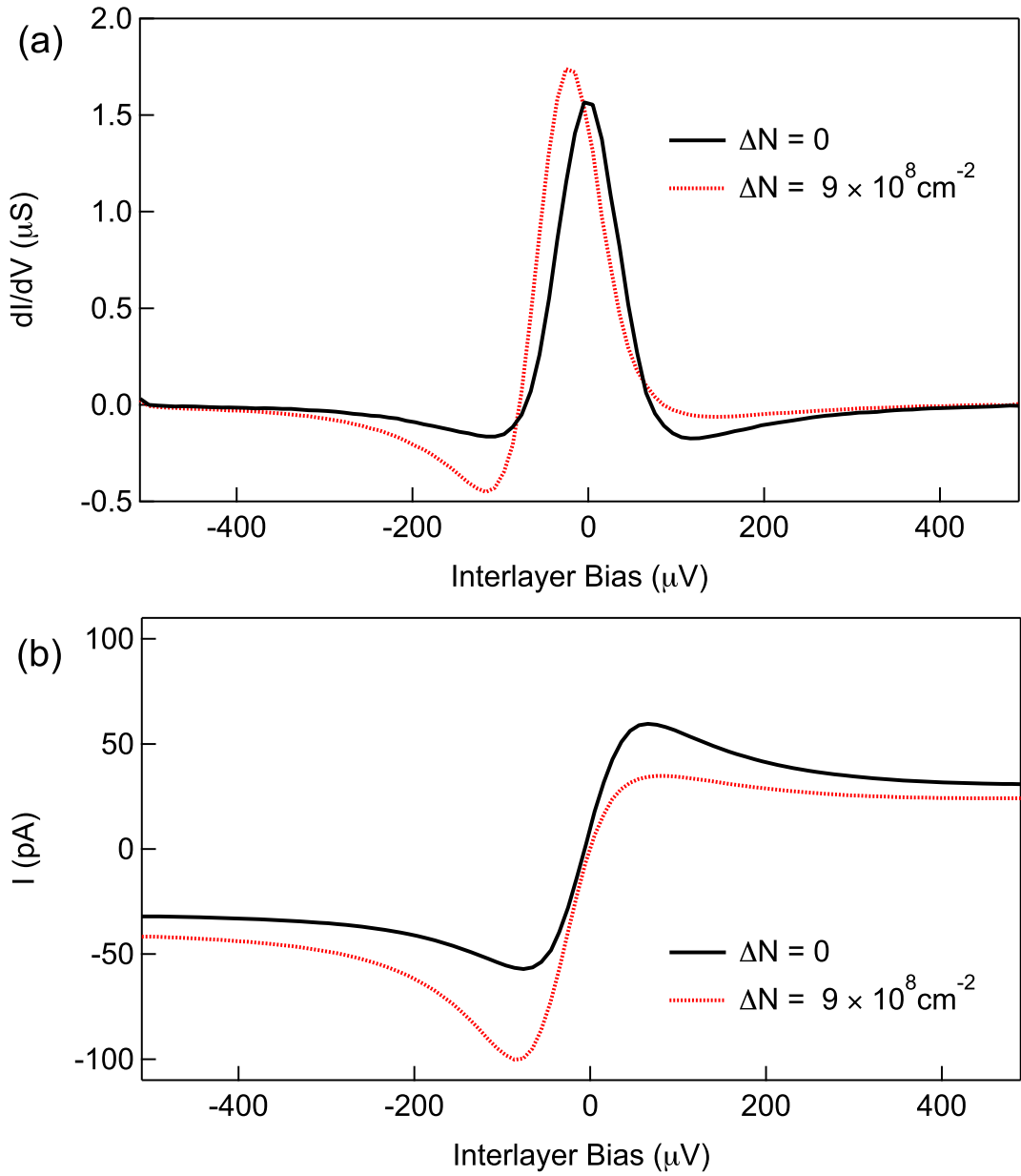
Figure 3.1: (a) Differential tunneling conductance and (b) DC tunneling current (determined by numerically integrating dI/dV) for sample 7-12-99.1JJ at $B = 0$ and $T = 15$ mK. Here, the solid traces corresponds to equal densities in the two layers ($\Delta N = 0$) and the dashed traces corresponds to a slight density imbalance ($\Delta N = 9 \times 10^8$ cm^{-2}). Here, $\Delta N = N_U - N_L$ and the density in the upper layer is kept at $N_U = 0.558 \times 10^{11}$ cm^{-2}.
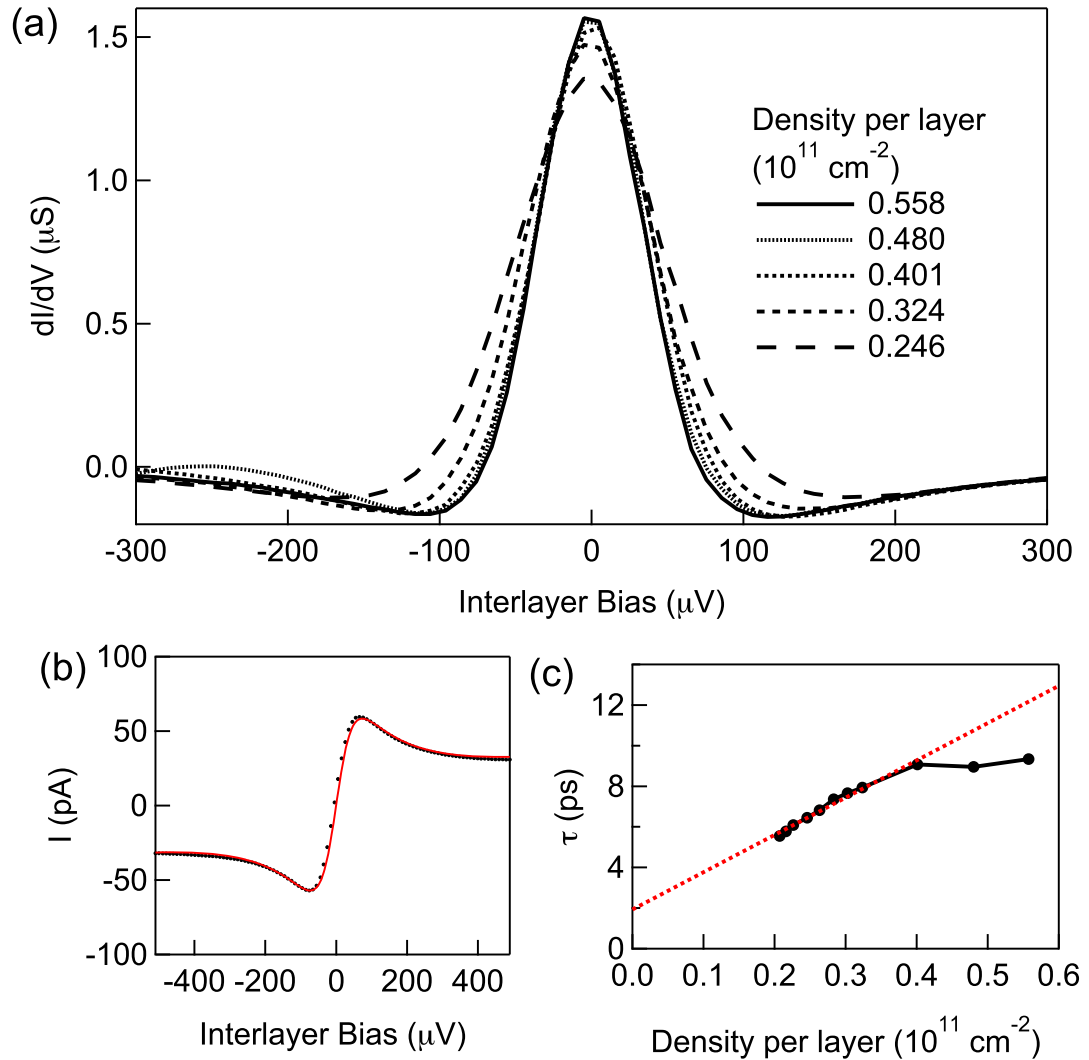
Figure 3.2: (a) Tunneling conductance versus interlayer bias for various densities. In each case, the two layers have equal density. (b) DC current versus interlayer bias at $N_U = N_L = 0.558 \times 10^{11}$ cm^{-2}. The dots come from numerically integrated measured dI/dV while the solid trace is a fitted curve. (c) Electron lifetime τ determined from width of tunneling resonance versus density in each layer. The dashed line is a fit to the linear portion of τ versus density.

equation (3.9). Here, one must also include a linear correction $\alpha_1 + \alpha_2 V$ to account for as yet unknown background sources of conductance in this rather large sample.[1] An example of such a fit is shown in figure 3.2b. After finding Γ from the fit, we then plot $\tau = 2\hbar/\Gamma$ versus density in figure 3.2c. The relation between electron lifetime and density does not seem to be precisely linear, as shown in the dashed line fitted to all but the highest two densities. One possibility is that some other mechanism (such as fringe fields) is limiting the apparent electron lifetimes at high density, where impurity scattering might be less prominent than other forms of disorder. Finally, we note that the lifetimes determined from tunneling are far smaller than the lifetime derived from mobility ($\tau \approx 40$ ps at nominal density). A likely explanation for this discrepancy is that measurements of mobility based on resistivity are not as sensitive to small-angle scattering as tunneling measurements are.

3.2 Interlayer Capacitance

We now consider the capacitive coupling between the two 2DESs in a bilayer system. This coupling can contain information about the thermodynamical properties of 2DESs. Furthermore, knowledge of some of the principles introduced in this section will help us understand how a bilayer can behave under conditions of density imbalance. Such behavior can be greatly affected by interactions at low density and high magnetic fields, which are the characteristic conditions used to study the $\nu_T = 1$ bilayer QHE.

3.2.1 Basic Theory

Interlayer capacitance reflects the energy cost for transferring charge from one layer to the other. One must account for not only the energy in the electrical fields generated by interlayer charge transfer, but also the change in energy of the 2DESs themselves. Consequently, the total capacitance C_{total} takes the form:

---

[1] The active tunneling region of sample 7-12-99.1JJ is approximately 750,000 μm^2.

$$\frac{1}{C_{total}} = \frac{1}{C_g} + \frac{1}{C_q}, \tag{3.10}$$

where $C_g = \epsilon S/d$ is the geometric capacitance and C_q is known as the quantum capacitance. We denote the dielectric constant of the insulating behavior as ϵ. The geometric capacitance is classical in origin and can be found using standard electrostatic theory. The quantum capacitance, however, reflects the fact that the 2DESs are Fermi systems with a finite compressibility; i.e., one must pay a price in energy to add an electron to either 2DES (for example, see reference [79]).

We first consider the general case of applying an interlayer voltage V to a bilayer system with interlayer separation d. We will assume that we can write the total energy of the bilayer system (i.e., the sum of the kinetic and interaction energies of the electrons) in the form $E_{bilayer}(N_T, \Delta N)$, where $N_T = N_U + N_L$ is the total number of electrons and $\Delta N = N_U - N_L$ is the difference in population between the two layers. In this case, the total energy of the system will be equal to the sum of three terms: the energy in the electric field between the two layers,[2] the energy of the bilayer system $E_{bilayer}$, and the classical potential energy of the charges residing in the two layers. We write this as

$$E_{total} = E_{field} + E_{bilayer} + \sum Q_i V_i, \tag{3.11}$$

where Q_i is the charge of layer i and V_i is the electrostatic potential of layer i.

The energy of the field is given by $E_{field} = \int \left(\frac{\epsilon}{2}\vec{E} \cdot \vec{E}\right) d^3r = \frac{de^2}{2S\epsilon}(\Delta N)^2$. The potential energy term is given by $\sum Q_i V_i = -e(N_U \frac{V}{2} - N_L \frac{V}{2}) = -\frac{e}{2}V(\Delta N)$. This gives us

$$E_{total} = \frac{de^2}{2S\epsilon}(\Delta N/2)^2 + E_{bilayer}(N_T, \Delta N) - \frac{e}{2}V(\Delta N). \tag{3.12}$$

Upon applying an interlayer voltage, one expects the total number of electrons to stay the same, but some charge $Q = e(\Delta N)/2$ will transfer from one layer to another

---

[2]Here we will ignore the possibility of fields extending beyond the bilayer system. This should be a good approximation if the interlayer separation is much smaller than the separation between the bilayer system and either the top or bottom gates.

layer. To find the resulting ΔN, we minimize E_{total} with respect to ΔN. By insisting that $\frac{\partial E_{total}}{\partial(\Delta N)} = 0$, we can find that

$$\frac{1}{C_{total}} \equiv \frac{V}{\frac{e}{2}(\Delta N)} = \frac{d}{S\epsilon} + \frac{4}{e^2}\frac{1}{(\Delta N)}\frac{\partial E_{bilayer}}{\partial(\Delta N)}. \tag{3.13}$$

In a classical bilayer system the $E_{bilayer}$ term is absent and the above equation would read

$$\frac{1}{C_{total}} = \frac{S\epsilon}{d}, \tag{3.14}$$

which is gives the expected capacitance for a parallel plate capacitor. Thus, we can now understand how the total capacitance C_{total} can be found by considering the geometric and quantum capacitances (the second term in equation (3.13)) to be connected in series with one another.

3.2.2 Special Case: Two Fermi Seas of Noninteracting Electrons

We will now use equation (3.13) to examine the simple case of a bilayer system consisting of two Fermi seas of noninteracting electrons at $T = 0$. We will neglect the influence of band-bending induced by changes in the space charge density. The total kinetic energy of a Fermi sea with N spin-degenerate electrons is $\frac{\pi\hbar^2}{2m^*}\frac{N^2}{S}$, where m^* is the effective mass. We can then express $E_{bilayer}$ as

$$\begin{aligned} E_{bilayer} &= \frac{\pi\hbar^2}{2m^*S}(N_1^2 + N_2^2) \\ &= \frac{\pi\hbar^2}{4m^*S}(N_T^2 + (\Delta N)^2). \end{aligned} \tag{3.15}$$

Thus, $\frac{\partial E_{bilayer}}{\partial(\Delta N)} = \frac{\pi\hbar^2}{2m^*S}(\Delta N)$ and equation (3.13) gives

$$\frac{1}{C_{total}} = \frac{d}{S\epsilon} + \frac{2\pi\hbar^2}{e^2 m^*S}. \tag{3.16}$$

Because the quantum capacitance is positive in this case, we expect that it will reduce the total capacitance from its purely classical value.

3.2.3   Compressibility and Interactions

Up until now we have ignored electron–electron interactions. Using the Hartree-Fock approximation, interactions can be treated by including both a Hartree term and exchange term for the bilayer energy $E_{bilayer}$ [93]. While the total Hartree term is positive and proportional to $(\Delta N)^2$, the exchange term for either layer is negative and proportional to $-(N_i)^{3/2}$. This negative exchange contribution to the compressibility of the 2DES has been measured by Eisenstein et al. [28, 29] by detecting the electric field penetrating a single 2DES. Such a method bypasses the geometric capacitance and directly reveals the *single-layer* compressibility $\frac{\partial E}{\partial N_i}$. The negative exchange energy is expected to influence interlayer capacitance by lowering the total energy cost of transferring charge from one layer to another.

At high magnetic fields, the large degeneracy of the Landau levels will quench the kinetic energy term in $E_{bilayer}(N_T, \Delta N)$. Interaction effects will become more important. As we will see in a later chapter, an instability similar in nature to the one proposed by Ruden and Wu [93] can occur within highly imbalanced bilayer systems at large magnetic fields. In that particular case, the exchange-driven instability causes an unexpectedly large number of electrons to transfer from one layer to another.

Thus, capacitance measurements can reveal interesting physics at $\nu_T = 1$. Due to excitonic effects, one expects that charge can transfer more easily from one layer to another. Consequently, one might anticipate anomalies in the temperature dependence of interlayer capacitance at $\nu_T = 1$ (for example, see reference [8]). Once again, the geometric contribution complicates the interpretation of interlayer capacitance measurements. The next subsection will consider these issues and provide suggestions for future measurements of interlayer capacitance at $\nu_T = 1$.

3.2.4 Measurements of Interlayer Capacitance

Here we will show some measurements of the interlayer capacitance, both with and without a magnetic field. First, we will briefly describe our measurement technique. Then we will present measurements of interlayer capacitance versus electron density at $B = 0$. Finally, we will consider the influence of a magnetic field on the interlayer capacitance.

Measurements of interlayer capacitance essentially use the same circuit as in tunneling. An AC voltage (usually 20 μV and 13 Hz) is applied to one layer and the resulting current from the other layer is measured with a current preamp and lock-in amplifier. In the limit of zero sheet resistance, one then expects the total conductance to be $G_{total} = G_{tunneling} + i\omega C$, where $G_{tunneling}$ is the tunneling conductance and ωC is the capacitive admittance. Thus, the out-of-phase current is proportional to the interlayer capacitance. So long as sheet resistance is not too large compared with $1/|G_{total}|$, the presence of tunneling is not expected to significantly affect the capacitance measurement because the tunneling currents and displacement currents effectively flow in parallel with one another.

A major concern in capacitance measurements is the presence of background capacitance. For example, there might be stray capacitance between the measurement wires. The use of independently shielded coax wires helps to strongly reduce this stray capacitance, which can often be of order $\sim$1 nF for the meters-long pairs of twisted wires commonly employed in cryostats.

Another source of background capacitance is within the bilayer system itself. Our samples generally have both gated and ungated regions, with the gated regions being of central interest during measurements. For tunneling measurements, the ungated regions usually provide only a small amount of background tunneling because they are either imbalanced (which suppresses tunneling near zero bias at $B = 0$) or not at $\nu_T = 1$ (and thus do not tunnel strongly at high magnetic fields). However, such ungated regions can still provide interlayer capacitive coupling despite their imbalanced state. Furthermore, the capacitance from the ungated regions is generally

not suppressed at high magnetic fields. Most annoyingly, this background signal can vary significantly with magnetic field as the ungated regions enter and leave incompressible QH states.

Fortunately, one can measure the background signal from the ungated regions with a special geometry. In figure 3.3a we show the topside of sample 11-1-04.1M. The geometry for this sample was created through improvised use of a variety of photolithography masks intended for other types of samples, hence its unusual appearance. Here, we have defined a central mesa with ohmic contacts, top and bottom arm gates for selective depletion, and a main gated region in the center of the photograph. Normally the mesa pattern used has four arms leading to the central region. However, we performed an additional etch to completely remove the bilayer 2DES in the two right arms. Thus, the bilayer 2DES only consists of two arms (with one ohmic contact each) leading to the main gated region.

We show a simplified drawing of the sample in figure 3.3b. The black dots denote ohmic contacts. The grey rectangles are the top and bottom arm gates that implement the selective depletion scheme. The hatched square shows the approximately $275 \times 200 \ \mu m^2$ region of the sample that is covered by the main top gate. The clear section symbolizes the ungated regions, which are not covered by the main top gate but might partially be depleted by the main bottom gate.

The geometry depicted in 3.3b allows one to directly measure the background capacitance signal from the ungated regions. To do this, one first performs a capacitance measurement while the main top and bottom gates are tuned to the desired biases. This will result in a capacitance signal containing the interlayer capacitance from both the gated and ungated regions. One then applies a large negative bias to the main top gate, depleting the gated region. But the ungated regions are essentially left undisturbed. By repeating the same capacitance measurement, one then directly measures the interlayer capacitance in the ungated regions alone. Subtracting the second measurement from the first results in the desired capacitance of only the gated region.

There is a small amount of error in this subtraction process due to the influence
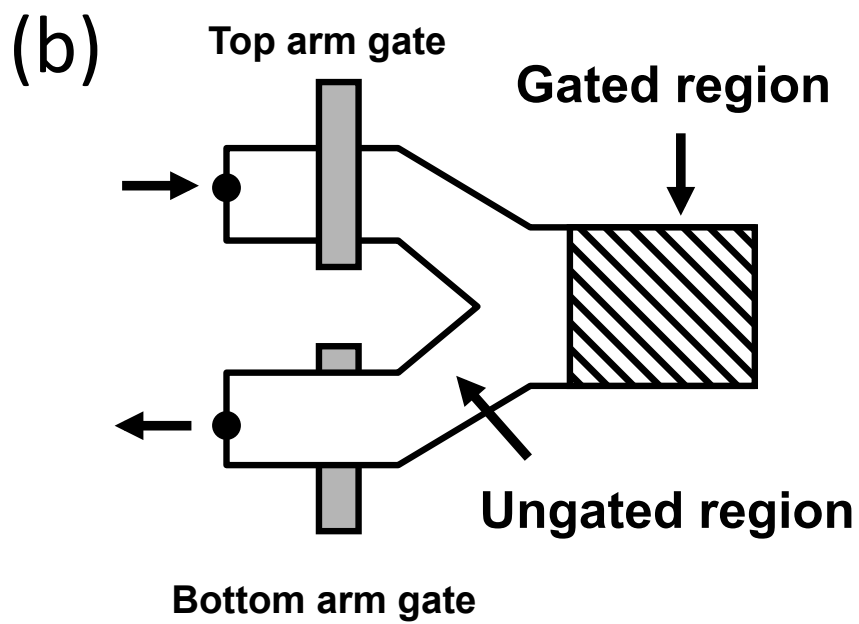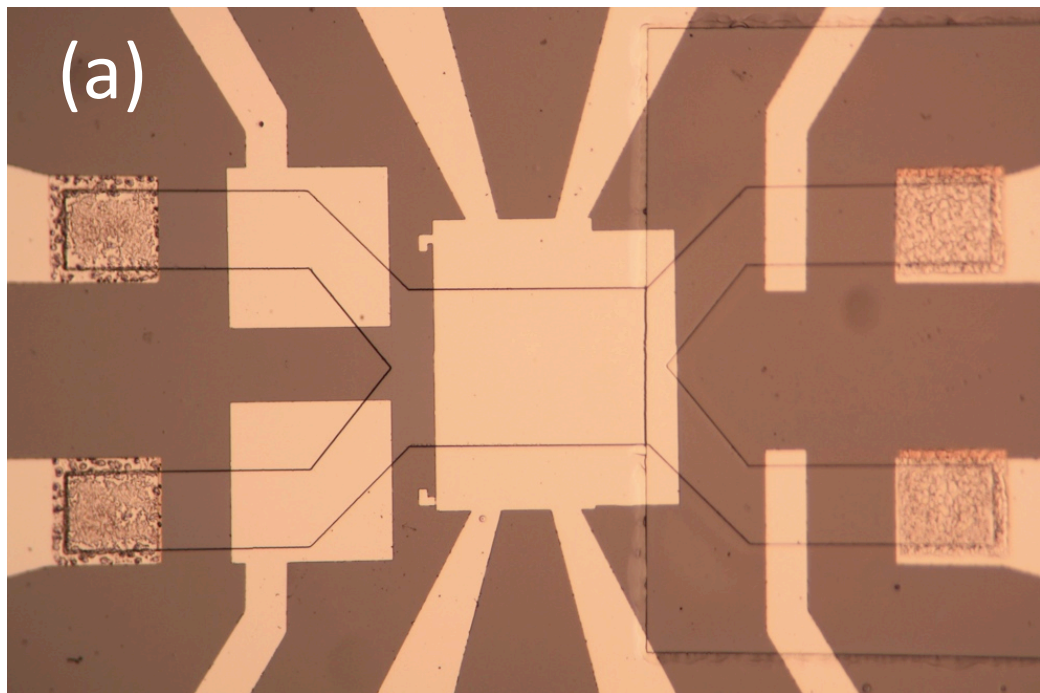
Figure 3.3: a) Top side photograph of sample 11-1-04.1M. The rightmost portions of the bilayer 2DES has been etched away. b) Schematic of sample 11-1-04.1M, showing gated and ungated regions. The gated region is approximately $275 \times 200 \ \mu m^2$.

of fringe fields from the top gate at the boundary between the gated and ungated region. We have demonstrated this by studying samples where the interface region has been shortened by reducing the width of the mesa at the boundary between the gated and ungated regions. Doing so eliminated certain anomalies associated with the determination of the capacitance signal from the gated region.

We now consider measurements of the capacitance of the gated region versus density at zero field and $T = 0.3$ K. Here, we adjust the biases for the main top and bottom gates to tune the total density but keep the densities in the two layers equal. As seen in figure 3.4a, the interlayer capacitance grows by 15% as the electron density in each 2DES is reduced from its nominal value of $\sim 0.508 \times 10^{11}$ cm^{-2} per layer to $\sim 0.2 \times 10^{11}$ cm^{-2} per layer. The capacitance from all background sources has already been subtracted off as explained above. We found that $C_{background} = 93$ pF for all studied 2DES densities.

One possibility for the observed increase of interlayer capacitance is that as density decreases, there is an enhanced influence of exchange effects, which can increase the interlayer capacitance by decreasing the value of the $\frac{\partial E_{bilayer}}{\partial(\Delta N)}$ term in equation (3.13).

Another possibility is that the geometric capacitance is changing in response to the alteration of charge density. As a bias is applied to the main top and bottom gates, the electron density in each layer decreases, but the background positive charge within the quantum wells remains the same. Consequently, each layer becomes more positively charged at lower carrier density. According to Gauss's law, the second spatial derivative of the electrostatic potential $\frac{d^2V}{dz^2}$ within a given quantum well is proportional to the net charge density within that well. Thus, when one depletes the bilayer system, one expects that the bottoms of the quantum wells will become more curved. These changes in quantum well shape could ultimately move the subband wave functions closer together as one depletes the two layers, leading to a reduced center-to-center separation d between the two 2DESs and thus an increase in the geometric capacitance.

The interlayer capacitance can be numerically estimated using a self-consistent Poisson-Schrödinger solver similar to the one described in reference [29]. By solving

both the Poisson equation for the electrostatic potential and the Schrödinger equations for the subband wave functions, we can predict how much charge shifts from one layer to another in response to a 1 mV applied interlayer bias. This numerical solution includes exchange and correlation effects using a local density approximation (LDA), in which the exchange and correlation energies are assumed to be purely a function of the local carrier density. Here, we use the Hedin-Lundqvist [52] functional for exchange and correlation energies.

The ratio of the interlayer charge transfer to the applied bias gives the expected capacitance for a particular total electron density in the bilayer system. In figure 3.4a, the dashed line represents this theoretical prediction. The entire theoretical curve has been rescaled somewhat so that it coincides with the observed capacitance at the density of $N = 0.5 \times 10^{11}$ cm^{-2} per layer. Without this rescaling, the numerical solver predicts $C = 230$ pF at this density; the source of this discrepancy is unknown. It could reflect various uncertainties in the barrier thickness, effective area of the gated region, or the effective dielectric constants of the barrier and quantum wells. Nonetheless, by multiplying the original theoretical curve by correction factor $\frac{180}{230}$, one can see that the resulting theoretical curve in figure 3.4a follows the observed data quite well for the entire range of studied densities.

Figure 3.4a should serve as a warning that one must be careful when performing interlayer capacitance measurements at $\nu_T = 1$. One generally acquires transport data at $\nu_T = 1$ for various values of the effective interlayer separation d/ℓ. In our bilayers, we tune d/ℓ by changing the density such that ℓ is altered. However, if one wants to measure interlayer capacitance at $\nu_T = 1$, one must be aware that the center-to-center distance d between the subband wave functions is likely to be density dependent. Thus, the geometric capacitance will evolve with d/ℓ as well. To mitigate this problem, one might focus on measurements of interlayer capacitance at fixed d/ℓ but varying temperature. This would keep the geometric capacitance constant but would use thermal fluctuations to disrupt the $\nu_T = 1$ and alter the interlayer compressibility alone.

Finally, we turn to the capacitance data taken at high magnetic fields, plotted
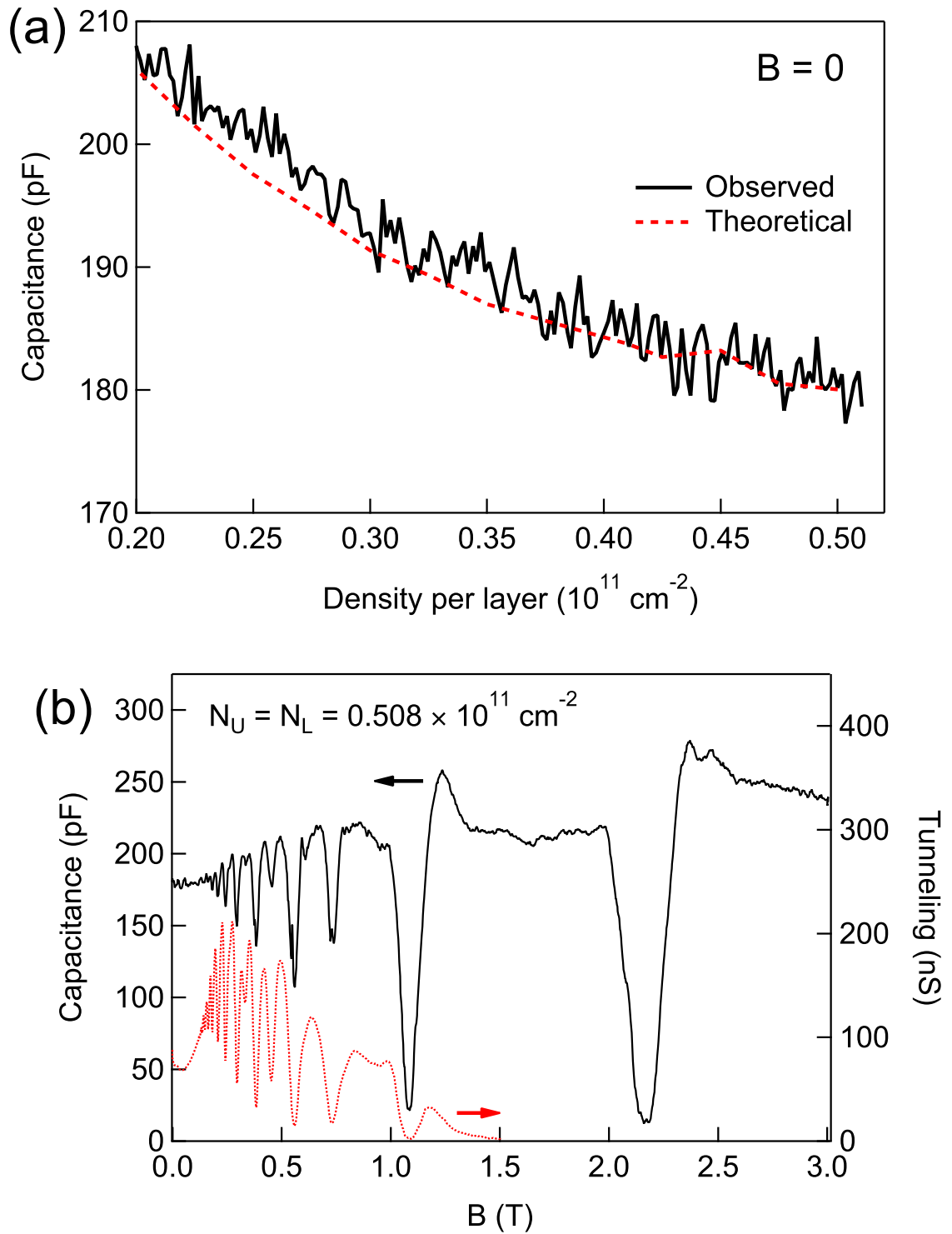
Figure 3.4: (a) Capacitance of gated region versus density at $B = 0$ and $T = 0.3$ K. Solid trace is observed data and the dashed line is the theoretical curve.
(b) Capacitance (solid trace) and tunneling conductance (dotted trace) of gated region versus magnetic field at $T = 0.3$ K. The bilayer is balanced at a density of $N = 0.508 \times 10^{11}$ cm^{-2} per layer.

in figure 3.4b. Here, each layer has a density of $N = 0.508 \times 10^{11}$ cm^{-2} and $T = 0.3$ K. One can see Shubnikov–de Haas oscillations, with clear minima each time the individual layers enters a quantum Hall state. For comparison, the interlayer tunneling conductance at the same density for up to $B = 1.5$ T is plotted as a dotted line. The reduction in C during a quantum Hall state in the individual layers is due to the combined effects of diminished compressibility and vanishing sheet conductance σ_{xx}. Unfortunately, σ_{xx} cannot be directly measured in this device, which contains only two contacts and precludes four-terminal transport measurements of ρ_{xx} and ρ_{xy}. Interestingly, interlayer capacitance does not completely vanish at $\nu_T = 2$ or $\nu_T = 4$, where the QH states are well formed and $\sigma_{xx} = 0$. Also note that in between the QH dips, the interlayer capacitance assumes a value that is larger than the zero field capacitance. This is consistent with the formation of highly degenerate Landau levels, which is expected to increase the compressibility of the individual 2DESs at high magnetic fields.

3.3   Conclusion

In this chapter, we have discussed the physics of interlayer tunneling at $B = 0$ and how it reflects the conservation of in-plane momentum. While one would expect singular behavior in the tunneling current without any disorder, various scattering mechanisms shorten the lifetime of electron states and lead to the experimentally observed broadening of the tunneling resonance. We have also considered how measurements of interlayer capacitance can reveal the energy cost $\frac{\partial E_{bilayer}}{\partial (\Delta N)}$ for transferring electrons from one 2DES to another. While we anticipate that the interlayer compressibility could be strongly altered at $\nu_T = 1$, we demonstrated through measurements of interlayer capacitance at zero field that the effective interlayer separation might change with total density. Thus, one must analyze interlayer capacitance measurements carefully to account for changes in the geometric capacitance. Alternatively, we might probe changes in the interlayer compressibility at $\nu_T = 1$ at fixed density but at variable temperature. Thus, geometric capacitance will remain constant, but thermal

fluctuations will alter interlayer compressibility.

Chapter 4

Phase Transition and Zeeman Energy

In the absence of interlayer tunneling, the $U(1)$ pseudospin symmetry is spontaneously broken within the $\nu_T = 1$ quantum Hall state. This suggests that there is a phase transition between the correlated quantum Hall regime and uncorrelated compressible regime. Indeed, as d/ℓ is raised beyond a critical value $(d/\ell)_c$, the characteristic transport properties of $\nu_T = 1$ (including enhanced interlayer tunneling and large Coulomb drag) disappear and the two layers eventually behave as two independent systems of composite fermions. Similar behavior is observed when d/ℓ is held fixed and temperature is instead increased. However, the nature of the phase transition is not understood.

In this chapter, we explore how the phase boundary between the correlated and uncorrelated phases evolves with Zeeman energy. This is motivated by previous studies that found evidence of a change in spin polarization across the phase boundary [106, 71, 42], suggesting that spin could play a role in the phase transition. This also leads to the question of how the phase transition might change when both phases are fully spin polarized. Here, we probe the phase transition by studying Coulomb drag in the presence of an in-plane magnetic field, which increases the Zeeman energy without changing the Landau filling factor. We find that when the Zeeman energy is large enough to fully spin polarize the uncorrelated phase, the phase transition as function of d/ℓ becomes dramatically broader than in the regime of low Zeeman en-

ergy. We interpret this finding using two different models in which both the correlated and uncorrelated phases are present during the phase transition.[1]

4.1 Nature of the Phase Transition

4.1.1 Overview

The nature of the phase transition between the correlated and uncorrelated phases at $\nu_T = 1$ is not well understood. Originally, a Kosterlitz-Thouless (KT) transition at finite temperature was anticipated [125, 131, 82] due to the XY universality class of the correlated regime. In this picture, the disappearance of bilayer transport anomalies would be governed by the unbinding of vortices in the order parameter at a characteristic temperature T_{KT}. This finite temperature phase transition would distinguish the $\nu_T = 1$ system from other quantum Hall systems, which only possess a $T = 0$ phase transition. Indeed, tunneling measurements near the phase boundary suggest a phase transition occurs at finite temperature [12]. However, measurements of counterflow dissipation show an activated behavior instead of the predicted discontinuity at a finite temperature for a KT transition [66]. The expected nonlinear superfluid response is also absent.

Alternatively, numerical studies have suggested a weakly first-order phase transition [95]. Measurements of Coulomb drag as a function of d/ℓ, however, reveal a rapid but smooth transition between the two phases [65]. This finite width of the phase transition might be due to disorder, which can cause the system to break up into spatially separated regions of correlated and uncorrelated fluids [108]. Another possibility is that the transition is a continuous crossover, during which the system is comprised of coexisting composite fermion and composite boson phases [100]. These two views of the phase boundary will be discussed in greater detail later on in this chapter.

---

[1]This chapter contains work first presented in A. D. K. Finck, J. P. Eisenstein, L. N. Pfeiffer, and K. W. West, *Phys. Rev. Lett.* **104**, 016801 (2010). Copyright 2010 by the American Physical Society.

4.1.2 Spin Transition

We now consider the spin transition as the system evolves between the correlated and uncorrelated regimes. Exchange interactions should favor full spin polarization in the correlated phase. However, the uncorrelated phase is only partially spin polarized at the low magnetic fields typically employed for low density bilayers at $\nu_T = 1$. This incomplete polarization has been observed in single-layer 2DESs [118, 75] and reflects a low Zeeman energy relative to the Fermi energy of the composite fermions, which is governed by the Coulomb energy. Thus, spin polarization changes across the phase boundary; this has been experimentally demonstrated. For example, Spielman and collaborators used NMR and heat pulses to depolarize nuclear spins and thus induce small increases in the Zeeman energy through the hyperfine coupling [106]. They found that such techniques enhanced the $\nu_T = 1$ tunneling near the phase boundary. An increase in the Zeeman energy could even lead to the appearance of a tunneling peak under conditions $(d/\ell > (d/\ell)_c)$ where ordinarily no tunneling anomaly was observed. Thus, $(d/\ell)_c$ can be tuned via Zeeman energy due to this difference in spin polarization of the two phases. Another study by Kumada and collaborators also detected this spin transition by observing an increase in the nuclear-spin-relaxation rate $1/T_1$ as they moved from the quantum Hall phase to the compressible phase [71]. Spielman *et al.* reported seeing similar behavior in $1/T_1$.

While the difference in spin polarization of the two phases allows us to shift the position of the phase boundary by tuning the Zeeman energy, one might wonder if the phase transition might qualitatively change if the Zeeman energy is large enough to fully spin polarize the uncorrelated phase. Such large increases in Zeeman energy can be realized by tilting the sample with respect to the magnetic field, allowing an increase in the total field (and thus Zeeman energy) while keeping the perpendicular field constant.

However, the Josephson-like tunneling at $\nu_T = 1$ is suppressed by the parallel field introduced by this method [104]; thus, one must resort to alternative probes of the phase boundary. For example, Giudici and collaborators utilized parallel transport

measurements to determine the presence of an incompressible quantum Hall state (i.e., the existence of a visible minimum in R_{xx}) at $\nu_T = 1$ [42]. They observed the expected increase in $(d/\ell)_c$ as they tilted the sample with respect to the magnetic field and approached the point where the uncorrelated phase was presumed to be fully spin polarized. However, they reported no qualitative change in the phase boundary.

4.2 Evolution of Phase Boundary with Zeeman Energy

4.2.1 Coulomb Drag and the Phase Boundary

In this chapter, we seek to explore the phase boundary as it evolves with Zeeman energy through measurements of Coulomb drag in the presence of a parallel magnetic field. Coulomb drag is a convenient probe of the phase boundary. Not only is it robust in the presence of a parallel magnetic field [67], it provides a direct measurement of interlayer correlations that are specific to the $\nu_T = 1$ phase. Coulomb drag also has a characteristic behavior across phase boundary. As the system passes from the uncorrelated to the correlated regime, a steady rise in Hall drag $R_{xy,D}$ is observed until it reaches a quantized value of h/e^2 deep within the correlated regime. This remarkable behavior is unexpected because no current is permitted to flow through the drag layer and thus no Lorentz force should exist to provide a Hall resistance. Ultimately, this reflects strong interlayer correlations that are far beyond the regime of perturbation theory. Meanwhile, the longitudinal drag $R_{xx,D}$ rises up to form a peak in the middle of the phase boundary and then drops to nearly zero in the correlated regime [65]. While there are various models [108, 100] to explain the observed peak in $R_{xx,D}$, for the purposes of this chapter it is sufficient to adopt the convention of identifying the position of the peak with the critical interlayer separation $(d/\ell)_c$. We also use the full width of the peak at its half-maximum points (FWHM) to define a characteristic width $\Delta(d/\ell)$ of the phase transition.

4.2.2   Sample and Methods

In this chapter, we study data collected from sample 7-12-99.1R. It was fabricated by Ian Spielman from a wafer having the usual GaAs/AlGaAs double quantum well structure consisting of two 18 nm GaAs quantum wells separated by a 10 nm $Al_{0.9}Ga_{0.1}As$ barrier. Consequently, the center-to-center separation of the 2DESs in the quantum wells is $d = 28$ nm. The 2DESs have a nominal density of $n \approx 5.5 \times 10^{10}$ cm^{-2} per layer and a low temperature mobility of $\mu \approx 1 \times 10^6$ cm^2/Vs. Using standard photolithographic techniques, a mesa is defined with a 250 μm square central region. Four narrow arms extend from the square (one from each side) to diffused NiAuGe ohmic contacts. Thermally evaporated aluminum top and bottom gates allow us to independently tune the density of the upper and lower layers within the central region. Throughout this chapter, we confine our attention to the case of equal densities in the two layers. Additional aluminum gates deposited on top of and beneath the arms allow us to selectively connect each NiAuGe ohmic contact to one, both, or none of the layers. The tunneling conductance in this sample is small (the peak tunneling is ~29 nS at zero magnetic field) such that even at $\nu_T = 1$ little current can leak between the two layers. For example, the maximum tunneling current at $\nu_T = 1$ for the lowest d/ℓ and lowest T studied is ~15 pA. This is only 3% of the drive current (0.5 nA) employed during drag measurements. Thus, tunneling is expected to play an insignificant role in Coulomb drag.

4.2.3   Hall Drag and Longitudinal Drag versus d/ℓ

We first focus on data taken at low temperatures (30 - 50 mK). Figure 4.1 shows $R_{xy,D}$ and $R_{xx,D}$ at $\nu_T = 1$ versus d/ℓ at two different tilt angles. Recall that we tune d/ℓ in our sample by changing the total density N_T of the bilayer system and adjusting the perpendicular magnetic field (and thus the magnetic length $\ell = \sqrt{\frac{\hbar c}{eB_\perp}}$) to achieve $\nu_T = 1$. The first data set was obtained when the applied magnetic field was perpendicular to the bilayer system ($\theta = 0$). It matches previously reported results at zero tilt angle [65]. Here, the phase transition is relatively narrow, with

$\Delta(d/\ell) \approx 0.025$.

The second set was collected when the sample was tilted to $\theta = 66°$ with respect to the magnetic field. As we will show below, the uncorrelated phase is fully spin polarized at this tilt angle. In the large Zeeman regime, the phase transition has clearly changed in two ways. First, the center of the phase boundary has shifted to a higher value of d/ℓ, from $(d/\ell)_c \approx 1.75$ to $(d/\ell)_c \approx 1.85$. This is consistent with previous reports that increasing the Zeeman energy will increase $(d/\ell)_c$ [106, 42]. Second, the width of the phase boundary is significantly larger than at $\theta = 0$, obtaining a value of $\Delta(d/\ell) \approx 0.086$. This broadening is visible in both the Hall and longitudinal Coulomb drag measurements and constitutes the main finding of this chapter.

4.2.4 Longitudinal Drag versus d/ℓ and η

We can see more clearly how the phase transition evolves with Zeeman energy in figure 4.2. Here, we show a color plot of longitudinal drag $R_{xx,D}$ at $\nu_T = 1$ and $T = 50$ mK versus both d/ℓ and the normalized Zeeman energy $\eta \equiv E_Z/(e^2/\epsilon\ell)$. We construct this plot from measurements of $R_{xx,D}$ versus d/ℓ at nine different tilt angles, ranging from $\theta = 0$ to $\theta = 66°$. Examples of such traces were already shown in figure 4.1. By fixing angle and tuning d/ℓ, we trace out a straight-line trajectory in $(d/\ell, \eta)$ space with a slope proportional to $\cos\theta$. For each tilt angle, we mark the center of the phase transition with a black dot on the graph. The bottom portion of the plot is the correlated quantum Hall phase while the top is the uncorrelated compressible phase.

A number of features are visible in figure 4.2. First, as we tilt the sample with respect to the magnetic field, the center of the phase transition initially moves toward higher d/ℓ. This is consistent with the increased Zeeman energy stabilizing the correlated phase with respect to the uncorrelated phase, leading to a larger critical interlayer separation $(d/\ell)_c$. Eventually, the large Zeeman energy will fully spin polarize the competing uncorrelated phase. One would then expect $(d/\ell)_c$ to remain
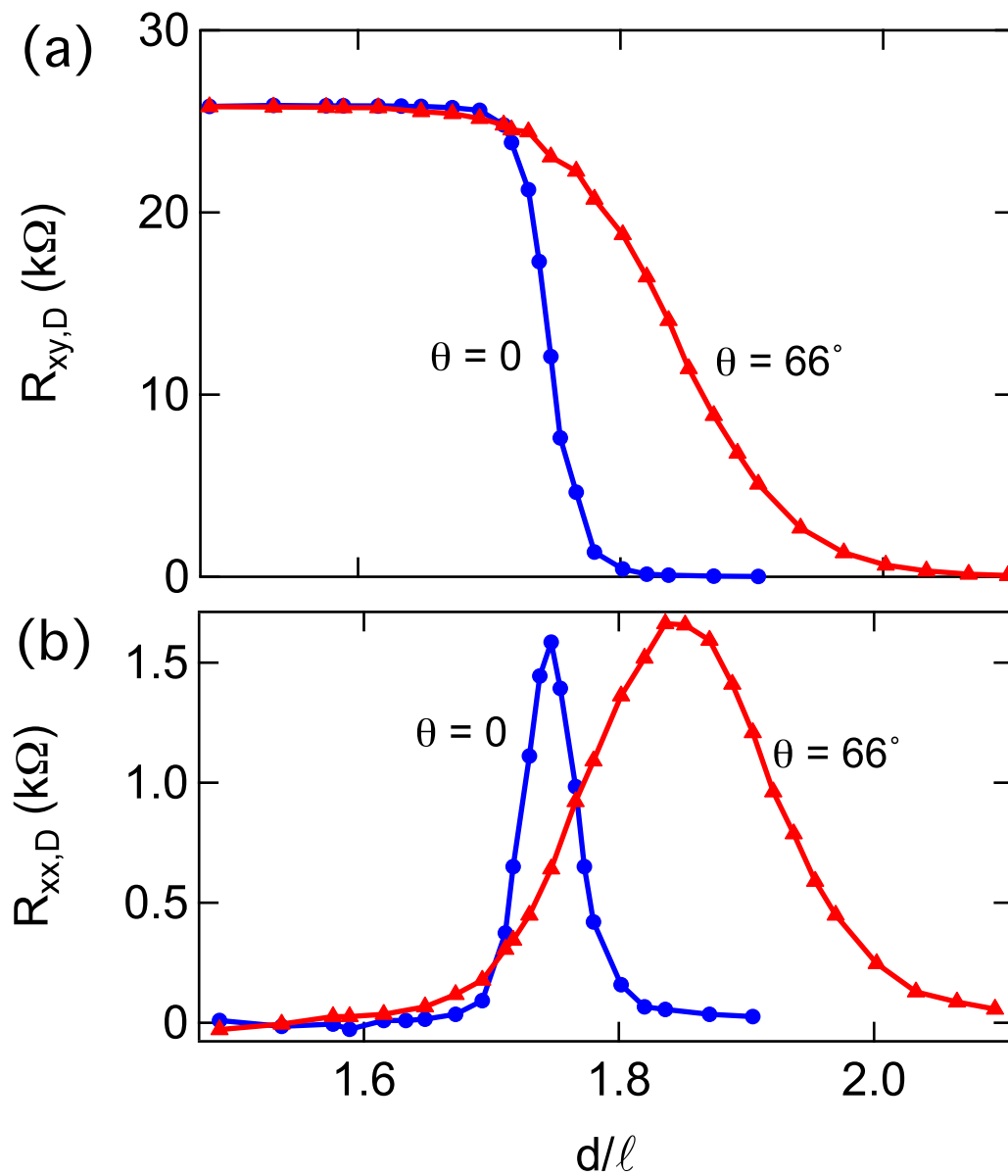
Figure 4.1: (a) Hall and (b) longitudinal Coulomb drag at $\nu_T = 1$ versus d/ℓ at $T = 30$ mK. dots, $\theta = 0$; triangles, $\theta = 66°$.
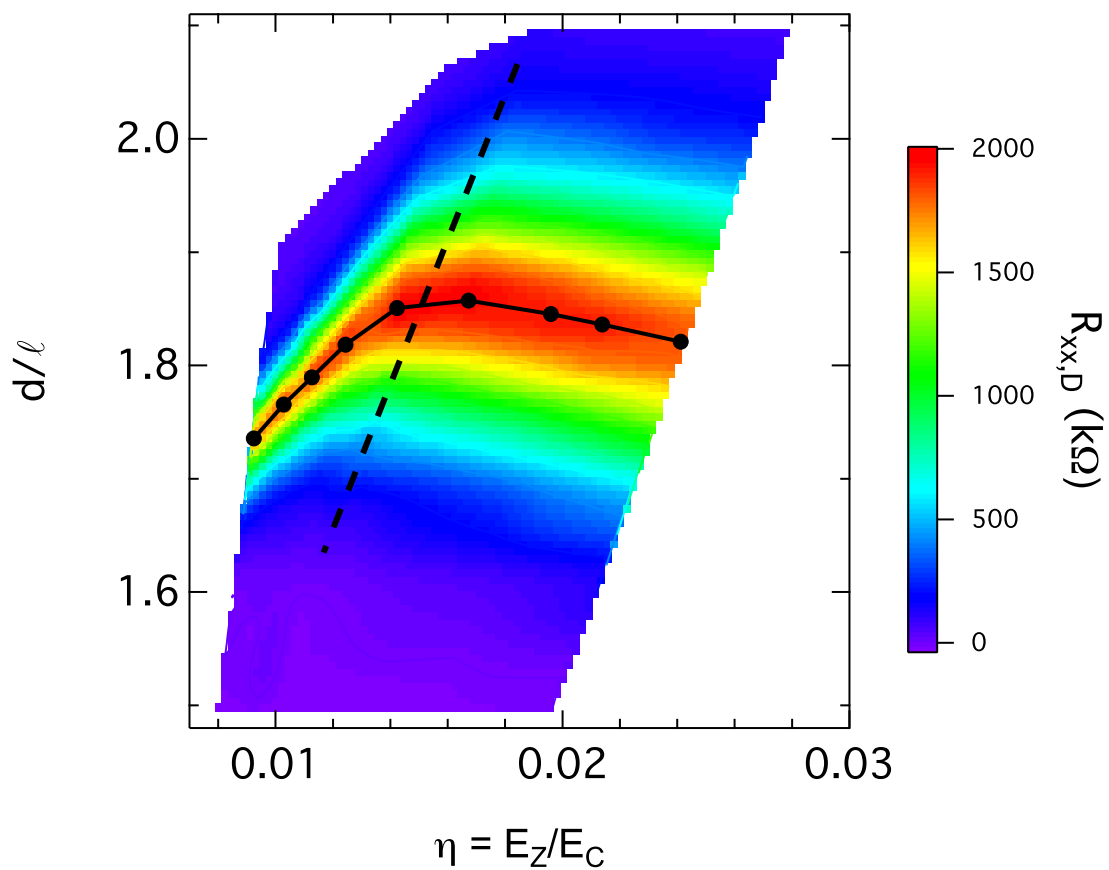
Figure 4.2: Longitudinal drag $R_{xx,D}$ versus d/ℓ and $\eta = E_Z/(e^2/\epsilon\ell)$ at $\nu_T = 1$ and $T = 50$ mK. Solid dots: phase boundary, $(d/\ell)_c$ versus η. Dashed line: approximate location of knee in drag contours. Left and right boundaries of colored region: $\theta = 0$ and $\theta = 66°$, respectively.

constant with respect to tilt angle after this point since both phases should be fully spin polarized, and any further rise in Zeeman energy should have no effect on the phase boundary.

Although we do find that beyond a certain angle the advancement of $(d/\ell)_c$ does halt, we also see that it then begins to slowly *decrease* toward even larger tilt angle. The gentle decline of $(d/\ell)_c$ is likely due not to the Zeeman energy but to an orbital effect induced by the large (>2 T) in-plane magnetic field. Because of the finite thickness of the 2DESs, the in-plane component can mix in the higher subbands of the quantum wells [22]. As depicted in figure 4.3, this can squash the subband wave function and increase the strength of intralayer interactions. Furthermore, subband mixing can shift the position of subband wave function in the z direction, thus increasing the separation between the two 2DESs and lower interlayer interactions. These modifications in the two types of interactions ultimately reduce the stability of the interlayer correlated phase relative to the uncorrelated phase (for example, see reference [135]). We expect such orbital effects when the magnetic length associated with the parallel field $\ell_{||} = \sqrt{\hbar/eB_{||}}$ is comparable to the width of either quantum well.

We also see in figure 4.2 that the width of the phase transition broadens continuously as Zeeman energy is increased. This is plotted explicitly in figure 4.4a. The dramatic rise in $\Delta(d/\ell)$ (overall, by a factor of about three) ceases once the uncorrelated phase is fully spin polarized. Beyond this point the width grows only weakly with further tilting of the sample. This rules out any orbital effects caused by the in-plane fields as the sole mechanism for the large increase in the phase transition width.

Finally, we remark on the location of the knee in the various drag contours in figure 4.2. We show their approximate positions with a dotted line in the color plot. These knees should indicate the location where the uncorrelated phase has become fully spin polarized. In a simple model of the uncorrelated phase in which the bilayer exists as two uncoupled systems of composite fermions, one would expect such systems to become fully spin polarized when the normalized Zeeman energy exceed a critical
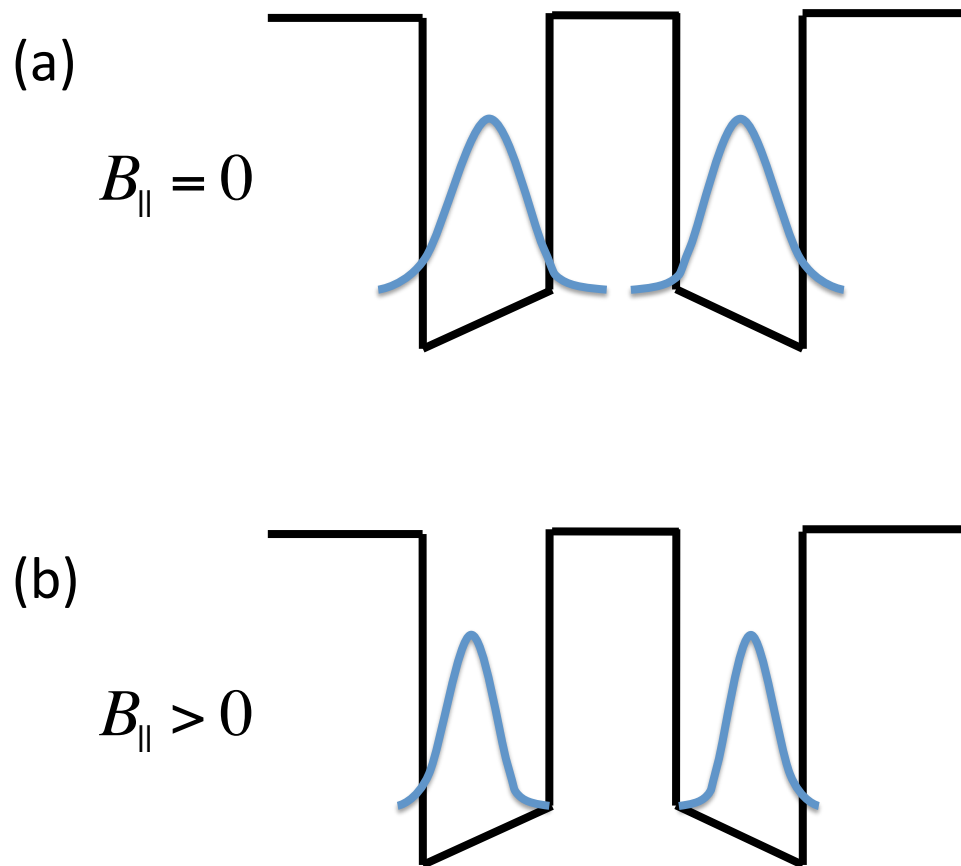
Figure 4.3: Subband wave functions in the (a) absence and (b) presence of a parallel magnetic field. A sizable $B_{||}$ will reduce the thickness of the 2DES and increase their separation from each other.

value that is independent of the effective interlayer separation. Instead, the finite slope of the dotted line in figure 4.2 suggests that the critical Zeeman energy has a d/ℓ-dependence. Regions of the phase boundary at lower d/ℓ and thus deeper within the correlated phase enter the regime of full spin polarization *before* those that are closer to the uncorrelated phase at high d/ℓ. This raises the possibility that somehow the presence of the excitonic phase makes it easier to spin polarize the competing compressible phase. Later in this chapter we will discuss the possible mechanisms by which this could occur, using two different theories of the phase boundary.

We close this section by commenting on the temperature dependence of $\Delta(d/\ell)$, as shown in figure 4.4b. Here, we plot the width of the phase transition versus temperature for $\theta = 0$ and $\theta = 66°$. As first reported by Kellogg *et al.* [65], the width of the transition at $\theta = 0$ extrapolates to relatively small value in the limit of $T \to 0$. However, in the high Zeeman regime the width of the transition is clearly nonzero even in the zero temperature limit. This eliminates the possibility that enhanced thermal fluctuations alone cause the broader phase transition at high tilt angles.

4.3 Mixed-fluid Models of the Phase Boundary

We turn now to two different models of the crossover between the strongly correlated regime at low d/ℓ and the weakly coupled regime at high d/ℓ. In one of the models, the phase transition is argued to be first order. In the other model, the transition is treated as a continuous crossover. Both describe the bilayer system in the transition region as consisting of a mixture of correlated and uncorrelated fluid. However, the spatial distribution of the two distinct types of fluids is different in these two models.

4.3.1 First-Order Phase Transition

Treating the phase transition as first order is motivated by the different spin polarizations of the two phases. If the transition between the two phases is a true thermodynamic phase transition, then it should be of first order because the spin
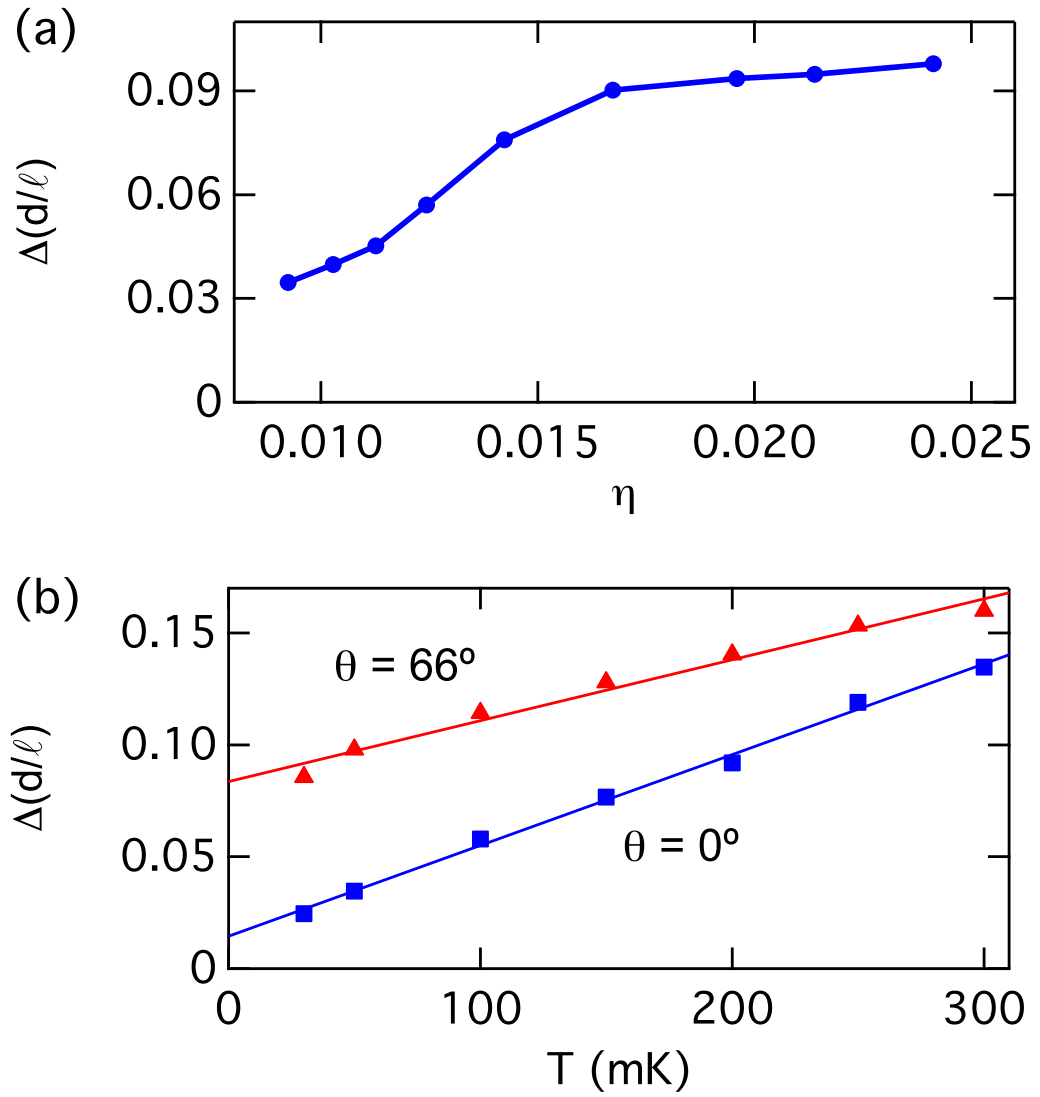
Figure 4.4: (a) Width, $\Delta(d/\ell)$, of the longitudinal drag peak at $\nu_T = 1$ and $T = 50$ mK versus normalized Zeeman energy η at the peak center. (b) Temperature dependence of $\Delta(d/\ell)$ at $\theta = 0$ (squares) and $\theta = 66°$ (triangles).

polarization (a thermodynamic quantity conjugate to the Zeeman field) changes discontinuously across the transition. Furthermore, Zou and collaborators find that a set of Clausius-Clapeyron relations seem to accurately and consistently describe the behavior of the phase transition in response to changes in not only Zeeman energy, but also temperature and density imbalance between the two layers [139].

A truly discontinuous first-order phase transition, however, is unlikely in real samples because of disorder. For example, Stern and Halperin conjecture that during the phase transition density fluctuations break up the system into spatially distinct regions of correlated and uncorrelated fluids [108]. At high d/ℓ, small puddles of the correlated fluid occupy a fraction f_{corr} of the system. As d/ℓ is lowered, the number and size of the puddles presumably grow until they percolate at some critical fraction f_{corr}^*. Stern and Halperin find that before percolation is achieved, the very different transport properties of the two fluid types lead to a large peak in $R_{xx,D}$ over a relatively narrow range of f_{corr}. Meanwhile, Hall drag rises monotonically with f_{corr}, from $R_{xy,D} = 0$ at $f_{corr} = 0$ to $R_{xy,D} = h/e^2$ at the percolation point of $f_{corr} = f_{corr}^*$. In particular, they derive a semicircle law for the longitudinal and Hall drag resistivities,

$$(\rho_{xx}^D)^2 + (\rho_{xy}^D + \pi\hbar/e^2)^2 = (\pi\hbar/e^2)^2. \tag{4.1}$$

This predicts a peak ρ_{xx}^D of $h/2e^2$ coincident with $\rho_{xy}^D = h/2e^2$, which qualitatively agrees with measurements of Coulomb drag across the phase boundary [65, 120, 38].

While this model was originally constructed assuming fully spin polarized electrons, it could be modified to permit unequal spin polarizations of the two phases. This leads to the possibility that since the density of states of the composite fermions in the uncorrelated phase drops by a factor of 2 upon full spin polarization, the ability to screen the disorder potential would be changed. Consequently, the transition width should grow in the high Zeeman regime, just as we observe. We depict the phase separation of the correlated and uncorrelated fluids for the two different Zeeman regimes in figure 4.5.

However, recall that the boundary between the two spin polarization regimes (the
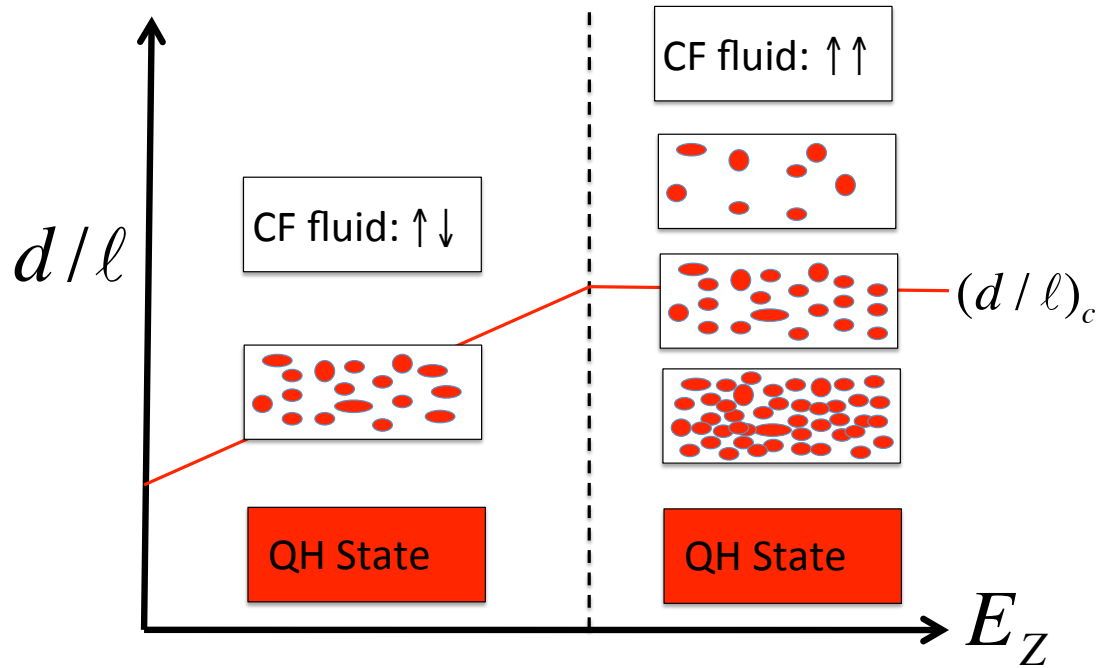
Figure 4.5: Depiction of first-order phase transition in the low Zeeman (left of dashed line) and high Zeeman (right of dashed line) regimes. In the high Zeeman regime, the uncorrelated composite fermion phase is fully spin polarized and only one Fermi sea exists to screen density fluctuations. Consequently, one anticipates disorder to be more prevalent and the phase transition to be broader than at low Zeeman energy.

dashed line in figure 4.2) is slanted in $(d/\ell, \eta)$ space. We might ask if this behavior is consistent with the first-order picture. In this scenario, the total area of CF regions shrinks as d/ℓ is decreased. However, the local density (and Fermi energy) of each CF region will remain fixed once normalized by the Coulomb energy. Thus, the CF regions should become fully spin polarized at a single value of normalized Zeeman energy that is independent of d/ℓ. This is in conflict with the boundary between the two spin polarization regimes, which we observe to have a finite slope rather than being a vertical line. We might explain this discrepancy by noting that exchange interaction effects might lower the critical Zeeman energy at which the CF regions become fully spin polarized. Such exchange interactions will become relatively more important at lower density. Since we achieve lower effective interlayer separation in our sample at fixed d by reducing the density of the 2DESs and tuning the magnetic field appropriately, we would then expect the critical Zeeman energy to decrease with d/ℓ. This model does not require the presence of the correlated fluid and thus could be tested by determining if the critical Zeeman energy is still density dependent in bilayer samples at high d/ℓ, when interlayer correlations are unimportant.

A second, more exotic possibility is that the spin polarized correlated fluid induces an effective Zeeman energy in the uncorrelated fluids through a proximity effect. As f_{corr} grows at lower d/ℓ, the influence of this proximity effect should also increase and lower the critical Zeeman energy required to fully spin polarize the uncorrelated regions.

4.3.2 Continuous Crossover

As an alternative, the finite width of the transition can be understood without invoking a first-order phase transition. For example, Simon, Rezayi, and Milovanovic (SRM) have suggested that instead of a true phase transition, a continuous crossover separates the correlated and uncorrelated phases [100]. SRM construct a set of wave functions for the $\nu_T = 1$ bilayer system in which some number of the electrons in the two layers act as composite fermions (CFs) and composite bosons (CBs). The CFs

consist of electrons bound to correlation holes only within their own layers. The CBs are constructed from electrons bound to one correlation hole in its own layer and to another correlation hole in the other layer. While the CFs fill up a Fermi sea, the CBs will eventually condense into the same state. The CBs provide the necessary interlayer correlations associated with the $\nu_T = 1$ phase while the composite fermions lack such interlayer correlations.

As the system evolves from the completely uncorrelated phase at $d/\ell = \infty$ (consisting only of composite fermions) to the correlated phase at $d/\ell = 0$ (consisting only of composite bosons), the composite fermions are one-by-one transformed into composite bosons. The growing number of composite bosons leads to a continuous increase in interlayer correlations. SRM find numerical evidence that this variation in composite boson number occurs over a range of d/ℓ, which would naturally explain the residual width of the phase transition even in the zero temperature limit [65]. They also construct a Chern-Simons transport theory that arrives at the same semicircle law for drag resistivities (equation (4.1)) as found by Stern and Halperin. A distinguishing feature of this view is that, unlike the first-order scenario, the two types of quasiparticles are permitted to *intermix spatially.* As we shall see, this leads to observable consequences when the Zeeman energy is increased and the composite fermion phase becomes fully spin polarized.

In order to interpret our results using this view of the phase boundary, we first create a simple mean-field model of the continuous crossover proposed by Simon, Rezayi, and Milovanovic. We assume that the CBs are fully condensed and fully spin polarized. The CFs fill up two Fermi seas that correspond to the two spin states and are displaced in energy from each other by the Zeeman energy. Let f_{CF} denote the fraction of electrons in the CF phase, with $f_\uparrow$ occupying the spin-up Fermi sea and $f_\downarrow$ occupying the spin-down Fermi sea. We use the constraint $f_{CF} = f_\uparrow + f_\downarrow$. Ignoring any interactions among the various flavors of composite particles or any dependence of the CF effective mass on f_{CF}, we write the total energy per electron as

$$E = \frac{1}{2}E_{F0}(f_\uparrow^2 + f_\downarrow^2) - \frac{1}{2}E_Z(f_\uparrow - f_\downarrow) + (1 - f)(C - \frac{1}{2}E_Z). \qquad (4.2)$$

Here, the first term in the sum represents the kinetic energies of the CFs, with E_{F0} being equal to the Fermi energy of the system when it consists only of spin polarized CFs. The second term is the contribution from the Zeeman energies of the two spin species of CFs. The third term includes the energy C of each condensed CB as well as the Zeeman energy of each spin polarized CB. In this model, C is a phenomenological parameter that represents the net Coulomb energy cost associated with converting a CF into a CB. Presumably, C includes contributions from both intralayer and interlayer interactions and thus is expected to be a function of d/ℓ. That is, as the effective interlayer separation becomes smaller it becomes energetically more cost effective to lower interlayer interactions by forming a CB from a CF, even if that gives rise to an increase of intralayer interactions. The simplest assumption is that C varies linearly with d/ℓ during the transition region.

To obtain the ground state, we minimize E and obtain the following solutions for $f_\uparrow$ and $f_\downarrow$:

$$f_\uparrow = C/E_{F0}, \tag{4.3}$$

$$f_\downarrow = (C - E_Z)/E_{F0}. \tag{4.4}$$

Thus, if $E_Z < C$, CFs of both spins are present and $f_{CF} = (2C - E_Z)/E_{F0}$. However, if $E_Z > C$, the CFs are fully spin polarized ($f_\downarrow = 0$) and $f_{CF} = C/E_{F0}$. A mixed phase ($0 < f_{CF} < 1$) will exist over a range of C in both the partially and fully spin polarized CF regimes. In the partially spin polarized regime, contours of fixed f_{CF} will satisfy the condition $C = (f_{CF}E_{F0} + E_Z)/2$ and thus will rise with E_Z. This is illustrated in upper-left half of figure 4.6 for the contours associated with $f_{CF} = 1/4$ and $f_{CF} = 3/4$.

However, when the Zeeman energy reaches $E_Z = C$ (denoted as a dashed line in figure 4.6), the CF phase becomes fully spin polarized, and the contours will become independent of Zeeman energy. This is indicated in the lower-right half of the phase diagram in figure 4.6. The knee in each contour should occur at $E_Z = f_{CF}E_{F0}$ and is thus proportional to the CF fraction, f_{CF}. This is consistent with the slanted
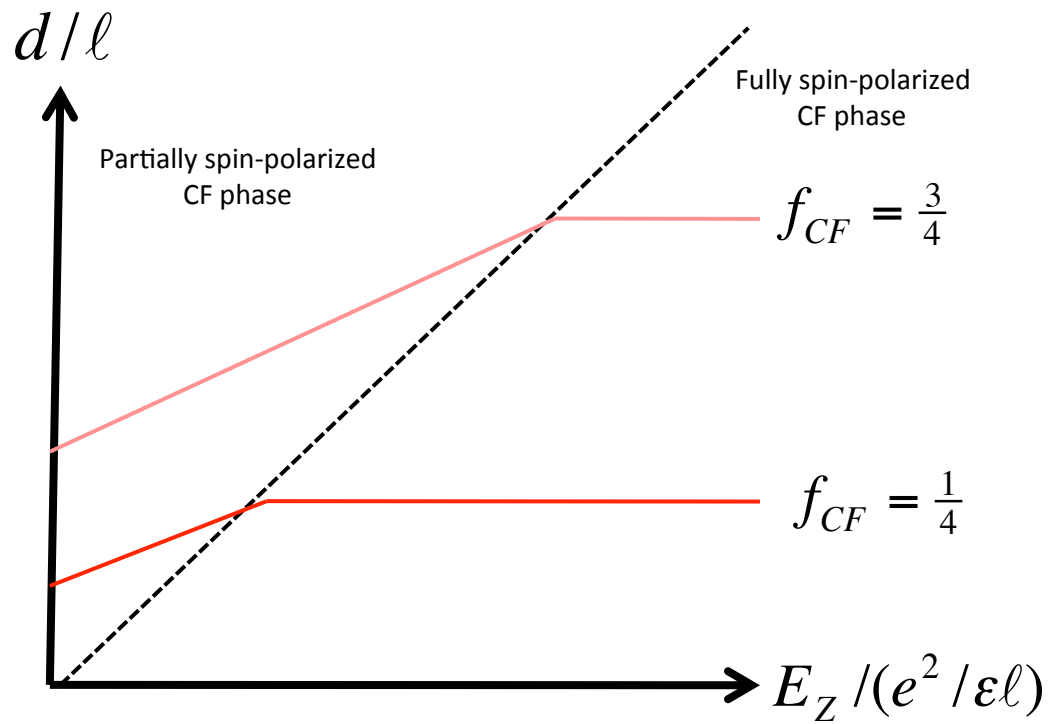
Figure 4.6: Depiction of phase diagram within the coexistence picture. At the dashed line, the Zeeman energy E_Z is equal to the Fermi energy of the composite fermion phase. Above the dashed line, the composite fermion phase is partially spin polarized. Below the dashed line, the composite fermion phase is fully spin polarized. Contours corresponding to composite fermion fractions $f_{CF} = \frac{3}{4}$ and $f_{CF} = \frac{1}{4}$ are shown as examples.

boundary separating the partially and fully spin polarized regimes that we observe in figure 4.2.

Figure 4.6 also illustrates how we can understand the broadening of the transition region at high E_Z within the coexistence picture. If we use the range $1/4 < f_{CF} < 3/4$ to define the transition width ΔC, we find that the width $\Delta C = E_{F0}/2$ in the fully spin polarized regime is twice as large as $\Delta C = E_{F0}/4$ in the partially spin polarized regime. For a linear relation between C and d/ℓ, one would also expect $\Delta(d/\ell)$ to grow by a factor of two between the low and high Zeeman regimes. This qualitatively agrees with our data near $T = 0$, but is lower than the observed factor of ~ 3 for the change in the transition width. A better comparison between this simple model and our Coulomb drag data might be obtained if there existed a theory relating f_{CF} and drag. However, such a theory remains lacking.

Before ending this section, we also note the possibility that both the first order and the continuous crossover pictures could provide faithful descriptions of the phase boundary, but under different regimes. That is, the phase transition could be first-order at low Zeeman energy, when there is a difference in spin polarizations for the two phases. However, as suggested by Zou and collaborators [139], the phase transition does not have to be first-order in the fully spin polarized regime. There, either a second-order transition or continuous-crossover might be allowed.

4.4 Phase Boundary at Finite Temperature

Until now, we have been focusing on the phase transition at low temperatures. In this section we will turn to Coulomb drag data taken at elevated temperature. When analyzing our data in the remainder of this chapter, we will restrict ourselves to using the first-order model of the phase transition because it is unclear how to extend the continuous-crossover model of Simon and collaborators [100] to finite temperature. In the first-order model, the slope of the phase boundary can be derived using Clausius-Clapeyron equations, as analyzed by Zou *et al.* [139].

To explore the evolution of the $(d/\ell, E_Z)$ phase diagram with temperature, we

repeated the procedure of measuring $R_{xy,D}$ at $\nu_T = 1$ versus d/ℓ at 9 different tilt angles and various temperatures. This results in traces similar to those seen in figure 4.1a for each tilt angle and temperature. In figure 4.7a we show the phase boundary in $(d/\ell, \eta)$ space at various temperatures ($T = 50, 100, 150, 200$, and 300 mK). Here, we use the condition $R_{xy,D} = \frac{1}{2}h/e^2$ to define the location of the phase boundary. As a guide to the eye, we have also plotted a cubic spline interpolation for the phase boundary line at each temperature.

We first turn our attention to the slope of the phase boundary at each temperature in the low Zeeman regime, when the compressible phase is not fully spin polarized. By employing Clausius-Clapeyron relations [139], one would predict that this slope is proportional to the difference in spin polarization $\Delta\xi = \xi_{corr} - \xi_{uncorr}$ of the correlated and uncorrelated phases. For each curve in 4.7a, we calculate the slope of the phase boundary in $(d/\ell, \eta)$ space at $\eta = 0.01$, using a linear fit to the three data points whose domain of η values contain $\eta = 0.01$. We plot the results versus temperature in figure 4.7b. The slope of the phase boundary appears to decline steadily with temperature in a linear fashion. This suggests a similar decrease in $\Delta\xi$ with temperature and that the correlated phase becomes more quickly depolarized by thermal fluctuations than does the uncorrelated phase.

Finally, we examine the critical Zeeman energy η_c at which the phase boundary lines in figure 4.7a begin to bend over, signifying that the uncorrelated phase has been fully spin polarized by the large Zeeman field. To consistently identify η_c for each temperature, we locate the local maximum in the cubic spline interpolation of our data points. Due to the limited angular resolution of our data, there is a large amount of uncertainty associated with this method. Nonetheless, as shown in figure 4.7b, the difference in η_c between $T = 50$ and 200 mK is large enough to conclude that the critical Zeeman energy increases with temperature. This is consistent with thermal excitations causing the population of the spin-reversed CF Fermi sea. Such spin-flips can occur even when $E_Z > E_F$, where E_F is the Fermi energy of the CFs in the uncorrelated phase. At finite temperature, complete spin polarization of the CFs requires $E_Z - E_F \gg k_b T$. Despite the large uncertainties in our determination of η_c,
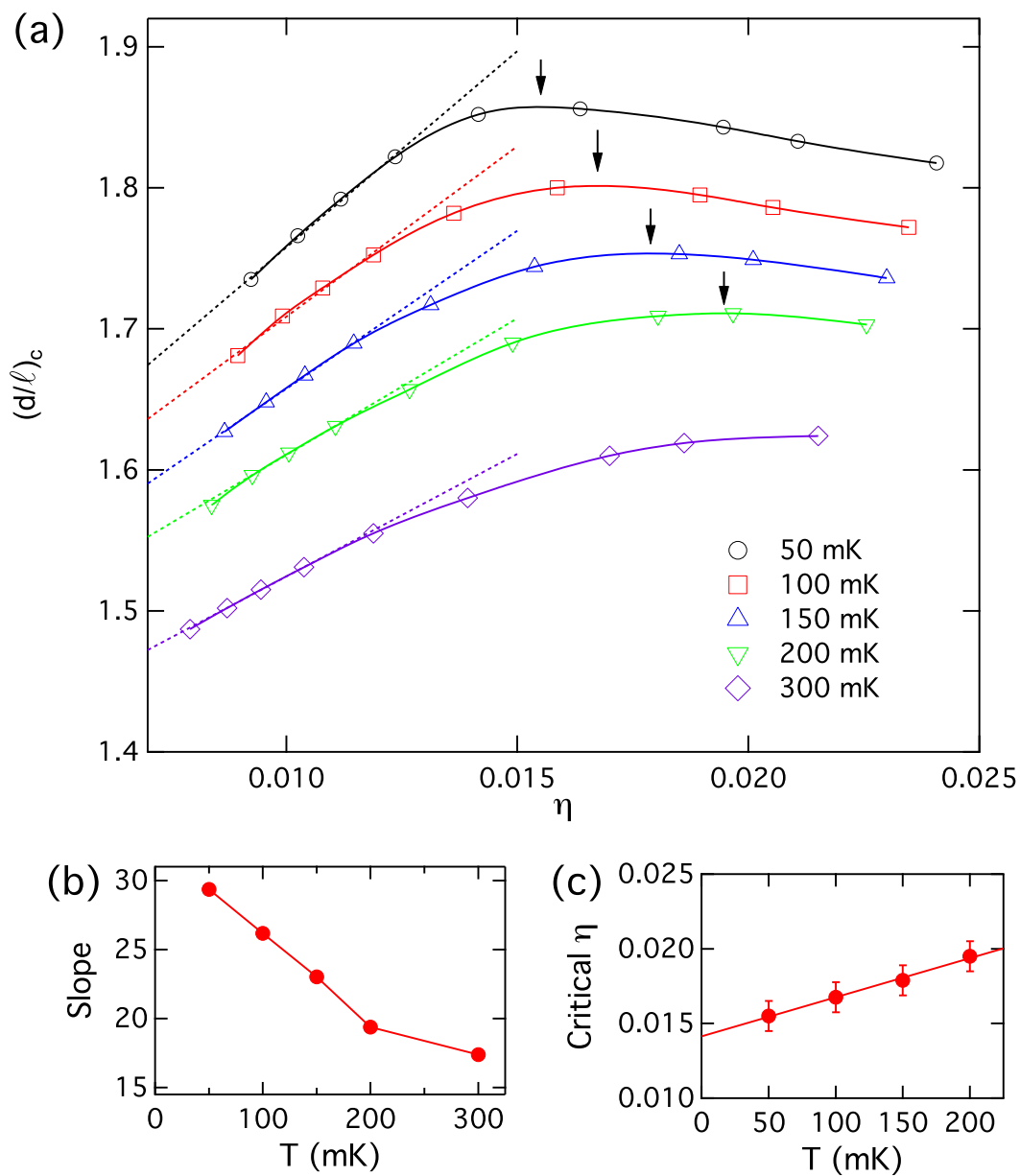
Figure 4.7: a) Critical interlayer separation $(d/\ell)_c$ versus normalized Zeeman energy $\eta = E_Z/(\frac{e^2}{\epsilon\ell})$ for $T = 50$, 100, 150, 200, and 300 mK. The solid lines are guides to the eye. Black arrows point at the approximate critical η for each temperature. The dotted lines are linear fits to the low Zeeman data. b) Slope of phase boundary at $\eta = 0.01$. c) Approximate critical η versus temperature.

we do see evidence for a linear trend in η_c versus T. Furthermore, we find that η_c extrapolates to 0.015 in the limit of zero temperature. This is in good agreement with the value found by Tracy *et al.* [118], who determined η_c from the resistively detected nuclear magnetic resonance signal in a single layer at half filling. However, our result for η_c is somewhat smaller than the values found by other groups [70, 81, 41, 42]. Those groups reported critical Zeeman energies that were in better agreement with the predicted value of $\eta_c = 0.022$ from Park and Jain [88].

4.5   Critical Temperature versus Energy Gap

The $\nu_T = 1$ is unique among quantum Hall states because of the possibility of having a phase transition at finite temperature [12]. In this scenario, interlayer correlations appear at a characteristic temperature T_c. This T_c would not necessarily be directly related to the energy gap. Instead, T_c would be governed by the free energy competition between the correlated and uncorrelated states. For example, if the phase transition is a first-order transition between the spin polarized excitonic state and the unpolarized CF state, then one would expect that T_c could be tuned with the Zeeman energy. Deep within the phase, an increase in Zeeman energy should not strongly affect the properties of the $\nu_T = 1$ state at low temperature, such as the energy gap for charged excitations. In this section, we attempt to compare the critical temperature for interlayer correlations and the energy gap. We will focus on the case of $d/\ell = 1.59$, which is far from the phase boundary.

4.5.1   Determination of T_c

To complete our analysis of exciton condensation at finite temperature, we examine Coulomb drag versus temperature at fixed d/ℓ. For each tilt angle, we tune the magnetic field and bilayer densities to achieve $\nu_T = 1$ at $d/\ell = 1.59$ and measure Coulomb drag while slowly increasing the temperature from 25 to 500 mK. This temperature sweep is done over the course of several hours so that the electrons and the main thermometer are fully equilibrated with each other during the sweep. In

figures 4.8a and 4.8b, we show $R_{xy,D}$ and $R_{xx,D}$ (respectively) versus temperature. We focus on the two extreme angles of $\theta = 0$ and $\theta = 66°$.

At $d/\ell = 1.59$ and $T = 0$, the bilayer system is far from the phase boundary separating the correlated and uncorrelated regimes. Consequently, for both tilt angles we observe that $R_{xy,D} = h/e^2$ and $R_{xx,D} \approx 0$ at the lowest temperatures. As temperature increases, $R_{xy,D}$ monotonically falls. Meanwhile, $R_{xx,D}$ rises to ~ 2 kΩ and then gradually decreases. Just as in figure 4.1, the peak in $R_{xx,D}$ occurs at nearly the same temperature at which $R_{xy,D} = \frac{1}{2}h/e^2$. Such behavior is reminiscent of Coulomb drag versus d/ℓ.

For the purposes of our analysis, we use $R_{xy,D} = \frac{1}{2}h/e^2$ to define a critical temperature T_c separating the strongly and weakly coupled regimes. Figure 4.8a shows that T_c has risen from 186 mK at $\theta = 0$ to 333 mK at $\theta = 66°$. This is analogous to the rise in critical d/ℓ with Zeeman energy at fixed temperature. The steady rise in T_c versus η can be seen in figure 4.8c. The critical temperature shows signs of almost saturating, but is still very slowly rising at tilt angle $\theta = 66°$. This is consistent with the $T = 300$ mK trace in figure 4.7, which demonstrates that thermal fluctuations are large enough at $T \geq 300$ mK to prevent complete spin polarization of the competing CF phase at $\theta = 66°$.

4.5.2 Measurement of Energy Gap from Coulomb Drag

Previous studies of Coulomb drag at $\nu_T = 1$ [65, 127] had reported activated behavior with an energy gap nearly the same as the one obtained by measurement of R_{xx} in parallel flow. Here we will also use Coulomb drag to determine the energy gap of charged excitations. We were unable to perform proper parallel flow measurements using the sample studied in this chapter because we found that one of the two layers had a larger series resistance[2] than the other layer. Thus, we could not ensure equal currents in the two layers as required in parallel flow.

An energy gap can be calculated from Arrhenius plots of either $R_{xx,D}$ or $\Delta R_{xy,D}$

---

[2]Here, series resistance is associated with the arms connecting the contacts with the active $\nu_T = 1$ region.
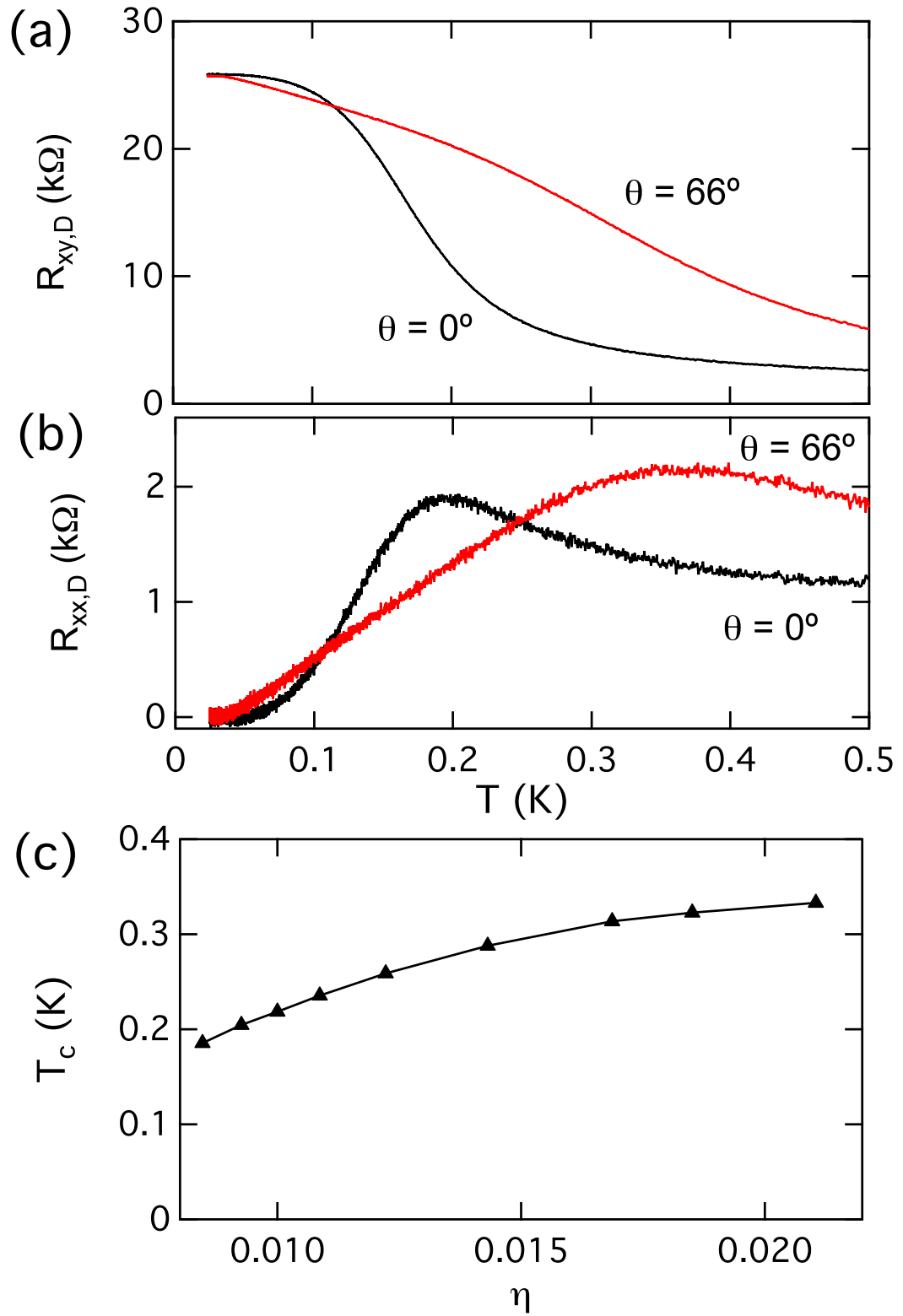
Figure 4.8: Temperature dependence of Coulomb drag at $d/\ell = 1.59$ and either $\theta = 0$ (black traces) or $\theta = 66°$ (red traces). a) $R_{xy,D}$ versus T. b) $R_{xx,D}$ versus T. c) Critical temperature T_c versus η at $d/\ell = 1.59$. The critical temperature is determined by the condition $R_{xy,D} = \frac{1}{2}h/e^2$.

versus $1/T$, where $\Delta R_{xy,D} \equiv h/e^2 - R_{xy,D}$. Here we use the condition $R_{xx,D} \propto \exp\left(-\frac{\Delta}{2k_BT}\right)$ to define the energy gap, such that $\Delta/2$ is the slope from a linear fit to portions of $R_{xx,D}$ in the Arrhenius plots. A similar method is used to extract an energy gap from $\Delta R_{xy,D}$ data.

We first concentrate on Arrhenius plots of $R_{xx,D}$. We show examples of such plots in figure 4.9a. While only a single energy gap is evident for $\theta = 0$, the $R_{xx,D}$ data at $\theta = 66°$ seem to show two different temperature regimes with two different slopes (figure 4.9a). The crossover point between the two regimes is near $T \approx 150$ mK. In figure 4.9a, the $\Delta R_{xy,D}$ data show a similar disparity between the slopes at high and low temperatures. The difference in slopes in the $\Delta R_{xy,D}$ Arrhenius plots is apparent even at zero tilt angle.

The appearance of two different temperature regimes in the Arrhenius plots requires us to be careful in interpreting their physical significance. Besides an energy gap between the ground state and charge-carrying extended states, the low temperature gaps might instead reflect the energy scales for alternative modes for bulk conduction of charged excitations, such as nearest-neighbor hopping or variable-range hopping between localized states in the bulk. Because the hopping conduction takes place between localized states with lower energy than the lowest unoccupied extended states, these alternative modes of conduction become more prevalent in more disordered samples and dominate transport at low temperature, when occupation of extended states has been frozen out. In this scenario, one would expect the high temperature slope in the Arrhenius plot to correspond to the band gap and the low temperature slope would be associated with hopping conduction [7].

We plot all four sets of the Arrhenius slopes at $d/\ell = 1.59$ versus normalized Zeeman energy in figure 4.10. All but one of the apparent energy gaps (that corresponding to $\Delta R_{xy,D}$ at high temperature) decreases essentially monotonically with Zeeman energy. The Arrhenius slope of $\Delta R_{xy,D}$ at high temperature rises somewhat with η, but then declines.

Either of the possible origins for these Arrhenius slopes are consistent with the observed decline with tilt angle. The previously mentioned orbital effect induced by
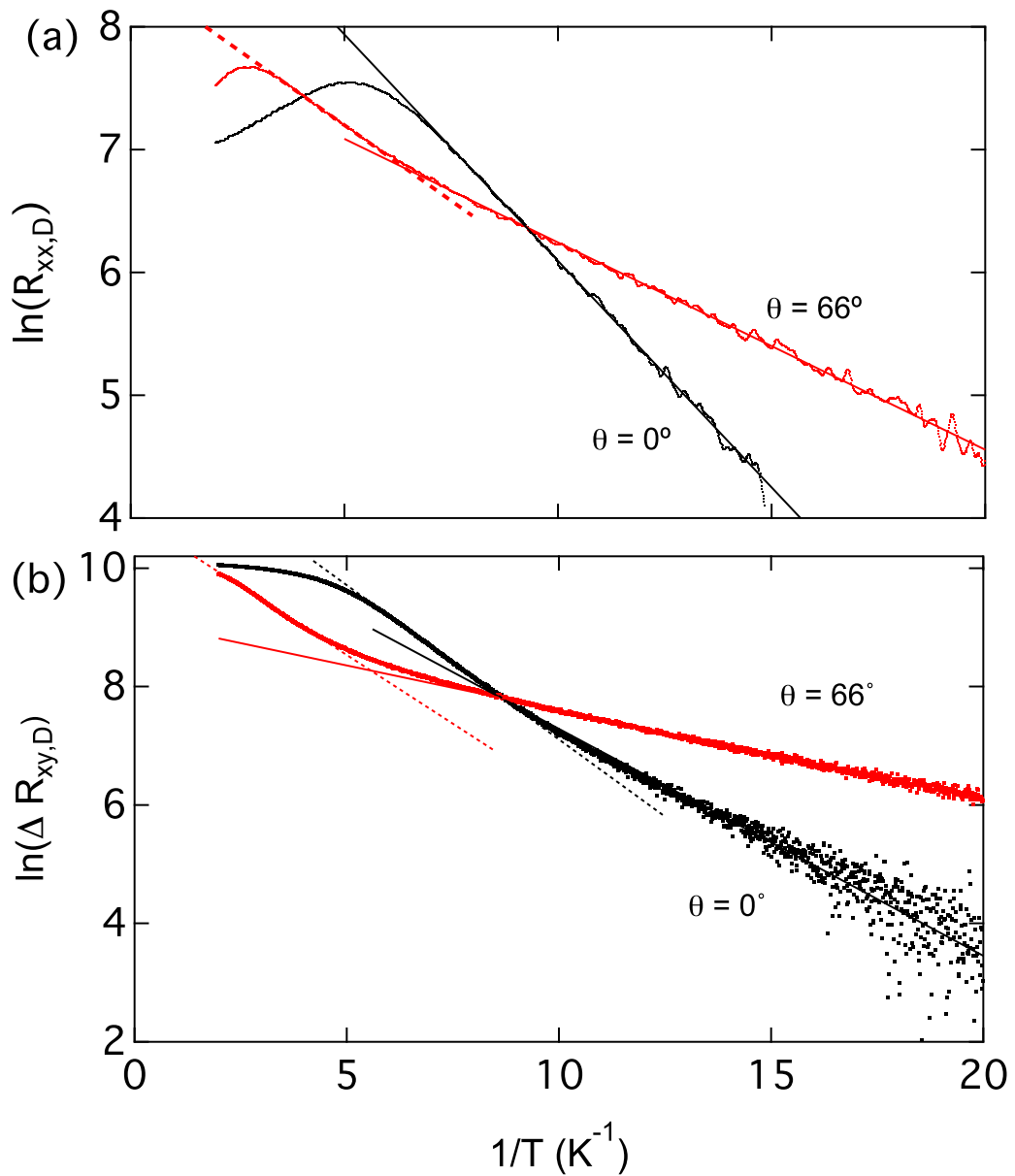
Figure 4.9: Arrhenius plot of (a) $R_{xx,D}$ and (b) $\Delta R_{xy,D}$ at $d/\ell = 1.59$ for both $\theta = 0$ and $\theta = 66°$. Dashed lines are linear fits to the data at either high temperature (dashed lines) or low temperature (solid lines). For $R_{xx,D}$ at $\theta = 0$, only the low temperature slope is shown.
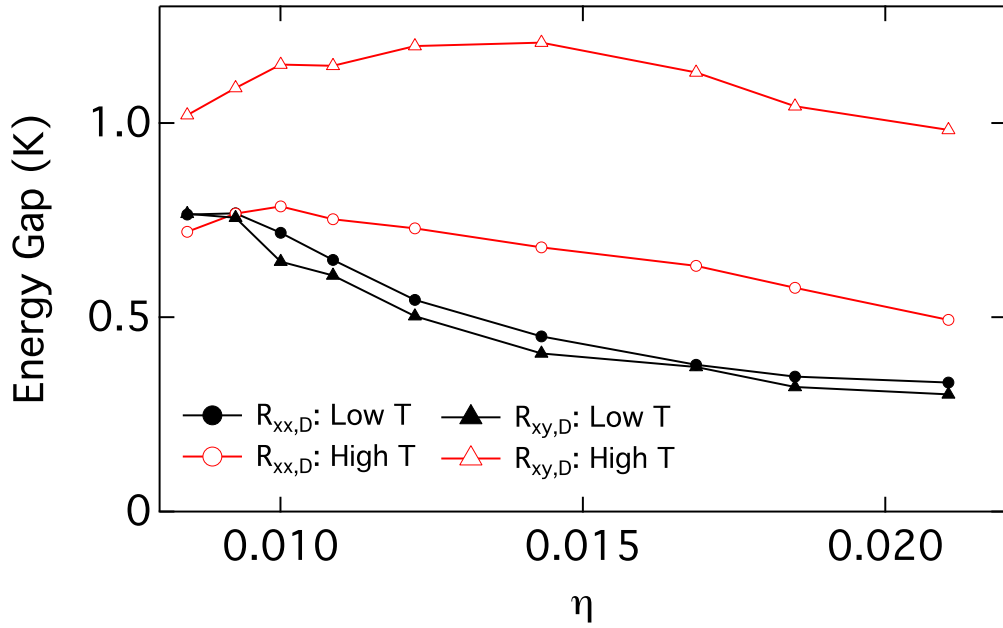
Figure 4.10: Apparent energy gaps versus normalized Zeeman energy η.

the in-plane magnetic field would reduce the stability of the correlated state and thus likely results in a decrease in a band gap for charged excitations. Also, the full spin polarization of the competing CF phase could lead to a lessened screening of disorder and enhanced hopping conduction between localized states; consequently, the energy scale associated with variable-ranged or nearest-neighbor hopping would decrease. In either case, figure 4.10 strongly suggests that the gap for charged excitations does not increase with tilt angles. This is in agreement with a previous study of transport at $\nu_T = 1$ in the presence of a large parallel field [42], which found that the charge gap at low d/ℓ was independent of Zeeman energy.

4.5.3 Discussion

Over the studied range of Zeeman energy, the critical temperature increases by nearly 80% while no concomitant rise is seen in the energy gap for charged excitations. This is consistent with a first-order phase transition occurring at finite temperature, where

the location of the phase boundary does not influence the properties of the correlated state at low temperature. Here, an increase in Zeeman energy increases T_c.

In a first-order phase transition, the location of the phase boundary should be governed by a series of Clausius-Clapeyron relations. For example, Zou *et al.* [139] did an extensive survey of the various experimental studies in which the $\nu_T = 1$ phase boundary shifted in response to Zeeman energy, temperature, and density imbalance. Assuming that the phase transition was first order, they calculated the behavior of the phase boundaries when these three parameters were tuned. They found good agreement between their model and experimental data using the approximation,

$$\frac{\partial(\Delta F)}{\partial x} = \gamma \frac{e^2}{\epsilon \ell^3}. \tag{4.5}$$

Here, $\Delta F \equiv F_{corr} - F_{uncorr}$ is the difference between the free energy densities of the correlated and uncorrelated phases and γ was a constant that they determined by fitting their models of F_{corr} and F_{uncorr} to the experimental results. They determined that the value of $\gamma = (1 \pm 0.1) \times 10^{-3}$ best fits the full set of data.

Although Zou et al. were focused on calculating $(d/\ell)_c$, we can extend their analysis to predict the evolution of T_c as a function of Zeeman energy. We first invoke the Clausius-Clapeyron relation

$$\frac{dT}{dE_Z} = \frac{N_T(\xi_{uncorr} - \xi_{corr})}{\frac{\partial F_{uncorr}}{\partial T} - \frac{\partial F_{corr}}{\partial T}} \tag{4.6}$$

to describe the slope of the phase boundary in $T - E_Z$ space. The numerator on the right-hand side of equation (4.6) reflects the difference in spin polarization of the two phases, with N_T denoting the total electron density. The denominator is the difference in entropy of the two phases.

We will invoke a number of simplifying assumptions about the correlated and uncorrelated phases, so as to derive a mainly qualitative prediction for the behavior of the phase boundary. First, we ignore any spin-flip excitations in the correlated phase, such that $\xi_{corr} = 1$ for the relevant temperatures. As suggested in the previous

section, this may not be a totally accurate statement at high temperature.

Second, to account for the thermal depolarization of the CF phase we use the estimate $\xi_{uncorr} = \eta/\eta_c^*$, where η_c^* is the critical Zeeman energy that is required to fully spin polarize the uncorrelated phase at a fixed, finite temperature. As seen in figure 4.7c, this term will grow with temperature and is expected to be $\eta_c^* \approx 0.02$ in the relevant temperature range of $T \approx 200 - 300$ mK. For now, we will assume that η_c^* is a constant whose value will be used as a fitting parameter when comparing the theoretical behavior of T_c with our observed data.

Third, we will ignore the contributions of both pseudospin waves and Chern-Simon gauge field fluctuations in the entropy term $\frac{\partial F_{uncorr}}{\partial T} - \frac{\partial F_{corr}}{\partial T}$. This is motivated by the observation of Zou et al. that such contributions are negligible compared to the noninteracting composite fermion entropy density. Finally, we will restrict ourselves to the case of $\eta \leq \eta_c^*$; beyond $\eta = \eta_c^*$, the critical temperature should be essentially constant.

These assumptions allow us to write equation (4.6) as,

$$\frac{dT}{dE_Z} = \frac{1 - \eta/\eta_c^*}{\alpha T}, \tag{4.7}$$

where $\alpha = \frac{4\pi^2}{3\hbar^2} m_{CF} \ell^2 k_b^2$, m_{CF} is the composite fermion mass, and k_b is Boltzmann constant. Choosing a proper value for m_{CF} can be incredibly tricky. We must emphasize that composite fermions can appear to have different effective masses in different contexts [58]. For example, one can define a polarization mass m_p based on the condition $E_F \equiv \frac{\hbar^2 k_F^2}{2m_p} = E_Z$; such a mass should reflect the full depth of the composite fermion Fermi sea. However, here we are interested in the thermodynamical properties of the composite fermions. The mass m_{CF} denotes the composite fermion mass if we could treat the system as comprising of nearly free fermions with the same entropy per particle as the composite fermion system. Consequently, m_{CF} should provide a measure of the density of states in the vicinity of the Fermi energy. A theoretical estimate [50] for this type of mass arrives at the value $m_{CF} \approx 0.079 \, m_e \sqrt{B_\perp[T]}$,

where m_e is the electron mass in vacuum.[3] However, the true value of m_{CF} in a given sample is expected to be strongly affected by the finite thickness of the quantum well, disorder, and Landau level mixing [133, 88, 89, 83]. Because such conditions should vary from sample to sample, there should not be a universal value for m_{CF}. For this reason, we will use m_{CF} as another fitting parameter that can be varied to best fit our data.

Simple algebraic manipulation and then integration of the ODE shown in equation (4.7) lead to

$$T^2 = \frac{2E_C}{\alpha}\eta - \frac{E_C}{\alpha \eta_c^*}\eta^2 + C_0, \qquad (4.8)$$

where C_0 is an arbitrary constant. Thus, one expects a plot of T_c^2 versus η to follow a parabolic curve whose peak coincides with the full spin polarization of the CF phase.

The square of the observed critical temperature as a function of normalized Zeeman energy is shown in figure 4.11. A parabolic fit to the data gives $T_c^2 = C_0 + C_1\eta + C_2\eta^2$, with $C_0 = (-0.00777 \pm 0.0044)$, $C_1 = (15.92 \pm 0.65)$, and $C_3 = (-329 \pm 22)$. From these fitting parameters, one obtains $\eta_c^* = 0.024$ and $m_{CF} = 1.36 m_e \sqrt{B_\perp[T]}$. These values are in partial agreement with the expected $\eta_c^* \approx 0.02$ (as expected for this range of temperatures in figure 4.7c) and $m_{CF} = 0.2 m_e \sqrt{B_\perp[T]}$, which is the CF mass as used by Zou et al. in reference [139]. This value for the composite fermion mass originates from the measurement of activation gaps in the vicinity of $\nu = 1/2$ by Du *et al.* [15, 17]. If one instead employs these values for η_c^* and m_{CF}, one arrives at the red dotted line in figure 4.11. Note that in the predicted T_c^2 versus η curve, we also choose to use a different value of the arbitrary constant C_0 so as to match with the observed T_c^2 value at zero tilt angle.

It should be clear from figure 4.11 that the observed critical temperature grows much more slowly with Zeeman energy than expected. There are several possible explanation for this discrepancy. One possibility is that our assumption that the entropy of the composite fermion phase scales linearly with temperature is an oversimplifica-

---

[3]Although the effective masses of composite fermions are often given in terms of m_e, this formalism is somewhat misleading because their properties should in principle be completely unrelated to the bare electron mass [58].
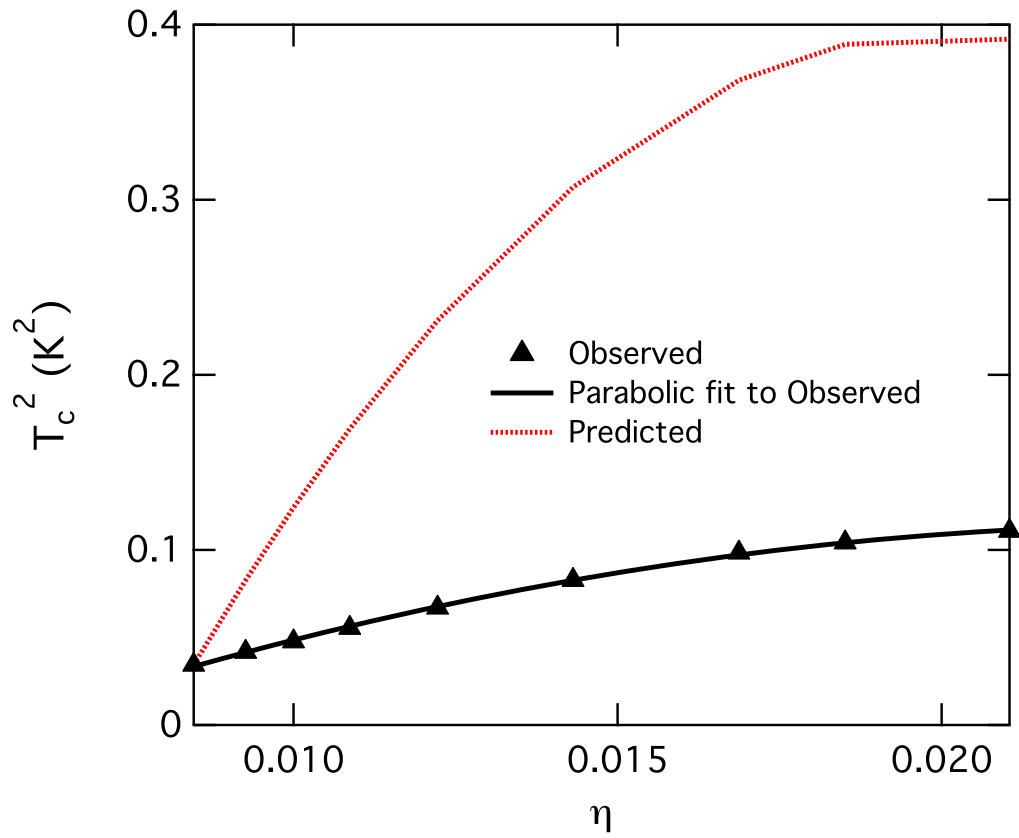
Figure 4.11: Expected and observed T_c^2 versus η at $d/\ell = 1.59$. The solid black line is a parabolic fit to the observed data points.

tion. While that behavior is reasonable for noninteracting fermions, the entropy of a composite fermion system at $\nu = \frac{1}{2}$ will include contributions from gauge fluctuations that scale either as $T^{2/3}$ for the case of short-range interactions or as $T \ln T$ for long-range Coulomb interactions (for example, see references [50] and [139]). Another possibility for the discrepancy between the theoretical curve and experimental curve is that our particular definition of T_c does not track precisely with the true location of the phase boundary. Also, the value of m_{CF} that Zou et al. uses might not be appropriate for our particular double quantum-well system in the presence of a large parallel magnetic field. As mentioned earlier, m_{CF} can be sensitive to the effective thickness of the quantum well and disorder, both of which might be modified by the in-plane field. Finally, we note the possibility that the correlated phase is not fully spin polarized at the phase boundary.

4.6   Conclusion

In this chapter, we studied the phase transition between the correlated and uncorrelated phases at $\nu_T = 1$ using Coulomb drag. We found that the phase transition becomes substantially broader when the Zeeman energy is large enough such that both phases are fully spin polarized. This observation is consistent with two different models of the phase boundary in which a mixture of correlated and uncorrelated fluids exists during the transition. We also find evidence that the characteristic temperature for interlayer correlations increases with Zeeman energy even though the apparent charge gap seems to decrease. Such behavior can be qualitatively described in a first-order model of the phase transition, although a quantitative understanding for the phase boundary at finite temperature is lacking.

Chapter 5

Area Dependence of Interlayer Tunneling at $\nu_T = 1$

Having studied the phase transition between the uncorrelated and correlated phase in a bilayer system, we now turn to studies of the correlated system itself. We first consider the anomalously large and Josephson-like interlayer tunneling [103]. In particular, we wish to learn about its spatial distribution across the $\nu_T = 1$ region by measuring the area dependence of the tunneling conductance.[1]

The enhanced tunneling at $\nu_T = 1$ is thought to reflect the development of spontaneous interlayer quantum phase coherence among the electrons in the bilayer (for example, see Refs. [6, 34, 40, 55, 56, 60, 90, 107, 123, 124]). In the exciton condensate picture, each electron is bound to a correlation hole in the opposite layer, and there is little energy penalty for the transfer of an electron from one layer to another. In this chapter, we investigate the spatial distribution of the interlayer tunneling throughout the $\nu_T = 1$ system. We accomplish this by measuring the dependence of the tunneling conductance on the area and perimeter of the $\nu_T = 1$ region. We thus find evidence that tunneling is a bulk phenomenon. This finding might seem unsurprising, but considerations of the Josephson-like tunneling in the clean limit would suggest that tunneling currents should be restricted to a narrow region around the source and drain contacts, in analogy with the same decay of the tunneling current in a

---

[1]This chapter contains work first presented in A. D. K. Finck, A. R. Champagne, J. P. Eisenstein, L. N. Pfeiffer, and K. W. West, *Phys. Rev. B* **78**, 075302 (2008). Copyright 2008 by the American Physical Society.

Josephson junction [31].

5.1 Simple Model of Tunneling

We begin with a simple model of tunneling, using the pseudospin picture. Recall that the interlayer phase angle ϕ obeys the following Hamiltonian in the long wavelength limit:

$$H = \int d^2 x \left[\rho_s \frac{|\nabla \phi|^2}{2} - \frac{\Delta_{SAS}}{4\pi \ell^2} \cos \phi + \frac{\beta}{2} |m_z|^2 \right].$$ (5.1)

Here, ρ_s is the pseudospin stiffness, Δ_{SAS} is the energy splitting between the symmetric and antisymmetric states in the double-well potential by single particle tunneling, and the third term is the renormalized capacitive energy [82, 107, 131]. Assuming the validity of the Josephson relations, this capacitance term is proportional to $(\partial_t \phi)^2$.

One can derive an equation of motion for ϕ from this Hamiltonian. After restricting to the time-dependent case, one arrives at the following sine-Gordon equation:

$$\sin \phi = \lambda_J^2 \frac{\partial^2 \phi}{\partial x^2}$$ (5.2)

In the limit of small ϕ (such that $\sin \phi \approx \phi$), this equation has exponential solutions that decay over the characteristic length scale given by

$$\lambda_J = 2\ell \sqrt{\frac{\pi \rho_s}{\Delta_{SAS}}}.$$ (5.3)

Estimates from mean-field theory (for example, see reference [60]) suggest that $\rho_s \approx 0.5$ K. The estimation of Δ_{SAS} can be tricky due to its exponential dependence on the thickness and height of the tunneling barrier. Disorder as well as thermal and quantum fluctuations should also modify the values of these two parameters, but the best approximations give $\lambda_J \approx 1 - 10$ μm.

Next, we apply our model to a one-dimensional tunneling geometry with a sample length of L, as depicted in figure 5.1. Here, current is injected into the top layer from the left edge and withdrawn from the bottom layer at the left edge as well. In the

small ϕ limit, the solutions to equation (5.2) are of the form $\sim e^{-\lambda_J x}$. Thus, for large samples in which $L \gg \lambda_J$, one would expect that most of the tunneling would take place within λ_J of the left edge of the sample. The tunneling conductance should be proportional to λ_J rather than L and thus be insensitive to further increases in the size of the sample.

This analysis can be made more sophisticated using the pseudospin-transfer torque theory [92, 112], in which one considers a fully two-dimensional sample geometry and accounts for the influence of the exciton condensate on the pseudospin degree of freedom for electrons traveling along the edge of the sample. Ultimately, though, one still expects that tunneling is confined to a small region along the perimeter of the sample. The total tunneling conductance would approximately be proportional to the perimeter of the sample instead of the system area due to relatively little tunneling taking place within the bulk of the $\nu_T = 1$ system.
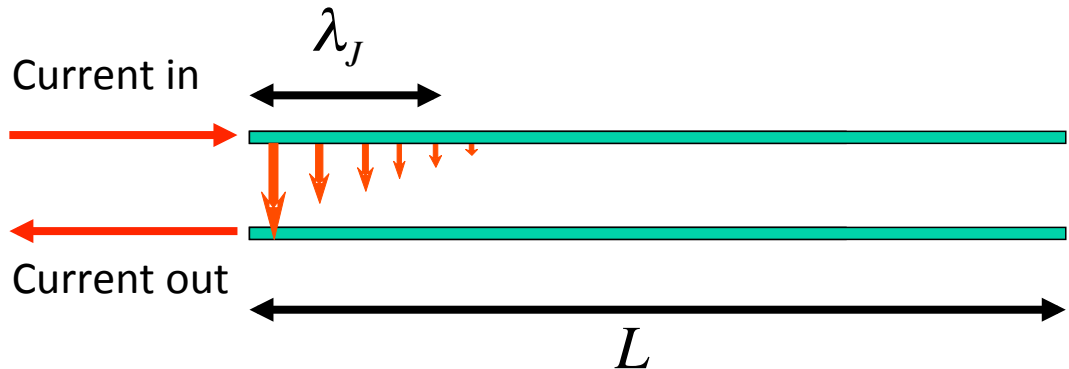
Figure 5.1: Depiction of tunneling in a clean, one-dimensional sample at $\nu_T = 1$. The majority of the interlayer tunneling occurs within λ_J of the left edge.

5.2 Area Tunneling Sample

To test these ideas, we seek to measure the area dependence of tunneling conductance at $\nu_T = 1$. We must induce $\nu_T = 1$ regions of different sizes within the same device to reduce systematic errors from sample variations. This is critical because tunneling

conductance can vary dramatically even among samples from the same wafer due to variations in the thickness of tunneling barrier. We accomplish this by studying devices in which multiple top gates cover a single mesa. By applying a voltage bias to a global back gate and to one of the top gates, we may create a section of the bilayer at $\nu_T = 1$. The remainder of the device remains in the uncorrelated state, contributing negligible tunneling conductance to the overall signal. Thus, within a single device we may create different sized regions of $\nu_T = 1$ *in situ* and meaningfully compare their individual interlayer tunneling conductances.

The first such device (sample 11-1-04.1K) can be seen in figure 5.2. It was fabricated from a GaAs/AlGaAs wafer with a double quantum well (DQW) structure. The DQW comprises of two 18 nm GaAs quantum wells separated from a 10 nm $Al_{0.9}Ga_{0.1}As$ barrier, such that the center-to-center separation of the 2DESs in the quantum wells is $d = 28$ nm. As grown, the 2DESs each have a density of $n \approx 5.5 \times 10^{10}$ cm^{-2} and low temperature mobility of $\mu \approx 1 \times 10^6$ cm^2/Vs. With standard photolithography techniques, we defined a mesa with a rectangular 300×200 μm^2 central region and four arms extending to diffused NiAuGe ohmic contacts. Each arm has both a top and bottom gate in order to implement the selective depletion scheme and have independent contact to either (or neither) layer. A single bottom gate can be used to tune the density in the bottom layer within the central region. Four separate top gates with lengths of 100, 50, 20, and 10 μm each extend over the 200 μm wide mesa. As mentioned above, these individual top gates allow us to tune the density in the top layer under each gate in order to induce $\nu_T = 1$ in a localized region of the device.

When the top layer is kept at nominal density and a small (-2.59 V) bias is applied to the bottom gate to match the lower layer density with the upper layer density, one can see a tunneling resonance at zero magnetic field with a height of $G(0) \approx 1$ μS. Under these conditions the total tunneling area, which includes the rectangular central region and the four arms, is approximately 126,000 μm^2. This is about twice the area of the standard 250×250 μm^2 tunneling square sample.

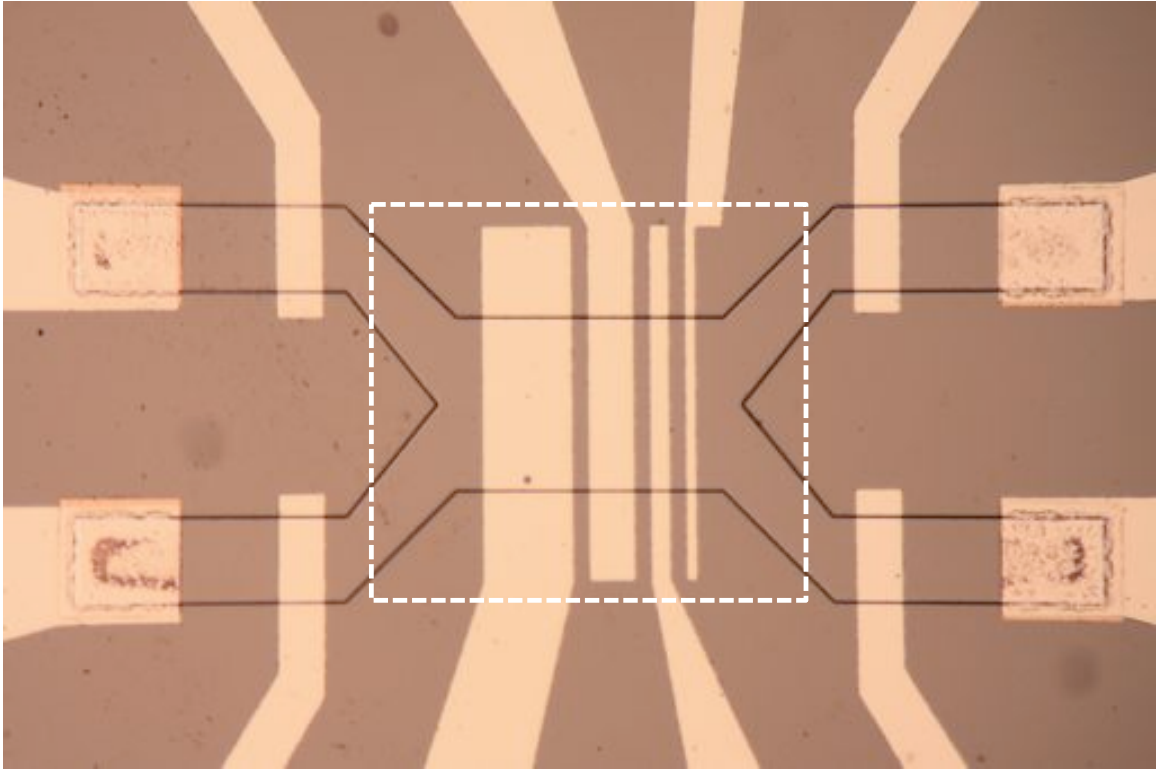Figure 5.2: Photograph of top side of Area Tunneling sample (11-1-04.1K). The mesa is 200 μm wide and the four top gates are (respectively) 100, 50, 20, and 10 μm long. A single back gate covers the central region of the mesa. The extent of this back gate is indicated by the white dashed rectangle.

5.2.1 Tunneling versus Area at $B = 0$

To test the device, we first measure tunneling conductance at zero magnetic field and $T = 60$ mK. In this regime, each layer behaves as a Fermi liquid and interlayer tunneling can be treated as a perturbation. As described in a previous chapter, conservation of in-plane momentum and energy together dictate that tunneling at zero interlayer bias is suppressed unless the electron densities in the two layers are equal. This is illustrated in figure 5.3, in which we plot the zero bias tunneling conductance $G(0)$ versus top gate bias for each of the top gates. Here, a bias of -15.18 V is applied to the back gate to reduce the bottom layer density from its nominal value. A peak in the conductance occurs when the top layer density under the swept gate matches that of the bottom layer, creating a balanced bilayer system.

Each peak sits on top of a background signal that comes from the rest of the sample, which remains in an imbalanced state. Though imbalanced, the ungated portions of the sample still shows a small tunneling conductance. By subtracting off this offset (derived from the tunneling conductance at zero top gate bias), we can plot the tunneling conductance from each top gated region versus top gate length in figure 5.3a. There is clearly a linear relationship between the two variables, signifying that the tunneling conductance is proportional to area at zero field. The fitted line has a small x-intercept of 3 ± 2 μm. Given that the top gates are situated 0.5 μm above the bilayer system, it is expected that the top layer density might smoothly vary over length scales of $\sim$1 μm at the edges of the gated regions. Consequently, the effective area of the balanced bilayer system would be reduced from that of the gated region, contributing to the observed x-intercept in figure 5.3b.

5.2.2 Tunneling versus Area at $\nu_T = 1$

Having confirmed that the effective tunneling area at zero magnetic field matches closely with the area of the lithographically defined regions, we now turn to tunneling data taken at $\nu_T = 1$. Below a critical interlayer separation $(d/\ell)_c$, a narrow tunneling resonance appears at zero interlayer bias. In this sample, $(d/\ell)_c \approx 1.91$ in the limit
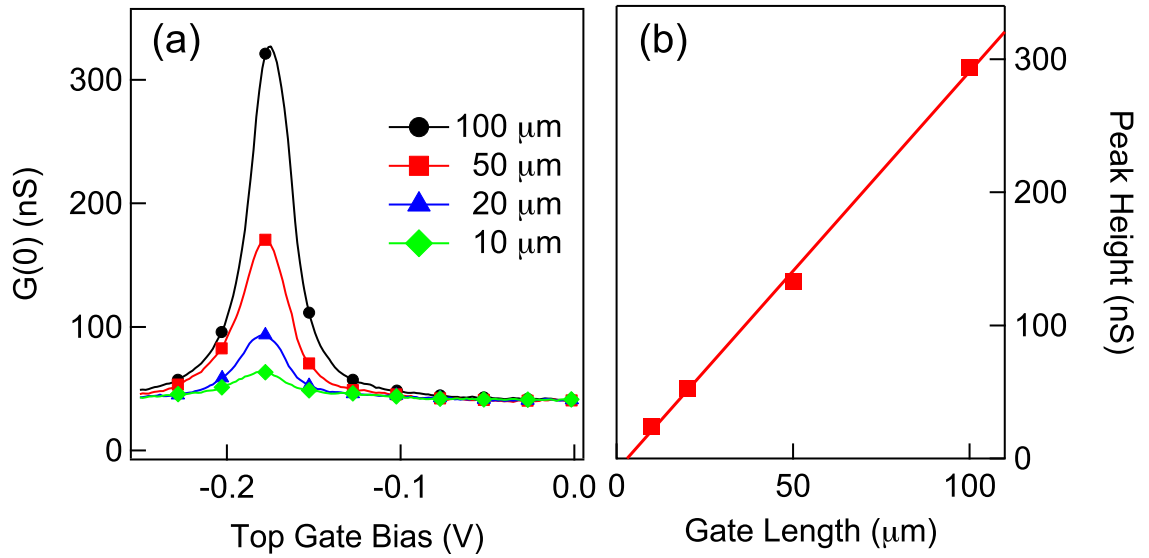
Figure 5.3: (a) Zero bias tunneling conductance $G(0)$ versus top gate bias taken at $B = 0$ and $T = 60$ mK and with an applied back gate bias of -15.18 V. Peaks correspond, in order of decreasing height, to the 100, 50, 20, and 10 μm long top gates. The traces are also identified by the corresponding symbol shown in the legend. (b) Background subtracted peak heights from (a) versus top gate length. The line fitted to these data has an x intercept of 3 ± 2 μm.

of $T \rightarrow 0$. Above this critical interlayer separation, we only observe incoherent tunneling, which is suppressed at zero bias by the Coulomb pseudogap [27].

For a range of d/ℓ and temperature, we apply a fixed bias to the back gate and each of the top gates to create a region of $\nu_T = 1$ and then measure the tunneling conductance dI/dV versus interlayer bias. For a given d/ℓ and temperature, this results in four different tunneling traces, one for each top gate.

In order to make meaningful comparisons, we must take care that the back gate and top gate biases are tuned so that the resulting correlated systems are at the same total density (i.e., at the same d/ℓ) and are density balanced. Such calibration at high magnetic fields requires a different strategy than at $B = 0$. It has been empirically found that the tunneling resonance remains centered at zero bias in spite of either moderate deviations from total filling factor $\nu_T = 1$ or small amounts of density imbalance (that is, $\nu_1 \neq \nu_2$) [13, 105]. This can be qualitatively explained by using the pseudospin picture of the $\nu_T = 1$ state to consider the linearly dispersing Goldstone mode that is the origin of the zero bias tunneling resonance. Here, the Goldstone mode is identified with the ability of the pseudospin vector to freely rotate around the z-axis; this angle of rotation about the z-axis is the order parameter ϕ. Inducing an imbalance by adjusting the top and back gate biases will cause the pseudospin vectors of the electrons to tend to tilt above or beneath the x-y plane in order to acquire a nonzero projection onto the z-axis, often denoted as $\langle m_z \rangle$. A nonzero $\langle m_z \rangle$ implies that a given electron is more likely to be in one layer or the other, consistent with the density imbalance. However, the energy will still be independent of the pseudospin vector's angle ϕ in the x-y plane. Consequently, the Goldstone mode will remain essentially massless and the tunneling resonance will still be located at zero energy (i.e., at interlayer voltage $V = 0$).

We perform the necessary density calibration by adjusting the back gate and each of the top gate biases so that $G(0)$ versus B has a peak at the desired magnetic field. To ensure density balance, further gate bias adjustments are made to perfect the symmetry of the tunneling resonance shape dI/dV versus interlayer bias. We find that there is a weak asymmetry of the tunneling resonance shape at $\nu_T = 1$ when the

bilayer is imbalanced. The origin of this asymmetry is not understood, but it may result from residual incoherent tunneling for which imbalance induced asymmetry is both expected and observed.

In figure 5.4, we show a characteristic set of the four tunneling resonances achieved at $d/\ell = 1.81$ and various temperatures ($T = 60$ to 150 mK). Because incoherent tunneling is suppressed at zero interlayer bias due to the Coulomb pseudogap [27], the background tunneling from ungated regions of the sample are comparatively much smaller than at zero magnetic field. Instead, the tunneling from the balanced $\nu_T = 1$ regions is by far the most prominent feature in the observed measurement of dI/dV versus interlayer bias. The exception is at higher temperatures, where the tunneling peak begins to disappear. We see that at $d/\ell = 1.81$ and $T = 175$ mK, thermal fluctuations have destroyed the interlayer coherence and no tunneling resonance is observable.

We plot the height of the tunneling peaks versus top gate length in figure 5.5 for a range of temperatures, all at $d/\ell = 1.81$. Once again, we find that the tunneling conductance is proportional to top gate length. A linear fit to the data still results in a positive x-intercept; for example, at $T = 60$ mK it is 3 ± 1 μm, similar to the value at zero field. As noted in figure 5.5, this linear relation holds for a range of temperatures. Indeed, we consistently find these results for a region near the phase boundary, as illustrated in figure 5.6.

However, deep within the correlated phase (i.e., at low d/ℓ and low temperature), our data deviate from a simple linear relation between tunneling peak height and top gate length. For example, in figure 5.7a we show tunneling traces taken at $d/\ell = 1.70$ and $T = 60$ mK. The relation between tunneling and top gate length now appears to be sublinear, as shown in figure 5.7b. Furthermore, the tunneling resonance from the 100 μm gate is clearly wider than the resonance from the 10 μm gate (FWHM $= 36$ μV and 22 μV, respectively). We believe that this behavior is not intrinsic to the $\nu_T = 1$ state, but rather can be explained by the extrinsic effects of the finite series resistance R_{series} between the contacts and the $\nu_T = 1$ region. Note that the tunneling measurements presented in this chapter are two-terminal. Thus, the finite
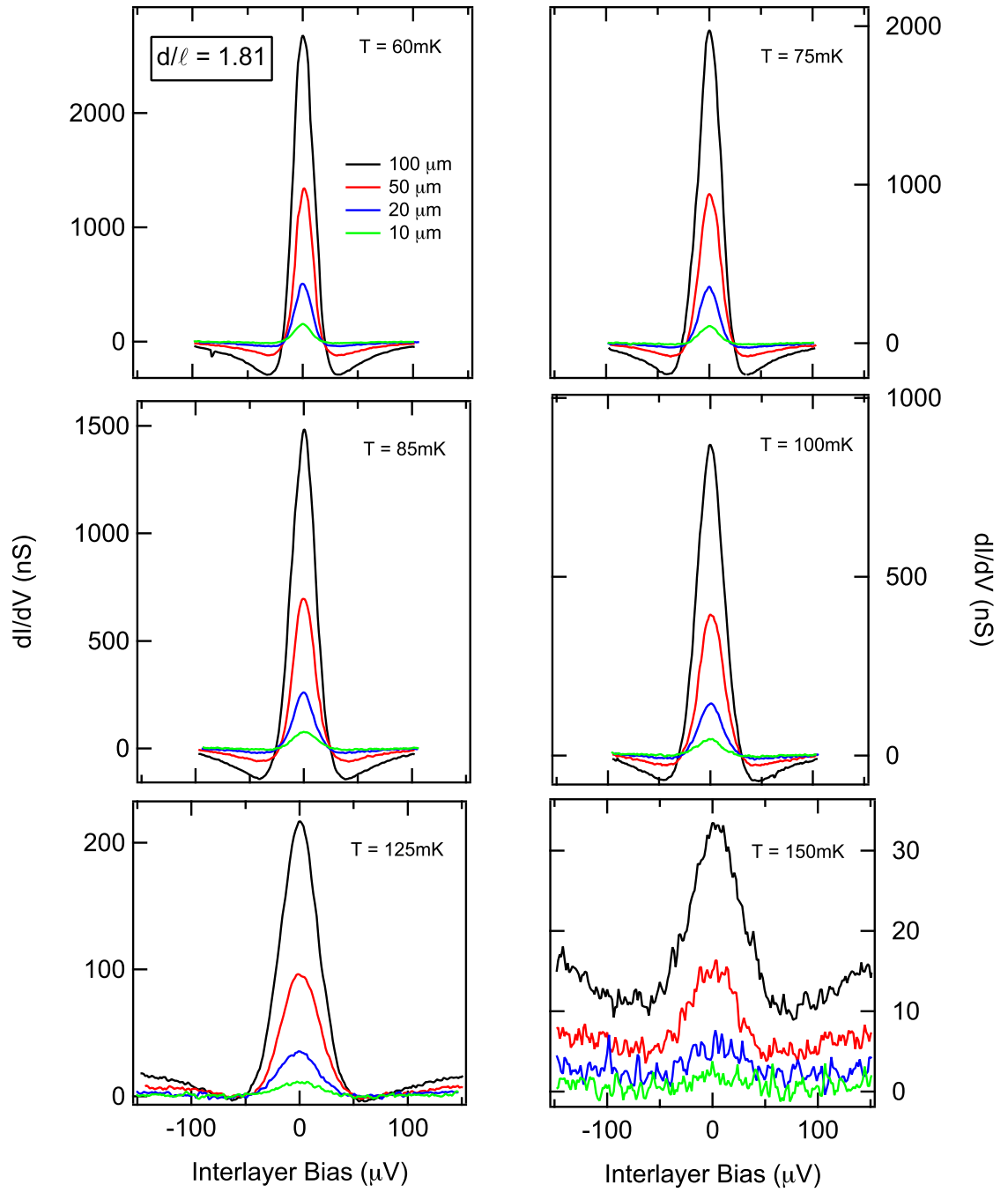
Figure 5.4: Tunneling spectra at $d/\ell = 1.81$ for various temperatures and all four top gates. Gate lengths 100, 50, 20, and 10 μm; tallest to shortest in peak height.
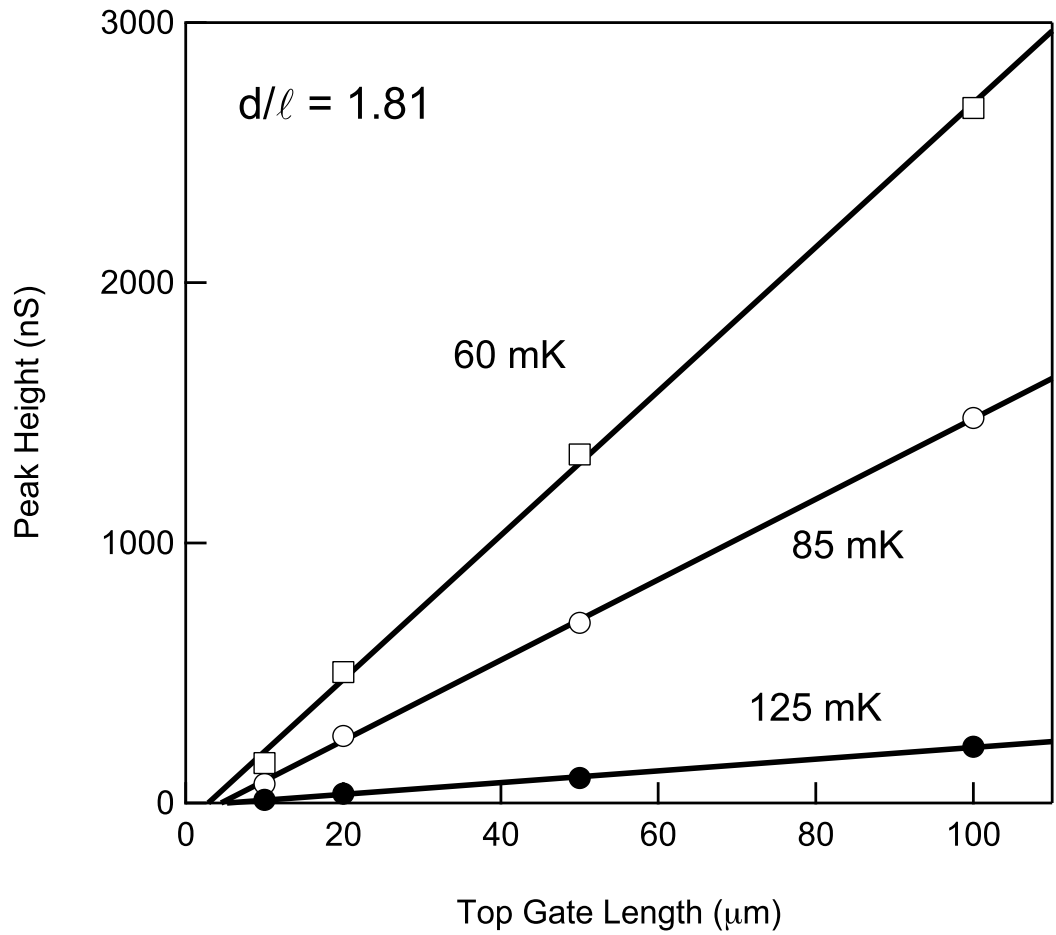
Figure 5.5: Peak height versus top gate length at $d/\ell = 1.81$ for $T = 60$, 85, and 125 mK.
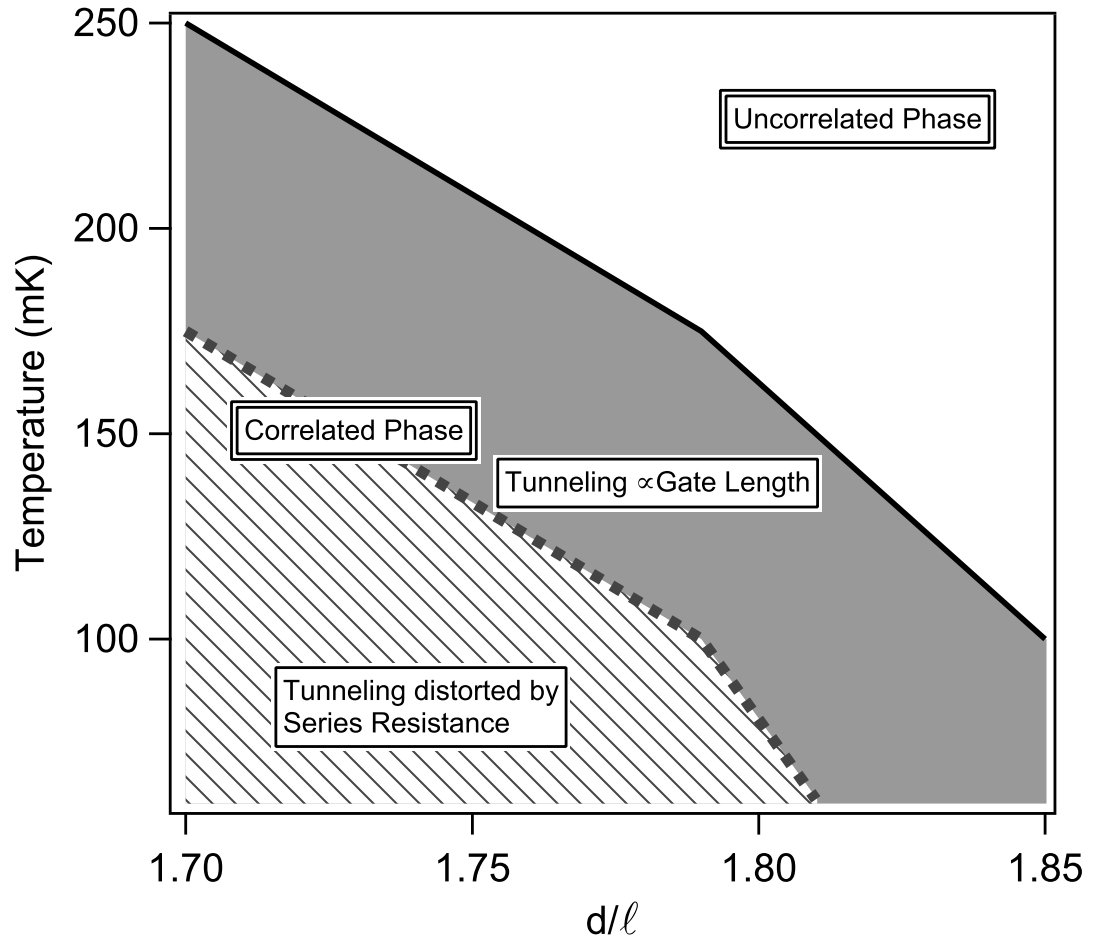
Figure 5.6: Phase diagram for area tunneling sample. The correlated $\nu_T = 1$ phase exists below the solid black line; above the line no tunneling resonance is observed at zero interlayer bias. In the solid grey region, the tunneling conductance appears to be proportional to top gate length. In the region below the dotted line, the tunneling spectra are too distorted by series resistance to compare the tunneling data from the various top gates.

series resistance can distort the observed dI/dV versus V whenever the tunneling conductance is large compared to $1/R_{series}$. In the regime of large tunneling, non-negligible voltage drops occur across the series resistance and the interlayer voltage across the tunneling junction significantly deviates from the applied voltage. Therefore, the apparent tunneling conductance peak becomes shorter and broader than it would be in the case of $R_{series} = 0$.

This distortion of the observed tunneling peak becomes more prominent as the tunneling conductance grows, and thus the data from the 100 μm top gate are more severely affected by finite series resistance than the tunneling traces from the 10 μm top gate. Therefore, we cannot meaningfully compare the various tunneling resonances from the four gates at low d/ℓ and low temperature. We instead limit our attention to the range of d/ℓ and temperature at which the four tunneling resonances have the same width and thus are not distorted by series resistance. We plot this region of parameter space in figure 5.6.

As the temperature is raised, the intrinsic tunneling conductance drops rapidly and the series resistance is expected to decrease somewhat. The sample then re-enters the regime where $1/G_{tunneling} \gg R_{series}$ and the two-terminal resistance is dominated by the tunneling resistance. For example, at $d/\ell = 1.70$ we observe that series resistance appears to no longer distort the tunneling spectra at $T \geq 175$ mK. As illustrated in figures 5.7c and 5.7d, at $T = 175$ mK the tunneling resonances for all four top gates have the same width and the relation between peak height and top gate length becomes linear once more.

Although we find that the tunneling conductance at $\nu_T = 1$ is proportional to top gate length near the phase boundary, we cannot yet conclude that tunneling is proportional to area because of the possibility that tunneling is somehow confined to the mesa edge. In that situation, the tunneling conductance would also increase linearly with top gate length. To rule this out, we must examine a second sample.
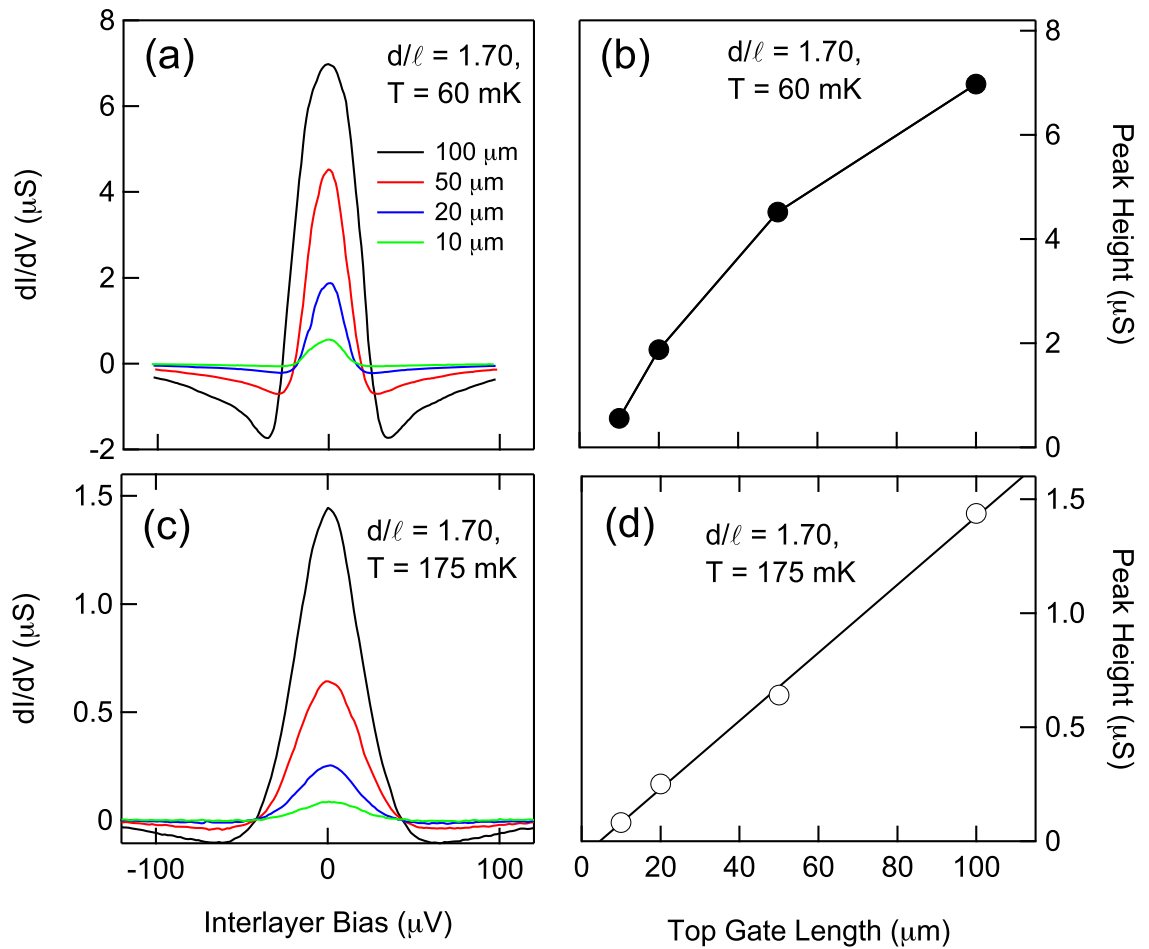
Figure 5.7: (a) Tunneling spectra at $d/\ell = 1.70$ and $T = 60$ mK. (b) Peak height versus top gate length from a). Line segments connect the data points, with no linear fit performed. (c) Tunneling spectra at $d/\ell = 1.70$ and $T = 175$ mK. (d) Peak height versus top gate length from c). A linear fit to the data is shown as well.

5.3 Perimeter Tunneling Sample

In order to fully probe the perimeter dependence of tunneling, we next turn our attention to a second device, sample 11-1-04.1L. This sample was created from the same wafer as the previous sample. A photograph of this sample's top side is shown in figure 5.8. Like the area tunneling device, this sample has multiple top gates covering a single mesa. However, the mesa now has two different widths: 100 μm and 200 μm. Consequently, the top gates now define two different kinds of regions: two identical 200 μm by 50 μm rectangles and a single 100 μm by 100 μm square. These two types of regions have identical areas (10,000 μm²) but different perimeters (600 μm versus 400 μm for the rectangles and square, respectively) and very different lengths along the mesa edge (100 μm versus 200 μm).

5.3.1 Tunneling versus Perimeter at $B = 0$

As with the area tunneling sample, we first test the sample at zero magnetic field by measuring the zero bias tunneling conductance $G(0)$ versus top gate bias for each of the gates. A representative sample of such data is shown in figure 5.9. A bias of -17.08 V is applied to the back gate. The solid trace corresponds to the 100 μm by 100 μm square region and the dotted trace is obtained by sweeping one of the 200 μm by 50 μm rectangles.

The tunneling resonance for the 100 μm square region is about 10 percent taller and the width is 10 percent smaller than that in the 200 μm by 50 μm rectangle. The origin of this discrepancy is not known precisely, but is likely due to differences in density inhomogeneities. Such inhomogeneities might be caused by different length scales of the fringe fields in the x and y directions, for example. Nonetheless, we can account for this apparent difference in effective area by renormalizing the tunneling data taken at $\nu_T = 1$ by the ratio of the heights of the tunneling peaks at $B = 0$. We determine this renormalization factor at each density (i.e., at each d/ℓ) studied.
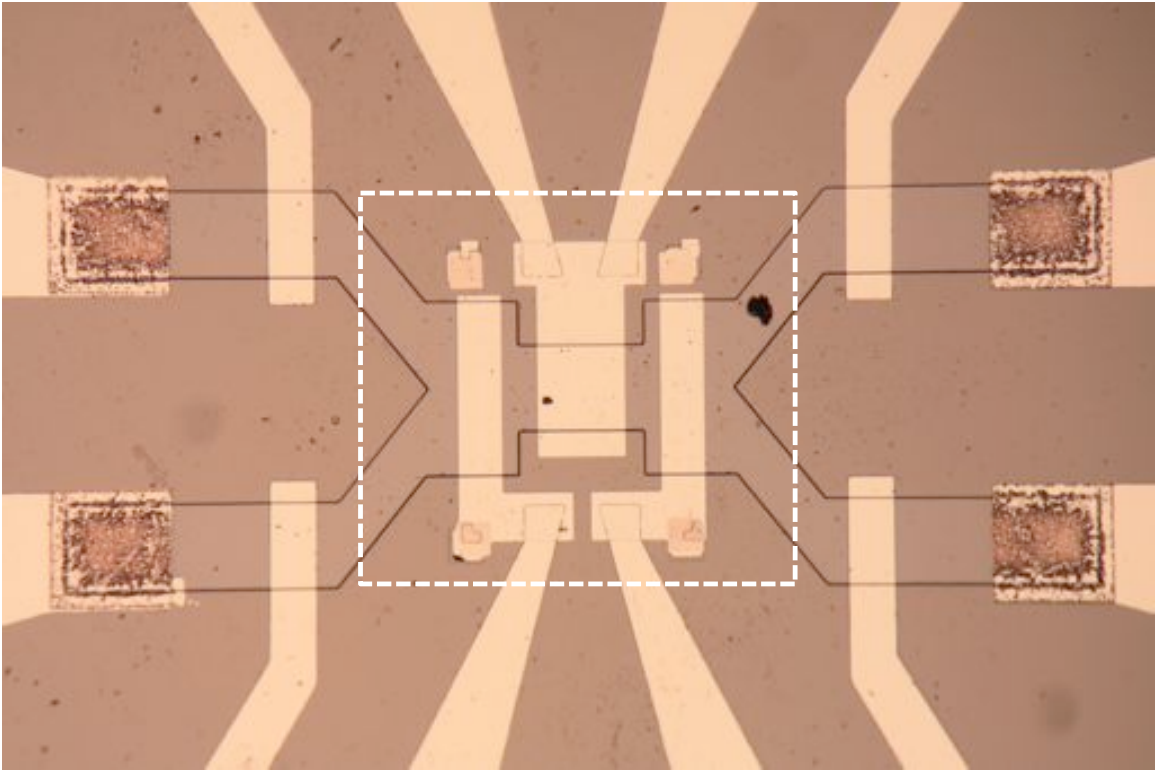
Figure 5.8: Photograph of top side of Perimeter Tunneling sample. The central top gate defines a $100 \times 100 \ \mu m^2$ square region. The other two gates define identical $200 \times 50 \ \mu m^2$ rectangular regions. A single back gate controls the density in the bottom layer for all three tunneling regions. The extent of this back gate is indicated by the white dashed rectangle.
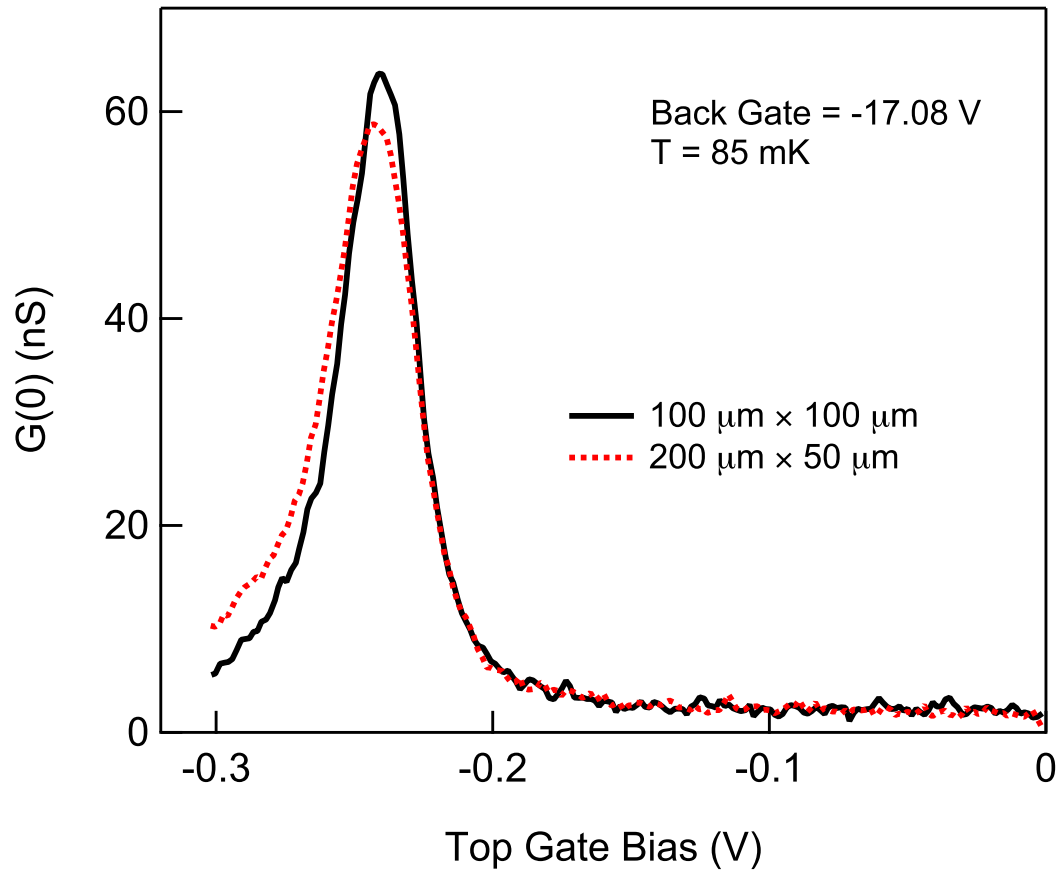
Figure 5.9: Zero bias tunneling conductance $G(0)$ versus top gate bias taken at $B = 0$ and with an applied back gate bias of -17.08 V. Solid trace is 100 μm by 100 μm top gate, dotted trace is 200 μm by 50 μm top gate.

5.3.2 Tunneling versus Perimeter at $\nu_T = 1$

After performing a calibration scheme identical to the one used for the area tunneling sample, we measured the tunneling spectra for each of the gated regions for a range of densities corresponding to $1.60 \leq d/\ell \leq 1.79$ and temperatures from $T = 60$ to 300 mK. A sample of such traces (after renormalization) are shown in figure 5.10. We focus on tunneling data taken from just one of the rectangular regions compared to the single square region.

The renormalized traces for the two differently shaped $\nu_T = 1$ regions are essentially identical for a wide range of d/ℓ and temperature. Thus, tunneling appears to be proportional to area rather than perimeter, even reasonably deep within the correlated regime.

It is important to note that we are able to use this sample to study tunneling farther away from the phase boundary than was possible for the area tunneling sample. There are two reasons for this. First, the bare tunneling matrix element appears to be somewhat smaller in the perimeter tunneling sample than in the area tunneling sample, leading to a diminished tunneling conductance overall. For example, 200 μm by 50 μm rectangular region results in a zero field tunneling conductance $G(0) = 60$ nS in the perimeter tunneling sample versus $G(0) = 130$ nS in the area tunneling sample. Consequently, the tunneling strength at $\nu_T = 1$ is also lower and one can perform two-terminal tunneling measurements at lower d/ℓ before finite series resistance significantly distorts the observed tunneling conductance.

Second, the two types of gated regions in the perimeter tunneling sample have nearly the same tunneling conductance at $\nu_T = 1$ and are identically affected by a fixed amount of series resistance. Thus, although at lower d/ℓ the two sets of tunneling traces might be broadened by the finite series resistance, we expect that they will still remain roughly equal to each other. We illustrate this in figure 5.11, in which finite series resistance has distorted the tunneling spectra recorded at $d/\ell = 1.60$ and $T = 60$ mK. Raising the temperature to 75 mK causes the tunneling resonances to grow in height and become narrower, indicating that the series resistance has lessened. For
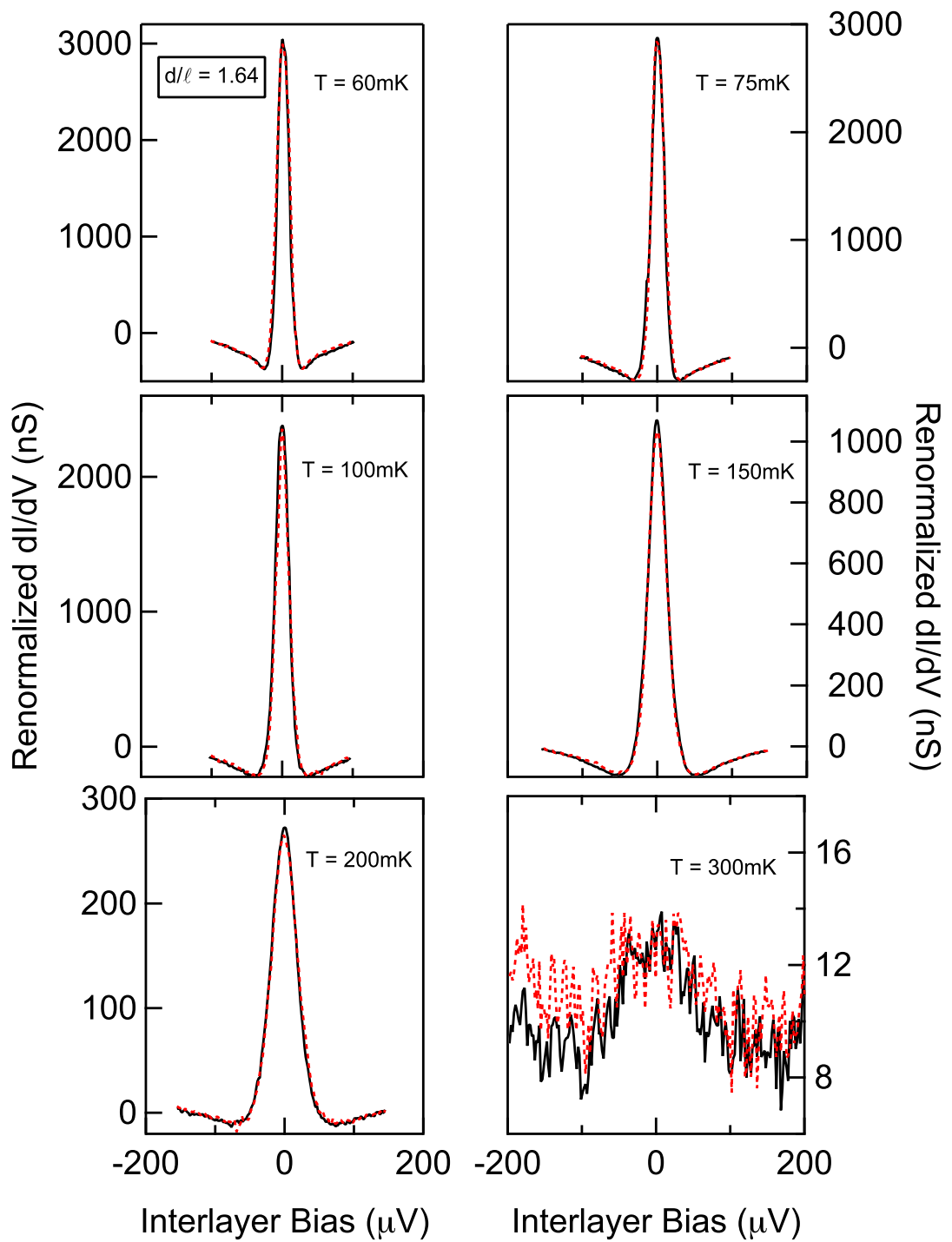
Figure 5.10: Tunneling conductance spectra at $\nu_T = 1$ with $d/\ell = 1.64$ and $T = 60$ to 300 mK. The solid (black) trace corresponds to the 100 μm square tunneling region and the dotted (red) trace to the 200×50 μm^2 rectangular region. The dotted trace has been multiplied by 1.086.

the entire range of temperatures studied, the tunneling resonances for the square and rectangular gates have essentially the same heights.

This is in contrast to the case in the area tunneling sample, in which the intrinsic tunneling conductance will vary by an order of magnitude between the smallest and largest $\nu_T = 1$ regions. As mentioned in the previous section, the tunneling traces for the 10 μm and 100 μm long regions will be qualitatively altered by finite series resistance quite differently and the tunneling conductance will no longer be proportional to top gate length.

5.4   Discussion

The results from the two samples described in this chapter provide strong evidence that the tunneling conductance of the $\nu_T = 1$ state is proportional to the system area, at least for a regime near the phase boundary. The data from the perimeter tunneling sample alone suggest that this conclusion is true even when relatively far away from the phase boundary. Thus, it is likely that the Josephson-like tunneling at $\nu_T = 1$ is a bulk phenomenon and not confined to the edges of the sample.

5.4.1   Disorder

Although the experimental evidence presented in this chapter might conflict with the expectation that tunneling should decay over the length scale of $\lambda_J \approx 1$ μm (as shown in figure 5.12a), a likely solution is that the simple model of tunneling that was presented earlier in the chapter is only appropriate in the limit of zero disorder. In reality, our samples are quite disordered, with variations in density caused primarily by inhomogeneity in the dopant layers. Such inhomogeneity leads to a disorder length scale of approximately 100–200 nm, set by the separation between the dopant layers and the 2DESs. Even the smallest $\nu_T = 1$ region examined in this chapter has dimensions much larger than this length. As depicted in figure 5.12b, such disorder in the form of density inhomogeneity could break up the sample into some regions
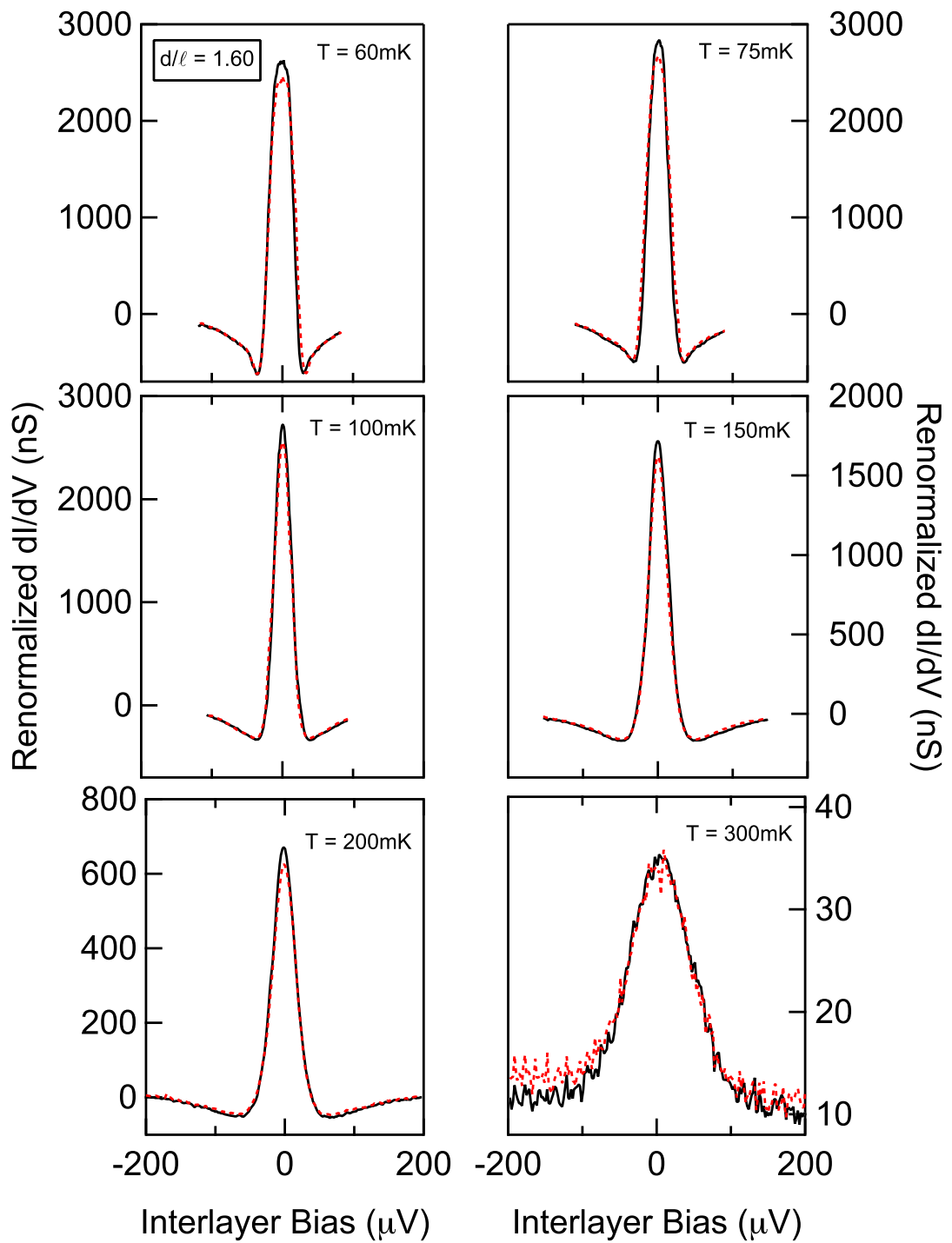
Figure 5.11: Tunneling conductance resonances dI/dV versus V (interlayer bias) at $\nu_T = 1$ with $d/\ell = 1.60$ and $T = 60$ to 300 mK. The solid (black) trace corresponds to the 100 μm square tunneling region and the dotted (red) trace to the 200×50 μm^2 rectangular region. The dotted trace has been multiplied by 1.088.

that are at $\nu_T = 1$ and some that are not. Thus, there could exist edges of $\nu_T = 1$ fluid throughout the bulk of the sample, causing tunneling to scale linearly with area.
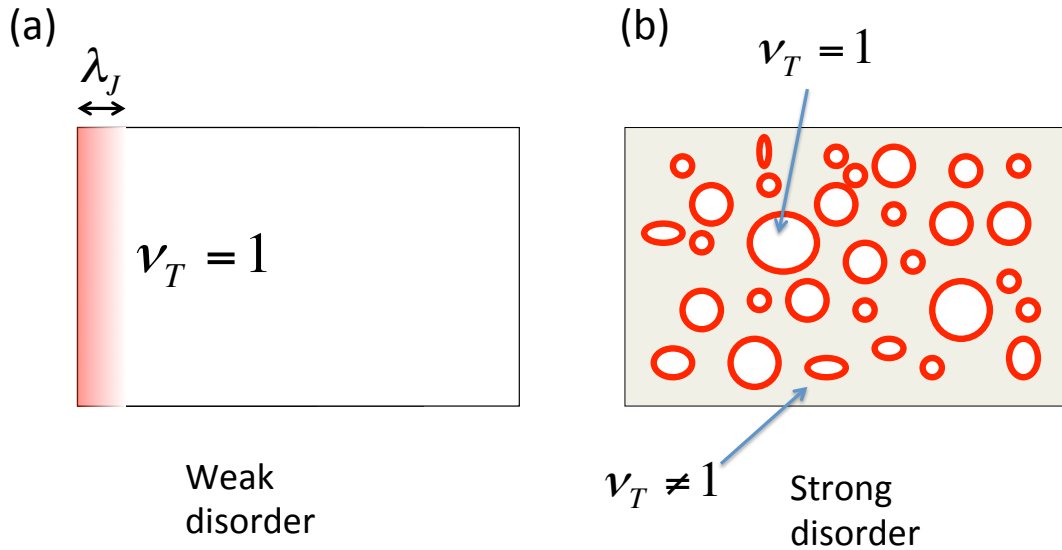
Figure 5.12: (a) Possible distribution of tunneling current in the clean limit, with all tunneling occurring within λ_J of the left edge, at which the current leads are located. (b) Possible distribution of tunneling current in a disordered sample, in which some fraction of the bilayer is at $\nu_T = 1$ and the remainder is not.

The important role that disorder could play in tunneling has been pointed out by multiple authors [6, 18, 33, 40, 91, 107]. The exact mechanism by which disorder reorganizes the tunneling current distribution is not fully known, though. Ultimately, disorder nucleates charged merons, which are vortices in the order parameter ϕ. For example, Fertig and Murthy [33] provide a model of disorder in which fluctuations in the 2DES density lead to a complex network of channels and nodes throughout the entire sample, in which the coherent $\nu_T = 1$ exists. Tunneling occurs at the nodes of the network, whose number are expected to be proportional to the sample area in large, highly disordered regions. Eastham, Cooper, and Lee [18] expand on this coherence network picture and describe how an emulsion of vortices-antivortices could suppress the spatial decay of the tunneling current by at least an order of magnitude. The disorder would effectively renormalize λ_J to a value comparable to the dimensions of the $\nu_T = 1$ regions examined in this chapter. Much larger samples would have to be

studied in order to observe the spatial decay of tunneling currents. We finally remark that strong disorder is also consistent with the unusually large width of the tunneling resonance [34] and the relatively small tunneling currents [112] that are observed experimentally. The small disorder length scale also agrees with the coherence length $\xi = 0.2$ μm derived from the decay of the tunneling resonance height with parallel magnetic field [102].

5.4.2   Bulk Counterflow Currents?

One might ask how the tunneling currents can be distributed throughout the bulk if charged excitations are confined to the edges due to the charge gap. Here, we cannot directly measure ρ_{xx} for charged excitations in the $\nu_T = 1$ regions due to our inability to perform four-terminal measurements on the gated regions. Furthermore, for the area tunneling sample we restrict our analysis to conditions close to the phase boundary, where the quantum Hall state is not fully formed. However, the data from the perimeter tunneling sample allow us to conclude that tunneling conductance remains proportional to area rather than to perimeter for regions of parameter space fairly deep within the correlated phase (down to $d/\ell = 1.60$ and $T = 60$ mK). A Corbino sample constructed from the same wafer as the samples considered in this chapter showed small conductivity of $\sigma_{xx} \approx 20 - 30$ nS for charged excitations under similar temperatures and interlayer separation. This bulk conductivity is far smaller than the 2500 nS of tunneling conductance observed under such conditions. This suggests that tunneling currents occur within the bulk of the $\nu_T = 1$ region despite the low conductance for charged excitations.

One possibility is that tunneling currents are equivalent to spatially decaying counterflow currents. Carried by neutral excitons, counterflow currents are conjectured to be able to flow through the interior of the $\nu_T = 1$ system, permitting tunneling in the bulk. The existence of such bulk counterflow currents will be explored and unambiguously demonstrated in the next chapter.

5.5 Conclusion

In conclusion, we observe that the Josephson-like tunneling conductance is proportional to the area of the $\nu_T = 1$ system when near the phase boundary. This implies that tunneling at $\nu_T = 1$ is a bulk phenomenon in this regime. With one sample we also find evidence for bulk tunneling deeper within the correlated phase. Our results suggest that disorder plays a strong role in determining the spatial distribution of interlayer tunneling at $\nu_T = 1$.

Chapter 6

Bulk Exciton Transport

While the previous chapter found evidence of tunneling occurring within the bulk of the $\nu_T = 1$ quantum Hall system, the analysis was mainly confined to regions of the phase diagram near the boundary between the correlated and uncorrelated phases. There, the interior of the bilayer system could remain relatively compressible with respect to charged excitations. We next consider studies deep within the correlated phase, where charge currents are highly suppressed and we find evidence of neutral excitonic currents in the bulk.[1]

This chapter contains the central result of this thesis: counterflowing currents may propagate through the bulk of the $\nu_T = 1$ system, where charged excitations are gapped out. These counterflow currents may carry energy through the insulating interior without transporting charge and are identical to exciton currents. To unambiguously detect the bulk exciton flow, we must resort to a Corbino geometry in which there are two sets of electrical contacts that are separated from each other by the bulk of the $\nu_T = 1$ system. Thus, these two sets of contacts are not connected to each other by charge-carrying edge currents, which could otherwise complicate measurements of bulk exciton currents. We also must contend with the large interlayer tunneling that is characteristic of the $\nu_T = 1$ system and could greatly pollute our results. These findings were first reported in reference [39].

---

[1]This chapter contains work that was first presented in A. D. K. Finck, J. P. Eisenstein, L. N. Pfeiffer, and K. W. West, *Phys. Rev. Lett.* **106**, 236807 (2011). Copyright 2011 by the American Physical Society.

6.1 Theory of Exciton Currents at $\nu_T = 1$

6.1.1 Previous Studies

Essentially all of the spectacular bilayer transport properties of $\nu_T = 1$ can be linked to the presence of neutral excitons that are condensed into a single state. The formation of these phase-coherent excitons is thought to capture the essential physics of the strong interlayer correlations at $\nu_T = 1$ that lead to enhanced interlayer tunneling [103, 104], large Coulomb drag [67, 65, 120], and vanishing Hall resistance when electrical currents are driven in opposite directions in the two layers (i.e., counterflow) [66, 121, 127]. These phenomena and the interlayer coherence that they imply motivate the description of the $\nu_T = 1$ QH state as a Bose-Einstein condensation of excitons.

However, the evidence for exciton transport at $\nu_T = 1$ has hitherto remained indirect. Nearly all of the previous experiments of $\nu_T = 1$ have employed samples with the same topology as Hall bars. That is, they studied devices in which all of the electrical contacts were along the same edge of a mesa. Thus, the contacts were connected by topologically protected edge channels with gapless charged excitations that are common to all quantum Hall systems. It is unclear if previous studies of Hall bars were merely probing the transport properties of the charge-carrying edge channels. Such samples cannot directly detect the flow of excitons in the bulk of the $\nu_T = 1$ system.

6.1.2 Hall Counterflow

For example, we consider the case of counterflow currents in a Hall bar sample at $\nu_T = 1$. Kellogg et al. [66] first found that when currents of equal magnitude were directed in opposite directions within the two layers of a bilayer 2DES, the Hall resistance R_{xy} of either layer vanished at low temperature and low d/ℓ. Similar results were reported by Tutuc et al. [121] using a bilayer hole system at $\nu_T = 1$. Such findings are consistent with exciton transport because excitons are charge neutral and

should therefore feel no Lorentz force. Furthermore, both groups also found that the longitudinal resistance R_{xx} was small, so that a naïve calculation of σ_{xx} seemed to imply unusually large conductivity of exciton flow. This provided the first evidence of the anticipated excitonic superfluidity [125, 30, 82, 80], in which the excitons flow with vanishing dissipation.

As a side note, we should point out that in two dimensions true superfluidity is thought to be impossible. The very act of driving current will cause the motion of vortices in the order parameter, leading to dissipation [2]. Instead, it was anticipated that the $\nu_T = 1$ state should exhibit a power-law $I - V$ curve for counterflow currents [82, 1], in which the differential resistance vanishes at zero current. Beyond zero current, resistance is expected to rise.
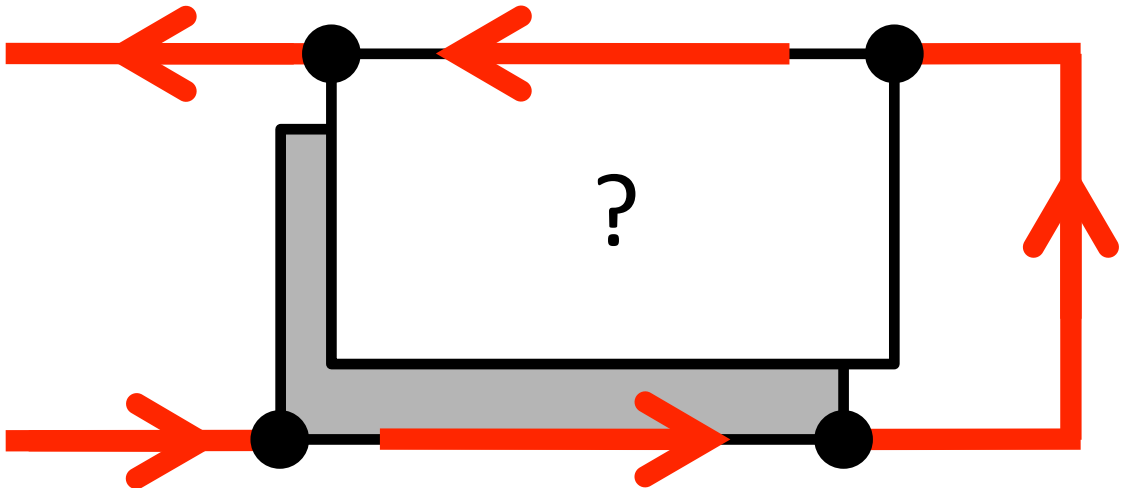
Figure 6.1: Hall bar sample during a counterflow measurement. The arrows indicate the possible flow pattern for charged currents in the edge channels as well as in the external circuitry. The black dots are ohmic contacts.

However, the results the Hall bar studies are ultimately ambiguous about the transport properties of the excitons themselves. For example, as depicted in figure 6.1, it is possible that charge currents are flowing through the edge channels during a counterflow experiment. When an electrical current is injected into one layer at a contact along the edge, it cannot enter the bulk because of the charged excitations are

gapped out in the interior and thus have zero conductivity in the bulk. Instead, the charge must continue to flow along the edge of the sample within the edge channels. Charged quasiparticles can hop from one layer to the other at the edge by emitting or absorbing an exciton (for example, see reference [112]), but charge conservation requires that they cannot disappear altogether.

The charge currents in the edge channels during a counterflow measurement are problematic for two reasons. First, measurements of dissipation in the form of longitudinal voltage drops (that is, R_{xx}) might merely reflect the dissipation of the charged quasiparticles rather than the excitons themselves. Like any other quantum Hall state, charged quasiparticles at $\nu_T = 1$ are expected to display activated dissipation $R_{xx} \propto e^{-\Delta/2T}$ that remains finite at nonzero temperature. This is in contrast to the absolute absence of dissipation below a critical temperature in the limit of zero current as expected in the case of two-dimensional superfluid. Indeed, measurements of counterflow in Hall bars do find activated transport and no nonlinear behavior [66, 121, 127]. Although this residual dissipation in counterflow has been explained by invoking the influence of topological defects such as merons (for example, see reference [107, 33, 91]), the quasiparticle flow in the edge channels remains as another possible source of resistance [112].

The second and more fundamental problem of charge currents at the edge is that they prevent Hall bars from being able to directly detect *bulk* exciton flow. Since excitons are neutral and not confined to the edges by the Lorentz force, they should be able to carry energy through the interior of the $\nu_T = 1$ system. However, it is not immediately clear if they are free to do so in real samples. For example, weak layer-antisymmetric disorder might pin exciton currents [19] or induce a pseudospin gauge-glass state [98, 109] that could prevent the excitons from penetrating the interior of the $\nu_T = 1$ system. One cannot demonstrate this key property of exciton transport using a Hall bar because the charged quasiparticles in the edge channels can also carry energy between the various contacts without ever having to move through the bulk.

While the observation of vanishing Hall resistance might suggest that counterflow

currents are not confined to the edges of the sample, the charge currents depicted in 6.1 could also lead to the appearance of $R_{xy} = 0$. Following the argument that Kun Yang gave to predict quantized Hall drag in bilayer QH states [129], driving a charge current I through a edge channel in the lower layer will cause the electrochemical potential of that edge channel to rise by an amount proportional to I. This reflects the occupation of higher energy states in the compressible edge channel. In the case of $\nu_T = 1$, the rise in the electrochemical potential is given by $\Delta\mu_L = \frac{h}{e^2}I$. Because of strong electron–electron repulsions, the electrons added to the lower layer will prevent the occupation of the corresponding states in the *upper* layer. An electron added to the upper layer must instead enter a state that is not directly above a filled state in the lower layer. Because the Fermi energy of the lower layer has risen by $\Delta\mu_L$, this means that the energy cost for adding an electron in the lower layer has risen by the same amount. Thus, when current flows along the edge in one layer the electrochemical potential for *both* layers rises by the same amount. Note that we did not have to explicitly invoke a bulk exciton current to arrive at this result.

We next consider this phenomenon in the case of counterflowing currents within a Hall bar. In figure 6.1, equal magnitude currents are flowing through two different edges of the sample. Within a given layer, the electrochemical potential along either edge will rise by the same amount: $\frac{h}{e^2}I$. For one of the edges, this rise in potential will be due to charge flowing through the chosen layer. For the other edge, the rise is because of charge flowing through the opposite layer. Thus, a measurement of Hall voltage (i.e., the difference in electrochemical potential between the two edges along a particular layer) will read zero.

In short, it seems possible that vanishing Hall resistance can be observed with or without bulk exciton currents. Measurements of Hall bar samples are ultimately unable to directly sense such exciton currents. In order to unambiguously demonstrate exciton transport, one must drive counterflow currents through the interior of the $\nu_T = 1$ region, where charged excitations are gapped out. This requires an alternative to the Hall bar topology.

6.2   Description of Corbino Sample

In order to probe the bulk conductance of counterflow currents, we studied a bilayer sample with a Corbino geometry. A photograph of this device (sample 7-12-99.1JJ) is shown in figure 6.2a. This sample was fabricated from a wafer with the usual double quantum well structure: two 18 nm wide GaAs quantum wells separated by a 10 nm $Al_{0.9}Ga_{0.1}As$ barrier. Each quantum well is populated with a 2DES with nominal density $n \approx 5.5 \times 10^{10}$ cm^{-2} per layer and low temperature mobility $\mu \approx 1 \times 10^6$ cm^2/Vs.

The sample is patterned into an annulus with inner diameter 1 mm and outer diameter 1.4 mm. Due to the relatively large size of the device, great care was taken during its fabrication in order to avoid any significant defects in the original GaAs wafer that could short the two layers together. Six 100 μm wide arms extend from the annulus to diffused NiAuGe contacts. There are four arms on the outer edge of the annulus and two on the inner edge. Each arm is crossed by front and/or back aluminum gates to implement the selective depletion technique. While each of the outer arms has both a top and bottom depletion gate associated with it, the two inner arms have either just a top depletion gate or just a bottom depletion gate. The annulus itself is covered by a large top gate and has a bottom gate directly underneath it. These two gates allow us to independently tune the 2DES densities in the upper and lower layers within the annulus. We will confine ourselves to the case where the two layers have equal densities.

In figure 6.2b we show a simplified picture of the sample, with the gates omitted. Each ohmic contact is numbered. Contacts 1 through 4 are connected to the outer edge of the annulus while contacts 5 and 6 are along the inner edge. We will refer to this numbering scheme in circuit diagrams throughout this chapter.

In figure 6.3, we show measurements of interlayer tunneling conductance dI/dV versus interlayer bias at zero magnetic field and $T = 14$ mK. Note we have subtracted off from the recorded bias a small offset (20 μV) induced by the input of the current preamp. Here, we show traces for two different densities: $N_T = 1.11 \times 10^{10}$ cm^{-2}
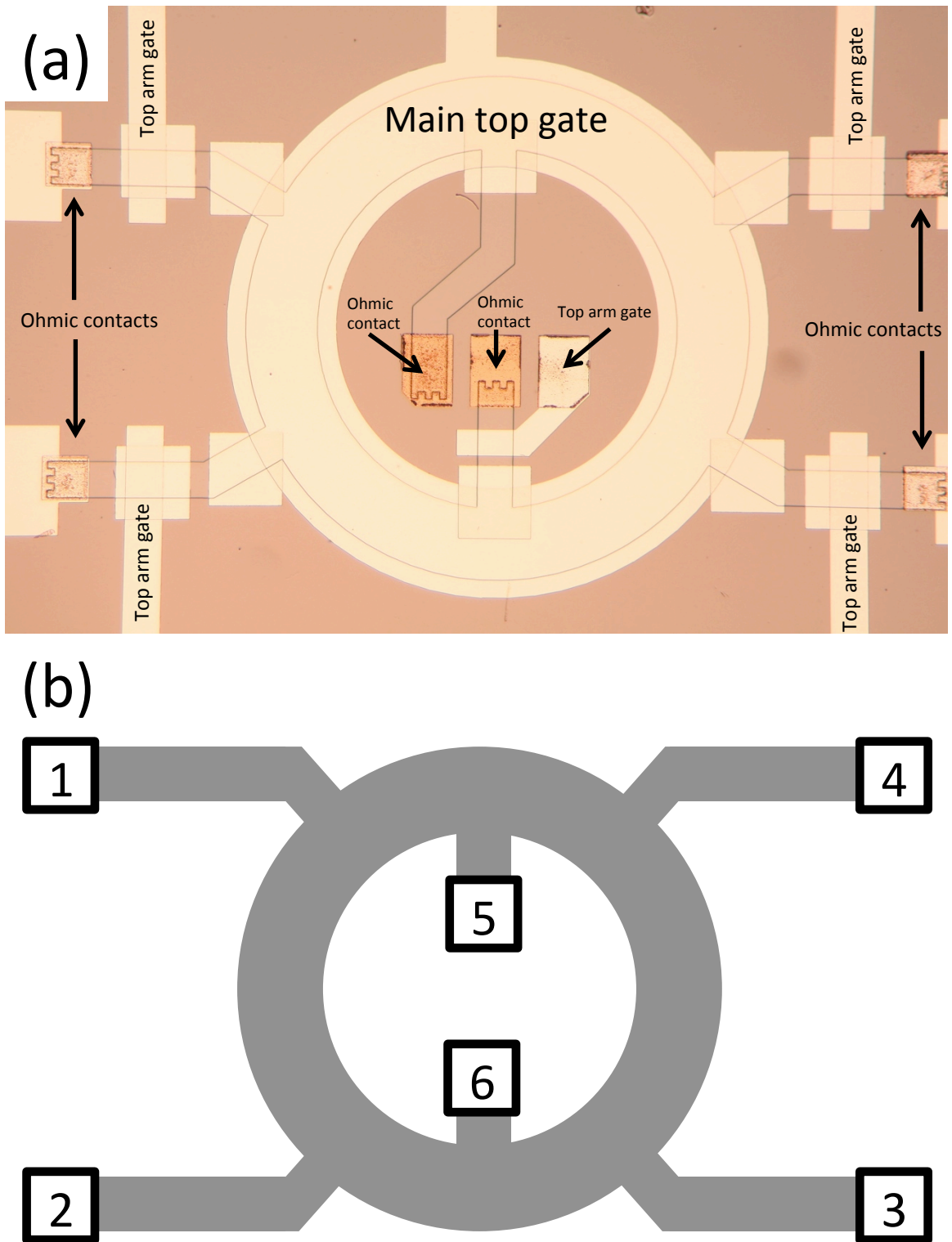
Figure 6.2: (a) Photograph of top side of sample 7-12-99.1JJ. (b) Simplified diagram of sample with labeled ohmic contacts. This labeling will be used throughout this chapter.

(nominal density) and $N_T = 0.45 \times 10^{10}$ cm^{-2} (corresponding to $d/\ell = 1.49$ at $\nu_T = 1$). Note that the peak tunneling conductance $G(0) \approx 1.5$ μS is much larger than seen in other samples made from the same GaAs/AlGaAs wafer. We attribute this primarily to the large size of the device, which has 12 times the area of the usual 250 μm square samples. The sample is wired to a rotating sample mount, allowing us to tilt the sample with respect to the magnetic field and introduce a field parallel to either 2DES. This will permit us to suppress the $\nu_T = 1$ tunneling current. We will reveal below why this is vital for our counterflow measurements. It is important to note that each wire is thermally sunk to the cold-finger of the dilution fridge using an RC filters, with $R = 10$ kΩ and $C = 500$ pF. The resistors in the RC filters will contribute to the series resistance in each measurement.
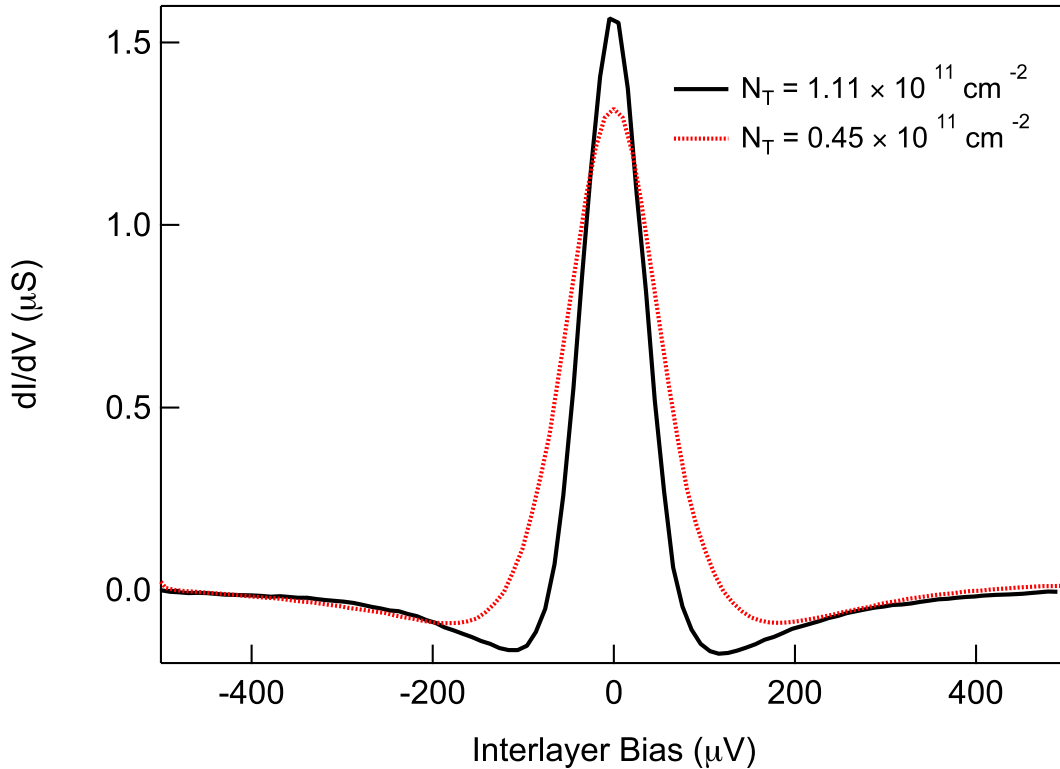
Figure 6.3: Interlayer tunneling at zero magnetic field and $T = 14$ mK for total density $N_T = 1.11 \times 10^{11}$ cm^{-2} (solid black trace) and $N_T = 0.45 \times 10^{11}$ cm^{-2} (dotted red trace).

6.3 Parallel Corbino Conductance

Corbino conductance[2] σ_{xx} is a measure of the ability for charged excitations to travel through the bulk of the bilayer system. In a single-layer system, σ_{xx} can be found by inverting the resistivity matrix:

$$\sigma_{xx} = \frac{\rho_{xx}}{\rho_{xx}^2 + \rho_{xy}^2}. \tag{6.1}$$

In a classical 2DES, σ_{xx} can be severely reduced by a sizable ρ_{xy} because current that is injected into an interior contact must circulate within the bulk multiple times before it reaches the outer edge. Within the bulk of a standard quantum Hall state, the Fermi energy lies within the energy gap separating two different bands of extended states. Thus, there are no states near the Fermi energy that can transport charge from one edge of the sample to the other. This implies that both $\rho_{xx} = 0$ and $\sigma_{xx} = 0$.

In a bilayer sample, one can consider both parallel Corbino conductance $\sigma_{xx}^{\parallel}$ and counterflow Corbino conductance σ_{xx}^{CF}. We first focus on parallel Corbino conductance, in which one drives currents within the same direction in the two layers from one edge of the annulus to another. As depicted in 6.4a, we realize this current flow pattern in our device by applying a small AC excitation voltage (20 μV at 13 Hz) to an ohmic contact on the outer rim (for example, contact 1) and detecting the current flowing to ground via a contact along the inner rim (contact 5). These two ohmic contacts are connected to both layers at the same time while all other ohmic contacts are fully disconnected from the annulus. The white triangle in the circuit diagram symbolizes a low impedance current preamp whose output is read by a lock-in amplifier.

In figure 6.4b, we plot parallel Corbino conductance versus magnetic field while the sample is near nominal density and $T = 50$ mK. Deep minima can be seen each time the individual layers enter a quantum Hall state. Both integer and fractional

---

[2]We will use the symbol σ_{xx} to denote both conductance and conductivity. In reality, the Corbino conductance is equal to the Corbino conductivity times the geometric factor $\frac{2\pi}{\ln(R_2/R_1)}$, where R_1 and R_2 are respectively the inner and outer diameters of the annulus. In our device, this geometric factor is approximately 18.7.

QH states are visible. Nominal density corresponds to $d/\ell = 2.34$ at $\nu_T = 1$, which is well above the critical interlayer separation $(d/\ell)_c \approx 1.8$. Thus, no quantum Hall state is observed at $\nu_T = 1$ in figure 6.4b.

In figure 6.4c, the density has been lowered to $N_T = 0.45 \times 10^{11}$ cm^{-2}, which corresponds to $d/\ell = 1.49$ at $\nu_T = 1$. At this low d/ℓ and low temperature ($T = 25$ mK), the $\nu_T = 1$ quantum Hall state is well formed and is centered on $B_\perp = 1.88$ T. As has been reported before by Tiemann et al. [117], parallel Corbino conductance vanishes at $\nu_T = 1$ because charged excitations are gapped out in the bulk. Note that the minimum in σ_{xx} at $\nu_T = 1$ is not as well developed as the minima associated with integer QH states in the individual layers. This is consistent with the disparity between the charge gaps for the relatively fragile $\nu_T = 1$ QH state and the robust integer states.

6.4 Tunneling and Counterflow with Zero Parallel Field

While the $\nu_T = 1$ QH state resembles single-layer QH states from the perspective of parallel (i.e., charge) transport, its unique excitonic properties become apparent in transport measurements that rely on contacting the two layers separately. In this section, we will focus on tunneling and counterflow measurements of our Corbino sample at zero tilt angle. In the absence of a parallel magnetic field, tunneling conductance at $\nu_T = 1$ is enormously enhanced beyond single particle tunneling. Strong interlayer tunneling complicates the interpretation of previous Corbino studies [117, 116] by effectively shorting out the bulk counterflow path and lead to bilayer transport anomalies that cannot directly demonstrate bulk counterflow currents. Here, we will show how to overcome the tunneling problem by driving more current through the sample than is allowed by interlayer tunneling [23, 117, 132]. This will permit us to demonstrate bulk counterflow currents even in the presence of strong interlayer tunneling.

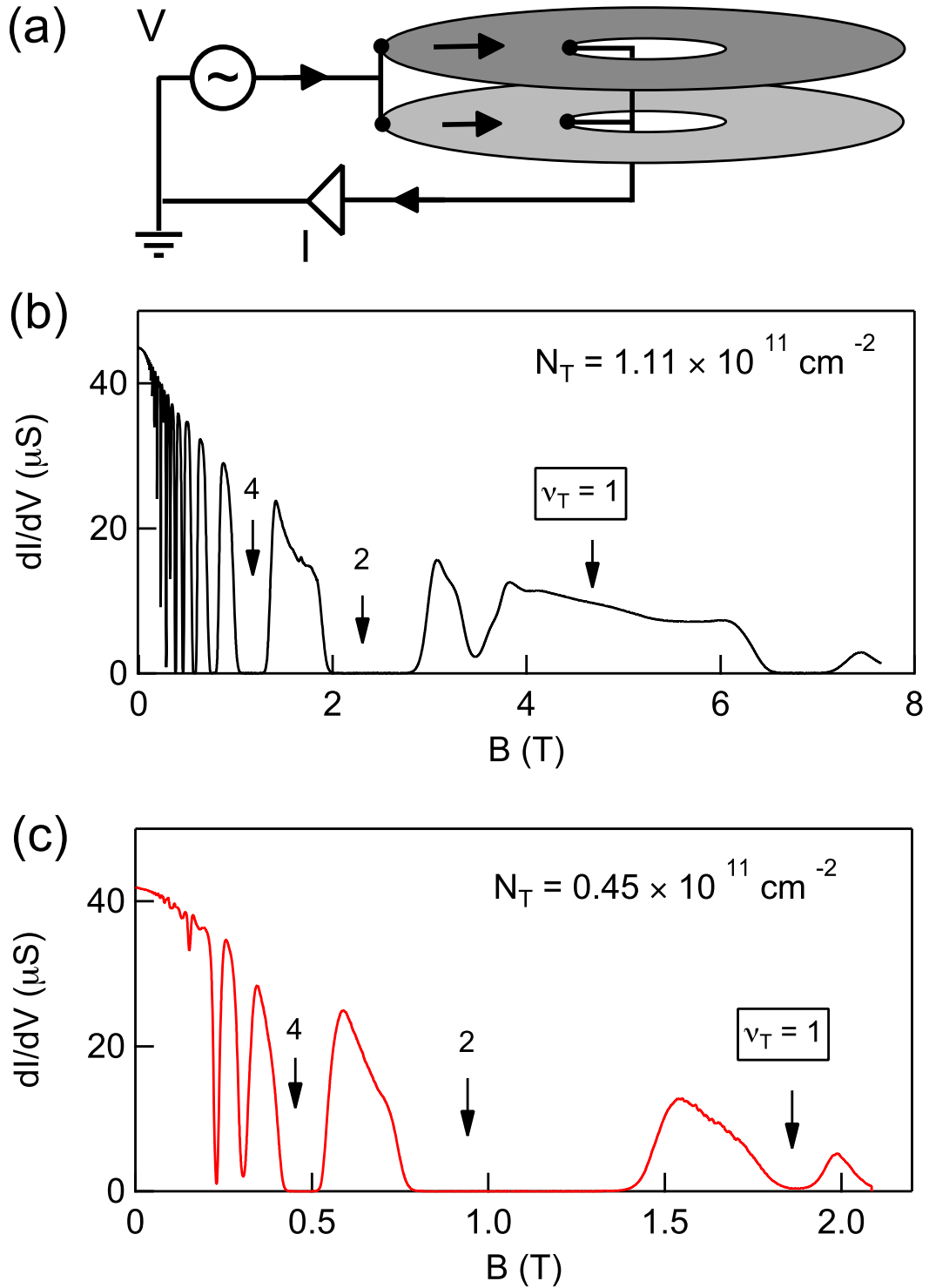Figure 6.4: (a) Circuit for parallel Corbino conductance. We show the main annular section of the sample as well as the external circuitry. (b) Parallel Corbino conductance at total density $N_T = 1.11 \times 10^{11}$ cm^{-2} and $T = 50$ mK. This corresponds to $d/\ell = 2.34$ at $\nu_T = 1$. No quantum Hall state is observed at $\nu_T = 1$. (c) Parallel Corbino conductance at $N_T = 0.45 \times 10^{11}$ cm^{-2} and $T = 25$ mK.

6.4.1 Two-Terminal Tunneling

We first consider two-terminal measurements of interlayer tunneling at $\nu_T = 1$. We employ the standard tunneling circuit, pictured in figure 6.5a. The two-terminal $I - V$ characteristics for tunneling are acquired by applying a bias to an ohmic contact connected only to the top layer and measuring the current that exits from a bottom layer contact. We denote this two-terminal bias as simply V. The interlayer bias has both a DC and AC (usually 20 μV and 13 Hz) component. The differential tunneling conductance for $d/\ell = 1.49$ and $T = 25$ mK is shown in figure 6.5b. The DC tunneling current is simultaneously recorded and shown in figure 6.5c.

A number of important features can be seen in the two-terminal tunneling traces. First, the differential tunneling conductance peak is dramatically wider than the narrow tunneling resonance first reported [103] in bilayers at $\nu_T = 1$. This is due to the large series resistance, which is expected to distort the tunneling spectrum whenever the resistance in series with the tunneling junction is large compared to the tunneling resistance (for example, see reference [117]). Although a finite bias is applied to the upper layer, nearly all of the voltage drop occurs along the 2DES leading to the $\nu_T = 1$ region rather than between the two layers at the tunnel junction. We will demonstrate this later by considering four-terminal measurements of tunneling.

A second observation is that the tunneling conductance is highly nonlinear in the region of -150 to 150 μV applied bias. One can see a clear dip in the two-terminal conductance at zero bias. Such behavior will reappear in other conductance measurements in this chapter. Thus, it is important to emphasize here that the dip is *not* an intrinsic property of the $\nu_T = 1$ state. Instead, the nonlinearity is associated with the extrinsic series resistance between the contacts and the $\nu_T = 1$ region. When the tunneling resistance is small the two-terminal resistance in the tunneling measurement should be dominated by this series resistance. The main contributors of the series resistance are the portions of the bilayer system that lie at the interface between the gated and ungated regions of the sample. In this interface, the electron density in both layers varies between the nominal value and the reduced value in the

$\nu_T = 1$ region. For example, because the back gate is 50 μm away, its fringe fields cause a density gradient in the bottom layer over a large region at the edge of the gated area. Some parts of this region have a single-layer filling factor of less than one but do not fall within the $\nu_T = 1$ quantum Hall state; thus, they will lack an edge channel. Consequently, their two-terminal conductance can be much less than e^2/h. Measurements of two-terminal conductance between two contacts that are connected to the same layer and are along the same edge of the same layer reveal nearly the same nonlinear behavior as seen in the two-terminal tunneling measurements. We will examine the behavior and causes of this series resistance in greater detail in Section 6.7.

Finally, the DC tunneling current in figure 6.5c appears to change discontinuously near applied bias $V = -150$ μV and $V = 150$ μV. This reflects an instability of the composite $I - V$ of the tunneling junction with finite series resistance [54].

6.4.2 Four-Terminal Tunneling

In a conventional four-terminal measurement, the influence of series resistance is eliminated by directly measuring both the current and voltage drop associated with the system of interest. For 2D to 2D tunneling, one might obtain the true $I - V$ curve by measuring both the tunneling current and the voltage difference between the two layers. The circuit that we used to accomplish this for our Corbino sample is shown in figure 6.6a. Voltage probes are on the same edge of the annulus as the current leads. We plot the tunneling current I versus the detected interlayer voltage V_{4pt} for various temperatures in figure 6.6b.

First we focus on the $T = 25$ mK data. Just as in the case for previous studies of strongly tunneling samples [116], we find that now the four-terminal $I - V_{4pt}$ trace appears to closely resemble the two-terminal $I - V$ traces measured using weakly tunneling samples (for example, see reference [23] and [102]). More precisely, when the applied bias falls within the range of -150 to 150 μV, the interlayer voltage V_{4pt} is nearly zero despite the large tunneling current flowing. Thus, as asserted earlier,
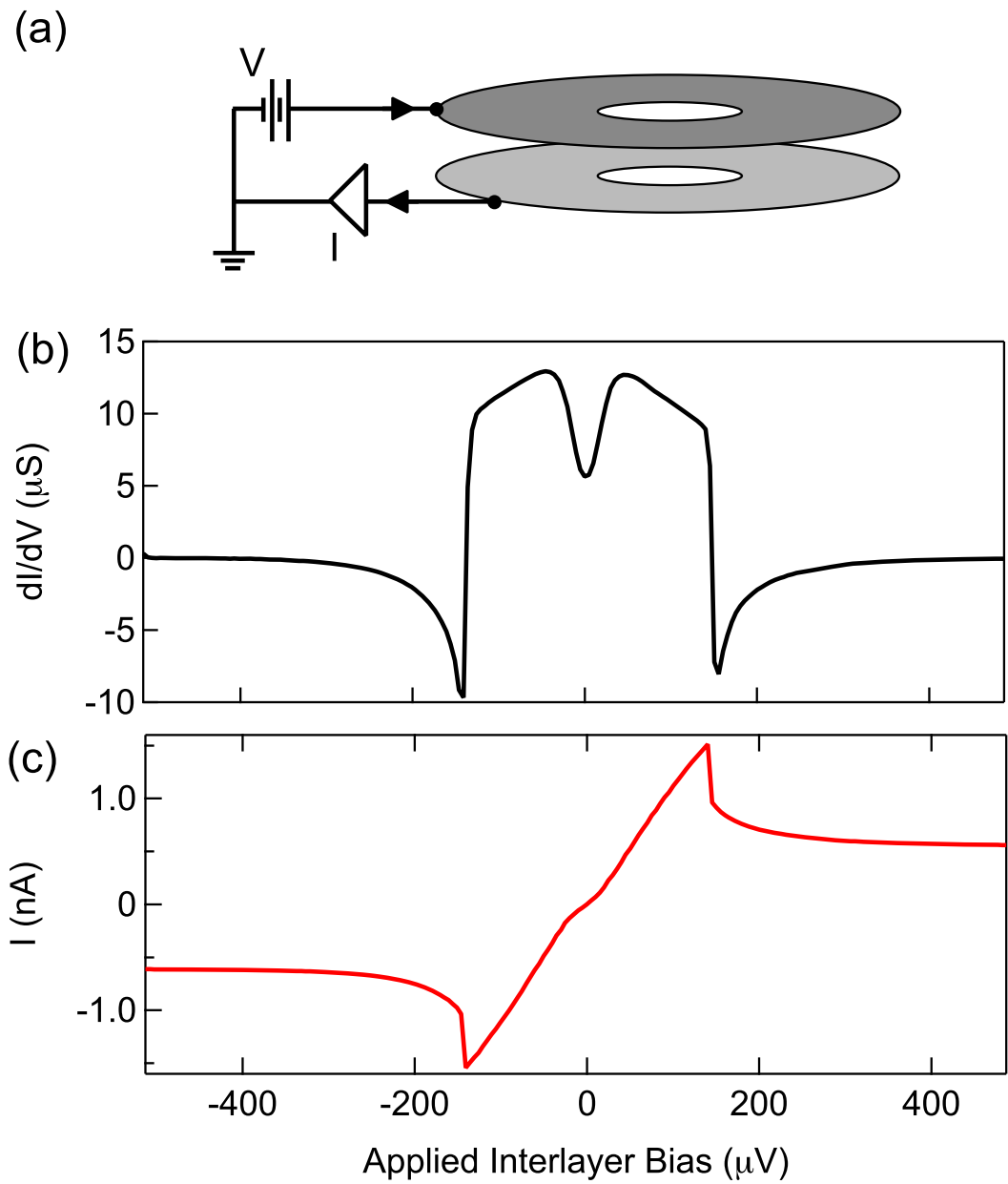
Figure 6.5: (a) Circuit diagram for interlayer tunneling, using one contact connected only to the top layer and a different contact connected only to the bottom layer. Here, both contacts are both on the outer edge of the annulus. (b) Example of two-terminal tunneling conductance and (c) tunneling current versus applied interlayer voltage at $d/\ell = 1.49$, $T = 25$ mK, and tilt angle $\theta = 0$. Note that these traces were taken using contacts along the inner edge of the annulus.

(a)

(b)
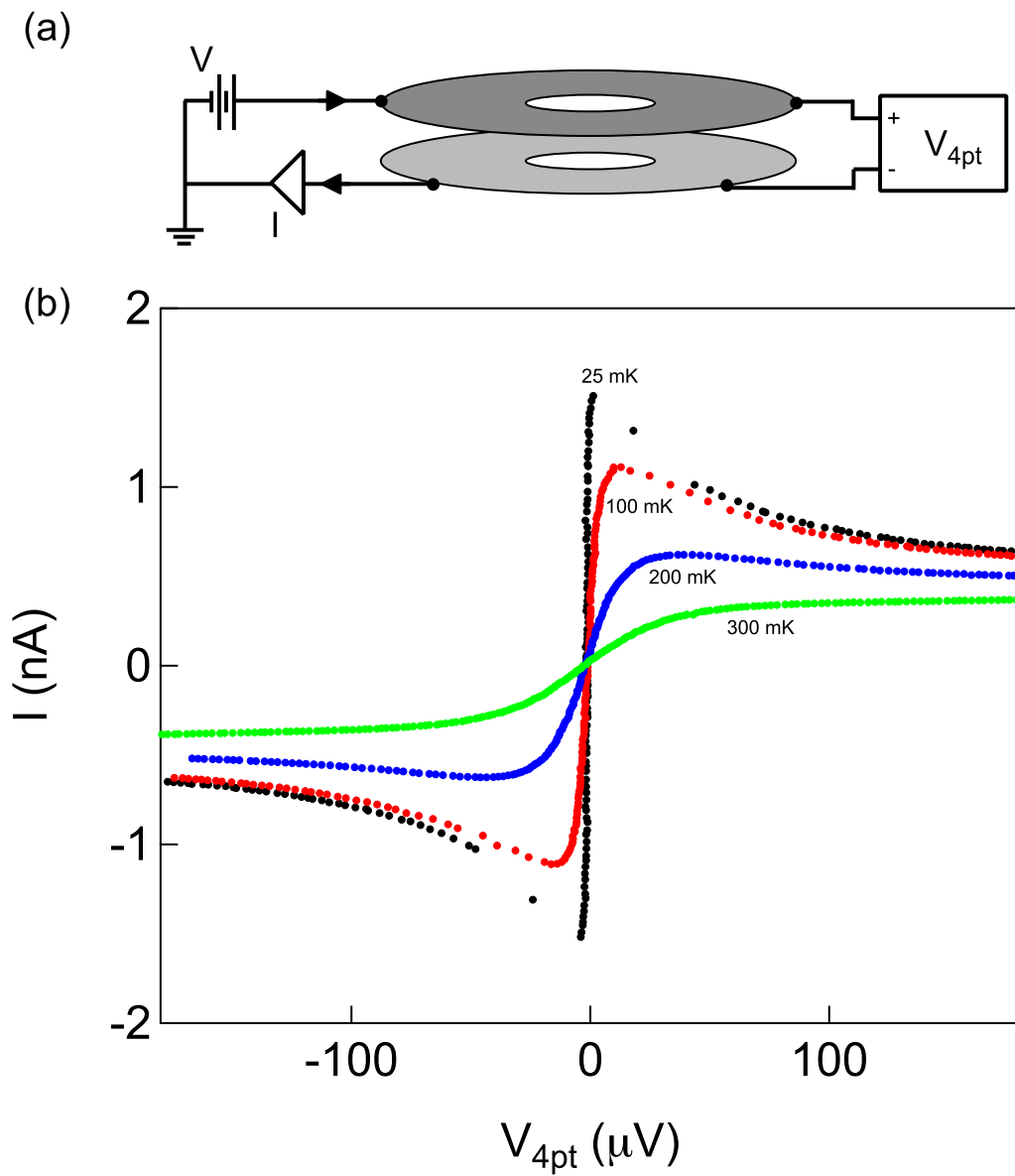
Figure 6.6: (a) Circuit diagram for four-terminal tunneling, employing four distinct ohmic contacts. Two contacts act as current leads while the other two are used as voltage probes. (b) Tunneling current versus 4-wire interlayer voltage at $d/\ell = 1.49$ and tilt angle $\theta = 0$. The four curves were taken at (in decreasing tunneling amplitude) $T = 25, 100, 200,$ and 300 mK.

nearly all of the voltage drops appear to occur along the series resistance. However, one must take care in interpreting this kind of four-terminal data because they alone do not specify where the tunneling is taking place within the sample. For example, because additional voltage drops and tunneling currents might occur between the current leads and the voltage probes [115], it is difficult to use the circuit in figure 6.6a to determine the actual value of R_{tunnel}. It is conceivable that additional interlayer voltage probes and a model of the system as a distributed circuit system could be used to extract R_{tunnel}.

Also in figure 6.6b we plot individual data points, showing the nearly discontinuous jump in V_{4pt} as the tunneling current reaches its maximum amplitude $I_{max} \approx \pm 1.5$ nA at an applied bias of $V \approx \pm 150$ μV. This rapid change from zero V_{4pt} to a finite value is frequently seen in strongly tunneling bilayers [116] as well as in other resonant tunneling junctions. It reflects a bistability that occurs whenever the intrinsic dI/dV of the junction is both negative and larger in magnitude than the inverse of the series resistance, $1/R_{series}$. Then there exist two different solutions for the current corresponding to the same value of applied bias. This bistability was recently explained in the context of $\nu_T = 1$ bilayers by Hyart et al. in reference [54]. As temperature increases and the tunneling conductance declines, the discontinuous behavior disappears.

6.4.3 Hall Counterflow, Revisited

We briefly consider a counterflow measurement using our device in which all of the contacts used are along the outer edge and thus connected by charge-carrying edge channels. We denote this type of measurement as Hall counterflow to distinguish it from Corbino counterflow, which will be described in detail later on. The circuit diagram for Hall counterflow is pictured in figure 6.7a. Here, we apply a voltage V to ohmic contact 1 (connected to the top layer), use an exterior 50 kΩ resistor as a resistive shunt between the two layers using ohmic contacts 3 and 4, and then collect the resulting current I_1 using ohmic 2 while it is connected to the bottom layer. By

measuring the voltage drop across the exterior shunt resistor, we will learn the current going through the shunt (I_S). This circuit mimics the one used by Kellogg et al. [65] to implement counterflow within a Hall bar sample.

The $I - V$ traces for Hall counterflow are shown in figure 6.7b. We plot both the counterflow current I_1 and shunt current I_S versus the applied interlayer bias V at $d/\ell = 1.49$ and $T = 25$ mK. We also plot the tunneling current $I_{Tunneling}$ obtained under the same conditions, but without the shunt resistor. As you can see, for -150 μV $<$V$<$ 150 μV, $I_1(V) = I_{Tunneling}(V)$ and $I_S = 0$. Due to the vanishing tunneling resistance, all of the injected current appears to be tunneling between the two layers before being able to reach the shunt. Such results were also seen by Yoon et al. [132] using a similar circuit in a Hall bar sample with strong interlayer tunneling.

For an applied interlayer bias $|V| > 150$ μV, the injected current exceeds the maximum tunneling current at zero bias. The tunneling resistance is no longer vanishingly small, and an interlayer voltage begins to develop. This interlayer voltage drives current through the shunt, and I_S begins to grow as the applied bias is further increased. Subsequently, the counterflow current I_1 begins to diverge from the tunneling current $I_{Tunneling}$ acquired at the same applied interlayer bias. If one were to calculate the sum $I_S + I_{Tunneling}$ (the results of which we do not show here), one would find that it is nearly same as I_1 for the whole range of applied bias, as expected from current continuity.

Thus, for large enough bias it appears that counterflow currents are propagating through the $\nu_T = 1$ system in order to reach the shunt resistor. But where do these counterflow currents travel? While counterflow currents may be carried by neutral excitons residing in the bulk, all of the contacts in figure 6.7a are along the same rim of the annulus and are connected by the edge channels. These edge channels might also be carrying the current that passes through the shunt resistor. Thus, it is unclear if the measurement depicted in figure 6.7 or any other counterflow measurement performed in a Hall bar [66, 121, 127, 132] reflect bulk excitonic currents or the charge-carrying edge channels. To distinguish between these two situations, one must perform a counterflow measurement in which the current leads are not connected to the shunt
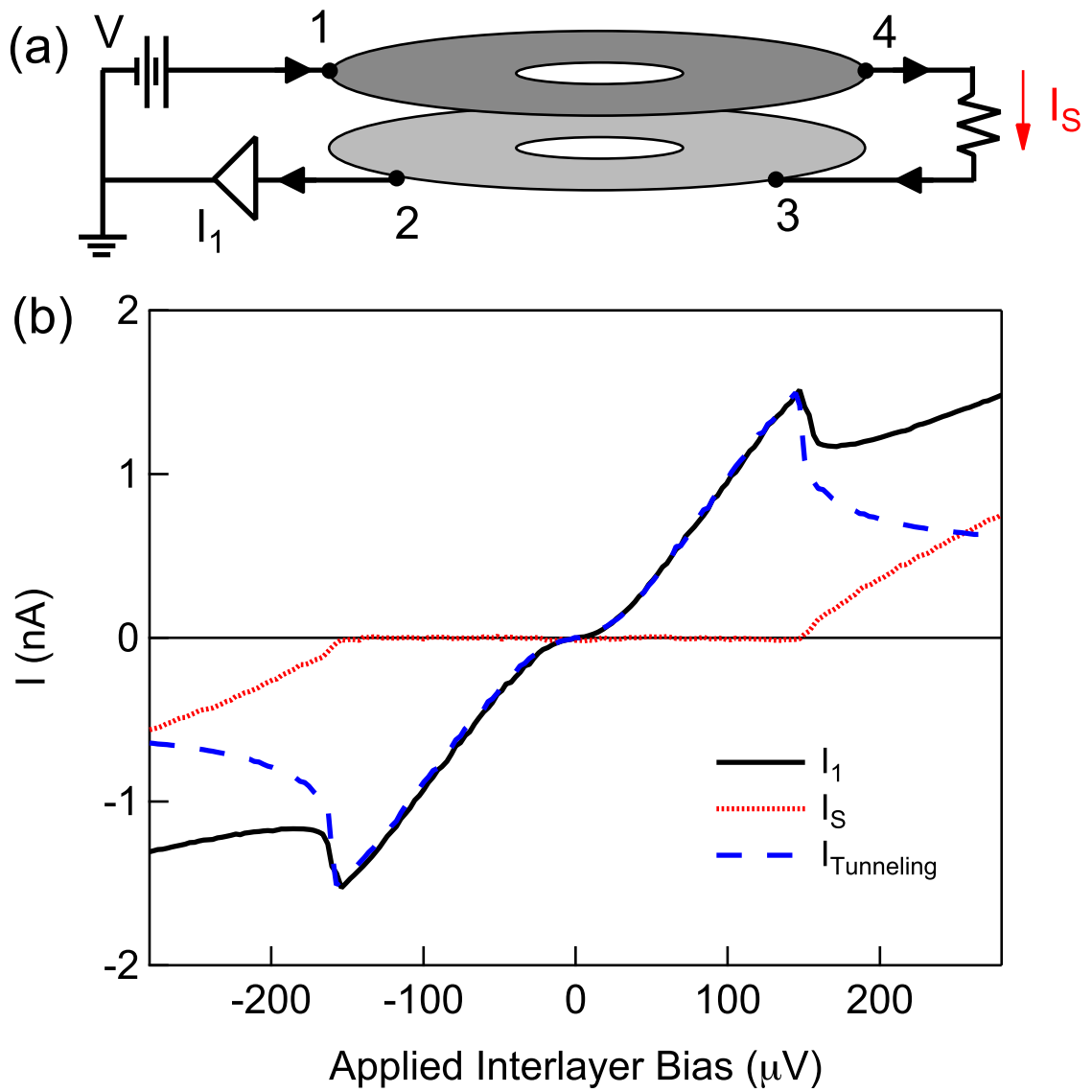
Figure 6.7: (a) Circuit for Hall counterflow. All contacts are along the outer edge of the annulus. (b) Hall counterflow measurement at $d/\ell = 1.49$, $T = 25$ mK, and $\theta = 0$. Only contacts along the outer edge are employed. The $I-V$ trace for tunneling $I_{tunneling}(V)$ using the same currents leads (but no interlayer shunt) is also shown.

resistor by the edge channels.

6.4.4   Corbino Counterflow

In our Corbino sample, ohmic contacts 5 and 6 are located along the inner edge of the annulus. Subsequently, they are not connected by any edge channels to contacts 1 through 4, located on the outer edge. Any current traveling from the inner edge to the outer edge (charged or neutral) must travel through the bulk. This allows us to perform counterflow measurements in which the current leads are separated from the shunt resistance by the bulk, where charged excitations are gapped out at $\nu_T = 1$. We denote this class of measurements as Corbino counterflow measurements. Throughout the rest of this chapter, we will present Corbino counterflow data under a variety of conditions in order to unambiguously demonstrate that excitons can flow through the bulk of the $\nu_T = 1$ system with relatively little dissipation.

The first and simplest example of a Corbino counterflow measurement is illustrated in figure 6.8a. Here, we apply a voltage to ohmic contact 5 (located on the inner edge and connected only to the top layer), provide a shunt between the two layers at the outer edge using ohmic contact 2 (connected to both layers and left floating), and then measure the resulting current I_1 flowing from ohmic contact 6 (located on the inner edge and connected to the bottom layer). If we could describe the bilayer system as two independent layers, this configuration would drive current through the bulk of the system in the top layer, through the shunt, and then back through the bulk in the bottom layer.

In figure 6.8b, we plot the $I - V$ trace for this Corbino counterflow measurement at $\nu_T = 1$ and compare it with a tunneling $I - V$ trace obtained using contacts 5 and 6 under the same conditions but with no shunt. There measurements were taken at $d/\ell = 1.49$ and $T = 25$ mK, where the $\nu_T = 1$ QH state is well formed and the bulk should permit few charged excitations. Just as in the case of Hall counterflow in figure 6.7, the counterflow I_1 and tunneling $I_{Tunneling}$ curves coincide for $|V| < 150\,\mu$V. Outside of this region, the two curve diverge and the detected counterflow current

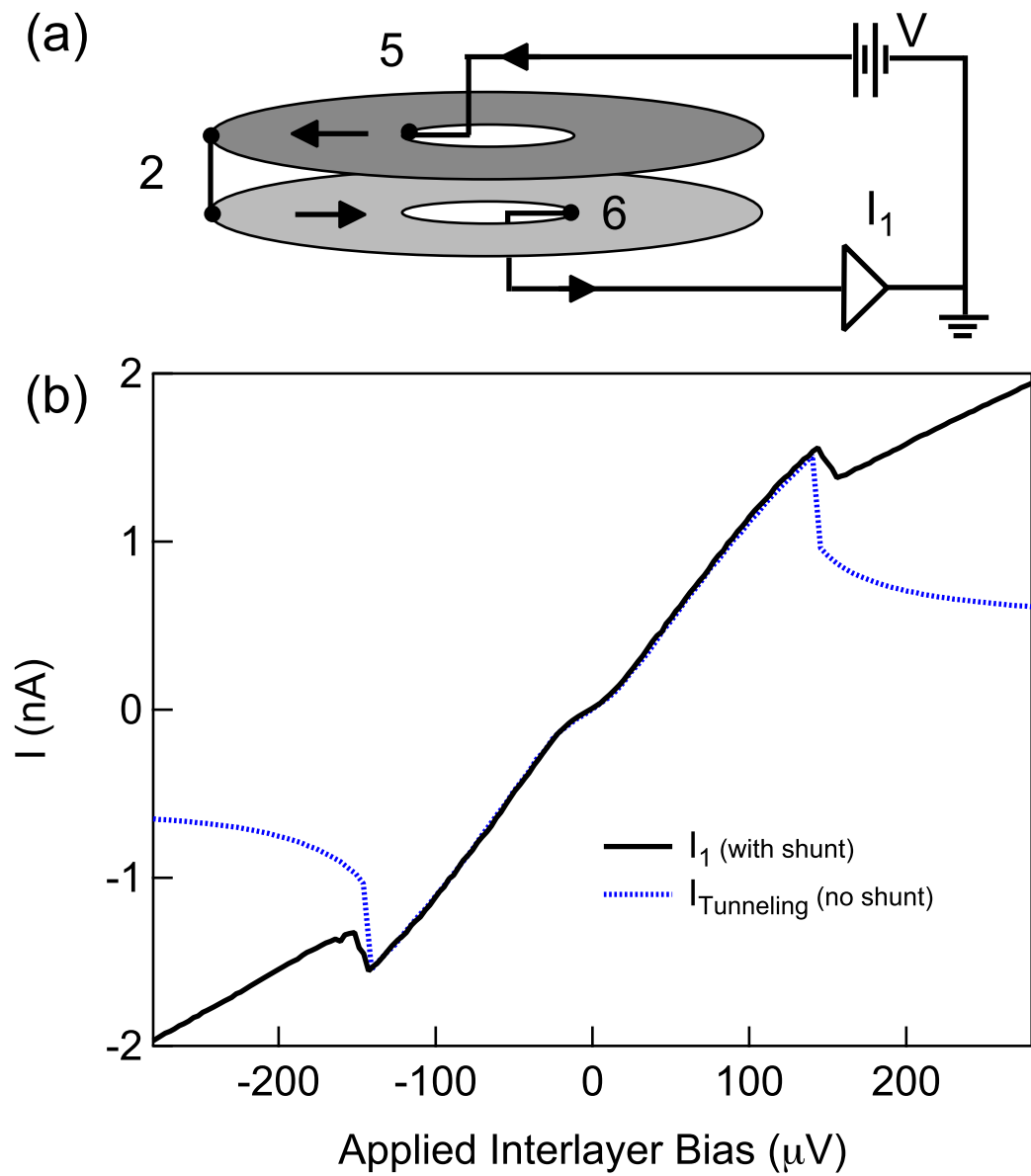Figure 6.8: (a) Circuit for Corbino counterflow measurement, with floated shunt. Ohmic contact 2 is along the outer edge of the annulus while ohmic contacts 5 and 6 are along the inner edge. (b) Corbino counterflow measurement $I_1(V)$ at $d/\ell = 1.49$, $T = 25$ mK, and $\theta = 0$. The $I - V$ trace for tunneling $I_{tunneling}(V)$ using the same currents leads (but no interlayer shunt) is also shown.

exceeds the maximum tunneling current.

The enhancement of I_1 due to the inclusion of the shunt resistance between the two layers seems to imply that counterflow currents are once again propagating through the sample from the current leads to the shunt. But this time no edge channel connects the current leads with the shunt resistance. What then accounts for the enhanced current I_1 at large bias? Due to the charge gap, one would expect that electrical currents through the bulk between the current leads and the shunt should be highly suppressed.

Instead, we assert that counterflow currents are propagating through the bulk in the form of excitons rather than charged currents flowing independently in the two layers. The flow of neutral excitons is unaffected by the large perpendicular magnetic field and thus counterflow transport should have a large bulk conductivity σ_{xx}^{CF}. In fact, in the limit of zero current the excitons should ideally exhibit superfluidity and have infinite conductance.

Although the data in figure 6.8b suggest that the presence of the shunt can dramatically change the $I - V$ curve, it does not tell us the whole story of what is occurring within the sample during counterflow. For example, we cannot yet rule out the possibility that some unusual tunneling process allowed by the shunt is taking place. Furthermore, it is unclear if the charge gap is not disrupted by the applied interlayer bias. Indeed, we will show later on that parallel Corbino conductance $\sigma_{xx}^{\parallel}$ can rise and become nonnegligible at a sufficiently large DC bias. Thus, it is conceivable that charged excitations might still be flowing during the counterflow measurement and explain our results instead.

To support the case of neutral exciton transport, we use a modification of the Corbino counterflow circuit. This modified circuit is shown in figure 6.9a. Here, we still drive current into the top layer at contact 5 and measure the current I_1 flowing from the bottom layer via contact 6. However, we now shunt the two layers together at the opposite edge using an exterior 50 kΩ shunt resistor connected to the top layer at contact 2 and to the bottom layer at contact 1. This exterior shunt resistor is located outside of the dilution refrigerator and kept at room temperature. By

measuring the voltage drop across the exterior shunt resistor, we can learn the actual current going through the shunt. Also, we connect one end of the exterior shunt resistor to the input of a current preamp, providing a low impedance (2 kΩ) path to ground. The current preamp will report the current I_2 that is flowing through this alternative path to ground. If the enhanced counterflow currents are due to charged excitations in its bulk, then one would expect this additional current preamp will short-out the original preamp recording I_1. That is, nearly all of the current flowing through the shunt would leak to ground at the second current preamp, and very little should return to the sample to complete the counterflow path, resulting in $I_1 \approx 0$.

In figure 6.9b, we show the results from this unusual counterflow circuit while $d/\ell = 1.49$, $T = 25$ mK, and tilt angle $\theta = 0$. We plot the three recorded currents I_1, I_2, and I_S along with the tunneling current that is observed while no shunt is present. At low applied bias, the counterflow current I_1 is identical to $I_{Tunneling}$ and both I_S and I_1 are zero. Once more, this is consistent with strong interlayer tunneling preventing any current from reaching the shunt. At large bias, we see that I_1 diverges from the tunneling $I - V$. This is coincident with the shunt current I_S beginning to grow in magnitude. Thus, counterflow currents are propagating all the way through the bulk of the $\nu_T = 1$ system in order to deliver the energy that is dissipated across the shunt resistance. Tunneling alone can not explain the large I_1.

We also notice that the current I_2 is much smaller than any of the other currents. This result is quite remarkable; it implies that a relatively large amount of current is flowing through the shunt yet most of it prefers to return to the sample to be detected the I_1 preamp. Even in the absence of a completely incompressible QH state, the return path through the sample should have a much larger resistance than the input impedance of the current preamplifier. Another unusual consequence of $I_2 = 0$ is that when a positive voltage is applied to contact 5, any current flowing through the shunt resistance and past the grounding point provided by the current preamp would require that contact 1 be at a *negative* voltage. We observe this behavior even when the second current preamp is replaced by a simple physical connection to ground.

The small size of the current I_2 leaking to ground from the shunt demonstrates
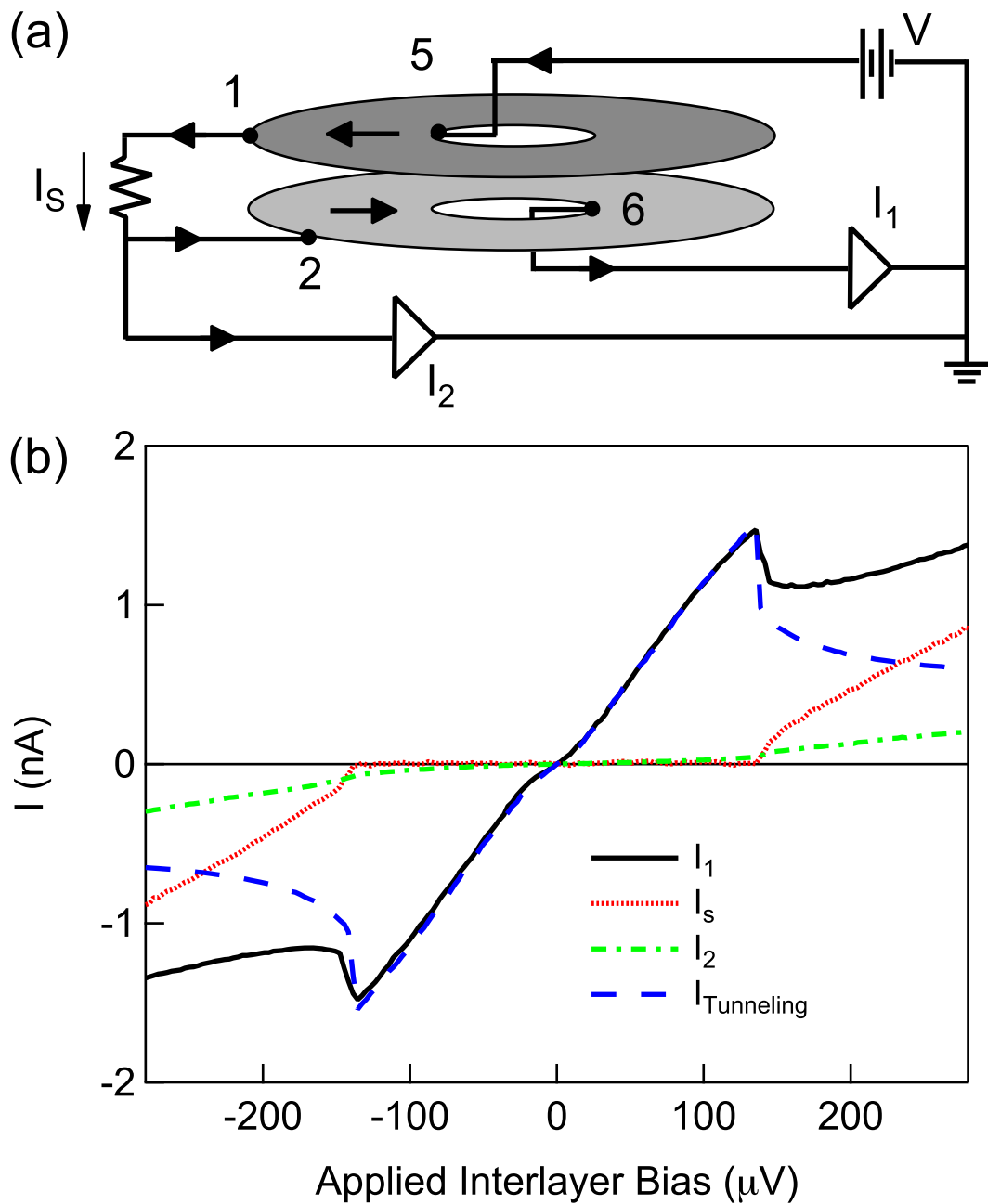
Figure 6.9: (a) Circuit for Corbino counterflow measurement with exterior shunt resistor. (b) Corbino counterflow measurement at $d/\ell = 1.49$, $T = 25$ mK, and $\theta = 0$. Current leads (I_1) are on the inner edge and an exterior shunt resistor (I_S) is placed between the layers using contacts on the outer edge. One end of the exterior shunt resistor is grounded using a current preamp (I_2). The $I - V$ trace for tunneling $I_{tunneling}(V)$ using the same currents leads (but no interlayer shunt) is also shown.

that parallel currents are still suppressed within the $\nu_T = 1$ system during the Corbino counterflow measurement. In order to allow $I_2 \neq 0$, net charge would have to flow from one edge of the annulus to another. That would require parallel currents to transport the charge across the bulk. However, only counterflow currents are allowed in the bulk of the $\nu_T = 1$ state. This is an important point to emphasize, because one might suggest that during the counterflow measurement there are certain regions in the bulk where more current is flowing in the top layer than in the bottom layer and that there are other regions where the reverse is true. In this scenario, one would only require that the *total* current flowing through the top layer be equal in magnitude to the *total* current flowing through the bottom layer. Such a hypothesis permits there to be charged excitations in the bulk of the sample that are localized in one layer or another. However, such charged excitations requires the presence of bulk parallel currents. As we have shown, those parallel currents are still suppressed during the counterflow measurement. Everywhere within the bulk the current in the top layer must be equal in magnitude and opposite in direction as the current in the bottom layer. Therefore, figure 6.9b demonstrates that counterflow currents can carry energy through the bulk of the $\nu_T = 1$ annulus without a net transfer of charge. These two characteristics are key properties of exciton flow.

6.5   Transport in a Tilted Magnetic Field

The results in the previous section provide strong evidence for bulk exciton transport. However, even at finite interlayer voltage (that is, $V_{4pt} \neq 0$) the tunneling current is still considerable. One might ask what sort of role tunneling might play during the Corbino counterflow measurements. Fortunately, we can strongly suppress the coherent tunneling at $\nu_T = 1$ by applying a moderate in-plane magnetic field [104]. In this section, we will describe transport measurements of our Corbino sample in a tilted magnetic field. We will discuss how this tilted field can influence tunneling (both coherent and incoherent) and the charge gap at $\nu_T = 1$. Here, coherent tunneling refers to the Josephson-like tunneling associated with phase-coherent excitons and reflects

a linearly-dispersing Goldstone mode. This mode is generated by the spontaneously broken $U(1)$ symmetry of the excitons. Meanwhile, incoherent tunneling is the hopping of charged quasiparticles between the two layers. Such tunneling can take place in the absence of any interlayer correlations and is typically much weaker than the coherent tunneling at $\nu_T = 1$ and low d/ℓ. We will focus on transport studies at the tilt angle $\theta = 28°$, where interlayer tunneling is insignificant but the charge gap is not aversely affected by the orbital effects induced by an in-plane magnetic field. Under these conditions, we can unambiguously observe large counterflow currents with little charge transport, thus clearly demonstrating exciton transport in the bulk of the $\nu_T = 1$ QH state.

6.5.1   Tunneling versus θ

By tilting the sample at an angle θ with respect to the magnetic field, we introduce a in-plane magnetic field $B_{||}$ that is parallel to the bilayer system. Assume for now that this in-plane field is in the y direction and we choose to express its vector potential in the Landau gauge, such that $\vec{A}_{||} = zB_{||}\hat{x}$. If we also include the perpendicular magnetic field with a Landau gauge, the canonical momentum in the x direction is thus $P_X = \hbar k_x + ezB_{||}/c - eyB_{\perp}/c$. Thus, there is a shift in canonical momentum between the two layers equal to $edB_{||}/c$. This shift will not affect purely in-plane motion, but it can influence electrons moving from one layer to another.

In the limit of small $B_{||}$, most of the transport properties at $\nu_T = 1$ such as Hall drag [67, 38] are not qualitatively altered.[3] However, the coherent interlayer tunneling that is linked to phase-coherent excitons can be strongly influenced by a relatively small $B_{||}$. With respect to interlayer charge transport, the parallel field provides a wave vector $q = eB_{||}d/\hbar c$, where d is the interlayer separation. In a semiclassical picture, this wave vector corresponds to the displacement in canonical momentum between the two quantum wells due to the vector potential of the in-plane magnetic field [53]. Loosely speaking, electrons tunneling from one layer to

---

[3]More precisely, when both $\ell_{||} \equiv \sqrt{\hbar/eB_{||}}$ is much larger than the quantum well width and the Zeeman energy is not significantly increased.

another will then access the collective Goldstone mode at finite q vector. In the absence of a parallel field, tunneling electrons will probe the linearly dispersing mode at $q = 0$. Because the mode is gapless in the limit of zero bare tunneling energy, the tunneling resonance will occur at zero energy and thus zero interlayer bias. But as $B_{||}$ becomes nonzero, the tunneling peak should split into two peaks located at finite bias $eV = \pm\hbar\omega(q)$, where $\hbar\omega(q)$ is the energy associated with the Goldstone mode [6, 107, 40]. In the low wave-length limit, $\hbar\omega(q) = \hbar\bar{c}q \propto B_{||}$, where $\bar{c}$ is the velocity of the linearly dispersive mode. This prediction was confirmed by Spielman *et al.* [104], who observed the appearance of side resonances in the tunneling spectra when an in-plane field was applied. Meanwhile, in the absence of disorder the central peak should become suppressed as the Goldstone mode is no longer accessible at $q = 0$. Spielman *et al.* did see the central peak at zero bias decrease in height as they introduced an in-plane field, but the decline was much slower than expected, most likely due to disorder [102].

We now comment on the coherent $\nu_T = 1$ interlayer tunneling that we observe in our sample in the presence of a parallel magnetic field. The two-terminal differential tunneling conductance for various tilt angles are plotted in figure 6.10. The zero bias conductance becomes suppressed as the tilt angle is increased, as expected. The incoherent tunneling persists at this moderate in-plane field, as explained later on in this section. One can also see the side resonances in tunneling dI/dV at finite bias that were first observed by Spielman *et al.* [104]. As expected, the side resonances move out to higher bias as the parallel field is increased.

Figure 6.10 also indicates that the zero bias tunneling resonance appears to become narrower in our two-terminal measurement as the tilt angle is increased. This can be understood in terms of the finite series resistance R_{series}. In the limit of vanishing tunneling resistance, when a bias is applied nearly all of the voltage drops are occurring along the series resistance. Thus, the two-terminal voltage width of the zero bias tunneling resonance is given by $\Delta V = 2I_{max}R_{series}$, where I_{max} is the maximum tunneling current that can flow at zero interlayer voltage. As both the intrinsic $\nu_T = 1$ tunneling conductance and I_{max} become reduced by the parallel field, the
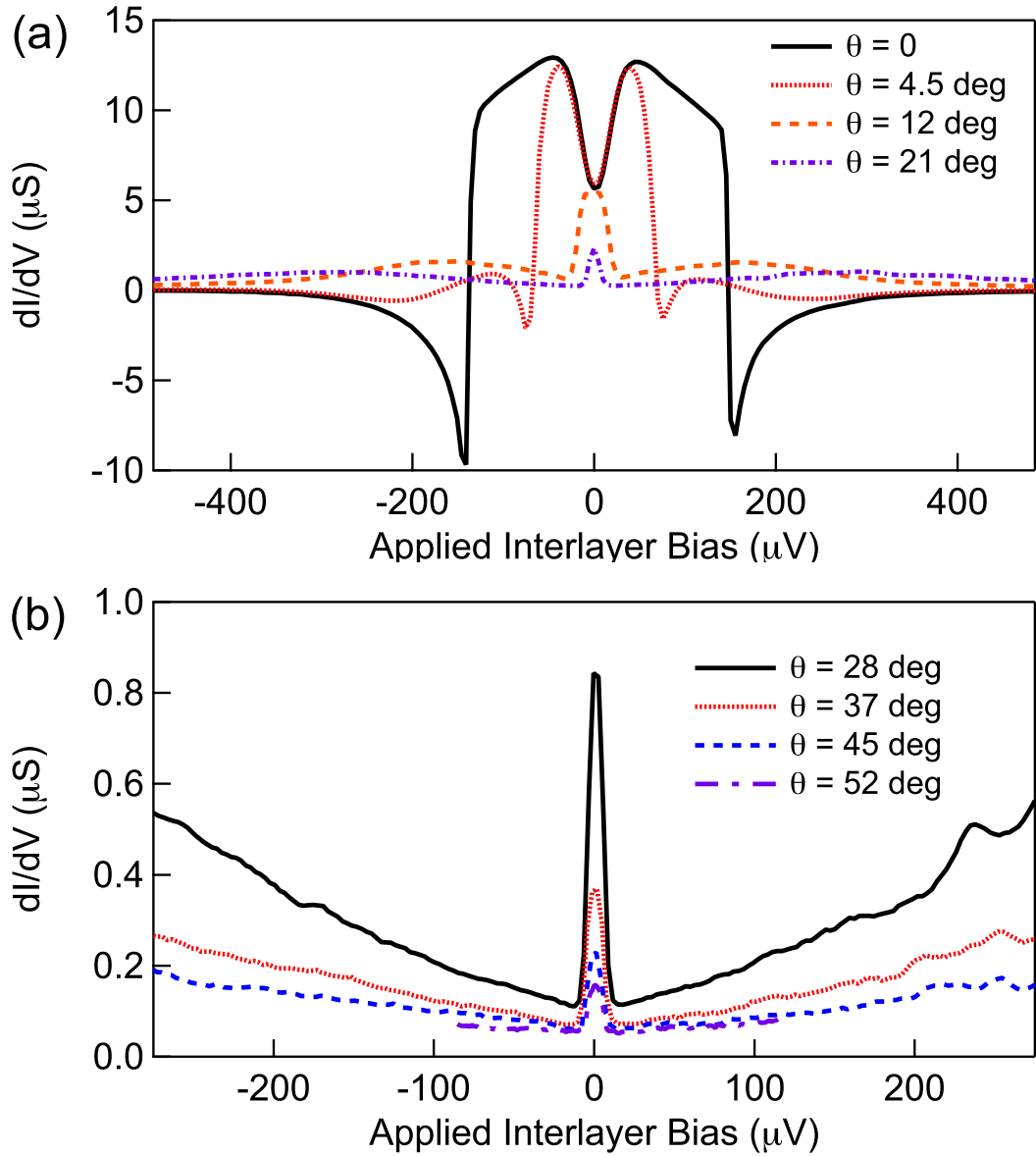
Figure 6.10: Interlayer tunneling conductance at $d/\ell = 1.49$ and $T = 25$ mK for various tilt angles.

two-terminal voltage width of the resonance decreases. The role of series resistance in determining the apparent width diminishes and other factors such as noise, thermal fluctuations, disorder, and the magnitude of the AC excitations (20 μV in this case) become relevant. This is why the width of the resonance saturates to a small value at high tilt angle in figure 6.10b.

As a side note, we point out that a large $B_{||}$ can also reduce the incoherent interlayer tunneling, which is not associated with the interlayer correlations present at $\nu_T = 1$. This can be illustrated by measuring tunneling at high temperature, where the coherent tunneling is negligible and only incoherent tunneling remains. We plot the tunneling current as a function of applied interlayer bias for four different tilt angles in figure 6.11. For each measurement, $T = 600$ mK and $d/\ell = 1.49$. Under these conditions, we observe that the zero bias $\nu_T = 1$ tunneling feature is essentially gone. Each tunneling $I - V$ has a maximum current I_+ at positive interlayer bias and a minimum current I_- at negative bias. To characterize the strength of tunneling in the presence of $B_{||}$, we compute the average peak tunneling $I_{avg} = \frac{1}{2}(I_+ + |I_-|)$ and plot the results versus $\tan\theta$. We focus on I_{avg} to reduce systematic errors stemming from preamp offsets and any interlayer asymmetries within the bilayer sample.

The average peak tunneling should be proportional to the square of the symmetric-antisymmetric tunneling splitting Δ_{SAS}. The tunneling splitting is reduced because the wave function overlap between sets of states in different layers and equal in-plane wave vector is reduced by the parallel magnetic field. Recall that in a large perpendicular magnetic field one can choose a gauge for the vector potential in which the wave functions are extended plane waves in the x direction and localized Gaussians in the y direction. Without an in-plane field each Gaussian is localized at the guiding center $y_0 = \ell^2 k_x$, where k_x is the wave vector in the x direction. We next consider the effect of an in-plane magnetic field, neglecting the finite thickness of the 2DESs. If an in-plane field is applied in the y direction, one must replace k_x in the Hamiltonian with the expression $k_x + ezB_{||}/\hbar c$. Thus, states in two different layers that correspond to the same guiding center y_0 will differ in k_x by an amount equal to $q = edB_{||}/\hbar c$. Because k_x still commutes with the Hamiltonian and must represent a conserved

quantity, an electron in one layer must tunnel into another state that is shifted in the y direction by $\Delta y_0 = \ell^2 q$. This displacement causes the overlap between the two states' wave functions to decrease as $B_{||}$ grows. The tunneling splitting is proportional to this wave function overlap and, as shown by Hu and MacDonald [53], this will lead to the equation

$$I_{avg}(\theta) = I_0 \exp\left[\frac{1}{2}\left(\frac{d}{\ell}\tan\theta\right)^2\right], \tag{6.2}$$

where we define $I_0 \equiv I_{avg}$ at $\theta = 0$. We see that there is good agreement between experiment and equation (6.2). While only a small parallel field is sufficient to suppress coherent $\nu_T = 1$ tunneling ($B_{||} \approx 0.1$ T is required to reduce the coherent tunneling by half [102]), a much larger parallel field (~ 1.4 T for $d/\ell = 1.49$) is needed to shrink the incoherent tunneling by the same fraction. However, because the incoherent tunneling is orders of magnitude smaller than the coherent tunneling at $B_{||} = 0$, we can ignore its effects on counterflow measurements.

6.5.2 Parallel Corbino Conductance versus θ

Bulk exciton transport is most clearly observed when charged currents are fully suppressed in the interior of the $\nu_T = 1$ system. However, there are situations in which the gap to charged excitations can be overcome. We illustrate this using measurements of parallel Corbino conductance versus applied bias at $d/\ell = 1.49$, $T = 25$ mK, and different tilt angles, shown in figure 6.12. The DC current is shown in panel (a) while the differential conductance is plotted in panel (b). It is immediately obvious that parallel Corbino conductance grows and becomes nonnegligible at large enough voltage. This rise in bulk conductance may be caused by a number of factors. For example, the large electric field from the applied bias can tilt the Landau levels in space. At sufficiently high bias, this deformation of the Landau levels can allow electrons to jump into excited states that are too high in energy to access at low bias, as shown in figure 6.13. This interband tunneling is known as Zener tunneling [136] and is akin to the process by which dielectrics break down and become conducting under large electric fields. The excited states extend across the bulk and permit
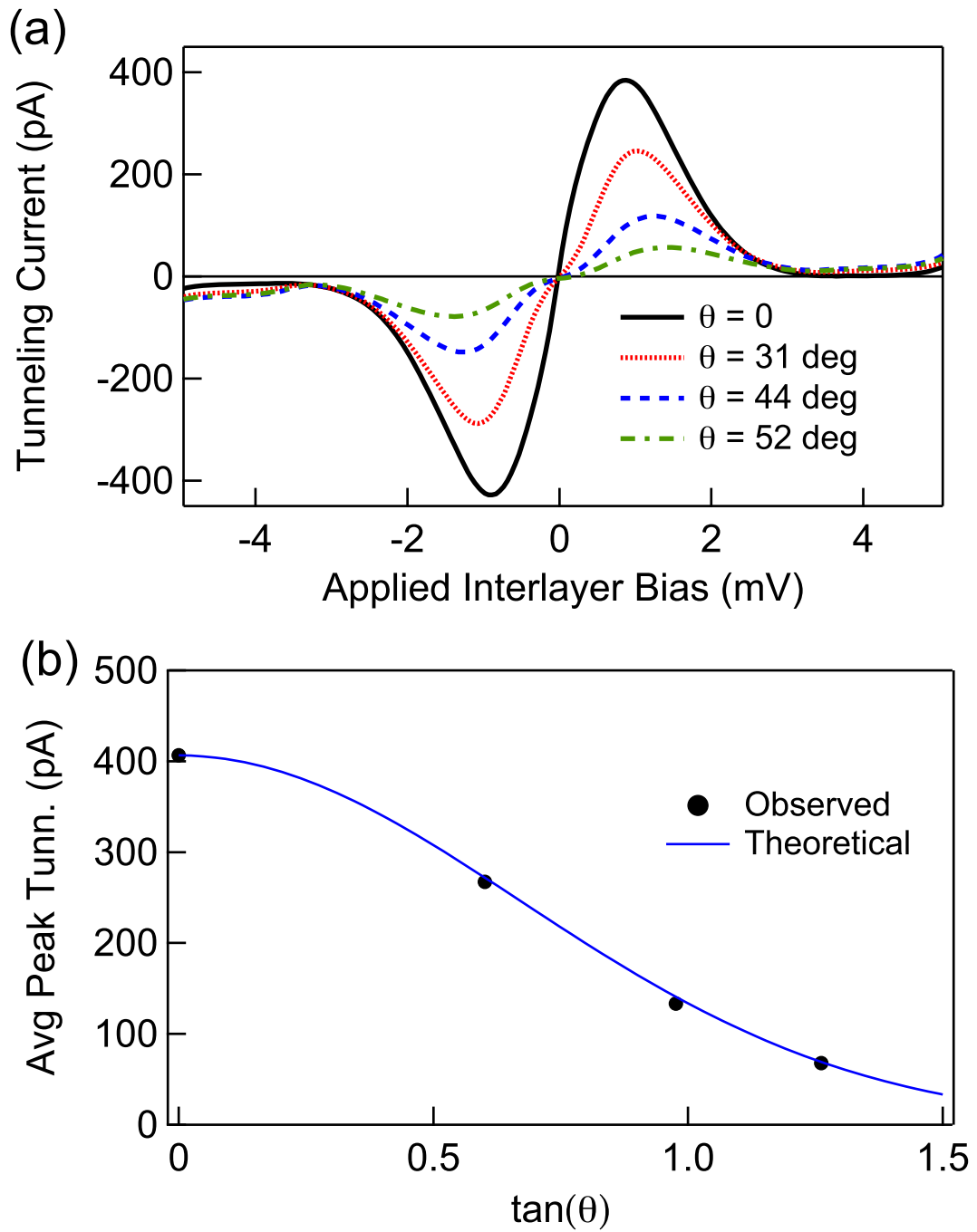
Figure 6.11: (a) Interlayer tunneling current at $d/\ell = 1.49$ and $T = 600$ mK for various tilt angles. (b) Average of peak tunneling versus $\tan\theta$, compared with expected curve.

conductance from one edge to another. A alternative explanation is that as both the applied voltage and current increase, the electrons are heated out of equilibrium. The rise in thermal fluctuations leads to the population of the extended excited states in the bulk. Regardless of the origins of this effect, during counterflow measurements one must remain at small bias; otherwise, one might induce charge currents that will pollute the exciton transport data.

Furthermore, figure 6.12 reveals that tilting the device with respect to the magnetic field can increase parallel Corbino conductance. This is consistent with orbital effects diminishing the charge gap [38], which were examined in greater detail within chapter 4. Thus, one should not tilt the sample too much or the charge gap will be compromised. Fortunately, it appears that tilt angle $\theta = 28°$ appears to have little effect on parallel Corbino conductance. As seen in figure 6.10b, this tilt angle is sufficiently large to suppress interlayer tunneling conductance to less than 1 μS. Therefore, we will focus on transport measurements taken at $\theta = 28°$.

6.5.3   Corbino Counterflow at $\theta = 28°$

At $\theta = 28°$, we repeat the Corbino counterflow measurement while using a single, floated ohmic contact as the shunt. We employ the same circuit as depicted in figure 6.8a. However, now the interlayer tunneling has been greatly weakened by the ~ 1 T parallel field and thus should play little role in our counterflow measurement. Once again, we perform our measurements at $d/\ell = 1.49$ and $T = 25$ mK, where the $\nu_T = 1$ QH state is well formed and charged excitations are strongly suppressed in the bulk. The $I - V$ for Corbino counterflow under these conditions is shown as the solid black trace in figure 6.14. We also plot the $I - V$ curve for tunneling, recorded under the same conditions but with no interlayer shunt. The counterflow current clearly exceeds the tunneling current for the whole range of applied bias. Thus, it appears that large counterflow currents do not rely on the presence of interlayer tunneling. Also, the counterflow $I - V$ curve has the same nonlinear behavior as the two-terminal tunneling trace at zero tilt angle. Once again, this behavior is due to the series resistance of
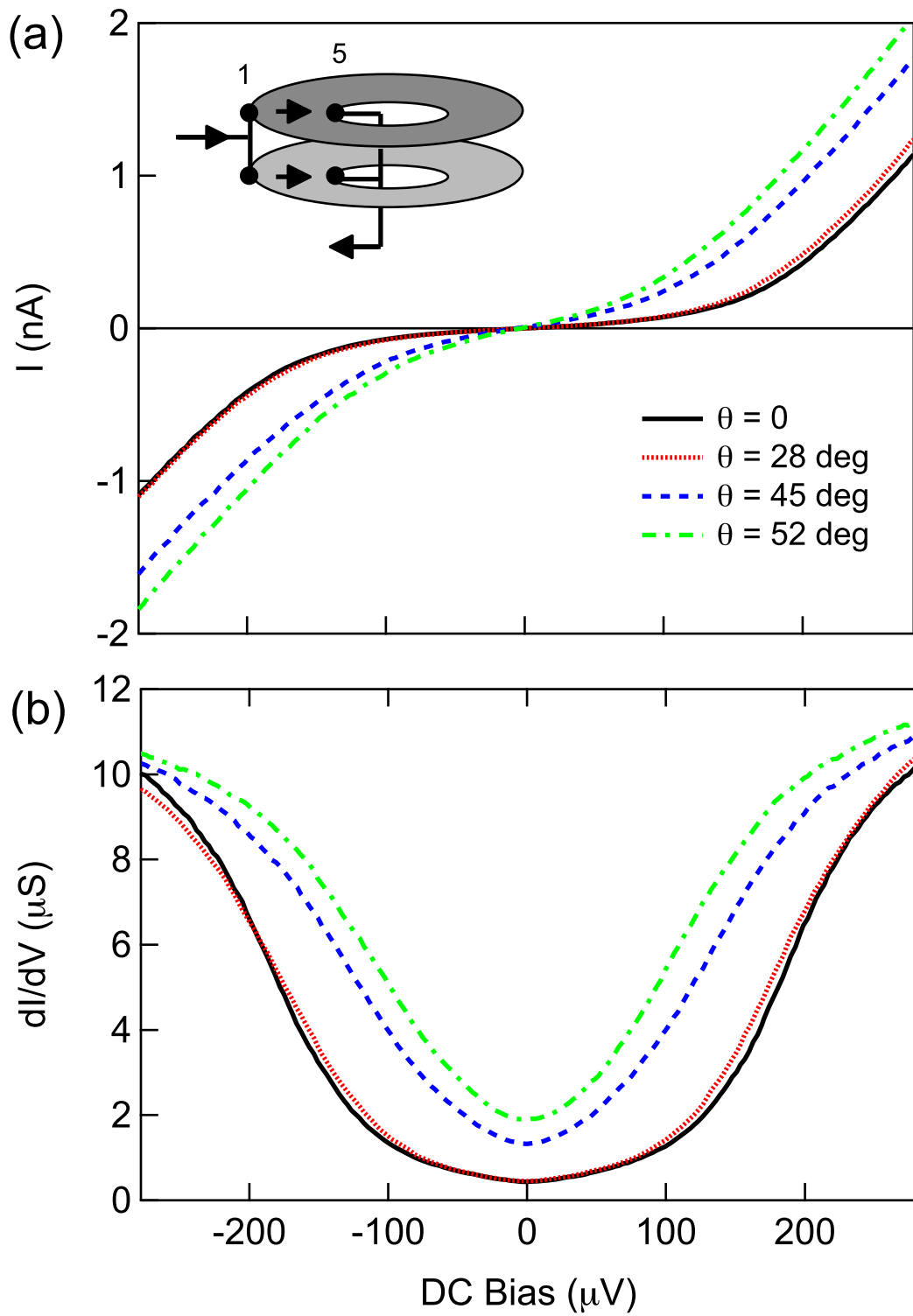
Figure 6.12: (a) DC current and (b) differential conductance versus DC bias for parallel Corbino measurement at $d/\ell = 1.49$ and $T = 25$ mK.
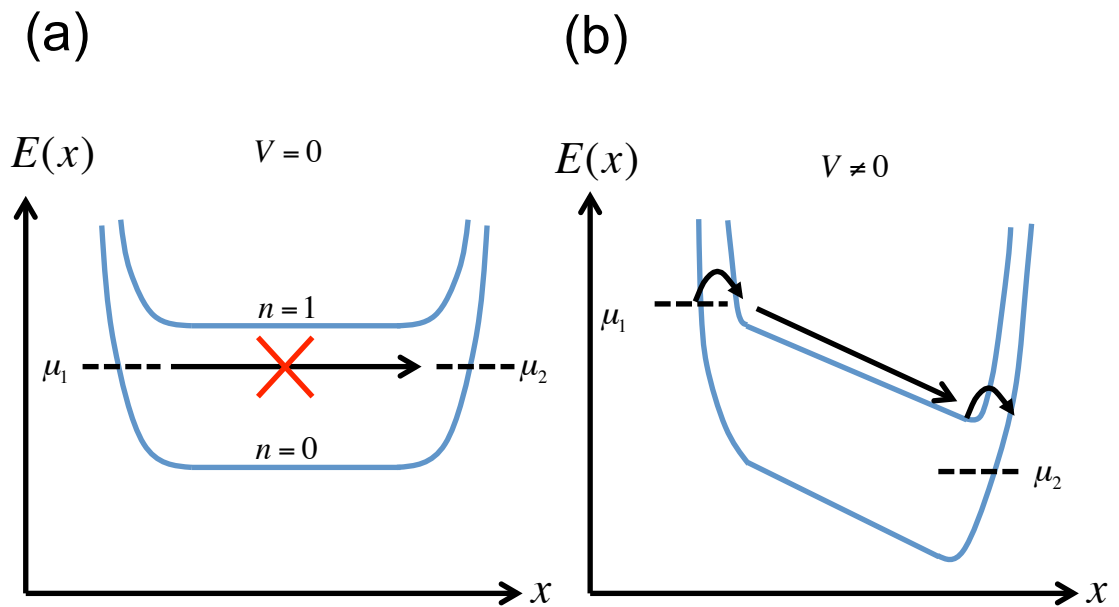
Figure 6.13: (a) Energy diagram of Landau levels when no voltage bias V is applied across the bulk of the device. The left and right sides of the diagram are two distinct edges of the system. Due to the charge gap, electrons cannot travel through the bulk to go from one edge to another. (b) Energy diagram when a bias V is applied across the sample. The Landau levels become tilted in space due to the resulting electric field. Electrons at the left edge can tunnel into a higher Landau level and then cross the bulk to the other edge.

the arms leading to the $\nu_T = 1$ state. We will later demonstrate that during this bulk counterflow measurement the extrinsic series resistance dominates the two-point conductance. The excitons themselves appear to flow with very little dissipation.
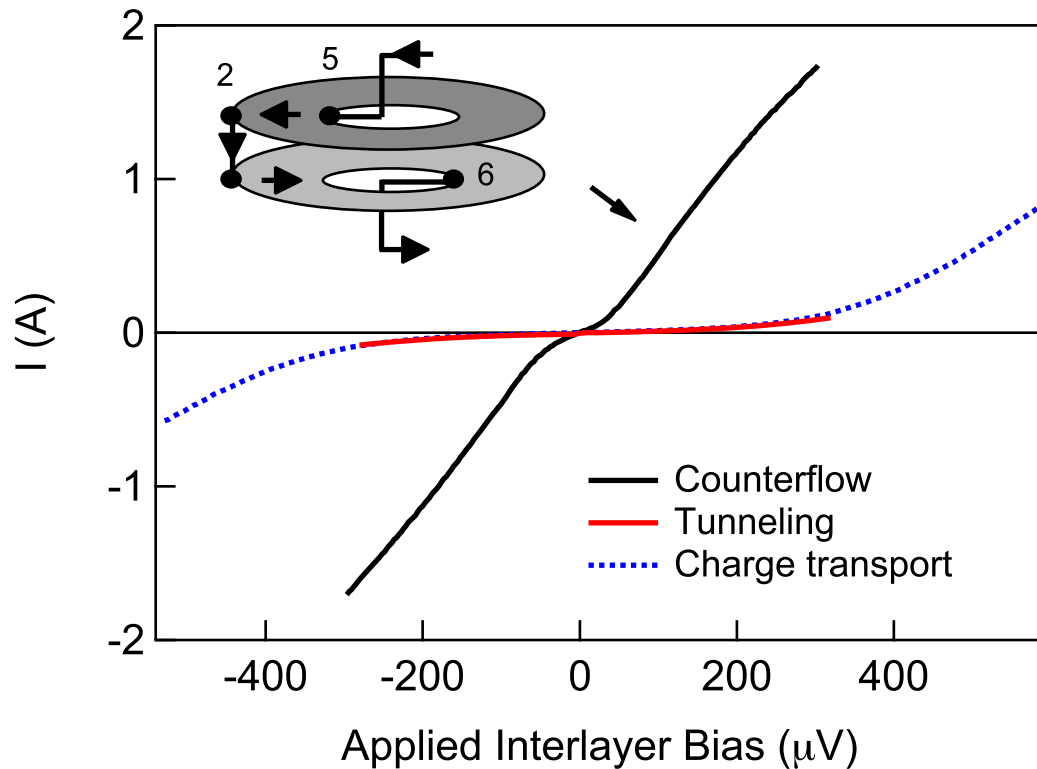
Figure 6.14: Corbino counterflow (black) at $d/\ell = 1.49$, $T = 25$ mK, and $\theta = 28°$. Compare with tunneling current (red trace) and the expected charge current at equivalent bias (dotted blue trace). The inset depicts the circuit used for the Corbino counterflow measurement.

We can also compare the Corbino counterflow trace in figure 6.14 with the expected $I - V$ for charged excitations traveling along the same counterflow route through the bulk, denoted as $I_{charge}(V)$. To estimate $I_{charge}(V)$, we make use of the $I - V$ obtained in the parallel Corbino measurement under identical d/ℓ, temperature, and tilt angle (shown in figure 6.12a). We first assume that the parallel Corbino measurement reflects the transport properties of charge through two individual layers, with each layer carrying half of the total current. Thus, if $I_{\parallel}(V)$ is the $I - V$ for the parallel Corbino measurement, then each layer carries a current $I_{U,L}(V) = \frac{1}{2}I_{\parallel}(V)$ for

a particular DC bias. This gives us the $I - V$ for charged excitations flowing through just one layer. In a counterflow measurement with two independent layers, one would expect that the $I - V$ for charge transport should be modeled by the two layers connected in series. This would require $I_{charge}(V) = I_U(V_L) = I_U(V_L)$, where $V_{U,L}$ is the voltage drop across a given layer and $V = V_U + V_L$ representing the total applied voltage. Invoking symmetry between the two layers, we can write $V_U = V_L = \frac{1}{2}V$. This results in the equation

$$I_{charge}(V) = \frac{1}{2}I_{\parallel}\left(\frac{1}{2}V\right).$$ (6.3)

In figure 6.14, we plot $I_{charge}(V)$ as a dotted line. It is clearly negligible for the bias range $|V| < 300~\mu$V. Therefore, the enhanced counterflow current likely comes neither from tunneling nor charge transport in the individual layers.

6.5.4   Expanded Corbino Counterflow

We now turn to the expanded Corbino counterflow measurement performed at tilt angle $\theta = 28°$. As a reminder, the circuit diagram for this measurement is shown in the inset of figure 6.15. Just like the measurement at $\theta = 0$, we use an exterior shunt resistor and directly measure the current I_S going through the shunt. Once again, the shunt resistor is grounded via a second current preamp. We denote the current detected by this second preamp as I_2. For now, we restrict ourselves to the case of $d/\ell = 1.49$ and $T = 25$ mK.

We plot the three currents I_1, I_2, and I_S in figure 6.15. We can see that I_1 is essentially the same value as I_S. Thus, the current I_1 reflects only the counterflow currents that propagate through the bulk of the $\nu_T = 1$ system to reach the shunt. This bolsters the view that tunneling plays practically no role in the large I_1 that we observe. In addition, I_2 is still nearly zero despite the large current going through the shunt. This allows us to conclude that still very little *net* current is flowing from one edge of the annulus to the other and that charged excitations are still suppressed during the counterflow measurement. Figure 6.15 constitutes the central finding of
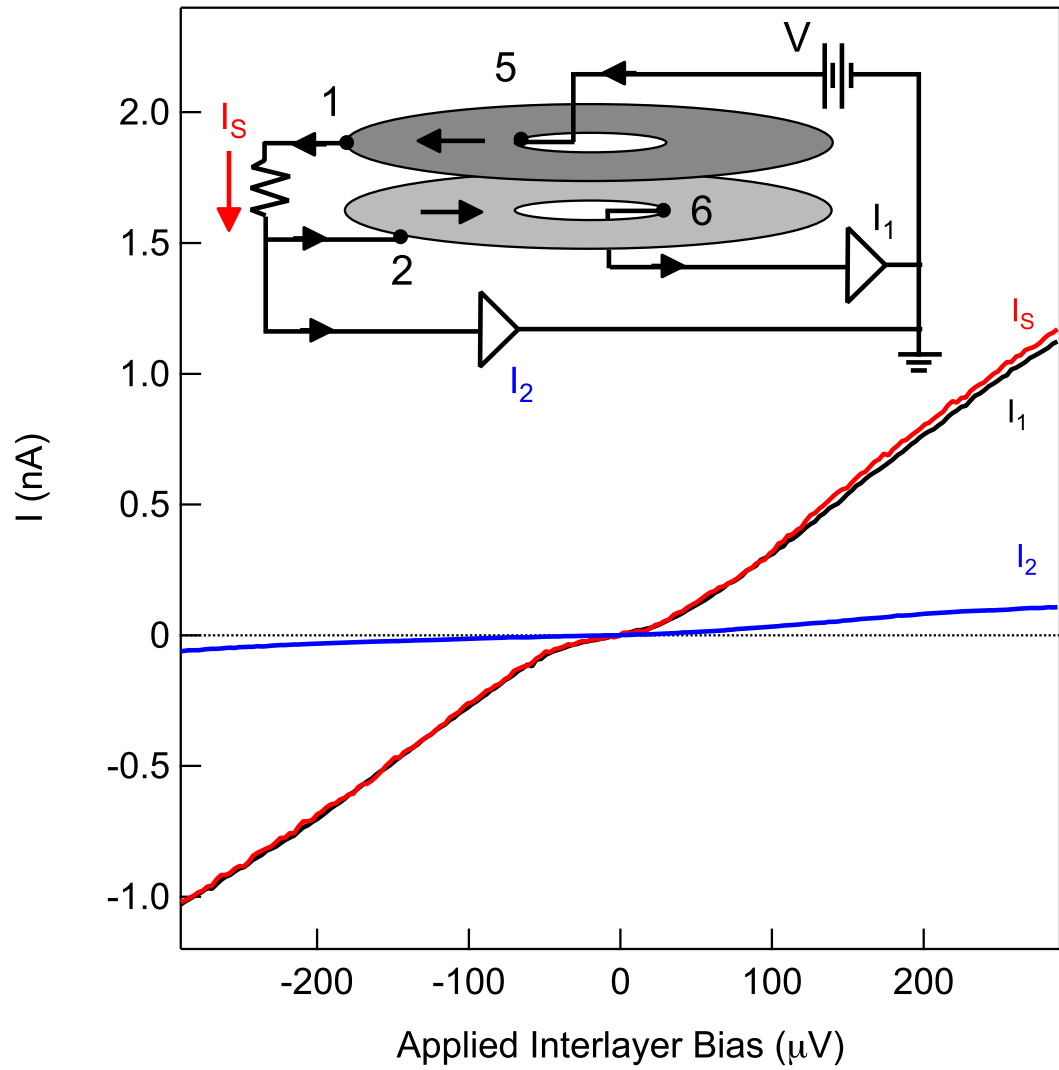
Figure 6.15: Expanded Corbino counterflow with grounded shunt at $d/\ell = 1.49$, $T = 25$ mK, and $\theta = 28°$. Inset depicts counterflow circuit.

this thesis: counterflow currents can travel through the bulk of the $\nu_T = 1$ system even while charged excitations are forbidden. These counterflow currents transport energy without carrying charge and thus are naturally interpreted within the exciton picture as being equivalent to excitonic currents.

6.6 Corbino Counterflow with Weaker Interlayer Correlations

Up until now, we have focused on data collected at low d/ℓ and low temperature, where the $\nu_T = 1$ QH state is fully formed. In this section, we examine a variety of situations where interlayer correlations have been weakened by elevated temperature or higher d/ℓ. Under these conditions, we find that the remarkable signatures of exciton transport are less prominent and gradually replaced by the transport properties of two independent 2DESs. In the fully compressible phase existing at either high temperature or high d/ℓ, our observed counterflow transport data can be explained entirely in terms of charge currents flowing through two individual layers.

6.6.1 Elevated Temperature

Thermal fluctuations destroy the correlated state at $\nu_T = 1$, as evidenced by the disappearance of its Josephson-like tunneling with temperature [12]. Here, we consider how Corbino counterflow measurements evolve as temperature is increased. Through comparisons with parallel Corbino conductance data, we will show how exciton transport fades with temperature.

We first show a set of Corbino counterflow data in figure 6.16a. Here we plot the temperature dependence of differential conductance for Corbino counterflow at $d/\ell = 1.49$ and $\theta = 28°$. For this set of traces, the shunt between the two layers is a single, floating ohmic contact. At low temperature (for example, $T = 25$ mK), the two-terminal conductance is strongly dependent on bias, reflecting the nonohmic series resistance. At zero bias and 25 mK, the conductance obtains the minimum value

of 2 μS. If excitons were dissipationless, this suggests that each arm would contribute 125 kΩ of series resistance under these conditions. Independent measurements of series resistance will bolster this assumption. As a finite bias is applied, the resistance per arm first rapidly declines to 36 kΩ and then slowly increases again. A hint of the coherent tunneling peak can also be seen, manifested as a small bump in the conductance at zero interlayer bias.

As the temperature rises, the nonlinearity in conductance goes away and is absent above 100 mK. But at high bias ($|V| > 100$ μV), the Corbino counterflow conductance monotonically declines with temperature. This is consistent with the thermal disruption of interlayer correlations required by exciton transport. Counterflow currents then begin to be carried by charged excitations instead, which are deflected by the strong perpendicular magnetic field.

For example, consider the Corbino counterflow trace obtained at $T = 274$ mK. In figure 6.17, we plot the observed counterflow current along with the expected charge transport trace, derived using equation (6.3). The two traces are practically identical, indicating that at this high temperature exciton transport is nearly absent and the two layers act independently of each other.

In a second set of Corbino counterflow traces (figure 6.18), the shunt is an exterior shunt resistor with one end grounded by a current preamp. Consequently, counterflow current (as detected by the current preamp recording I_1) falls to zero because $\sigma_{xx}^{\parallel}$ is becoming finite and is permitting the current preamp recording I_2 to essentially short out the other current preamp. For comparison, we show parallel Corbino conductance for multiple temperatures at $d/\ell = 1.49$ in figure 6.19. The rapid drop in counterflow current in figure 6.18 between $T = 48$ and 94 mK is coincident with a sharp rise in parallel Corbino conductance during that same temperature range.

To better illustrate how signatures of exciton transport disappear at elevated temperature, we calculate the difference between the observed Corbino counterflow current $I_{CF}(V)$ and the expected charge transport $I_{charge}(V)$ for a given bias V. We will focus on the case where the shunt is left floated and effective interlayer separation $d/\ell = 1.49$. We limit ourselves to $\theta = 28°$ so that we can ignore tunneling. The

Figure 6.16: Corbino counterflow (a) conductance and (b) DC current at $d/\ell = 1.49$ and $\theta = 28°$. As depicted in the inset of (a), the shunt resistance is provided by a single, floating ohmic contact.
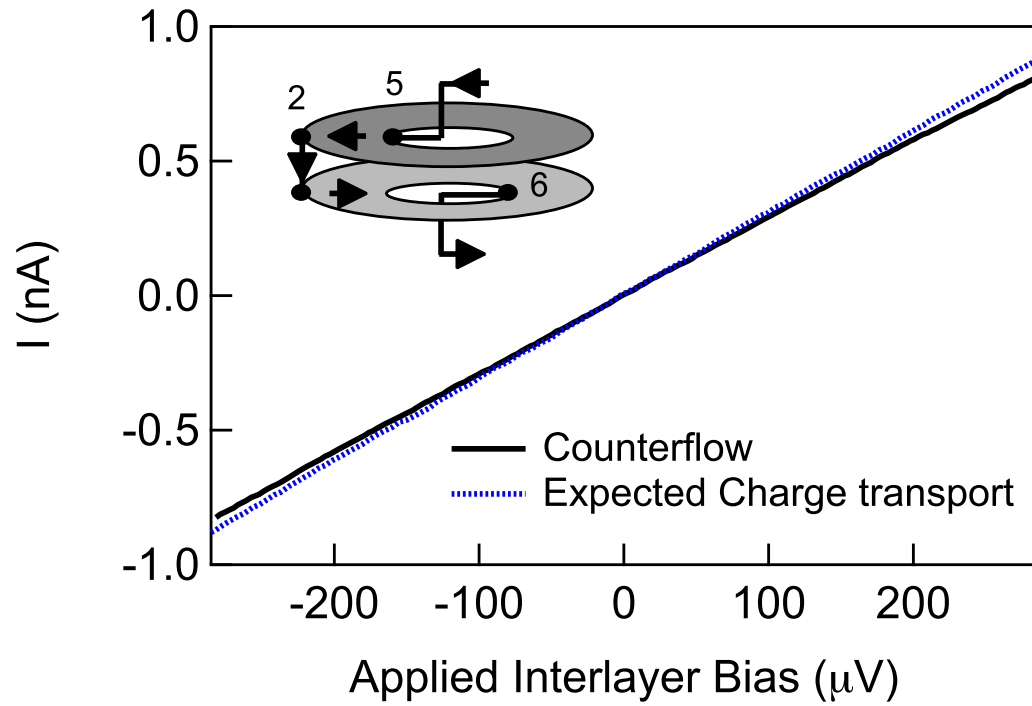
Figure 6.17: Solid black trace: Corbino counterflow $I - V$ for $d/\ell = 1.49$, $T = 274$ mK, and $\theta = 28°$. The dotted blue trace is the expected $I - V$ for charged excitations, as determined from a parallel Corbino measurement under the same conditions using equation (6.3.
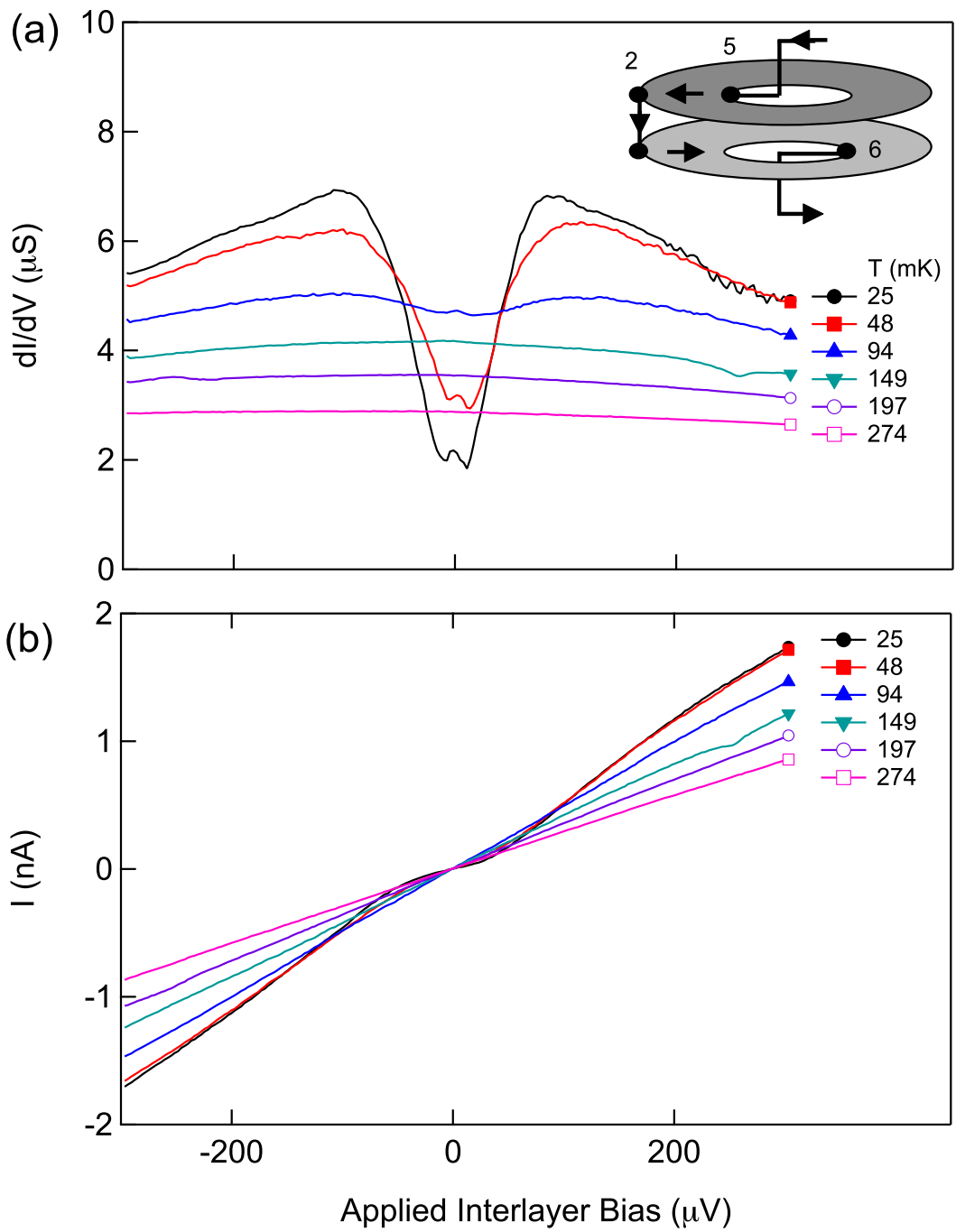
Figure 6.18: Corbino counterflow (a) conductance and (b) DC current at $d/\ell = 1.49$ and $\theta = 28°$. Here, the shunt resistance is provided by an exterior 50 kΩ resistor that is grounded at one end by a current preamp.
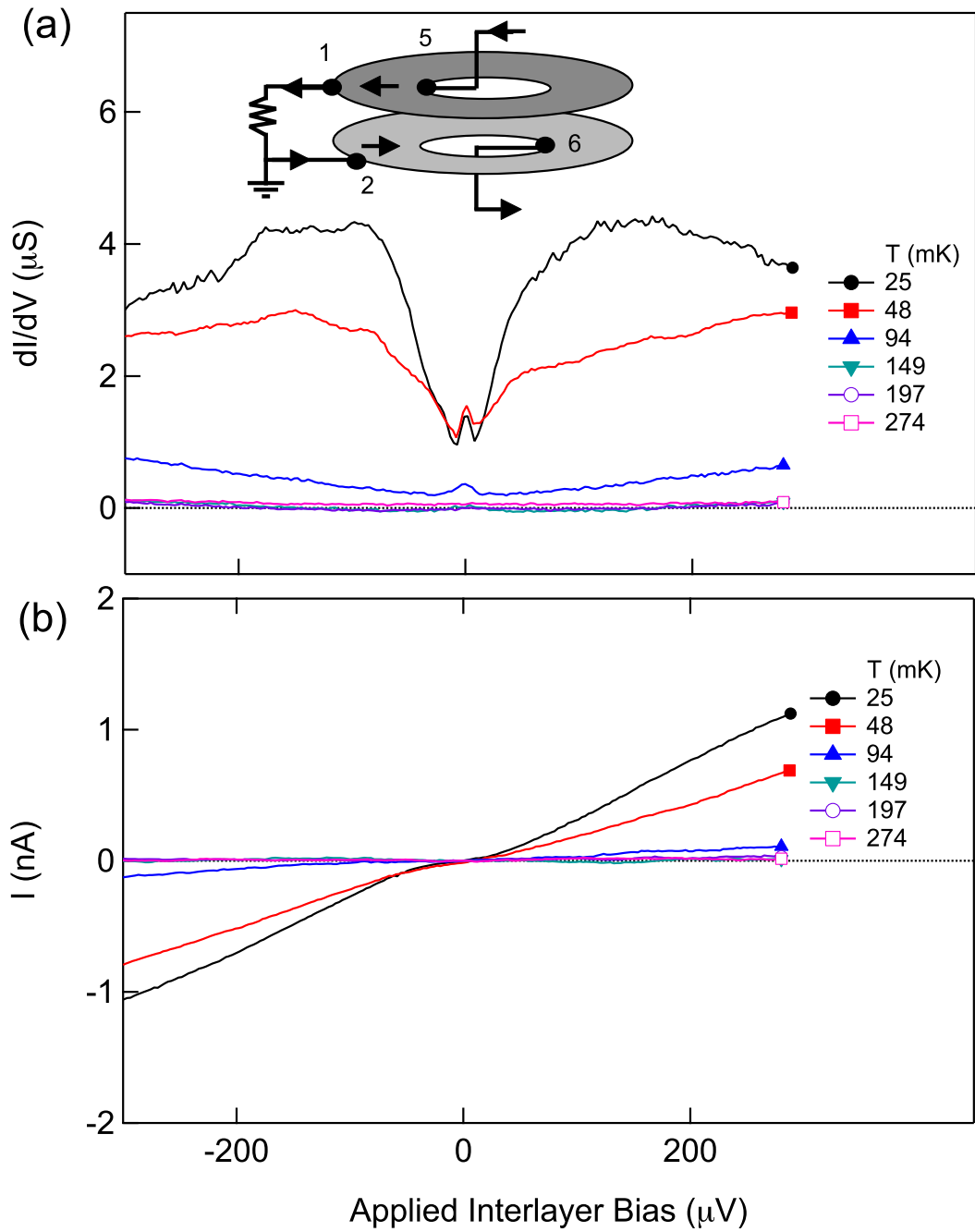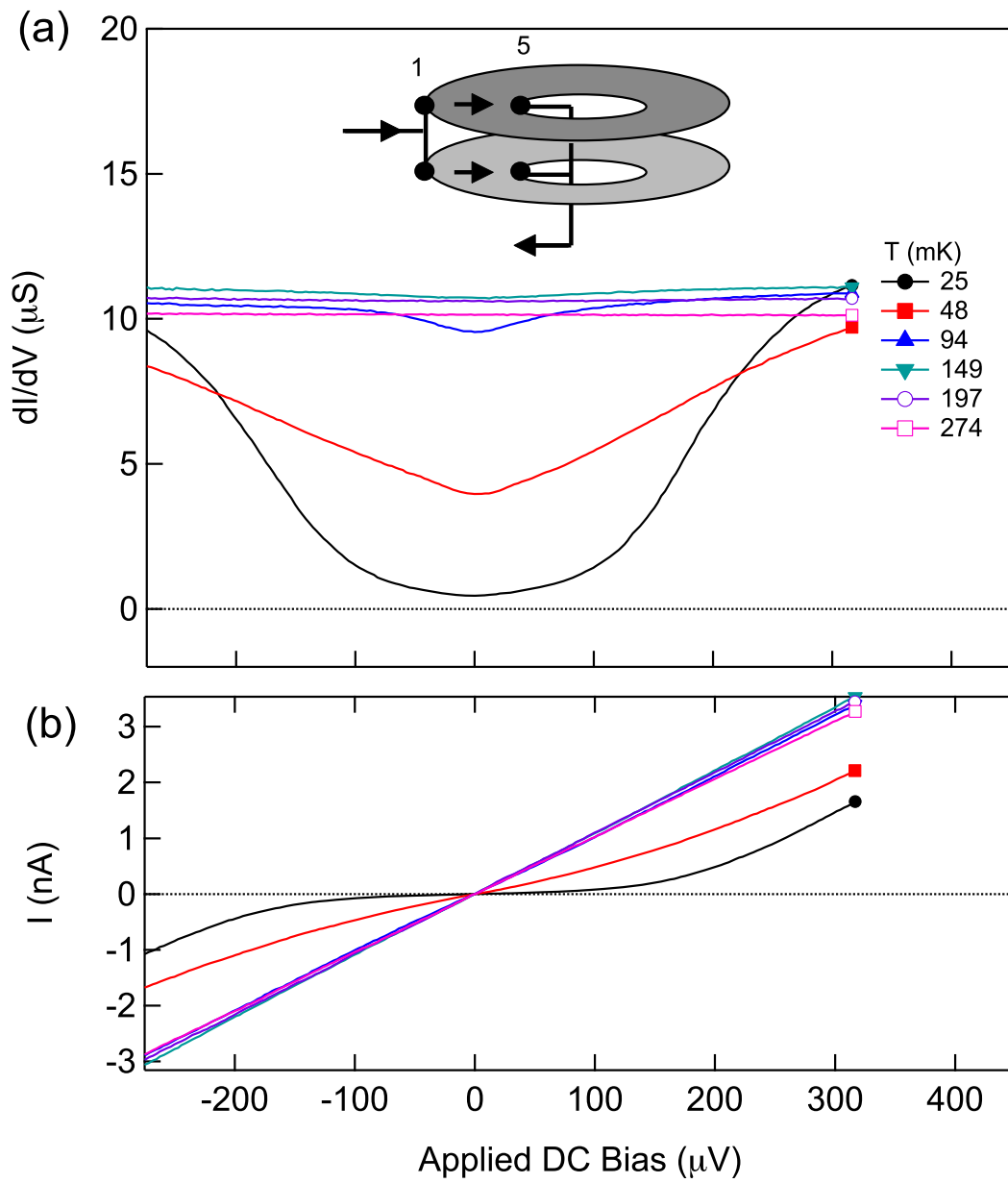
Figure 6.19: (a) Parallel Corbino conductance and (b) Parallel Corbino current versus applied DC bias at $d/\ell = 1.49$, $\theta = 28°$, and multiple temperatures.

Corbino counterflow current was recorded under the same conditions as shown in figure 6.16. We will use equation (6.3) and the data in figure 6.19b to determine I_{charge}. We plot the difference $\Delta I(V) \equiv I_{CF}(V) - I_{charge}(V)$ versus V for various temperatures in figure 6.20. Note that ΔI is positive even at moderate temperature, when charge current is not fully suppressed. It becomes negative at $T = 274$ mK likely because the series resistance during the counterflow measurement is somewhat larger than in the parallel flow measurement from which $I_{charge}(V)$ is calculated. In the counterflow measurement, an interlayer voltage is present due to the applied bias. Because of the capacitive coupling between the two layers, this interlayer voltage will induce a transfer of charge density from one layer to another. The layer with reduced density will experience an increase in resistivity while the other layer will generally have a nearly unchanged resistance. The total resistance for current traveling through the bilayer system will ultimately increase. This effect is not present in the parallel flow measurement.

We close our discussion of finite temperature effects on exciton transport by commenting on interlayer tunneling at $\theta = 28°$. In figure 6.21 we plot the tunneling conductance versus interlayer bias for $T = 25$ to 274 mK. Interestingly, the height of the zero bias tunneling peak declines with temperature at approximately the same rate as ΔI. It is difficult to interpret the meaning of this similarity because the precise origin of the tunneling peak while at large $B_{||}$ is not known. Nonetheless, the persistence of the $\nu_T = 1$ tunneling peak suggests that stationary, long-range phase coherence is not completely destroyed by the sizable $B_{||}$ or thermal fluctuations. This might also be reflected in the gradual decline of ΔI with temperature.

6.6.2 Higher d/ℓ

Although we have only considered measurements at the low effective interlayer separation of $d/\ell = 1.49$, we emphasize that signatures of excitonic transport are still visible in counterflow at higher d/ℓ. For example, in figure 6.22 we compare the Corbino counterflow $I - V$ at $d/\ell = 1.61$ and $T = 25$ mK with the expected charge transport
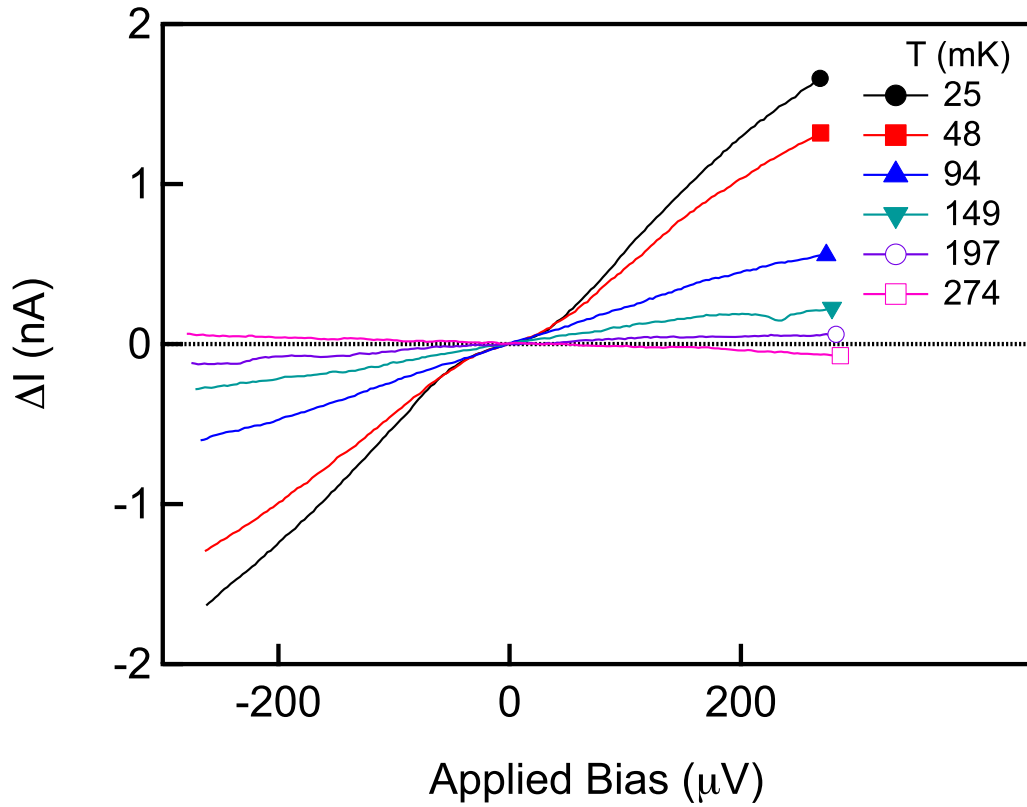
Figure 6.20: Difference between counterflow current and expected current from parallel transport for various temperatures. $d/\ell = 1.49$ and $\theta = 28°$.
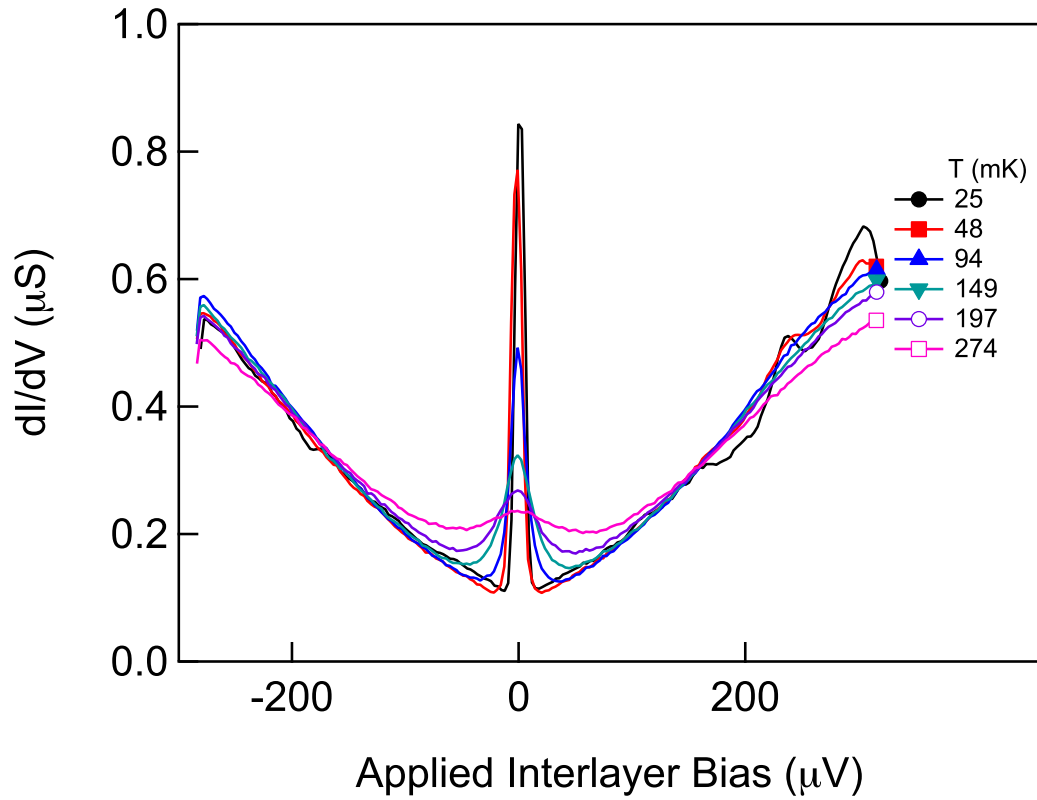
Figure 6.21: Tunneling conductance versus interlayer bias for various temperatures. $d/\ell = 1.49$ and $\theta = 28°$.

$I_{charge}(V)$ derived from parallel Corbino conductance measurements under the same conditions. Even when charged excitations are not fully gapped out, we observe that the counterflow current is still larger than expected from parallel conductance. Thus, at this moderate d/ℓ we can still detect evidence for exciton currents at $\nu_T = 1$. We also note that the counterflow $I - V$ curve at $d/\ell = 1.61$ has less pronounced nonlinear behavior near zero bias than does the same curve at $d/\ell = 1.49$. The 2DES density is larger at higher d/ℓ and the bilayer system generally has higher mobility than at lower d/ℓ. This will tend to lead to a smaller longitudinal resistivity in the portions of the sample leading to the $\nu_T = 1$ region.
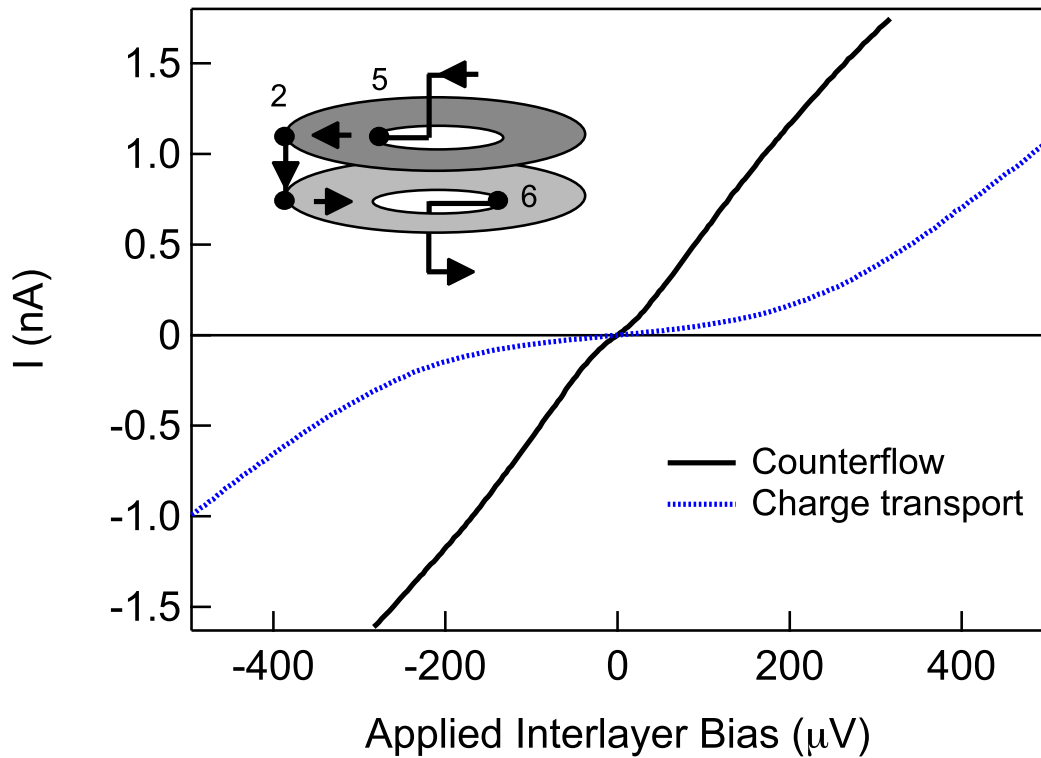
Figure 6.22: Solid black trace: Corbino counterflow (floated shunt) $I - V$ for $d/\ell = 1.61$, $T = 25$ mK, and $\theta = 28°$. Dotted, blue trace: predicted charge transport $I - V$, based on parallel Corbino conductance measured under the same conditions.

However, if d/ℓ is raised above the critical interlayer separation of $d/\ell \approx 1.8$, then interlayer correlations disappear and the two layers act independently of one another.

We illustrate this in figure 6.23. Here, we compare observed Corbino counterflow with charge transport at $d/\ell = 2.34$, which is far from the phase boundary. The two curves are essentially the same, indicating that counterflow currents and parallel currents have the same bulk conductance at this high d/ℓ. This is consistent with other transport measurements such as tunneling [103, 12] and Hall drag [65, 38], which show no excitonic anomalies at this d/ℓ. Instead, transport measurements reflect two compressible and essentially uncorrelated CF metals, both at half Landau filling factor.
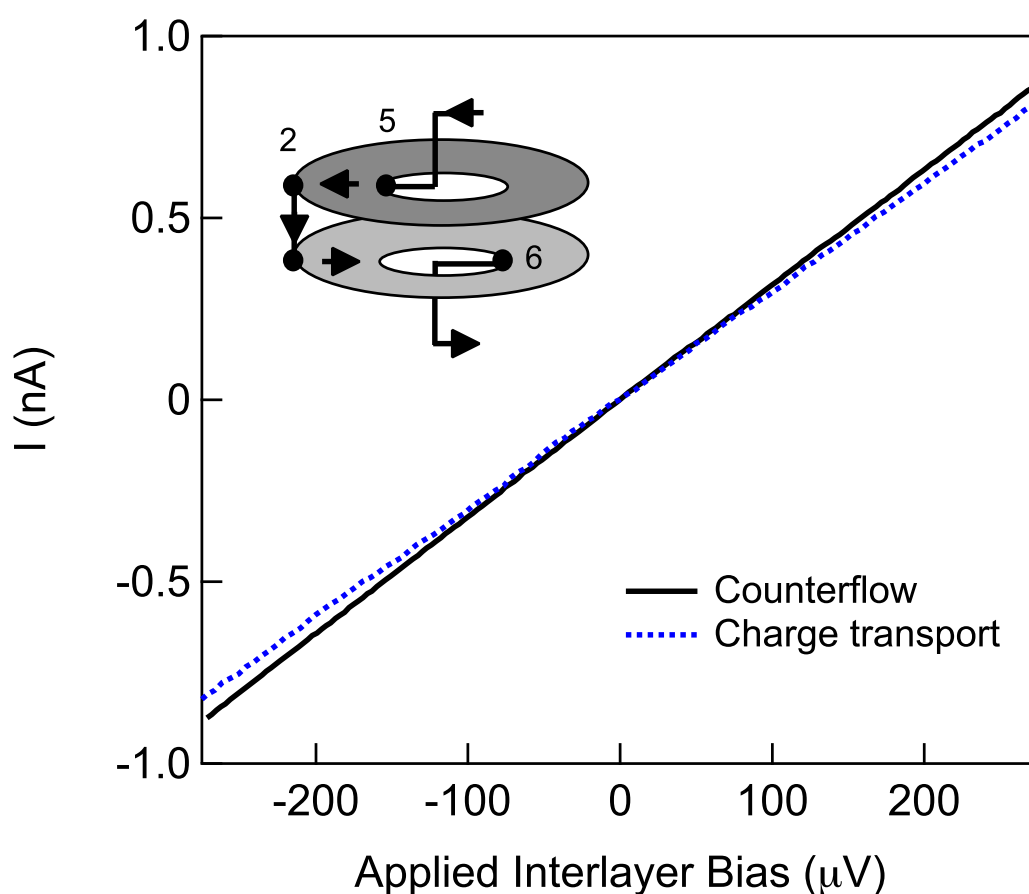
Figure 6.23: Solid, black trace: Corbino counterflow (floated shunt) $I - V$ for $d/\ell = 2.34$, $T = 50$ mK, and $\theta = 0$. Dotted, blue trace: predicted charge transport $I - V$, based on parallel Corbino conductance measured under same conditions.

6.6.3 Transport at $\nu_T = 2$

For the sake of completeness, we consider the bilayer system at $\nu_T = 2$. The system is not expected to exhibit any interlayer correlations. Instead, it should be described as two independent $\nu = 1$ QH states. We affirm this in our Corbino sample by tuning the total density to $N_T = 0.45 \times 10^{11}$ cm^{-2} and adjusting the perpendicular field to produce $\nu_T = 2$. We then repeated the Corbino counterflow measurement at $T = 25$ mK and $\theta = 28°$ at this total filling factor. We used a single floating ohmic as the interlayer shunt. In figure 6.24, one can see that the Corbino counterflow conductance is highly suppressed at ν_T and is essentially the same as the tunneling conductance. Practically no current is reaching the shunt due to the very large charge gap in each $\nu = 1$ layer.
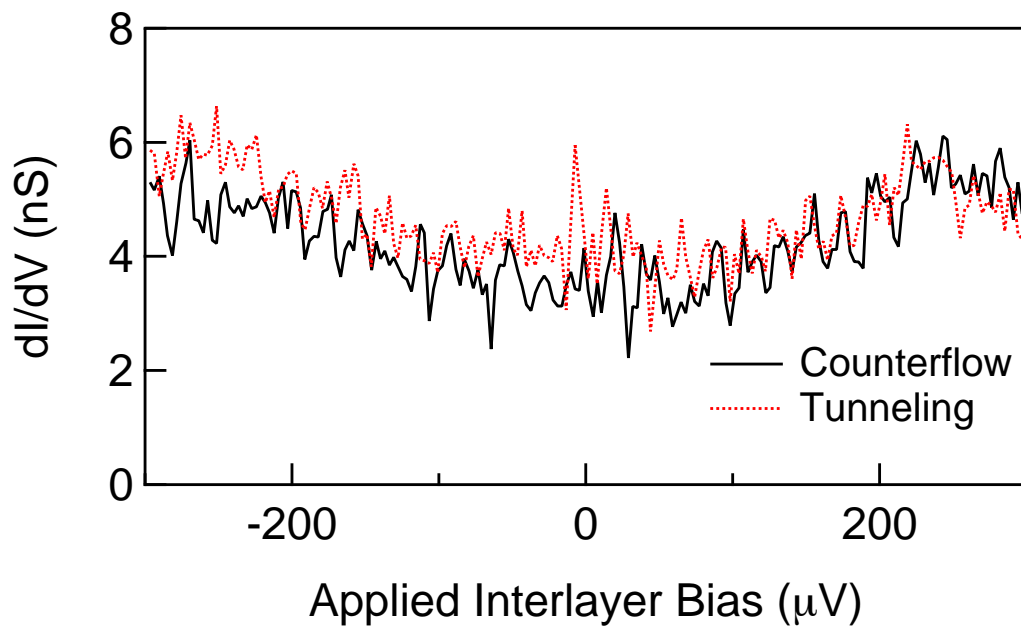
Figure 6.24: Corbino counterflow conductance (solid black trace) and tunneling (dotted red trace) for $\nu_T = 2$ at total density $N_T = 0.45 \times 10^{11}$ cm^{-2}. $T = 25$ mK and $\theta = 28°$. Note that this density corresponds with $d/\ell = 1.49$ at $\nu_T = 1$.

6.7   Series Resistance

The Corbino counterflow measurements that we have presented so far are purely two-terminal in nature. They include the effects of finite series resistance between the electrical contacts and the exciton condensate. This includes not only the 10 kΩ of resistance from RC filters but also the regions of the bilayer that are not at $\nu_T = 1$. In this section we will describe measurements in which we estimate the total series resistance. We find that the low density 2DESs in series with the $\nu_T = 1$ region are responsible for the vast majority of the two-terminal resistance in the Corbino counterflow measurements as well as its highly nonlinear behavior near zero bias.

6.7.1   Edge Conductance

We begin our examination of the large series resistance by examining measurements of two-terminal conductance between contacts that share a common edge. We will only consider data taken at $d/\ell = 1.49$. In figure 6.25 we plot the conductance between the contacts 5 and 6 as a function of DC bias. These contacts are both on the inner edge and thus connected by the QH edge channels. For this measurement, the two contacts are connected to both of the layers simultaneously and the sample is tilted to $\theta = 28°$ with respect to the magnetic field. Therefore, interlayer tunneling should play no role in this measurement. All of the contacts on the outer edge are isolated from the annulus and thus bulk conductance should also be unimportant. We see that at $T = 25$ mK, there is a clear dip in the two-terminal conductance between contacts 5 and 6 at zero DC bias. Raising the temperature to 100 mK causes the dip to disappear, and the two-terminal conductance between contacts 5 and 6 becomes constant with respect to DC bias. When current is driven through only one layer between contacts 5 and 6, we still observe dips in conductance through both the bottom layer (figure 6.26a) and the top layer (figure 6.26b). Interestingly, the conductance dip is broader when probing only the upper layer than while only probing the lower layer. Although not pictured here, the results are qualitatively the same when we use two contacts (1 and 2) along the outer edge instead. Note that

the minima in conductance in figures 6.26a and 6.26b both correspond to a resistance of roughly 250 kΩ. Ignoring the contribution of any edge channels, this would imply that the resistance of each arm has a maximum possible value of ~125 kΩ. This is consistent with the minimum two-point conductance seen in figure 6.16a.
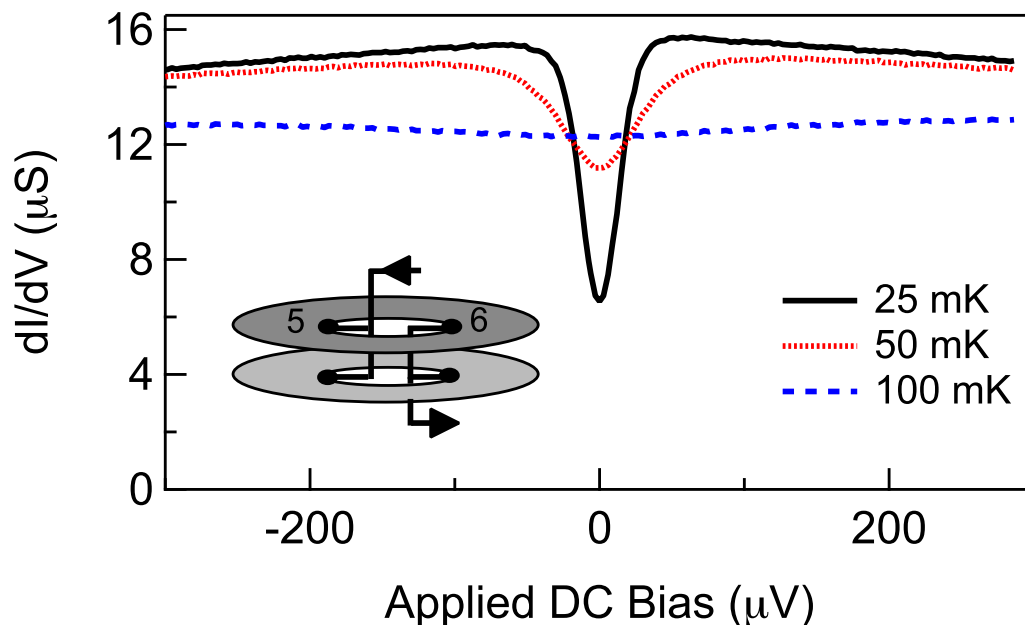
Figure 6.25: Conductance between two inner contacts (5 and 6), connected to both layers. $d/\ell = 1.49$ and $\theta = 28°$.

The edge conductance data in figures 6.25 and 6.26 resemble the nonohmic behavior of Corbino counterflow conductance (for example, see figure 6.16) and two-terminal tunneling conductance (e.g., figure 6.5b). They suggest that the nonlinearities observed in Corbino counterflow originate from the 2DESs connecting the contacts with $\nu_T = 1$ bulk.

The perimeter of the $\nu_T = 1$ QH state is characterized by a dissipationless edge channel with two-terminal resistance of h/e^2. This is small compared with the ~250 kΩ observed at zero bias in figure 6.26. Thus, we hypothesize that the low edge conductance is to be blamed on the low density 2DESs in the arms leading from the ohmic contacts to the $\nu_T = 1$ region. While most of these arms are kept at
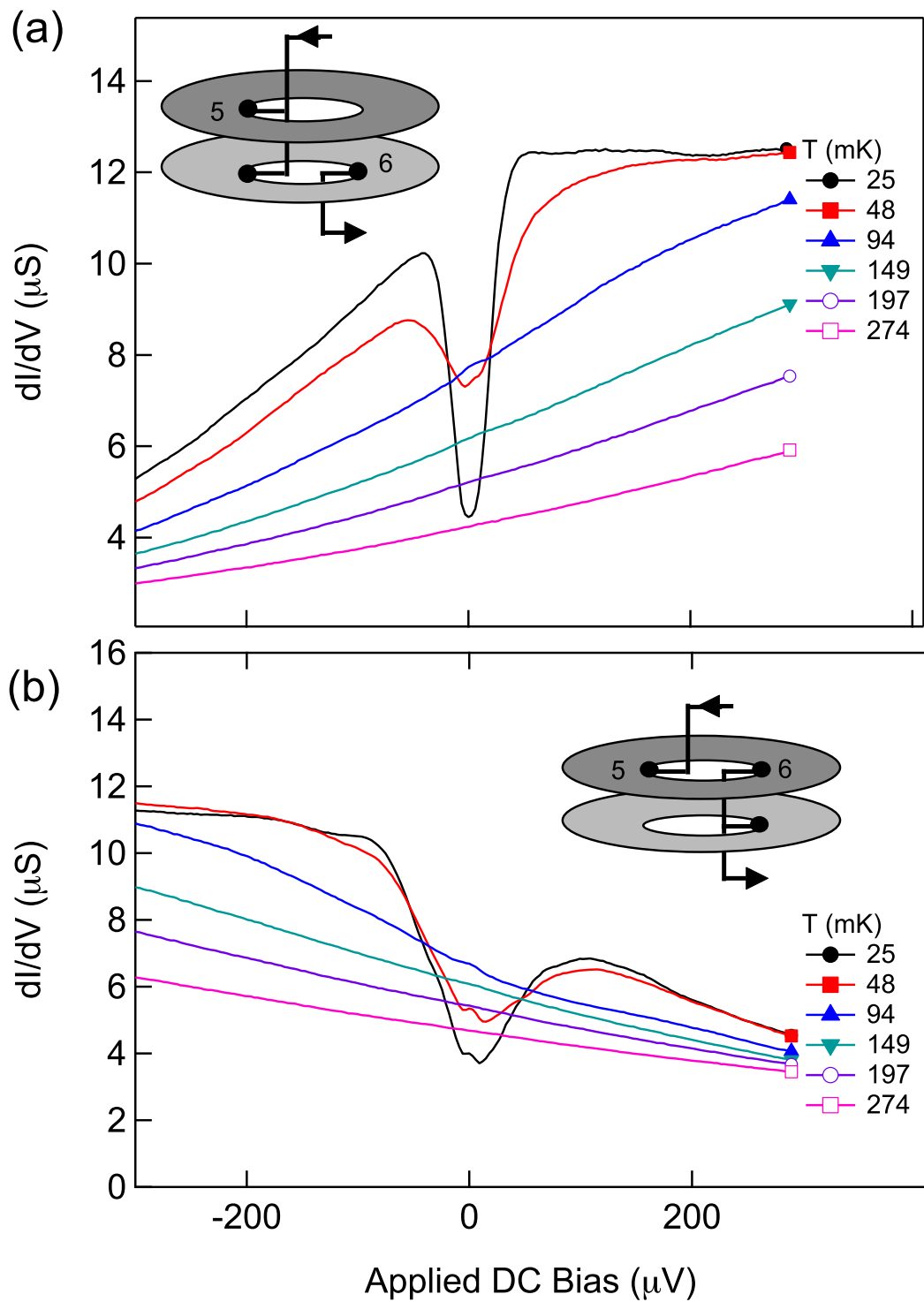
Figure 6.26: Conductance between two inner contacts (5 and 6), in the (a) bottom layer or the (b) top layer alone. $d/\ell = 1.49$ and $\theta = 28°$.

nominal density, parts of the arms fall within the fringe field region of the back gate. We depict this in figure 6.27a. The main back gate is vertically separated from the bilayer system by 50 μm, so its fringe fields could extend over a large area in which the bottom layer is partially depleted by the back gate. This will create a situation within certain sections of the arms near the $\nu_T = 1$ region where the top layer is at nominal density but the bottom layer is at a much lower density.

At high magnetic fields, the imbalanced bilayer is unstable to an additional transfer of charge from the lower density layer to the higher density layer. This increase in imbalance beyond the amount at zero field is caused by exchange interaction effects whose importance are enhanced by the quenching of the kinetic energy in the lowest Landau level. The exchange energy can drive a 2DES to have negative compressibility at low density [28, 29] and counteract the geometric capacitive energy costs for interlayer charge transfer from the lower density layer to the higher density layer. Subsequently, the lower density layer is deprived of even more electrons and rendered highly resistive due to its low Landau filling factor. Such changes in imbalance at high fields have been observed before in our bilayer samples (for example, see reference [13]). The conductance rises at finite bias either because the electrons can access extended states at higher energies or because the in-plane electric field tilts the random potential and facilitates the hopping of electrons between the valleys and hills induced by disorder. As depicted in figure 6.27b, there are even portions of the arm where the top layer is at a lower density than the bottom layer. Thus, one would also expect sections in the top layer to become highly resistive for similar reasons.[4]

To present evidence for this claim, we consider sample 7-12-99.1II. This is another Corbino sample constructed from the same wafer and almost the same geometry as sample 7-12-99.1JJ. However, the main top gate in sample 7-12-99.1II does not fully overlap with the main bottom gate. Thus, it had much larger regions within its arms in which the bottom layer was depleted by the bottom gate but the top layer was left at nominal density. As one might expect, we found even more severe issues with

---

[4]Although here we ignore the fringe fields of the back arm gates (separated from the main back gate by 100 μm), they may also somewhat perturb the bilayer system at the interface between the main gated and ungated regions.
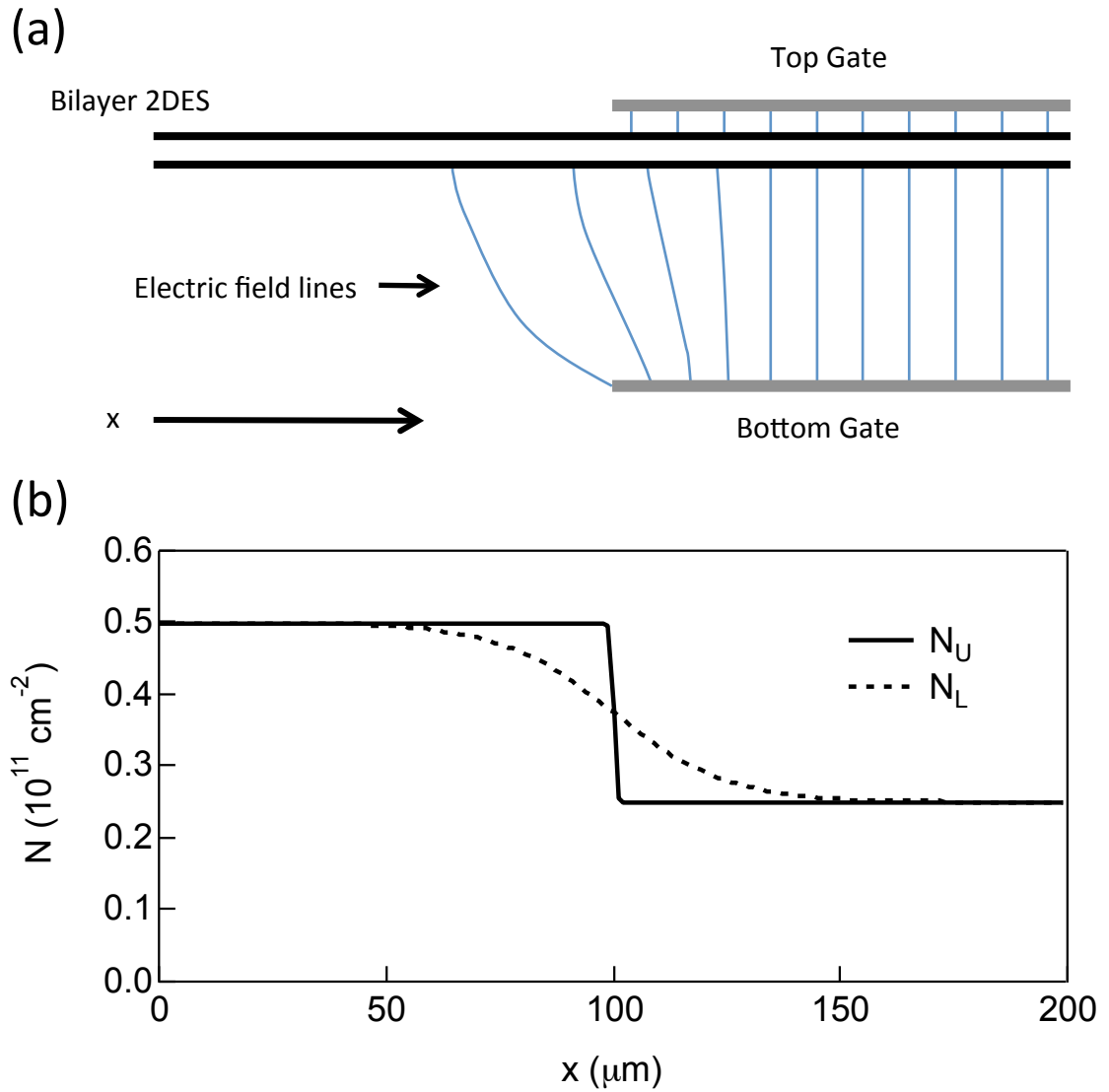
Figure 6.27: (a) Side view of bilayer system at the fringe field region. Both the top and bottom gates terminate at the x-coordinate $x = 100$ μm. (b) Qualitative density profile of upper layer (solid line) and lower layer (dashed line) expected at the fringe field region.

series resistance within this sample. For example, the tunneling $I - V$ in figure 6.28a shows that the arms in sample 7-12-99.1II were essentially insulating at zero bias.

We illustrate the interlayer charge transfer effect as a mechanism for nearly insulating behavior by considering sample 7-12-99.1II under two different conditions: while the bilayer system in the annulus is at balanced density and when a density imbalance is purposefully created. The solid trace in figure 6.28b shows the Corbino conductance of the top layer while the top gate and back gates are biased to create a balanced bilayer system with $N_U = N_L = 0.219 \times 10^{11}$ cm^{-2}. One can see a dip in the conductance for $\nu_T = 1$ at $B = 1.817$ T. Immediately on either side of this dip, the conductance in the top layer remains finite. For the dotted trace in figure 6.28b, the top gate gate is kept at the same bias as during the solid trace. However, now the back gate is left grounded so that the bottom layer is near nominal density. This results in large difference between the densities of the two layers within the annulus. The QH minima for $\nu_U > 1$ have shifted to lower magnetic field, indicating that now N_U has been reduced from its value when the two layers were at the density. By raising the density in the bottom layer, we have made it energetically favorable for additional charge to transfer away from the top layer to the bottom layer. Consequently, the upper layer becomes nearly insulating at high magnetic fields.

6.7.2 Estimation of Series Resistance from Tunneling

Although we are limited to making two-terminal measurements of Corbino counterflow resistance, we would like to estimate the series resistance within the arms and compare it to the observed counterflow $I - V$ trace. To estimate the series resistance, we can analyze tunneling data at $\theta = 0$, $d/\ell = 1.49$, and $T = 25$ mK. Here, the tunneling resistance at $\nu_T = 1$ is vanishingly small so long as the injected current does not exceed the maximum tunneling current. Thus, the two-terminal resistance will be dominated by the series resistance. If we perform tunneling measurements using contacts along the inner edge and then along the outer edge, we can obtain, respectively, the $I - V$ characteristics $I_{inner}(V)$ and $I_{outer}(V)$ for the series resistance
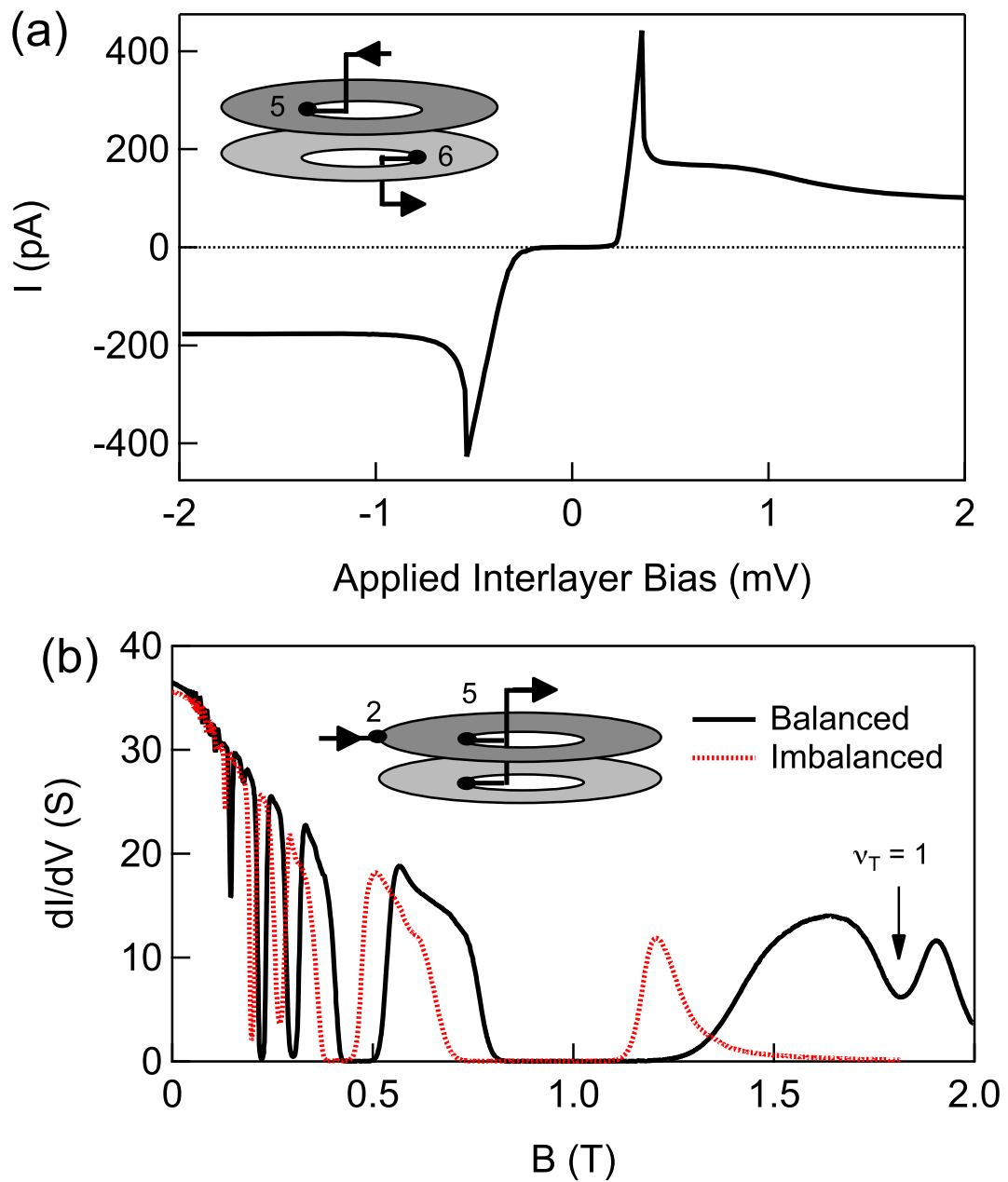
Figure 6.28: (a) Tunneling $I - V$ trace for sample 7-12-99.1II at $d/\ell = 1.47$, $T = 25$ mK, and $\theta = 0$. (b) Corbino conductance in top layer for sample 7-12-99.1II at $T = 50$ mK while a significant bias is applied to the top gate. In the solid black trace, a bias is also applied to the bottom gate so as to produce a balanced bilayer system with $N_U = N_L = 0.219 \times 10^{11}$ cm^{-2}. In the dotted red trace, the top gate is at the same bias as used in the solid trace but the bottom gate is kept grounded so as to produce a highly imbalanced bilayer system. The arrow indicates $\nu_T = 1$ for the balanced curve.

of the arms. However, we must restrict our analysis to where the total current I does not exceed the maximum tunneling current. Beyond that bias range, an interlayer voltage develops and the tunneling resistance is no longer negligible.

Each tunneling measurement reveals only the series resistance associated with two arms. For the Corbino counterflow measurement in figure 6.15, four arms are employed in addition to a 50 kΩ exterior shunt resistor. Thus, we must derive their total resistance. We combine the two $I - V$ traces from tunneling by inverting them numerically and defining a composite $I - V$ relation for the total series resistance as

$$V_{total}(I) = V_{inner}(I) + V_{outer}(I) + R_s I, \tag{6.4}$$

where $V_{inner}(I)$ and $V_{outer}(I)$ are the inverted $I-V$ traces from the tunneling measurements and R_s is the external shunt resistance. After numerically inverting equation (6.4), one obtains $I_{total}(V)$, the estimated $I - V$ characteristics of a circuit composed solely of the series resistance and the external shunt resistor.

In figure 6.29, we plot $I_{total}(V)$ and compare it to the Corbino counterflow measurement at the same d/ℓ and T but at $\theta = 28°$. One can see that the two traces are very similar to one each other. Indeed, the observed counterflow current can be made to coincide with the estimated series resistance by numerically adding only an additional ~ 15 kΩ resistance to the observed $I - V$ trace. This strongly suggests that the two-terminal resistance in the observed counterflow current circuit is almost entirely due to the series resistance and not from the excitonic condensate. Excitons can flow through the bulk with comparatively little dissipation.

It should be pointed out that the dotted trace in figure 6.29 is likely an *underestimate* of the true series resistance encountered during the actual counterflow measurement. First, the tunneling measurements used to determine the series resistance were taken at $\theta = 0$; we expect the conductivity of the low density 2DESs to decrease somewhat in the presence of a parallel field, as in the case for the counterflow measurement at $\theta = 28°$. Second, the observed counterflow $I - V$ trace was measured while the shunt resistor was grounded at one end. Thus, a small amount of current is

flowing to ground from the shunt, equivalent to I_2 in figure 6.15. This loss of current at the shunt could be causing at least some of the discrepancy between the solid and dotted traces, leading to an overestimation of the excitonic dissipation.
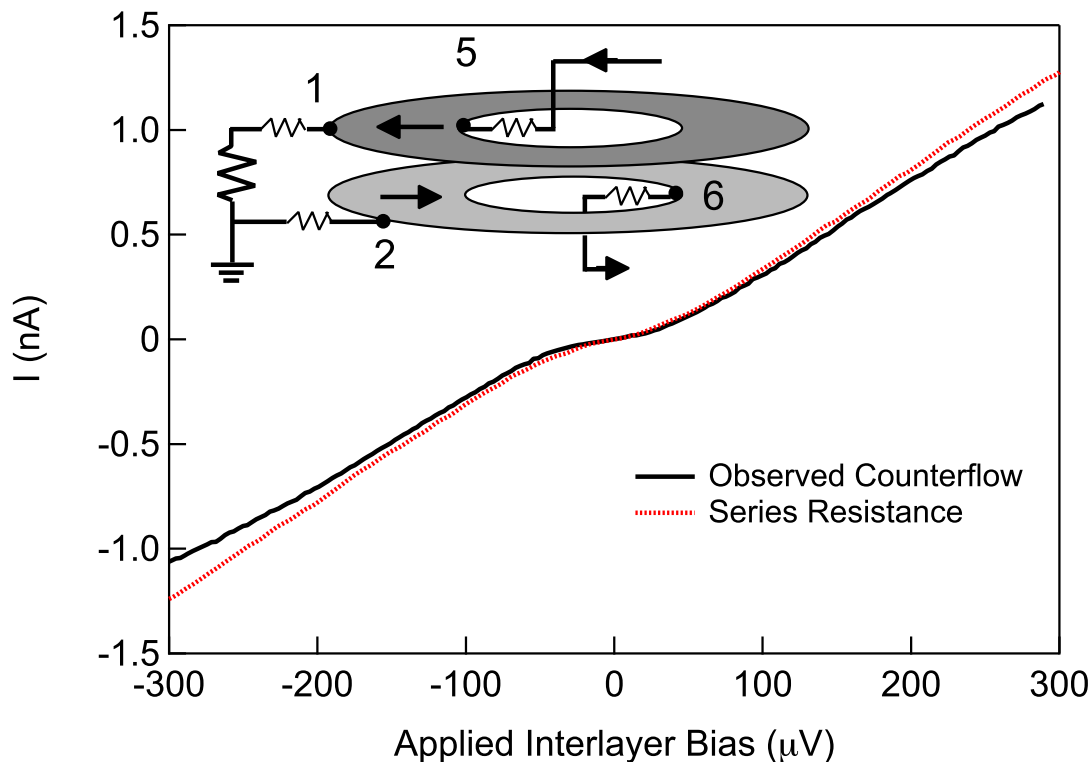
Figure 6.29: Solid, black trace: observed $I-V$ for Corbino counterflow with grounded exterior shunt resistance at $d/\ell = 1.49$, $T = 25$ mK, and $\theta = 28°$. Dotted, red trace: estimated $I - V$ for series resistance alone. The inset depicts the counterflow circuit with the series resistance from the arms explicitly shown.

6.7.3 Four-Terminal Corbino Measurements?

The significant series resistance in our Corbino sample raises the question of how to directly measure the dissipation of the bulk excitonic current. One might naïvely argue that if counterflowing electrical currents are propagating through the bulk of the annulus, then dissipation of such currents might be detected by measuring the voltage drop from one edge of the annulus to another within a single layer. Such a circuit is depicted in figure 6.30a. There, a bias is applied to a contact on the

bottom layer and along the outer edge of the annulus. A shunt between the two layers is provided along the inner edge, and the counterflow current is measured from a top layer contact along the outer edge. Here, the shunt is grounded and the voltage drop across the bulk is measured using contacts on the bottom layer. If counterflow currents were dissipationless, one might guess that $V_{bottom} = 0$. If counterflow currents had any residual dissipation, then presumably V_{bottom} would be a small but positive number.
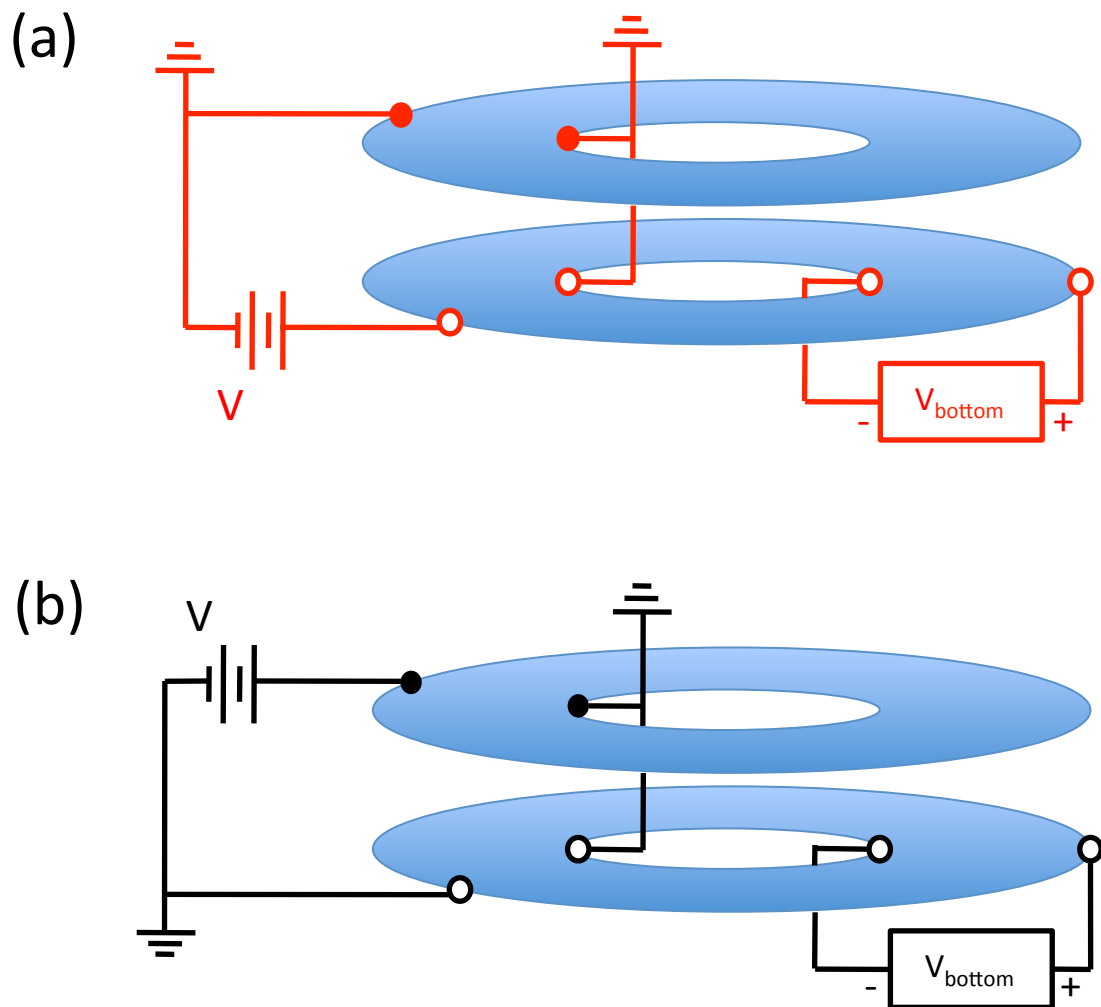
Figure 6.30: Depiction of circuit for four-terminal Corbino counterflow measurements in which the interlayer voltage is applied to either (a) the bottom layer or (b) the top layer.

However, this sort of measurement is ultimately insufficient because it only reveals the electrochemical differences across just one layer. However, excitons do not directly couple to this sort of chemical potential difference. We can demonstrate this by also considering an alternative circuit shown in figure 6.30b. There, the bulk voltage difference is measured across the same layer from which the current exits at the outer edge. With the polarity of the voltage probes shown in the figure, one might guess that in this circuit V_{bottom} would be zero for the case of dissipationless counterflow currents and V_{bottom} would be a small and negative value in the case of residual counterflow dissipation.

We have performed both such measurements at $d/\ell = 1.49$, $T = 25$ mK, and $\theta = 28°$. Under these conditions, tunneling and charge currents are suppressed. As shown in plot 6.31, we find that the magnitude of V_{bottom} is relatively large in both measurements: about half of the applied DC bias. We also see that, contrary to the naïve expectations, V_{bottom} is *positive* for both circuits. One can now see why measuring the voltage across the bulk of one layer is inappropriate for determining exciton dissipation. The results of such a measurement would reflect the dissipation of *charged* excitations traveling through the individual layers. However, during a counterflow measurement at $\nu_T = 1$, essentially no charge flows across the bulk. Otherwise, in the case of the circuit in figure 6.30a it would appear that any charged excitations traveling in the bottom layer would be going in the *opposite* direction as the radial electric field in that layer.

The circuits in figure 6.30 are the Corbino equivalents of measuring longitudinal voltage drops V_{xx} along the edge of a single layer in Hall bars [66]. They both only address dissipation of *charge* currents and do not direct detect bulk *exciton* dissipation. Instead, we assert that one must compare interlayer voltages measured at both edges simultaneously. According to the Josephson relations, the time derivative of the order parameter is proportional to the interlayer voltage. If the interlayer voltage is found to differ from one edge of the annulus to other in the presence of an excitonic flow, then phase slips must be occurring in the order parameter. These phase slips represent dissipation in the excitonic flow.
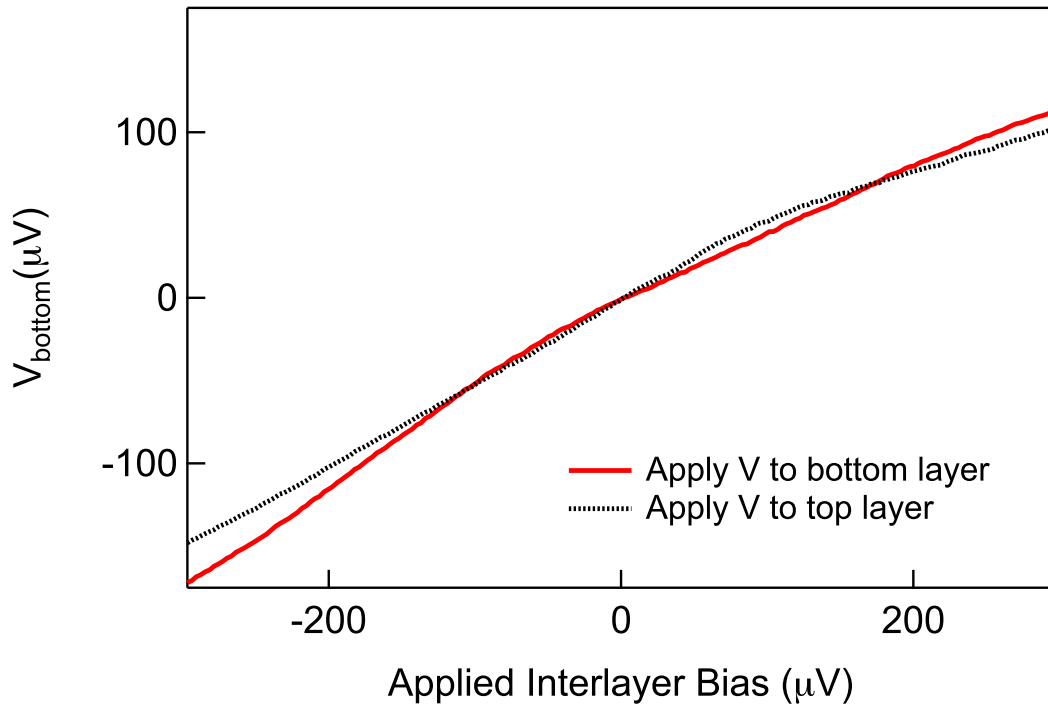
Figure 6.31: Voltage drop across bulk on bottom layer (outer − inner) during Corbino counterflow measurement at $d/\ell = 1.49$, $T = 25$ mK, and $\theta = 28°$. For the solid trace, the voltage is applied to the bottom layer at the outer edge, and the current leaves from the top layer at the outer edge. For the dotted trace, the voltage is applied to the top layer at the outer edge and the current leaves from the bottom layer at the outer edge. A single, grounded ohmic contact along the inner edge shunts the two layers together.

One may arrive at this conclusion through an alternative argument. If one treats the bilayer system as a two-conductor transmission line, then in order for counterflow currents to be dissipationless then the power injected at one end would have to be equal to the power received at the other. The power entering or leaving either edge would be equal to the current $I_{L,R}$ passing into or out of a given edge times the voltage difference $\Delta V_{L,R}$ between the two conductors at that edge. Thus, dissipationless counterflow currents would imply $I_L \times \Delta V_L = I_R \times \Delta V_R$. Assuming that there is no tunneling current or loss of current to ground at the shunt, this would also require equal interlayer voltages at either edge. Within this picture a time-independent order parameter is not necessary. Indeed, a transmission line constructed from two superconductors would have a phase difference $\Delta\phi = \phi_1 - \phi_2$ that evolves with time when delivering current to a load resistor. The counterflowing currents would be dissipationless within the superconductors and any power loss would occur within the load.

Unfortunately, our sample does not have a sufficient number of contacts to simultaneously measure the interlayer voltages at both edges of the annulus in the presence of a bulk exciton flow. Thus, we cannot directly measure exciton dissipation.

6.8   Discussion

6.8.1   Andreev-Like Reflection

Following Su and MacDonald [111], the enhanced counterflow conductivity can be interpreted in terms of Andreev reflection. Usually, Andreev reflection describes the scattering phenomenon occurring when a low-energy electron from a normal metal is incident on an interface with a superconductor. While single-particle transmission is blocked within the superconductor's energy gap, the electron can generate a Cooper pair with charge $2e$ within the conductor. To conserve charge, the incident electron is subsequently reflected as a hole in the metal [4]. For the $\nu_T = 1$ QH state, an analogous process occurs by which the electrical currents in the normal leads generate

the bulk exciton flow in the condensate. We depict this in figure 6.32. Here, the left and right sides of the diagram correspond to the inner and outer edges of our Corbino disk, separated from each other by the electrically insulating bulk. When an electron is injected into the top layer at one edge (shown in the upper left of figure 6.32), it is unable to enter the bulk but can generate a neutral exciton. To conserve charge, the condensate ejects an electron into the lower layer at the left side of the diagram, which can be detected by our current preamp. The exciton flows through the bulk until it hits the other edge, where it produces an electron in the upper layer and pulls in another electron from the lower layer. This generates another electrical current that passes through the shunt resistance. Without the shunt resistor in figure 6.32, the system requires the exciton current to vanish at the other edge because nothing would available to absorb it there. This corresponds to the spatially decaying solutions to the sine-Gordon equation (equation (5.2)) and thus one will observe the usual tunneling response.
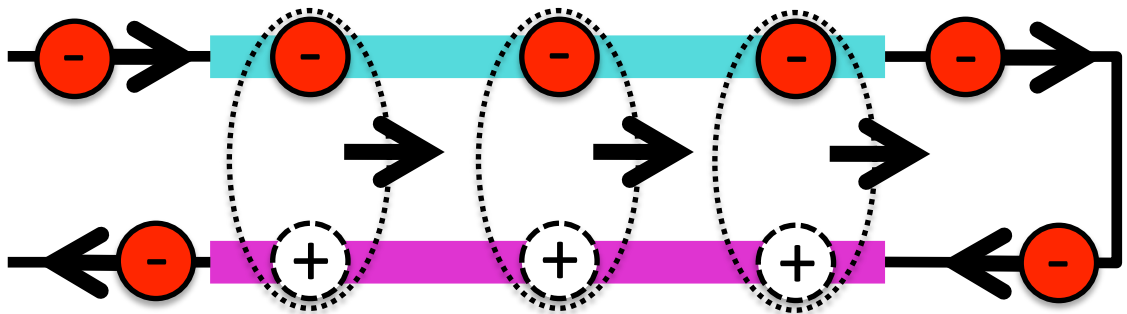
Figure 6.32: Depiction of bulk exciton current being generated by the current leads on the left edge and absorbed by the shunt on the right edge. Based on the diagrams by Su and MacDonald [111].

Please note that figure 6.32 is merely a one-dimensional picture of the exciton flow. In real samples, we anticipate that one must consider a fully two-dimensional

model that takes into account the electrical current flowing through edge channels from one contact to another along the edge of the annulus. In this case, the charged quasiparticles' coupling with the exciton condensate will generate the exciton flow and the concomitant transfer of charge from one layer to the other within the edge channel. For example, one might adopt the pseudospin transfer torque model [92, 112] originally developed to analyze the tunneling geometries. Then the relaxation rate of the quasiparticle pseudospin vector would govern the length of the region along the edge over which the excitons are created or absorbed.

6.8.2   Excitonic Superfluidity?

While we have demonstrated bulk exciton currents, it is an open question whether the $\nu_T = 1$ QH state can support a completely dissipationless flow of excitons. Using a Corbino device we can remove the edge channels as a source of dissipation. But there are other mechanisms that might impede excitonic superfluidity, which we briefly describe here.

A prime villain is disorder, which can inhibit superfluidity in bilayers in a number of ways. As mentioned earlier in this chapter, antisymmetric gauge fluctuations could induce a gauge glass phase by pseudospin phase frustration [109, 98]. However, layer-symmetric disorder could nucleate charged defects consisting of vortex-antivortex pairs [34]. These defects may not be fully pinned by disorder and could experience thermally activated hopping from one defect to another. The motion of these vortices in the excitonic order parameter induces voltage drops and thus destroys superfluidity. Although one would expect the vortex-antivortex pairs to bind to each other below the Kosterlitz-Thouless temperature T_{KT}, quenched disorder in bilayers may allow them to become mobile under certain circumstances [34, 33, 91].

For example, in the coherence network model by Fertig and Murthy [33] doping fluctuations create puddles of compressible, incoherent fluid surrounded by narrow strips of coherent $\nu_T = 1$ fluid. While the vortex-antivortex pairs are normally confined in these regions of incoherent fluids, they might thermally hop from one puddle

to another and contribute to dissipation in counterflow. Sun *et al.* [114] build on this coherence network picture by modeling quenched disorder as a periodic potential. They find that this potential produces a quadratically dispersing mode that is normally gapped but can become nearly gapless at certain strengths of the periodic potential. The quadratic mode lowers the energy of vortices, so when it becomes gapless it greatly reduces the pseudospin stiffness and T_{KT}.

Thus, there is a strong need to produce a Corbino device that would allow the measurement of dissipation in bulk exciton flow. This would allow us to determine whether or not disorder is undermining excitonic superfluidity.

We close this section by noting that there might be inherent problems with the particular counterflow circuit employed in this chapter [35, 111, 36]. In order to support an exciton flow within the $\nu_T = 1$ region, there must be a current passing through the resistive shunt. This requires an interlayer voltage and thus the Josephson relation $V = i\frac{\hbar}{e}(\partial_t \phi)$ would imply a time-dependent order parameter. Fil and Shevchenko [35, 36], for example, argue that this interlayer voltage both forces Josephson vortices to move and create dissipation through the second viscosity of the condensate. It is unclear if the motion of such vortices could be pinned by disorder, just as they are in type-II superconductors. Spatial and temporal variations in the interlayer voltage could also lead to charged quasiparticle currents and another source of residual resistance in counterflow that scales with the square of the bare-electron tunneling amplitude.

Su and MacDonald [111] come to a similar conclusion and suggested an alternative counterflow circuit known as drag-counterflow, depicted in figure 6.33. Here, the shunt resistance is placed between contacts on one layer at the outer and inner edges of the Corbino annulus. A current can then be injected and withdrawn from two corresponding contacts on the other layer. It resembles a drag measurement, except it allows a current to flow through the shunt and enables a counterflow current. No interlayer voltage is required in this geometry and a stationary order parameter is permitted. This drag-counterflow circuit is not with its own issues, however. First, it would not necessarily avoid the disorder effects mentioned earlier. Second, this

circuit does not appear to transmit energy from one edge to another [36] and cannot be used to demonstrate bulk exciton currents. Indeed, this circuit has been studied before by Tiemann *et al.* [116], but they were unable to distinguish their results from the case of strong interlayer tunneling occurring at either edge of their Corbino ring. Nonetheless, our group is in the process of studying our own Corbino device using the drag-counterflow circuit. Preliminary results suggest that large currents can be induced to flow through the shunt even in the absence of strong interlayer tunneling.
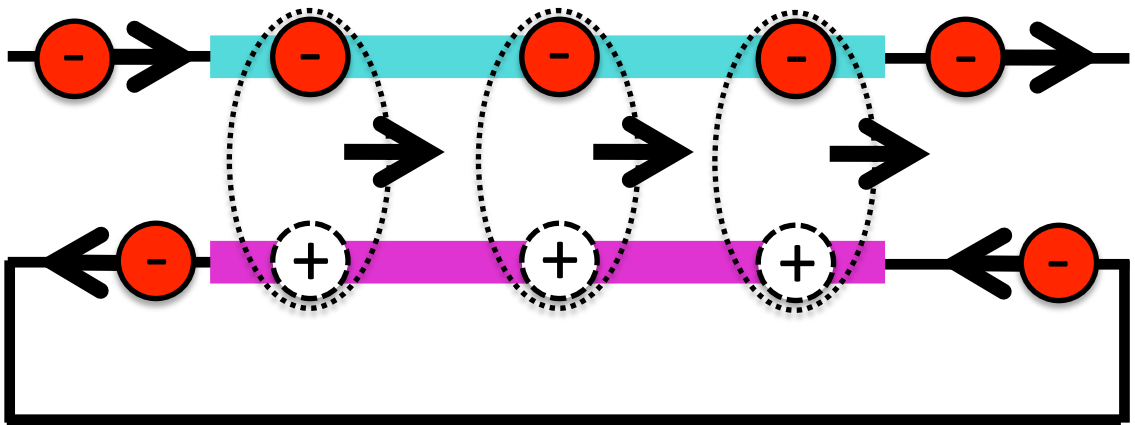
Figure 6.33: Depiction of circuit for drag-counterflow, based on Su and MacDonald [111]. This form of counterflow permits a time-independent order parameter.

6.9 Conclusion

In this chapter, we have presented unambiguous evidence that counterflowing current can propagate through the bulk of the $\nu_T = 1$ quantum Hall system, even as charged currents cannot. Deep within the correlated phase, these counterflowing currents can transmit energy through the bulk without a net transfer of charge, which are key signatures of exciton transport. The conductance of counterflowing currents appear to be larger than that of parallel currents even at elevated temperatures. Our findings

help to confirm the excitonic nature of the $\nu_T = 1$ system.

Conclusion

The data presented in this thesis have shed light on exciton condensation in bilayer quantum Hall systems. Here, we summarize our findings and consider future directions for studying this unique system of correlated electrons.

At low Zeeman energy, we find evidence that is consistent with a first-order phase transition between the correlated and uncorrelated phases, broadened by disorder. This is in agreement with other recent studies of the phase boundary, including evidence for a spin transition at the phase boundary. It is likely that the first-order phase transition preempts the previously predicted KT transition. However, when both phases are fully spin polarized at high Zeeman energy, we see that the phase transition becomes significantly broader. This could signal a change in a nature of the phase transition to an intrinsically continuous one. The identity of this hypothetical continuous transition is still unclear.

Near the phase boundary, we find that the magnitude of the Josephson-like tunneling peak scales linearly with the area of the $\nu_T = 1$ region. In one sample, we find hints that this linear relation holds true relatively far away from the phase boundary. These results disagree with a simple model of the exciton condensate in which nearly all of the tunneling current occurs within the Josephson length of the perimeter. This suggests that disorder has a major effect on the spatial distribution of tunneling current by causing fluctuations in the excitonic order parameter.

Finally, we have clearly demonstrated the ability of counterflow currents to travel through the bulk of the $\nu_T = 1$ bilayer system. These counterflow currents are identified with exciton transport. While charged excitations are confined to the edges of the quantum Hall system, we find that neutral excitons may propagate freely through

the system interior with relatively little dissipation. The existence of a neutral mode in the bulk distinguishes the $\nu_T = 1$ system from other quantum Hall states.

While we have made progress in expanding our understanding of the $\nu_T = 1$ quantum Hall state, many questions still remain. The following is an incomplete list of future directions.

Exciton dissipation

Our Corbino studies can only provide an upper bound on exciton dissipation. We anticipate performing more direct measurements of dissipation in counterflow by fabricating a Corbino sample with additional ohmic contacts in the interior. Such a geometry would permit simultaneous measurements of the power transmitted into and received from the edges of the $\nu_T = 1$ system via excitons passing through the bulk.

Continuous phase transition at high Zeeman energy

The nature of the phase transition at full spin polarization is largely unknown. We have only performed Coulomb drag measurements in this regime. Other probes are needed in order to distinguish between various candidates for this apparently continuous phase transition.

Interlayer capacitance and compressibility

We have yet to perform an extensive study of the interlayer capacitance at $\nu_T = 1$. A more thorough investigation at dilution fridge temperatures could reveal the anticipated anomalies caused by the excitonic phase. This thesis has described our progress in overcoming certain technical difficulties relating to background signals such as the ungated regions of the bilayer and the geometric capacitance.

Time-domain spectroscopy

Bilayer transport studies have generally been confined to low frequencies. Measurements such as reflectometry at modestly high frequencies (megahertz to gigahertz) could explore the collective modes of excitons. One would need to overcome the key hurdle of the strong capacitive coupling between the two layers. Such strong coupling could impede measurements of high frequency counterflow currents in a manner similar to how strong tunneling can prohibit detection of bulk exciton currents.

Coupling with surface acoustic waves

Related to time-domain transport is the use of audio frequency surface acoustic waves (SAW) to study the $\nu_T = 1$ state. SAWs are expected to induce an interlayer electric field, which can couple directly with excitons. The velocity of SAWs driven through the bulk of the $\nu_T = 1$ state could be altered by the counterflow conductance. Thus, SAWs can probe the exciton condensate at finite wave-vector and provide information about exciton dissipation at low temperature and the role of spatial fluctuations during the phase transition.

Mesoscopic structures

Up until now, our group has only published results from bilayer samples whose dimensions were no smaller than 10 μm. This is far larger than the coherence length $\xi = 200$ nm inferred from the rate at which the central tunneling peak collapses in the presence of a parallel magnetic field [102]. Samples with dimensions no larger than the coherence length would presumably permit a number of measurements that are inhibited by disorder in larger devices. This includes the observation of Fraunhofer diffraction (for example, see [102]), a sharper phase transition in the low Zeeman energy regime, and coherent tunneling of excitons between two weakly coupled $\nu_T = 1$ regions [90]. Our current bilayer samples require both top and bottom gating in order to reduce the density enough to achieve the $\nu_T = 1$ QH state. The presence of the top gate seems to rules out the usual quantum dot and quantum pot contact (QPC)

structures, which are also defined using top gates. One possible solution is to etch away channels in the aluminum top gate in order to define the desired geometry. This could be combined with reactive ion etching of the GaAs mesa [11]. As demonstrated in chapter 6, one must be sure to place the top gates for selective depletion fairly close to the $\nu_T = 1$ region in order to minimize the area of highly imbalanced bilayer 2DES between the $\nu_T = 1$ region and the ohmic contacts.

Submillikelvin temperatures

The height and width of the Josephson-like tunneling resonance continues to evolve even down to $T = 15$ mK [102]. It is not known what new excitonic physics might pop up if the temperature were lowered by another order of magnitude or more. Nonetheless, there is a long history in condensed matter physics of exotic quantum states being discovered by getting closer to absolute zero. Our lab is highly motivated to do the same. To this end, we have installed and tested a dilution refrigerator with a nuclear demagnetization stage. Our goal is to achieve electron temperatures of $T \approx 1$ mK. Initial tests have shown that the nuclear coolant can reach submillikelvin temperatures, but it will be an enormous challenge to cool the electrons in our 2DESs to a similar temperature.

Appendix A

Properties of the 2DES in GaAs

Units:	Carrier Density	N_S	10^{11} cm^{-2}
	Resistivity	ρ	Ω per square
	Mobility	μ	10^6 cm^2/Vs
	Magnetic Field	B	T
	Energy		K or meV

Effective Mass (conduction band)	$m^* = 0.067 m_0$
g-factor:	$g = -0.44$
Dielectric constant (appx.)	$\epsilon = 13 \times \epsilon_0$
Fermi Wavevector:	$k_F = 7.93 \times 10^5 \times N_s^{1/2}$ cm^{-1}
Fermi Energy:	$E_F = 3.58 \times N_S$ meV
	$E_F = 41.5 \times N_s$ K
Fermi Velocity:	$v_F = 1.37 \times 10^7 \times N_S^{1/2}$ cm/s
Mobility from Resistivity:	$\mu = 62.4 \times N_S^{-1} \times \rho^{-1}$
Mobility Lifetime:	$\tau = 38.1 \times \mu$ ps
Mean Free Path:	$\lambda = 5.22 \times \mu \times N_S^{1/2}$ μm
Magnetic Length:	$\ell = 257 \times B^{-1/2}$ Å
Classical Cyclotron Radius:	$R_c = 522 \times N_S^{1/2} \times B^{-1}$ Å
$\nu = 1$ Magnetic Field:	$B_{\nu=1} = 4.14 \times N_S$ T
Cyclotron Energy:	$\hbar\omega_c = 20.1 \times B$ K
Zeeman Splitting:	$g\mu_B B = 0.29 \times B$ K
Coulomb Energy:	$e^2/\epsilon\ell = 50 \times B^{1/2}$ K

Appendix B

List of Samples

The following chart lists the samples used in this thesis. The first column is the name of the sample. The second column gives the chapter in which the sample appeared in this thesis. The third column contains a brief description of the sample's purpose. The fourth column provides a characteristic tunneling conductance of the sample at zero magnetic field and low temperature ($T \leq 300$ mK) as well as the area of the particular region in which that tunneling measurement was obtained. Some samples (such as 11-1-04.1K and 11-1-04.1L) have multiple top gates covering a large mesa; the tunneling conductance and system area given below reflect the properties of only a single top gate.

Sample	Chapter	Purpose	Zero field tunneling (area)
7-12-99.1R	4	Simple square sample	30 nS (62,500 μm^2)
7-12-99.1II	6	Corbino counterflow	540 nS ($\sim$750,000 μm^2)
7-12-99.1JJ	6	Corbino counterflow	1300 nS ($\sim$750,000 μm^2)
11-1-04.1M	3	Interlayer capacitance	100 nS (51,400 μm^2)
11-1-04.1K	5	Area tunneling	285 nS (20,000 μm^2)
11-1-04.1L	5	Perimeter tunneling	65 nS (10,000 μm^2)

Sample are made from two double quantum well wafers (7-12-99.1 and 11-1-04.1) with essentially identical 18 nm:10 nm:18 nm (GaAs:Al$_{0.9}$Ga$_{0.1}$As:GaAs) structures described in chapter 2. The wafers were grown by L.N. Pfeiffer and K.W. West at Bell Labs.

All samples have nominal densities of roughly $n_{1,2} \approx 5.5 \times 10^{10}$ cm^{-2} and mobility of $\mu \approx 10^6$ cm^2/V-s at low temperatures. The name of each sample consists of the name of the wafer plus a letter code.

Appendix C

Sample Processing

The following is a list of steps I have used for to process bilayer GaAs samples. This procedure is mostly based on the recipes of others, but I have made a few modifications.

1. **Cleaving**

   Cleave off a 5 mm × 5 mm piece from wafer using stylus and clean, plastic tweezers. Cleave the piece on a lab book covered with a KimWipe.

2. **Mesa Etch**

   (a) Clean sample by rinsing with acetone and isopropanol (IPA). Blow-dry.

   (b) Spin on photoresist, AZ5214E, 5000 RPM, 30 seconds. Before adding the photoresist, clean eye dropper by rinsing with IPA and blow-drying thoroughly.

   (c) Bake sample on hot plate at 100 °C for 45 seconds.

   (d) Expose with mesa pattern on mask aligner for 15 seconds with UV intensity of 15 mW/cm^2. Choose a defect-free section of the sample (especially for the tunneling region); defects might "short" the two layers together.

   (e) Develop in premade AZ400K (1:4) solution for 40 seconds. This solution is 1 part developer per 4 parts deionized (DI) water, by volume. Rinse in DI water twice for 20 seconds each. Blow-dry (10 seconds) and evaluate under the microscope.

(f) Postbake on hot plate at 100 °C for 75 seconds.

(g) Phosphoric etch: Mix 10 mL H3PO4 (85%), 2 mL H2O2 (30%), and 100 mL of DI water. Stir with magnetic stirrer (stir setting = 7, stir for 30 seconds). Place sample in solution in covered Petri dish for 6 minutes. Rinse in water and dry (10 seconds). Make sure no bubbles are present on the top surface of sample during the etch. If you see any, use a sharpened wood dowel to gently nudge them off.

It is also possible to use a premade phosphoric acid etch solution and keep it in a sealed bottle in the refrigerator. If so, be sure to remove the acid solution from the refrigerator and let it sit in a small bath of water for at least 30 minutes prior to using it in order to allow it return to room temperature.

(h) (optional) use Dektak to measure height of mesa + photoresist. In general, try to DekTak a "nonfunctional" or "nonessential" part of the mesa (e.g., a corner where one of the ohmics will be). Avoid bringing the DekTak probe over your tunneling region; you do not want to possibly damage that area. One could also try measuring the height of two different parts of the mesa and comparing them.

(i) Remove photoresist by placing sample in n-butyl acetate at 75 °C for 15 minutes. Let cool at room temp for 5 minutes. Rinse in IPA and blow-dry. DekTak mesa and evaluate.

3. **Ohmic Contacts (evaporated Ni/AuGe)**

(a) Clean sample again by rinsing in acetone and IPA. Blow-dry. Then turn on evaporator (mechanical pump, cooling water, and diffusion pump). Be sure to let the diffusion pump warm up for at least 30 minutes prior to using the evaporator.

(b) Spin on photoresist, AZ5214E, 5000 RPM, 30 seconds.

(c) Bake at 100 °C, 45 seconds.

(d) Expose with ohmic contact pattern for 15 seconds.

(e) Before developing, prepare the evaporator: put liquid nitrogen into cold trap, insert boats and slugs for nickel (2 slugs) and AuGe (1 slug). Put the nickel boat in stage 3 (the farthest one in) and the AuGe boat on stilts in stage 2 (the middle one).

Note: the purpose of getting the evaporator ready ahead of time is to minimize the amount of time that the developed portions of the sample are exposed to air, thus reducing oxidation. Double-check tooling factors for two different materials. Check the crystal in the thickness monitor by pressing and holding the Life button. Replace crystal if life is less than 60%. Be wary if the life is between 60% and 70%: if the crystal gets too old, its reading can be vary flaky.

(f) Develop sample in premade AZ400K (1:4) solution for 40 seconds. Rinse in DI water twice, 20 seconds each. Blow-dry and evaluate.

(g) Evaporate Ni/AuGe. First evaporate 135 angstroms of Ni. Let cool for 5 minutes. Then evaporate 1600 angstroms AuGe. Wait 15 minutes before venting and opening up chamber to allow everything to cool down.

(h) Lift-off: place sample in n-butyl acetate at 60 °C for 30 minutes. Do not remove sample from n-butyl acetate until all excess metal has been removed! You can facilitate lift-off after 30 minutes by squirting at sample with eye dropper while the sample is still submerged in the n-butyl acetate (be sure to hold the sample down with your plastic tweezers while squirting at it with the eye dropper). If you get desperate, hold the n-butyl acetate container in the sonicator and sonicate for 10 seconds. Check the sample under the mask aligner microscope while the sample is still in the n-butyl acetate, to make sure all excess metal has been removed.

(i) Clean sample again by rinsing in acetone and IPA. Dry.

(j) (optional) Photograph sample.

(k) Place sample in center of annealing strip. Close the chamber and flow forming gas (15% H_2, 85% N_2) for 5 minutes. Set flow rate to 2 units. Anneal at 440 °C for 15 minutes. After the anneal is done, wait until the annealing strip cools down to below 40 °C before opening up the chamber.

(l) (optional) Photograph sample. The surface of the Ni/AuGe should now look very rough and wrinkled.

4. **Top Gates**

(a) Clean sample by rinsing in acetone and IPA. Blow-dry. If it is not still on, turn on evaporator (mechanical pump, water, and diffusion pump).

(b) Spin on photoresist, AZ5214E, 5000 RPM, 30 seconds.

(c) Bake on hot plate at 100 °C for 45 seconds.

(d) Expose with top gates pattern for 15 seconds.

(e) Prepare evaporator (add liquid nitrogen to cold trap, put a new aluminum boat and 3 Al slugs in position 2 (without stilts)). Check program (program 1), tooling factor, and life of crystal. To reach 2000 angstroms, put 4 Al slugs in position 2 (without stilts).

(f) Develop sample in premade AZ400K (1:4) solution, 40 seconds. Rinse in DI water twice, 20 seconds each. Blow-dry and evaluate.

(g) Evaporate aluminum: 1600-2000 angstroms. The thickness of the film should be large enough so that the gates are continuous as they go over the mesa edge. We have had problems with discontinuous top gates, likely because not enough aluminum was evaporated.

(h) Lift-off in n-butyl acetate, 60 °C, for 30 minutes. As above, do not remove sample from n-butyl acetate at all until all metal has been removed (check with microscope). This is particularly important for aluminum top gates, which might have small spacing between some of the gates, in which metal can easily get caught.

(i) (optional) Photograph sample.

5. **Sample thinning**

   Warning: this step can be very dangerous and very tricky. You should get first-hand training with someone knowledgeable before attempting it by yourself.

   (a) Pick out 3 pieces of scrap GaAs. These are the dummies and help to keep the sample level during the etching. Try to find three that are nearly the same thickness and slightly thicker than the sample itself. If possible, cleave off three dummies from the sample piece of scrap GaAs. Watch out: I have seen at least one piece of scrap GaAs with some kind of blocking layer that was impervious to the bromine etch solution, thus forcing me to restart the etch with a new set of dummies.

   (b) Clean sample and 3 dummies by rinsing them in acetone and IPA. Blow-dry. Clean quartz disk by rinsing in acetone and IPA. Blow-dry.

   (c) Mount sample on disk with wax. First, add 1-2 grains of wax to the center of the disk. Use the grey hot plate at setting = 3 for 5 minutes to melt the max. Gently place the sample upside down on the wax and then push down firmly and smoothly with a thick wooden dowel. One wants to push the sample down toward the quartz glass as much as one can without breaking the GaAs. Try not to let the sample move during this step or you might scratch the top side.

   (d) Mount the dummies using a similar procedure, while the disk is still hot. For each dummy, place 1-2 grains of wax at a spot that is about 10 mm away from the center of the disk and then mount the dummy there. The three dummies should be evenly spread around the sample, each located at the vertex of an imaginary triangle centered on the sample.

   (e) Remove excess wax by squirting with acetone and then IPA while holding the quartz disk with plastic tweezers over a medium or large beaker. Blow-dry and check to see that no wax or acetone residue is left behind.

(f) In the acid hood, prepare the quartz square and filter paper. Fold the filter paper in half and wrap it around the quartz square. Secure with masking tape. You want one surface that is as smooth and taut as reasonably possible.

(g) In the acid hood, mix the bromine-methanol etch solution: 80 mL MeOH and 5 mL Br_2. Do not forget to wear lab coat, apron, heavy neoprene gloves, and face shield. The original etch solution recipe calls for 40 mL of MeOH and 5 mL of Br_2, but Alex Champagne has found that diluting the bromine in more methanol helps the etch to go slower and more evenly. This helps to keep the back side of the sample smooth. The etching will be performed in the acid hood. Be sure to keep acetone away from the acid hood. Keep the bromine-methanol solution covered with glassware to prevent the spread of bromine fumes.

(h) Perform etch. Place the quartz disk in a Teflon chuck by dropping three drops of water onto the chuck and pressing the quartz disk down into the depression with the sample facing out. There is a coarse side (indicated by a divot on the chuck) and a fine side; start with the course side. Stir up the etch solution with a wooden dowel (to homogenize the bromine-methanol solution) and pour some onto the quartz square with the filter paper. Add enough etch solution to get the filter paper to be evenly wet. While holding onto the chuck with a neoprene glove, rub the sample against the filter paper with the etch solution. Do large figure-eight motions. Start off by performing 50 such motions and then rinse off the sample in DI water. Pop off the quartz disk with pressurized air from a spigot inside the acid hood (carefully!) and rinse it again with water. Blow-dry. Measure the thickness of the sample. Also try to measure the thickness of dummies as you etch to get a sense of whether you have a tendency to etch one side of the sample more than the other.

After measuring the thickness of the sample, put the quartz disk back into

the Teflon chuck and pour some more etch solution on the filter paper to prepare for more etching. Be sure to stir the etch solution with a thin wooden dowel just before each time you pour it onto the filter paper. Otherwise, we have found that the bromine will tend to settle to the bottom of the beaker as time goes on, leading to an increase in bromine concentration and etch rate as time goes on. Keeping the etch rate constant helps to keep the back side of the sample smooth.

(i) Etch until the sample is 50 μm thick. Measure the thickness of the sample more frequently as time goes on. Once the sample is less than 350 μm, switch to the fine side. Be careful not to scratch the sample with the thickness monitor's probe.

(j) Once done with etching, clean up. Pour remaining etch solution in an open glass container with sodium thiosulfate. I have found that pouring just a little bit of water along with the bromine solution helps to neutralize the bromine. At the very least, it makes the orange stain of the bromine go away, which suggests it has been neutralized. Rinse out filter paper, quartz disk, and tray with water in acid hood. Clean up glassware.

(k) Scrape off dummies from the quartz disk with a razor blade. Rinse off with IPA and blow-dry. Keep the sample on the quartz disk. Try not to let pieces of GaAs fly onto the sample.

6. **Back gates**

(a) While it is still on the quartz disk, clean sample by squirting with acetone and IPA. Dry. Meanwhile, set hot plate to 100 °C and turn on evaporator (mechanical pump, water, diffusion pump) if it is not already on.

(b) Spin on photoresist, AZ5214E, 5000 RPM, 30 seconds. After the quartz disk disk has stopped spinning, quickly add another dose of photoresist and spin again for 30 seconds.

(c) Bake on hot plate at 100 °C for 90 seconds.

(d) Expose with back gates pattern for 15 seconds. Use IR camera to align sample properly.

(e) Prepare evaporator (add liquid nitrogen to cold trap, put new aluminum boat and 4 slugs of aluminum to stage 2, without stilts).

(f) Develop in premade AZ400K (1:4) solution, 40 seconds. Rinse in DI water twice, 20 seconds each. Blow-dry. Evaluate.

(g) Evaporate aluminum: ~1600 angstroms. Technically you could just add 1000 angstroms, but we often like to add more, just to make sure the back gates are nice and continuous.

(h) Lift-off in n-butyl acetate at 60 °C for 30 minutes. Once again, do not remove sample from n-butyl acetate until metal has been completely lifted off.

(i) Rinse sample and disk in IPA. Blow-dry.

(j) Sample slide-off: place a piece of filter paper on the bottom of Petri dish. Place the quartz disk upside down while using a clean magnetic stir bar to prop up one edge of the disk. The sample should be facing down and suspended over the filter paper without actually touching the filter paper. Add enough acetone to completely submerge the sample, plus a little bit extra (the acetone will evaporate during sample slide-off). Cover the Petri dish with its top and let sit in the middle of the chemical hood (away from the two vents at the front and back). The wax should be dissolved within 2 or 3 hours. You can watch its progress with a magnifying eyepiece. If all of the wax becomes dissolved but the sample still seems to be stuck to the quartz disk, try squirting a little bit more acetone into the Petri dish to disturb it enough to fall off.

(k) Once the sample falls off of the quartz disk, carefully remove the quartz disk (try not to let it slip and fall on top of the sample) and magnetic stir bar from the Petri dish. Carefully remove the sample from the Petri dish by grabbing one end of the submerged filter paper with a pair of plastic

tweezers and then slowly lifting the filter paper with the sample out of the Petri dish. While still submerged, the very thin sample might move around a bit, but once it is out of the acetone the sample will tend to stick to the wet filter paper. Place another piece of filter paper in another (dry) Petri dish. Move the wet filter paper (holding your sample) over the filter paper and flip it upside down and on top of the dry filter paper. The sample should remain sticking to the wet filter paper while you flip the paper over. Wait for the sample to fall off of the wet paper onto the dry paper. Gently remove the wet paper, leaving the sample exposed. Very gently squirt some drops of IPA onto the sample. Once again, transfer the sample to another piece of dry filter paper in a Petri dish and squirt IPA a second time. To dry off the sample, just transfer it to a new dry piece of filter paper a few times.

7. **Wire-Up**

   (a) Clean the Teflon wire-up chuck (usually kept in the shared drawer near the wire-up station) by blowing with nitrogen gas.

   (b) Set convection oven to 125 °C (set knob to a little bit less than 5). During the rest of the wire-up procedures, check the temperature in the oven and adjust the temperature knob accordingly. Try to get it to within 2 degrees of 125 °C.

   (c) Solder wires to ohmic contacts and top gates with indium. Using pieces of 0.002" gold wire that are about 1-1.5 inches long. After soldering each wire, test its connection by nudging it with tweezers. You should be able to get the wire to bend near the solder blob without the wire becoming disconnected.

   (d) Transfer the sample (facing up) to the center of a circle of filter paper. Take a small glass beaker, turn it upside down, and place it over the sample, covering it. The wires should be poking out. Solder 4 of the top gate wires to the lip of the beaker using indium.

(e) Mix silver conducting epoxy (EpoTek H20E epoxy): 0.2 g of component A plus 0.2 g of component B. Measure out the epoxy components onto a glass slide covered with clean aluminum foil. Mix together the two components and stir with a clean wooden dowel for two minutes. Do not cross-contaminate the bottles with the two epoxy components.

(f) Epoxy wires to back gate pads. Use a sharpened wooden dowel to apply small blobs of epoxy and then lower or push the tips of gold wires into it. You can try adding a small blob on top of the wire's tip to reinforce the connection.

(g) Bake in oven at 125 °C for 25 minutes.

(h) Detach sample from glass beaker.

(i) Clip away the pins of an 18-pin header (leave behind a 1 mm of each pin so that you can wrap wires around them). Clean header by squirting with IPA and drying. Solder wires to header. Try to get the sample as level as possible. Any small amount of tilt could introduce a parallel magnetic field, which would influence interlayer tunneling at $\nu_T = 1$. Try to wrap excess wire around the header pins instead of just clipping them off; the excess might be useful when transferring the sample to a rotating sample holder.

Appendix D

Wire Bonding to Thin GaAs Samples

The Corbino samples used in this thesis contain a number of small contacts in their central regions. These contacts are not quite large enough to be soldered to by hand. Instead, we use a wire bonder to create conducting bridges from the inner contacts to much larger contact pads on the outer portions of the 5×5 mm^2 wafer piece. One can then solder gold wires to these outer pads using a soldering iron. Due to fabrication constraints, the wire bonding must be done after the GaAs piece has been thinned down to 50 μm. The thin sample is exceedingly delicate and light, so we must remount the sample with wax to provide mechanical support and to hold down the sample during wire bonding. This appendix describes this procedure.

First, one must complete all of the sample fabrication steps listed in Appendix C up until the back gates have been evaporated and the sample has been removed from the quartz disk. At this point, all lithography steps are done but the sample has not yet been wired up. To get the sample ready for wire bonding, one first solders a short ($\sim$1 inch) length of 0.002" gold wire with indium to one of the corners of the wafer piece. Choose a bare, unused region. The purpose of this wire is to allow one to pick up and manipulate the sample while it is thin.

Next, return to the clean room and place two or three grains of mounting wax next to each other in the center a quartz disk. Ideally, this should be a different disk then the one used for sample thinning. Melt the wax by using the grey hot plate on

setting 3. Make sure that there is a piece of aluminum foil covering the top of the hot plate; its reflective surface will prove useful for monitoring the mounting process. Wait for a few minutes to ensure that the wax has been completely melted. Try to obtain a single puddle of melted wax that is roughly 2 mm in diameter. While holding the attached gold wire with a pair of tweezers, lift up the thin sample directly over the puddle of wax and gently lower the sample onto the puddle. Do not force or pull it down once the sample is in contact with the wax. Instead, let go of the gold wire and let the weight of the sample squash the puddle. The wax will slowly spread out and cover most (if not all) of the back side of the sample. One can watch its progress in the reflective surface of the aluminum foil.

After a minute or two, the puddle of wax should have flowed out to cover the entire back side of the sample. Do not wait for so long that the wax begins to flow up onto the top side of the sample. Once satisfied, turn off the heat to the hot plate and gently remove the quartz disk. Allow to cool for five minutes. The sample should now be firmly mounted onto the quartz disk by the wax and is ready for wire bonding.

Take the sample to the West-Bond wire bonder.[1] The settings of the wire bonder must be chosen with care and will probably have to be adjusted each time you use it on a thin sample. We have found that the following settings are a good starting point:

Ultrasonic power (bond 1)	150 to 300
Ultrasonic power (bond 2)	300
Ultrasonic time (bond 1)	80 - 150 ms
Ultrasonic time (bond 2)	150 ms
Tool heat	5 - 6

Create the first bond on one of the outer Ni/AuGe bonding pads.[2] Make the second bond on one of the inner pads. Repeat for all of the other inner pads. Try

---

[1] West-Bond Model 7476E two way convertible, wedge-wedge bonder from West-Bond.

[2] For our particular wire bonder, we have had the most luck with bonding to annealed Ni/AuGe rather than just evaporated aluminum. Even annealed Ni/AuGe covered with aluminum will work fine. We have had a lot of difficulty of bonding to aluminum alone, however. We suspect that the rough surface of annealed Ni/AuGe helps with the bonding.

not to make the bridges too tall.

Once the wire bonding is completed, return to the clean room. Place the quartz disk with the sample in a Petri dish with a small circle of filter paper on the bottom. The side with the sample should be facing up, of course. Using a squirt bottle, gently squirt acetone into the Petri dish. Do not squirt directly at the sample! Add enough acetone to completely immerse the sample. Cover and let it sit at room temperature for 2 or 3 hours until the wax is completely dissolved. You can test this by using a pair of tweezers to gently nudge at the gold wire soldered to the sample; if the sample moves in response to this nudge, then the wax has been dissolved.

Get another Petri dish with filter paper and the isopropanol squirt bottle ready. Grasp the gold wire with tweezers and carefully (but firmly) pull the sample out of the acetone. The surface tension of the acetone will provide resistance. Without delay (do NOT let the acetone dry fully or it will leave behind a residue), transfer the thin sample to the other Petri dish and wet it with isopropanol. Again, do not squirt directly at the sample. Merely let some drops of the isopropanol fall close to the sample, but not directly onto it. One wants to quickly wash away any acetone before it forms a residue. After the sample has been fully wetted with isopropanol, remove it from that Petri dish and transfer to another (with filter paper on the bottom, once again) and allow to air dry.

You may now proceed with the standard wire-up steps. Be sure to use the soldering iron to remove the extra gold wire that was soldered to the corner of the sample.

Bibliography

[1] M. Abolfath, A. H. MacDonald, and L. Radzihovsky. *Phys. Rev. B*, 68:155318, 2003.

[2] V. Ambegaokar, B. I. Halperin, D. R. Nelson, and E. D. Siggia. *Phys. Rev. Lett.*, 40:783, 1978.

[3] P. W. Anderson. Coherent matter field phenomena in superfluids. In A. Gelbert, editor, *Some Recent Definitions in the Basic Sciences*, volume 2, pages 21–40. Belfer Graduate School of Science, Yeshiva University, New York, 1965-66.

[4] A. F. Andreev. *Sov. Phys. JETP*, 19:1228, 1964.

[5] D. Arovas, J. R. Schrieffer, and F. Wilczek. *Phys. Rev. Lett.*, 53:722, 1984.

[6] L. Balents and L. Radzihovsky. *Phys. Rev. Lett.*, 86:1825, 2001.

[7] G. S. Boebinger, H. L. Stormer, D. C. Tsui, A. M. Change, J. C. M. Hwang, A. Y. Cho, C. W. Tu, and G. Weimann. *Phys. Rev. B*, 36:7919, 1987.

[8] A. A. Burkov and A. H. MacDonald. *Phys. Rev. B*, 66:115320, 2002.

[9] M. Büttiker. *Phys. Rev. B*, 38:9375, 1988.

[10] T. Chakraborty and P. Pietiläinen. *Phys. Rev. Lett.*, 59:2784, 1987.

[11] A. R. Champagne. private communication.

[12] A. R. Champagne, J. P. Eisenstein, L. N. Pfeiffer, and K. W. West. *Phys. Rev. Lett.*, 100:096801, 2008.

[13] A. R. Champagne, A. D. K. Finck, J. P. Eisenstein, L. N. Pfeiffer, and K. W. West. *Phys. Rev. B*, 78:205310, 2008.

[14] J. H. Davies. *The Physics of Low-Dimensional Semiconductors: An Introduction.* Cambridge University Press, 1998.

[15] R. R. Du, H. L. Stormer, D. C. Tsui, L. N. Pfeiffer, and K. W. West. *Phys. Rev. Lett.*, 70:2944, 1993.

[16] R. R. Du, H. L. Stormer, D. C. Tsui, L. N. Pfeiffer, and K. W. West. *Solid State Commun.*, 90:71, 1994.

[17] R. R. Du, H. L. Stormer, D. C. Tsui, A. S. Yeh, L. N. Pfeiffer, and K. W. West. *Phys. Rev. Lett.*, 73:3274, 1994.

[18] P. R. Eastham, N. R. Cooper, and D. K. K. Lee. *Phys. Rev. B*, 80:045302, 2009.

[19] P. R. Eastham, N. R. Cooper, and D. K. K. Lee. *Phys. Rev. Lett.*, 105:236805, 2010.

[20] A. L. Efros and F. G. Pikus. *Phys. Rev. B*, 48:14694, 1993.

[21] J. P. Eisenstein. private communication.

[22] J. P. Eisenstein. In S. Das Sarma and A. Pinczuk, editors, *Perspectives in Quantum Hall Effects.* John Wiley, 1997.

[23] J. P. Eisenstein. *Solid State Commun.*, 127:123, 2003.

[24] J. P. Eisenstein. Course 2: Novel phenomena in double layer two-dimensional electron systems. In H. Bouchiat, Y. Gefen, S. Gueron, G. Montambaux, and J. Dalibard, editors, *Les Houches Summer School Proceedings, Nanophysics: Coherence and Transport, École d'été de Physique des Houches Session LXXXI*, volume 81, pages 129–176. Elsevier, 2005.

[25] J. P. Eisenstein, G. S. Boebinger, L. N. Pfeiffer, K. W. West, and Song He. *Phys. Rev. Lett.*, 68:1383, 1992.

[26] J. P. Eisenstein, L. N. Pfeiffer, and K. W. West. *Appl. Phys. Lett.*, 57:2324, 1990.

[27] J. P. Eisenstein, L. N. Pfeiffer, and K. W. West. *Phys. Rev. Lett.*, 69:3804, 1992.

[28] J. P. Eisenstein, L. N. Pfeiffer, and K. W. West. *Phys. Rev. Lett.*, 68:674, 1992.

[29] J. P. Eisenstein, L. N. Pfeiffer, and K. W. West. *Phys. Rev. B*, 50:1760, 1994.

[30] Z. F. Ezawa and A. Iwazaki. *Phys. Rev. B*, 47:7295, 1993.

[31] R. Ferrell and R. Prange. *Phys. Rev. Lett.*, 10:479, 1963.

[32] H. A. Fertig. *Phys. Rev. B*, 40:1087, 1989.

[33] H. A. Fertig and G. Murthy. *Phys. Rev. Lett.*, 95:156802, 2005.

[34] H. A. Fertig and J. P. Straley. *Phys. Rev. Lett.*, 91:046806, 2003.

[35] D. V. Fil and S. I. Shevchenko. *Low Temp. Phys.*, 33:780, 2007.

[36] D. V. Fil and S. I. Shevchenko. *J. Phys.: Condens. Matter*, 21:215701, 2009.

[37] A. D. K. Finck, A. R. Champagne, J. P. Eisenstein, L. N. Pfeiffer, and K. W. West. *Phys. Rev. B*, 78:075302, 2008.

[38] A. D. K. Finck, J. P. Eisenstein, L. N. Pfeiffer, and K. W. West. *Phys. Rev. Lett.*, 104:016801, 2010.

[39] A. D. K. Finck, J. P. Eisenstein, L. N. Pfeiffer, and K. W. West. *Phys. Rev. Lett.*, 106:236807, 2011.

[40] M. M. Fogler and F. Wilczek. *Phys. Rev. Lett.*, 86:1833, 2001.

[41] N. Freytag, M. Horvatić, C. Berthier, M. Shayegan, and L. P. Lévy. *Phys. Rev. Lett.*, 89:246804, 2002.

[42] P. Giudici, K. Muraki, N. Kumada, Y. Hirayama, and T. Fujisawa. *Phys. Rev. Lett.*, 100:106803, 2008.

[43] V. J. Goldman, B. Su, and J. K. Jain. *Phys. Rev. Lett.*, 72:2065, 1994.

[44] T. J. Gramila, J. P. Eisenstein, A. H. MacDonald, L. N. Pfeiffer, and K. W. West. *Phys. Rev. Lett.*, 66:1216, 1991.

[45] T. J. Gramila, J. P. Eisenstein, A. H. MacDonald, L. N. Pfeiffer, and K. W. West. *Phys. Rev. B*, 47:12957, 1993.

[46] F. D. M. Haldane. *Phys. Rev. Lett.*, 51:605, 1983.

[47] B. I. Halperin. *Phys. Rev. B*, 25:2185, 1982.

[48] B. I. Halperin. *Helvetica Physica Acta*, 56:75, 1983.

[49] B. I. Halperin. *Phys. Rev. Lett.*, 52:1583, 1984.

[50] B. I. Halperin, Patrick A. Lee, and Nicholas Read. *Phys. Rev. B*, 47:7312, 1993.

[51] M. Z. Hasan and C. L. Kane. *Rev. Mod. Phys.*, 82:3045, 2010.

[52] L. Hedin and B. I. Lundqvist. *J. Phys. C*, 4:2064, 1971.

[53] J. Hu and A. H. MacDonald. *Phys. Rev. B*, 46:12554, 1992.

[54] T. Hyart and B. Rosenow. *Phys. Rev. B*, 83:155315, 2011.

[55] R. L. Jack, D. K. K. Lee, and N. R. Cooper. *Phys. Rev. Lett.*, 93:126803, 2004.

[56] R. L. Jack, D. K. K. Lee, and N. R. Cooper. *Phys. Rev. B*, 71:085310, 2005.

[57] J. K. Jain. *Phys. Rev. Lett.*, 63:199, 1989.

[58] J. K. Jain. *Composite Fermions*. Cambridge University Press, 2007.

[59] A.-P. Jauho and H. Smith. *Phys. Rev. B*, 47:4420, 1993.

[60] Y. N. Joglekar and A. H. MacDonald. *Phys. Rev. B*, 64:155315, 2001.

[61] P. Johansson and J. M. Kinaret. *Phys. Rev. Lett.*, 71:1435, 1993.

[62] T. Jungwirth and A. H. MacDonald. *Phys. Rev. B*, 53:7403, 1996.

[63] W. Kang, H. L. Stormer, L. N. Pfeiffer, K. W. Baldwin, and K. W. West. *Phys. Rev. Lett.*, 71:3840, 1993.

[64] M. Kellogg. PhD thesis, California Institute of Technology, 2005.

[65] M. Kellogg, J. P. Eisenstein, L. N. Pfeiffer, and K. W. West. *Phys. Rev. Lett.*, 90:246801, 2003.

[66] M. Kellogg, J. P. Eisenstein, L. N. Pfeiffer, and K. W. West. *Phys. Rev. Lett.*, 93:036801, 2004.

[67] M. Kellogg, I. B. Spielman, J. P. Eisenstein, L. N. Pfeiffer, and K. W. West. *Phys. Rev. Lett.*, 88:126804, 2002.

[68] C. Kittel. *Introduction to Solid State Physics, Seventh Edition*. John Wiley, 1996.

[69] I. V. Kukushkin, J. H. Smet, K. von Klitzing, and W. Wegscheider. *Nature*, 415:409, 2002.

[70] I. V. Kukushkin, K. v. Klitzing, and K. Eberl. *Phys. Rev. Lett.*, 82:3665, 1999.

[71] N. Kumada, K. Muraki, K. Hashimoto, and Y. Hirayama. *Phys. Rev. Lett.*, 94:096802, 2005.

[72] R. Landauer. *Philos. Mag.*, 21:863, 1970.

[73] R. B. Laughlin. *Phys. Rev. Lett.*, 50:1395, 1983.

[74] D. R. Leadley, R. J. Nicholas, C. T. Foxon, and J. J. Harris. *Phys. Rev. Lett.*, 72:1906, 1994.

[75] Y. Q. Li, V. Umansky, K. von Klitzing, and J. H. Smet. *Phys. Rev. Lett.*, 102:046803, 2009.

[76] M. P. Lilly, J. P. Eisenstein, L. N. Pfeiffer, and K. W. West. *Phys. Rev. Lett.*, 80:1714, 1998.

[77] A. Lopez and E. Fradkin. *Phys. Rev. B*, 44:5246, 1991.

[78] O. V. Lounasmaa. *Experimental Principles and Methods Below 1K*. Academic Press, 1974.

[79] S. Luryi. *Appl. Phys. Lett.*, 52:501, 1988.

[80] A. H. MacDonald. *Physica B*, 298:129, 2001.

[81] S. Melinte, N. Freytag, M. Horvatić, C. Berthier, L. P. Lévy, V. Bayot, and M. Shayegan. *Phys. Rev. Lett.*, 84:354, 2000.

[82] K. Moon, H. Mori, K. Yang, S. M. Girvin, A. H. MacDonald, L. Zheng, D. Yoshioka, and S.-C. Zhang. *Phys. Rev. B*, 51:5138, 1995.

[83] R. H. Morf. *Phys. Rev. Lett.*, 83:1485, 1999.

[84] S. Q. Murphy, J. P. Eisenstein, G. S. Boebinger, L. N. Pfeiffer, and K. W. West. *Phys. Rev. Lett.*, 72:728, 1994.

[85] S. Q. Murphy, J. P. Eisenstein, L. N. Pfeiffer, and K. W. West. *Phys. Rev. B*, 52:14825, 1995.

[86] D. D. Osheroff, W. J. Gully, R. C. Richardson, and D. M. Lee. *Phys. Rev. Lett.*, 29:920, 1972.

[87] D. D. Osheroff, R. C. Richardson, and D. M. Lee. *Phys. Rev. Lett.*, 28:885, 1972.

[88] K. Park and J. K. Jain. *Phys. Rev. Lett.*, 80:4237, 1998.

[89] K. Park, N. Meskini, and J. K. Jain. *J. Phys.: Condens. Matter*, 11:7283, 1999.

[90] K. Park and S. Das Sarma. *Phys. Rev. B*, 74:035338, 2006.

[91] B. Roostaei, K. J. Mullen, H. A. Fertig, and S. H. Simon. *Phys. Rev. Lett.*, 101:046804, 2008.

[92] E. Rossi, A. S. Núñez, and A. H. MacDonald. *Phys. Rev. Lett.*, 95:266804, 2005.

[93] P. P. Ruden and Z. Wu. *Appl. Phys. Lett.*, 59:2165, 1991.

[94] V. W. Scarola and J. K. Jain. *Phys. Rev. B*, 64:085313, 2001.

[95] J. Schliemann, S. M. Girvin, and A. H. MacDonald. *Phys. Rev. Lett.*, 2001:1849, 2001.

[96] J. H. Scofield. *Am. J. Phys.*, 62:129, 1994.

[97] R. Shankar and G. Murthy. *Phys. Rev. Lett.*, 79:4437, 1997.

[98] D. N. Sheng, L. Balents, and Z. Wang. *Phys. Rev. Lett.*, 91:116802, 2003.

[99] D. N. Sheng, X. Wan, E. H. Rezayi, K. Yang, R. N. Bhatt, and F. D. M. Haldane. *Phys. Rev. Lett.*, 90:256802, 2003.

[100] S. H. Simon, E. H. Rezayi, and M. V. Milovanovic. *Phys. Rev. Lett.*, 91:046803, 2003.

[101] S. L. Sondhi, A. Karlhede, S. A. Kivelson, and E. H. Rezayi. *Phys. Rev. B*, 47:16419, 1993.

[102] I. B. Spielman. PhD thesis, California Institute of Technology, 2004.

[103] I. B. Spielman, J. P. Eisenstein, L. N. Pfeiffer, and K. W. West. *Phys. Rev. Lett.*, 84:5808, 2000.

[104] I. B. Spielman, J. P. Eisenstein, L. N. Pfeiffer, and K. W. West. *Phys. Rev. Lett.*, 87:036803, 2001.

[105] I. B. Spielman, M. Kellogg, J. P. Eisenstein, L. N. Pfeiffer, and K. W. West. *Phys. Rev. B*, 70:081303, 2004.

[106] I. B. Spielman, L. A. Tracy, J. P. Eisenstein, L. N. Pfeiffer, and K. W. West. *Phys. Rev. Lett.*, 94:076803, 2005.

[107] A. Stern, S. M. Girvin, A. H. MacDonald, and N. Ma. *Phys. Rev. Lett.*, 86:1829, 2001.

[108] A. Stern and B. I. Halperin. *Phys. Rev. Lett.*, 88:106801, 2002.

[109] A. Stern, S. Das Sarma, M. P. A. Fisher, and S. M. Girvin. *Phys. Rev. Lett.*, 84:139, 2000.

[110] H. L. Stormer, A. Chang, D. C. Tsui, J. C. M. Hwang, A. C. Gossard, and W. Wiegmann. *Phys. Rev. Lett.*, 50:1953, 1983.

[111] J.-J. Su and A. H. MacDonald. *Nature Physics*, 4:799, 2008.

[112] J.-J. Su and A. H. MacDonald. *Phys. Rev. B*, 81:184523, 2010.

[113] Y. W. Suen, L. W. Engel, M. B. Santos, M. Shayegan, and D. C. Tsui. *Phys. Rev. Lett.*, 68:1379, 1992.

[114] J. Sun, G. Murthy, H. A. Fertig, and N. Bray-Ali. *Phys. Rev. B*, 81:195314, 2010.

[115] L. Tiemann. PhD thesis, University of Bielefeld, 2008.

[116] L. Tiemann, W. Dietsche, M. Hauser, and K. von Klitzing. *New J. of Phys.*, 10:045018, 2008.

[117] L. Tiemann, J. G. S. Lok, W. Dietsche, K. von Klitzing, K. Muraki, D. Schuh, and W. Wegscheider. *Phys. Rev. B*, 77:033306, 2008.

[118] L. A. Tracy, J. P. Eisenstein, L. N. Pfeiffer, and K. W. West. *Phys. Rev. Lett.*, 98:086801, 2007.

[119] D. C. Tsui, H. L. Stormer, and A. C. Gossard. *Phys. Rev. Lett.*, 48:1559, 1982.

[120] E. Tutuc, R. Pillarisetty, and M. Shayegan. *Phys. Rev. B*, 79:026402, 2009.

[121] E. Tutuc, M. Shayegan, and D. A. Huse. *Phys. Rev. Lett.*, 93:036802, 2004.

[122] K. von Klitzing, G. Dorda, and M. Pepper. *Phys. Rev. Lett.*, 45:494, 1980.

[123] Z. Q. Wang. *Phys. Rev. Lett.*, 92:136803, 2004.

[124] Z. Q. Wang. *Phys. Rev. Lett.*, 94:176804, 2005.

[125] X. G. Wen and A. Zee. *Phys. Rev. Lett.*, 69:1811, 1992.

[126] X. G. Wen and A. Zee. *Phys. Rev. B*, 47:2265, 1993.

[127] R. Wiersma, J. G. S. Lok, S. Kraus, W. Dietsche, K. von Klitzing, D. Schu, M. Bichler, H.-P. Tranitz, and W. Wegscheider. *Phys. Rev. Lett.*, 93:266805, 2004.

[128] R. L. Willett, R. R. Ruel, K. W. West, and L. N. Pfeiffer. *Phys. Rev. Lett.*, 71:3846, 1993.

[129] K. Yang. *Phys. Rev. B*, 58:R4246, 1998.

[130] K. Yang, K. Moon, L. Belkhir, H. Mori, S. M. Girvin, A. H. MacDonald, L. Zheng, and D. Yoshioka. *Phys. Rev. B*, 54:11644, 1996.

[131] K. Yang, K. Moon, L. Zheng, A. H. MacDonald, S. M. Girvin, D. Yoshioka, and S.-C. Zhang. *Phys. Rev. Lett.*, 72:732, 1994.

[132] Y. Yoon, L. Tiemann, S. Schmult, W. Dietsche, K. von Klitzing, and W. Wegscheider. *Phys. Rev. Lett.*, 104:116802, 2010.

[133] D. Yoshioka. *J. Phys. Soc. Jpn.*, 55:885, 1986.

[134] D. Yoshioka, A. H. MacDonald, and S. M. Girvin. *Phys. Rev. B*, 39:1932, 1989.

[135] D. Yoshioka and N. Shibata. *J. Phys. Soc. Jpn*, 79:064717, 2010.

[136] C. Zener. *Proc. R. Soc. A*, 145:523, 1934.

[137] S. C. Zhang, T. H. Hansson, and S. Kivelson. *Phys. Rev. Lett.*, 62:82, 1989.

[138] L. Zheng and A. H. MacDonald. *Phys. Rev. B*, 47:10619, 1993.

[139] Y. Zou, G. Refael, A. Stern, and J. P. Eisenstein. *Phys. Rev. B*, 81:205313, 2010.